



COPYRIGHT AND USE OF THIS THESIS

This thesis must be used in accordance with the provisions of the Copyright Act 1968.

Reproduction of material protected by copyright may be an infringement of copyright and copyright owners may be entitled to take legal action against persons who infringe their copyright.

Section 51 (2) of the Copyright Act permits an authorized officer of a university library or archives to provide a copy (by communication or otherwise) of an unpublished thesis kept in the library or archives, to a person who satisfies the authorized officer that he or she requires the reproduction for the purposes of research or study.

The Copyright Act grants the creator of a work a number of moral rights, specifically the right of attribution, the right against false attribution and the right of integrity.

You may infringe the author's moral rights if you:

- fail to acknowledge the author of this thesis if you quote sections from the work
- attribute this thesis to another author
- subject this thesis to derogatory treatment which may prejudice the author's reputation

For further information contact the University's Copyright Service.

sydney.edu.au/copyright

A new approach to classical spectroscopy.

by

Christopher H. Betters



A THESIS SUBMITTED IN FULFILMENT
OF THE REQUIREMENTS FOR THE DEGREE OF

DOCTOR OF PHILOSOPHY
FACULTY OF SCIENCE
THE UNIVERSITY OF SYDNEY

SEPTEMBER, 2015

© CHRISTOPHER H. BETTERS
ALL RIGHTS RESERVED, 2015

Abstract

In this thesis I demonstrate a new approach to classical fibre-fed spectroscopy. My method is to use a photonic lantern device that converts an arbitrary (e.g. incoherent) input beam into N diffraction-limited outputs. For the highest throughput, the number of outputs must be matched to the total number of unpolarised spatial modes on input. This approach has many advantages: (i) after the lantern, the instrument is constructed from ‘commercial off the shelf’ components; (ii) the instrument is the minimum size and mass configuration at a fixed resolving power and spectral order; (iii) the throughput can be better than 60% (slit to detector, including detector QE of $\sim 80\%$); (iv) the scattered light at the detector can be less than 0.1% (total power). I have designed and built 3 such instruments, one operating in the infrared and two operating in the visible wavelengths of light. What follows is a study of the design implications for such a spectrograph, and an experimental exploration of their characteristics. I also present a versatile data reduction package I have developed in tandem with the instruments.

Acknowledgements

Fist off I would like to thank my supervisors Joss Bland-Hawthorn and Sergio Leon-Saval. Without your support (and encouragement) this thesis would never have been finished. I'd also like to thanks Gordon Robertson for his insightful comments on both my first paper and the super fast turnaround on providing feedback for this thesis. I was funded in part by tuition scholarship from the Faculty of Science and directly by Joss, again with out this support none of this would have been possible. During my candidature I've had some terrific opportunities, from launch a high altitude balloon in South Australia to presenting my work at SPIE Astronomy meetings Amsterdam (2012) and Montreal (2014).

Thanks to all the people of the School of Physics and Sydney Institute for Astronomy for various bits of help and friend ship. I've made some great friends, whom I hope never become strangers. I'd also like to thanks everyone at the Australian-Astronomical Observatory, in particular Jon Lawrence, who allowed me to join several trip to Sidings Springs and loaned use various bit of equipment.

Thanks to my parents, Tim and Melissa, your unwavering support in ev- erything has been unreal. Thanks to friends new and old who have made the past four years great (and those shared all of the beer): Maz Ali, Nicola Asquith, Cameron Boon, John Ching, Jason Drury, Pascal Elahi, Claire Francis, Jane Kaczmarek, Charles Kuehn, Emma Lindley, Rebecca McEl- roy, Vanessa Moss, Matthew Nichols, Barnaby Norris, Aideen O'Connor, Sarah Reeves, David Rossetto, Fiona Schleyer, Kiri Simon, Paul Stewart, David Webster, Nick Wilson, Tim White. You are all awesome.

Declaration of Originality

This thesis describes work carried out in the Sydney Institute for Astronomy, within the School of Physics, University of Sydney, between February 2011 and March 2015. The work presented in this thesis is, to the best of my knowledge and belief, original except as acknowledged in the text. I hereby declare that I have not submitted this material, either in full or in part, for a degree or diploma at this university or any other institution.



Christopher H. Betters
Tuesday 21st April, 2015

Publications And Contribution

Journal Papers

- **Paper 1:** C. H. **Butters**, S. G. Leon-Saval, J. G. Robertson, and J. Bland-Hawthorn (2013). “Beating the classical limit: A diffraction-limited spectrograph for an arbitrary input beam”. *Optics Express* 21.22, p. 26103. doi: [10.1364/OE.21.026103](https://doi.org/10.1364/OE.21.026103). arXiv: [1310.4833 \[astro-ph.IM\]](https://arxiv.org/abs/1310.4833)
Contents included as part of Sec. 4.1 and throughout Chap. 3.
- N. Cvetojevic, N. Jovanovic, C. **Butters**, J. S. Lawrence, S. C. Ellis, G. Robertson, and J. Bland-Hawthorn (2012a). “First starlight spectrum captured using an integrated photonic micro-spectrograph”. *A&A* 544, L1. doi: [10.1051/0004-6361/201219116](https://doi.org/10.1051/0004-6361/201219116). arXiv: [1208.4418 \[astro-ph.IM\]](https://arxiv.org/abs/1208.4418)

Refereed Conference Papers

- Christopher H **Butters**, Joss Bland-Hawthorn, and Sergio G. Leon-Saval (2012c). “Results of a single-mode multicore fibre bundle fed diffraction-limited spectrograph”. In: *37th Australian Conference on Optical Fibre Technology*
Contents included as part of Sec. 4.1 and Sec. 3.1.2.
- C **Butters**, I H Cairns, J Bland-Hawthorn, X Wu, L Fogarty, J Funamoto, S G Leon-Saval, A Monger, and S Z A Xiao (2011). “Instrumentation of the i-INSPIRE satellite.” In: *Proceeding of the 11th Australian Space Science Conference*. Ed. by Wayne Short and Iver Cairns. National Space Society of Australia Ltd, Sydney, Australia, pp. 257–266. ISBN: 978-0-9775740-5-6
Contents include as part of Sec. 4.3 and Sec. 6.3.
- Lisa Fogarty, Iver H Cairns, Joss Bland-Hawthorn, Xiaofeng Wu, Christopher H **Butters**, Jiro Funamoto, S G Leon-Saval, Tony Monger, and Size Xiao (2011). “The initial INtegrated SPectrograph, Imager and Radiation Explorer (i-INSPIRE) - a university satellite project.” In: *Proceeding of the 11th Australian Space Science Conference*. Ed. by Wayne Short and Iver Cairns. National Space Society of Australia Ltd, Sydney, Australia, pp. 249–256. ISBN: 978-0-9775740-5-6

-
- Size Xiao, Xiaofeng Wu, Iver H Cairns, Joss Bland-Hawthorn, Christopher H **Butters**, Jiro Funamoto, S G Leon-Saval, Lisa Fogarty, Tony Monger, and Xueliang Bai (2011). “i-INSPIRE Tube-Satellite Bus Design”. In: *Proceeding of the 11th Australian Space Science Conference*. Ed. by Wayne Short and Iver Cairns. National Space Society of Australia Ltd, Sydney, Australia, pp. 267–274. ISBN: 978-0-9775740-5-6

Conference Papers

- C. H. **Butters**, S. G. Leon-Saval, J. Bland-Hawthorn, and G. Robertson (2012b). “Demonstration and design of a compact diffraction limited spectrograph”. In: *Proc. SPIE*. vol. 8446, 84463H. doi: [10.1117/12.925824](https://doi.org/10.1117/12.925824)
Contents included as part of Sec. 3.2.1, Sec. 3.2 and Sec. 4.1.
- C. H. **Butters**, S. G. Leon-Saval, and J. Bland-Hawthorn (2012a). “NanoSpec: a diffraction limited micro-spectrograph for pico- and nano-satellites”. In: *Proc. SPIE*. vol. 8442, 84424B. doi: [10.1117/12.925819](https://doi.org/10.1117/12.925819)
Contents included as part of Sec. 4.3.
- S. G. Leon-Saval, C. H. **Butters**, and J. Bland-Hawthorn (2012). “The Photonic TIGER: a multicore fiber-fed spectrograph”. In: *Proc. SPIE*. vol. 8450. The Univ. of Sydney (Australia), 84501K. doi: [10.1117/12.925254](https://doi.org/10.1117/12.925254). arXiv: [1208.3006 \[astro-ph.IM\]](https://arxiv.org/abs/1208.3006)
Contents included as part of Sec. 3.1.2.
- C. Schwab, S. G. Leon-Saval, C. H. **Butters**, J. Bland-Hawthorn, and S. Mahadevan (2012). “Single mode, extreme precision Doppler spectrographs”. In: *Proceedings of the 2012 IAU GA*. arXiv: [1212.4867 \[astro-ph.IM\]](https://arxiv.org/abs/1212.4867)
- L. M. R. Fogarty, S. Z. (Xiao, J. Funamoto, I. H. Cairns, J. Bland-Hawthorn, X. Wu, C. H. **Butters**, S. G. Leon-Saval, and A. G. Monger (2012). “The i-INSPIRE satellite: a university pico-satellite project”. In: *Proc. SPIE*. vol. 8442, 84421B. doi: [10.1117/12.925709](https://doi.org/10.1117/12.925709)
- Jon Lawrence, Christopher H **Butters**, Joss Bland-Hawthorn, Nick Cvetojevic, Simon Ellis, Roger Haynes, Anthony Horton, Nemanja Jovanovic, Sergio Leon-Saval, and Gordon Robertson (2010). “Development of an Array-Waveguide Grating Astronomical Spectrograph”. In: *Frontiers in Optics*. Washington, D.C.: OSA, FTuU4. doi: [10.1364/FIO.2010.FTuU4](https://doi.org/10.1364/FIO.2010.FTuU4)
- J. Bland-Hawthorn, J. Lawrence, G. Robertson, S. Campbell, B. Pope, C. **Butters**, S. Leon-Saval, T. Birks, R. Haynes, N. Cvetojevic, and N. Jovanovic (2010). “PIMMS: photonic integrated multimode microspectrograph”. In: *Proc. SPIE*. vol. 7735, 77350N. doi: [10.1117/12.856347](https://doi.org/10.1117/12.856347)

Contents

Abstract	iii
Acknowledgements	i
Declaration of Originality	ii
Publications And Contribution	iii
List of Figures	vii
List of Tables	ix
1 Classical Spectroscopy	1
1.1 An Introduction	1
1.2 Types of Spectrographs	3
1.3 The Diffraction Limit	7
1.4 Figures of Merit	8
2 Astrophotonics	13
2.1 The Photonic Lantern	16
2.2 PIMMS	17
3 PIMMS Design Principles	20
3.1 Photonic Lantern as input to a spectrograph	21
3.2 Spectral Resolution/Resolving Power	28
3.3 Detector Area Implications	30
4 The Spectrographs	35
4.1 PIMMS IR	35
4.2 PIMMS Visible	51
4.3 NanoSpec	63

CONTENTS

5 Reduction package and calibration	72
5.1 MISPRINT	72
5.2 Fabry-Perot Etalon (Laser Comb) Calibration	82
5.3 Image Aberration Correction	83
6 Applications of PIMMS	87
6.1 PIMMS Visible: Solar Oscillations	87
6.2 PIMMS Visible: Telescope	93
6.3 NanoSpec: High Altitude	96
7 Conclusions	98
7.1 Future Work	99
References	102
Acronyms and Definitions	110
A MISPRINT Class	112
B ZEMAX Macro to setup échelle wavelength and orders	135
C Included Papers	137
C.1 Paper 1 — Beating the classical limit: A diffraction-limited spectrograph for an arbitrary input beam, Optics Express Vol. 21, No. 22	138

List of Figures

1.1	Interferometric Spectrometers	5
1.2	Schematic of a dispersive spectrograph	6
1.3	Sample Echellogram	7
1.4	Étendue illustration	9
1.5	Comparison standard resolution elements.	11
2.1	Comparison of multi-mode (MM) and single-mode (SM) slit.	15
2.2	Schematic photonic lantern types	17
2.3	Diagram of the PIMMS#0 basic layout.	18
2.4	Diagram of the PIMMS#1 basic layout	19
3.1	Image of a fibre V-groove array.	22
3.2	Sample Image from TIGER spectrograph	23
3.3	Linear vs. Hexagonal Slit	24
3.4	Schematic diagram of a hexagonal grid core spacing.	25
3.5	Simulated Photonic TIGER spectra.	27
3.6	Power transmitted and K truncation factor	30
3.7	Schematic of the multi-mode fibre (MMF) slit and single-mode fibre (SMF) pseudo-slit.	31
4.1	3D layout of the PIMMS IR.	38
4.2	Ray tracing spot diagrams of PIMMS IR.	41
4.3	Physical optics profiles of PIMMS IR	43
4.4	PIMMS IR PSF	44
4.5	Resolution Vs Dynamic Range of PIMMS IR	46
4.6	Resolving power vs Wavelength of PIMMS IR	47
4.7	Images showing rotation of a 1×7 fibre bundle	48
4.8	PIMMS IR Solar Spectrum	49
4.9	Image of the actual PIMMS visible bench setup	52
4.10	pot Diagrams PIMMS visible orders 73, 79 and 86	55
4.11	Full-field ray-trace PIMMS Visible.	56

LIST OF FIGURES

4.12 Typical profiles (in échelle dispersion and cross-dispersion direction) of the physical optics propagation (POP) simulation (the profiles are actually the 2D image collapsed in one dimension and normalised). The red dashed line shows the residual between the Gaussian fit and POP simulation.	58
4.13 Simulated and measured image quality of PIMMS visible	59
4.14 Raw Thorium-Argon (ThAr) echellogram.	60
4.15 ThAr Cross-Correlation Mosaic	61
4.16 PIMMS visible stability	62
4.17 Diagram of i-INSPRE satellite and PCB dimensions	64
4.18 Čerenkov cone diagram	66
4.19 Photonic crystal fibre end-face and MFD	67
4.20 NanoSpec Optical Layout	68
4.21 Ray tracing spot diagram of NanoSpec	69
4.22 CAD drawings and photographs of both NanoSpec housings	71
5.1 Basic Reduction Process Flow Chart	73
5.2 Cross-dispersion profile of flat-field.	75
5.3 Interpolated position trace plotted on raw echellogram and the corresponding extracted spectra.	76
5.4 Example of model profiles used in spectral extraction.	79
5.5 Wavelength Calibration GUI	81
5.6 PIMMS visible etalon spectrum	83
5.7 and spot diagram of modified PIMMS visible	84
5.8 Single Order Etalon Spectrum	85
5.9 Etalon PSF and aberration correction	86
6.1 PSD of BiSON	88
6.2 Simulations of solar oscillations observations.	89
6.3 PIMMS Visible Sun Spec	90
6.4 Spectral Line Shifts of Solar Observations	92
6.5 Solar PSD	93
6.6 Spectra of Alpha-Centauri	95
6.7 Integration Photo	97
6.8 Ballon Spectra	97

List of Tables

3.1	Definition of key parameters in Fig. 3.4.	25
4.2	Estimated resolving power of PIMMS IR	42
4.3	Summary of the maximum contrast required to resolve neighbouring spectral lines shown in Fig. 4.5	46
4.4	Summary of PIMMS#0 échelle design specification	51
4.5	Wavelength coverage of PIMMS visible diffraction orders	57
5.1	Definitions of variables used in reduction process	74

1

Classical Spectroscopy

1.1 An Introduction

Spectroscopy is study of the interaction between matter and electromagnetic radiation using measurements of relative intensities as a function of wavelength or frequency. It is one of the most fundamental techniques available to astronomers, or indeed any experimental scientist. With it, a plethora of physical properties including (but not limited to) chemical composition, age (with theoretical models), distance, temperature and even dynamics can be probed. The tools used to obtain a spectrum are collectively known as spectrographs or spectrometers and come in a variety forms to suit a variety of purposes. Here I will only be considering ‘optical’ spectrographs (i.e. operating in the **ultraviolet (UV)** through to the **near-infrared (NIR)** and using conventional optics, or \sim 300nm to $2\ \mu\text{m}$).

Astronomical spectrographs tend to be highly specialised bespoke instruments, designed for a specific telescope and science goal(s). Further, these instruments are normally designed to match the expected **seeing¹** of the site of its host telescope. Consequently the size of the spectrograph increases proportionally to the diameter, D , of the telescope, and the cost increases as D^2 (Bland-Hawthorn and Horton 2006). In the current generation of large telescopes (8-10m class) these instruments are already approaching a physical limit, beyond which optics become impractically large (especially with transmissive optics) and overall costs begin to rival that of the telescope. This presents a particular challenge for the next generation of 20-30 m class telescopes. There are currently three projects, the European Extremely Large Telescope (E-ELT; McPherson et al. 2012; Zeeuw et al. 2014); the Thirty Metre Telescope (TMT; Stepp 2012), and the Giant Magellan Telescope (GMT; Bernstein et al. 2014). Some proposed instrumentation

¹Blurring of a telescope image due to atmospheric turbulence

1.1 An Introduction

for these telescopes have projected costs similar to that of an 8 m class telescope (~\$50-100 million).

One of the most promising solutions is the so called ‘divide and conquer’ approach. By splitting light from the telescope across multiple replicated instruments the overall complexity can be reduced (Hill 2014). The principle has already successfully been demonstrated by VIRUS (Hill et al. 2012) on the Hobby-Eberly Telescope and MUSE (Bacon et al. 2010), a 2nd generation instrument, on the Very Large Telescope (VLT). One of the key advantages of these replicated spectrographs is that they begin to weaken the dependence of the spectrograph size on the telescope diameter. However, they are still fundamentally limited by the size of relay optics (say an optical fibre or an image slicing device) that are used to split the light from the telescope. Additionally, while the replication helps reduce costs, they are still bespoke instruments that do not yet enjoy the benefits of economies of scale. The ideal instrument for this approach would be usable at multiple telescopes, allowing it to be replicated on a larger scale.

One of the great advantages of the larger telescopes is the increased collecting area, leading to reduced integration times and/or greater sensitivity, but obtaining observation time on these larger telescope is extremely competitive/expensive (e.g. the Keck telescope operating costs are ~\$100K per night). As a result most observatories routinely deploy smaller (and much cheaper) telescopes that can be devoted to a single task for extended periods (such as monitoring a star for the radial velocity signature of orbiting planets, or performing a detailed survey of the entire night sky). It is these smaller telescopes that would most benefit from a highly replicable spectrograph design.

In order for a spectrograph to be truly independent of the input telescope, the telescope would need to be diffraction-limited, and thus the spectrograph design could then be diffraction-limited. With the most advanced adaptive optics (AO) systems some telescopes are getting close, however the vast majority are still fundamentally limited by atmospheric seeing. This is especially true when operating in the visible wavelengths where AO systems are still an unsolved problem (although things are improving, e.g. Close et al. (2014) achieves 30% of the diffraction-limit at 630 nm). Nonetheless, in the vast majority of spectrographs it is this seeing that determines the size of the entrance aperture/slit. Image slicers can reduce this size, bringing the spectrograph closer to the diffraction limit. The most promising technology for doing this efficiently is called the photonic lantern (PL) (cf. Leon-Saval et al. 2013, and Sec. 2.1). It allows for the efficient conversion of a multi-mode fibre (MMF) (which can couple efficiently to the seeing-limited focus of a telescope) to several single-mode fibres (SMFs) (which are by definition diffraction-limited). This technology is discussed in Chap. 2 and its implications for spectrograph design form the main focus of this thesis.

However, regardless of whether a spectrograph is a behemoth paired to the largest telescope or a small hand-held laboratory device there are some fundamental similarities they all share. These will be discussed in the remaining sections of this chapter. The contents of Chap. 2 are an introduction to the details of the PL and the new field it enables, Astrophotonics. In Chap. 3, I discuss the key design considerations of a PL-fed diffraction-limited spectrograph. This is then followed by the design and characterisation of three such spectrographs (two ostensibly

1.2 Types of Spectrographs

astronomical applications, one intended for use on a small satellite) in Chap. 4. My reduction package for analysing and producing 1D spectra from the raw spectrograph data is presented in Chap. 5. In Chap. 6 I present three experiments completed with these spectrographs, the first to measure 5 minute period solar oscillations, the second giving a short observation of the star Alpha Centauri and finally of high altitude balloon test of my smallest spectrograph. Finally, in Chap. 7, are my concluding comments.

1.2 Types of Spectrographs

Spectrographs¹ can be classified into four primary categories:

1. Fabry-Pérot (FP) interferometers/etalon and interference filters (Fabry and Perot 1901)
2. Fourier transform spectrometer (FTS)
3. Direct detection (i.e. energy sensitive)
4. Dispersive (generally grating and/or prism based)

Dispersive spectrographs are by far the most common, especially in optical/infrared astronomy. The design and application of dispersive spectrographs at the diffraction limit will be the primary focus this thesis, but for completeness a summary of FP, FTS and direct detection instruments follows.

1.2.1 Fabry-Pérot Interferometers

FP etalon's and interference filters operate on the same basic principle, a collimated beam is partially reflected multiple times between parallel, partially reflective surfaces. The separation of the reflective surfaces (l) along with the cavity refractive index (n) introduce a fixed phase offset in the wavefront between each reflection. When these beams re-combine, only wavelengths that satisfy the usual condition for constructive interference are transmitted, that is,

$$m\lambda = 2nl \cos \theta \quad (1.1)$$

where m is an integer and θ is the refracted angle in the filter/etalon. Most interference filters will contain a series of cavities (i.e. thin film reflective layers), tuned to allow a specific waveband

¹I've found the distinction between spectrometer, spectrograph and spectroscope generally to be fairly vague. Some sources claim a spectrometer is a device that makes measurements over large wavelength ranges. While a spectroscope is a device without quantitative measurement of intensity (i.e. the detector is the user's eye). Spectrographs are devices that use recording devices, initially photograph film or plates and now electronic detectors. Yet, surely the spectrometer must record its spectrum, so is it a spectrograph? In a modern context it seems the terms spectrometer and spectrograph are more or less interchangeable, and the distinction a mater for the pedantic. In this thesis (for no particular good reason, other than to provide some consistency) I will refer to dispersive devices as spectrographs and interferometric devices as spectrometers and collectively all wavelength discrimination devices as spectrographs.

1.2 Types of Spectrographs

with a specific response function. A schematic diagram of a filter and an etalon is shown in Fig. 1.1b.

A more complete definition of the transmitted intensity for an etalon is the square modulus of the summed complex amplitudes of the transmitted wavefronts (Bland-Hawthorn 1995). This produces a periodic Airy function,

$$I = \left(1 + \frac{4N^2}{\pi^2} \sin^2 2\pi nl \lambda^{-1} \cos \theta \right)^{-1}, \quad (1.2)$$

where N is the Finesse and is given in terms of the mirror reflectivities, R_1 and R_2 , as,

$$N = \frac{\pi \sqrt[4]{R_1 R_2}}{1 - \sqrt{R_1 R_2}} = \frac{\Delta\lambda}{\delta\lambda}. \quad (1.3)$$

The quantities $\Delta\lambda$ and $\delta\lambda$ are the separation of maxima or the **free spectral range (FSR)** and width of maxima respectively.

The scanning **FP** interferometer, for example, is a case where the cavity separation is increased/decreased thus changing the transmitted peak's position in wavelength. This is often combined with a low order monochromator or another interference filter to separate/remove neighbouring orders. Later in this thesis I explore another use for the etalon, where the spacing and reflectivity are chosen to produce many narrow peaks with a relatively small **FSR** to produce a 'laser comb' spectrum. Such a spectrum can be used to calibrate a dispersive spectrograph's wavelength scale and image quality (cf. Sec. 5.2).

More detailed reviews of **FP** interferometers can be found in Bland-Hawthorn (1995), Hernandez (1988), and Vaughan (1989).

1.2.2 Fourier Transform Spectrometer

The **FTS** is essentially a Michelson interferometer (Michelson and Morley 1887), where the wavefront is split into two parts, reflected and finally recombined. The basic layout required is illustrated in Fig. 1.1a. In order to obtain a spectrum, the interferometer's movable arm is scanned through discrete positions (or continuously) while recording the intensity of the interference fringes produced when the beams recombine. The spectrum can then be reconstructed from this series of measurements via a **Fourier transform (FT)**.

Because a **FTS** is sampling in Fourier space, it benefits from a multiplex advantage (Fellgett 1951). That is, each fringe measurement is effectively sampling the entire spectrum. Thus, in a single-pixel detector read-noise limited scenario the **FTS** has a square root N advantage **single-to-noise ratio (SNR)** vs a dispersive spectrograph. However, in the photon noise (shot noise) limited case, this advantage is negated and in the case of array detectors becomes a disadvantage. More detailed descriptions can be found in Bell (2012) and Steel (1983).

1.2.3 Direct Detection

The marvel of direct detection techniques is their ability to achieve photon counting sensitivity while simultaneously resolving the energy (wavelength) of each photon. Such technologies will

1.2 Types of Spectrographs

likely someday make redundant many of the techniques of classical spectroscopy. Currently, however, they are limited to small array sizes, low energy (spectral) resolution and sub-kelvin temperatures required by their superconductor materials. Promising technologies include the transition edge superconductors, superconducting tunnelling junctions and magnetic kinetic inductance. None are yet able to achieve a resolving power higher than ~ 100 in the visible, and only the latter has a clear path to arrays larger than a few hundred pixels (Day et al. 2003; Mazin et al. 2012). A notable mark of progress is the ARCONS imagers, which utilise a 2024 pixel microwave kinetic inductance detector (Mazin et al. 2013). A good overview of these technologies can be found in Berggren et al. (2013).

1.2.4 Dispersive Spectrographs

Fundamentally every dispersive spectrograph consists of the same key components: an entrance slit, collimator, dispersive element, camera and detector. The details of exactly how each of these is implemented can vary substantially. In many astronomical spectrographs, **multi-object spectrographs (MOFs)** in particular, it is common for the entrance slit to be formed by an array of optical fibres that relay the image from a telescope focal plane. Other examples use a concave diffraction grating (i.e. Rowland circle) to merge collimator, disperser and camera into a single element. A more exotic case is the **arrayed waveguide grating (AWG)** based **integrated photonic spectrograph (IPS)**, where dispersion is generated by the difference in path length along an array of **single-mode (SM)** waveguides (cf. Sec. 2.2.2). The free propagation regions and curvature of the array of input waveguides act as the collimator and camera.

Fig. 1.2 shows the layout of a simple transmission grating spectrograph in the ‘Littrow’ configuration. The diffraction grating essentially splits a collimated beam into N beams. These

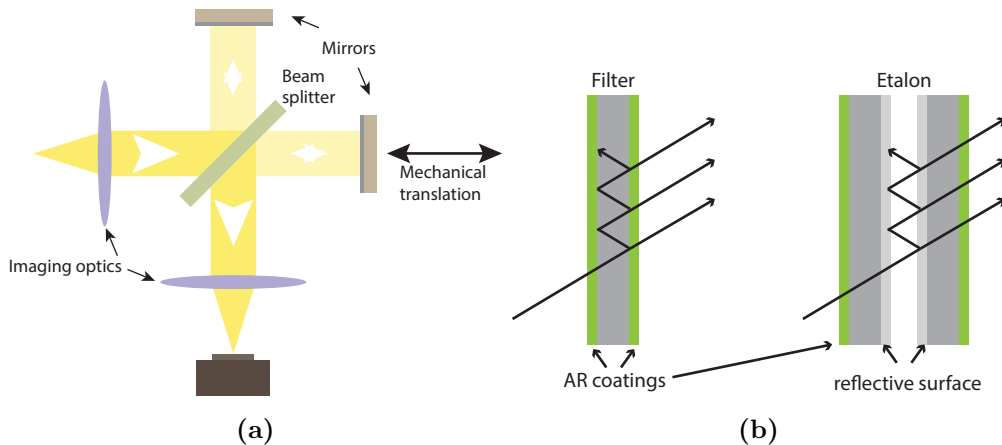


Figure 1.1: a) In a **FTS** the source beam is split into two parts by a beam splitter. These two parts are reflected off of a fixed mirror and a translatable mirror and recombined b) Simple diagram of interference filter and **FP** etalon. In both multiple beams are generated by partial reflection at interfaces.

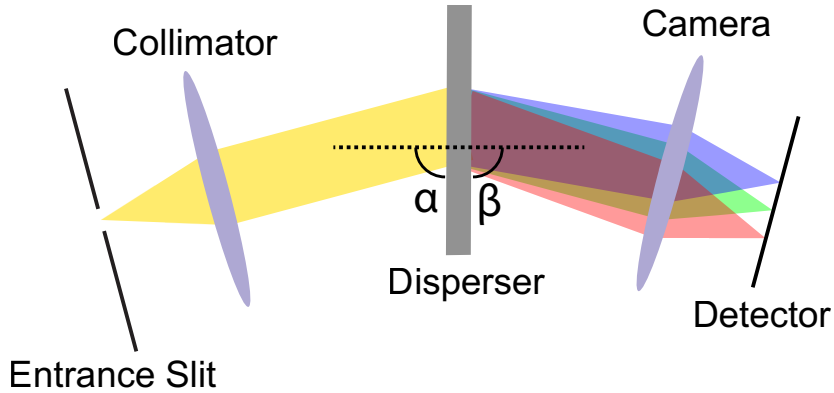


Figure 1.2: Fundamental layout of a dispersive spectrograph. Light path is left to right. Light emerging from the entrance slit is collimated, dispersed and finally re-imaged on to a detector/light sensor.

beams interfere leading to peaks of constructive interference. The grating equation that describes the position of these peaks for a given wavelength is:

$$m\lambda = d \cos \gamma (\sin \alpha + \sin \beta) \quad (1.4)$$

$$= 2d \cos \gamma \sin \alpha \quad (1.5)$$

where α and β are incidence and diffraction angles respectively and γ is rotation of the grating out the plane of the diagram. In Eqn. 1.5 it had been assumed that $\alpha = \beta$ for central wavelength λ_c . This assumption is known as the Littrow condition.

Échelle gratings

The échelle diffraction grating is a special case of a ruled reflection grating. It operates at high diffraction orders (i.e. $m \gtrsim 10$). In order to do so the line density of the grating is lower than the traditional gratings (36 lines/mm vs 100s to 1000s). They are blazed for high angle of incidence and diffraction, normally around 60-70 degrees, and normally operated very close to the Littrow condition, but with a non-zero out of plane γ angle. Without the γ angle the dispersed image would be collocated with the slit, making detector placement difficult. The high diffraction orders also mean the diffraction orders will overlap significantly. As a result, an échelle based spectrograph requires either cross-dispersion (i.e. a grating or prism with perpendicular dispersion) to separate the images of each order, producing an echellogram like the one shown in Fig. 1.3. Another common approach is to use a filter (often an interference filter) that only transmits light with wavelengths that correspond to the FSR of a given diffraction order, thus eliminating the overlap concern. Using cross-disperser allows the spectrograph to have a relatively large bandwidth, but it also limits the amount of spatial information that can be recorded in a single exposure (as the slit length is limited by the extent of the separation of the diffraction orders provided by cross-disperser). On the other hand, using the order sorting

filter results in a narrower bandwidth but with increased capacity for spatial information (i.e. a long slit on 2D detector).

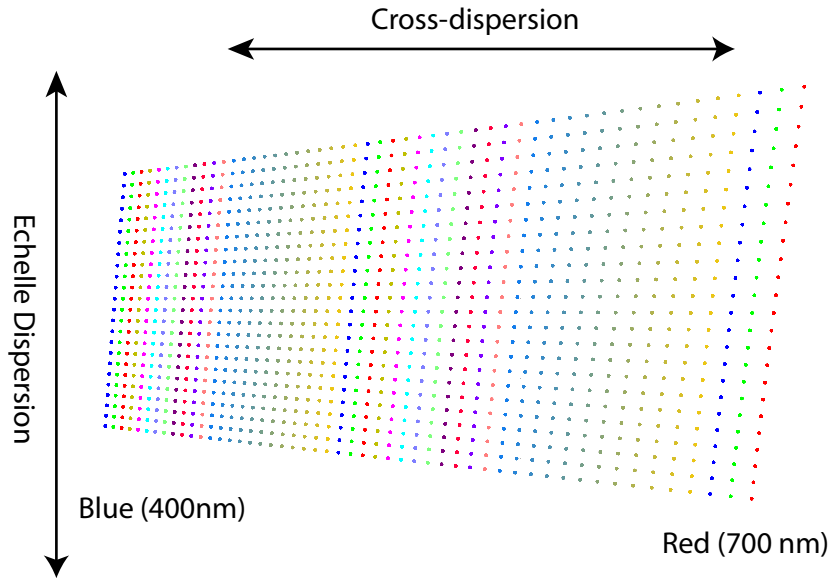


Figure 1.3: Schematic of an echellogram with 51 diffraction orders (colour changes indicate different). The echelle dispersion is in the vertical direction and the cross-dispersion is in the horizontal direction. The cross-dispersion separates the diffraction orders orthogonally to echelle dispersion direction. Without it all the diffraction orders would overlap.

Volume Phase Holographic gratings

Rather than the physical lines ruled in a traditional diffraction grating, a **volume-phase holographic (VPH)** grating consists of a dichromate gelatine layer with a controlled thickness between two pieces of protective glass with an anti-reflective coating. The light is diffracted via fringes of refractive index variation written in the gelatine layer by holographic techniques, rather than the physical lines/rulings found in traditional gratings (Barden et al. 2000; Rallison et al. 2003). Control of the contrast, tilt and thickness of the fringes allows the grating to be blazed with very high efficiency ($> 80\%$) to a given wavelength range (in the first order).

1.3 The Diffraction Limit

The description, ‘diffraction-limited’, can have multiple connotations. It can be referring to an optical system’s imaging performance (quantified by geometric and diffractive aberrations) being dominated by diffraction effects. That is, the geometric aberrations are sufficiently small that the aperture size and optical surface quality become the dominant effects in determining the shape/size of the **point spread function (PSF)**. In the context of spectroscopy, a slightly

more specific definition, which I use in this thesis, requires the size of the entrance slit to also be limited by diffraction (i.e. smallest possible slit for a given wavelength or minimum **étendue**; cf. Sec. 1.4.1). This has an important impact on the spectral resolution and spectrograph design, as is detailed throughout this thesis.

1.4 Figures of Merit

1.4.1 Étendue

A key characteristic of any spectrograph is the amount of light collected, dispersed and re-imaged onto a detector. This quantity is often characterised by the geometrical extent or **étendue**¹, defined as the product of entrance/collection surface area, A , and the solid angle of acceptance of the optical system, Ω . In a perfect optical system the **étendue** is conserved. Conventionally, in order to maximise the **throughput** of a spectrograph, the **étendue** of all optical elements (e.g. from a telescope to the detector) must be well matched and maximised. This presents a challenge for large telescopes (diameter > 8 m), as the spectrograph must also scale in size in order to fulfil this requirement.

This is illustrated in Fig. 1.4, which shows a simple schematic of a telescope that feeds a simple spectrograph. In an optimised system,

$$S'_T \Omega'_T = S_{COL} \Omega_{COL} = S_D \Omega_{CAM}. \quad (1.6)$$

This is the relationship which ties the size of spectrograph to the input telescope. Generally the spectrograph collimator will have an *f/#* (ratio of focal length and aperture/pupil diameter) that is much lower than the telescope, and thus will require a smaller surface area at the collimator to satisfy **étendue** conservation. The *f/#* of a circular lens is related to the solid angle Ω by the following,

$$\Omega \approx \frac{\pi}{4(f/\#)^2} \quad (1.7)$$

assuming the beam with solid angle Ω fills the lens aperture.

1.4.2 Resolving Power

The **resolving power** (\mathcal{R}) of a spectrograph is a measure of its ability to distinguish neighbouring spectral features (namely emission or absorption lines). It is defined as,

$$\mathcal{R} = \frac{\lambda}{\Delta\lambda} \quad (1.8)$$

where λ is the wavelength of interest and $\Delta\lambda$ is the minimum separation in wavelength required for two equal intensity features to be resolved. This can be expressed in terms of the angular

¹Sometimes also referred to as throughput, however I will use a related but more specific definition where **throughput** is **ratio of photons detected to photons collected**.

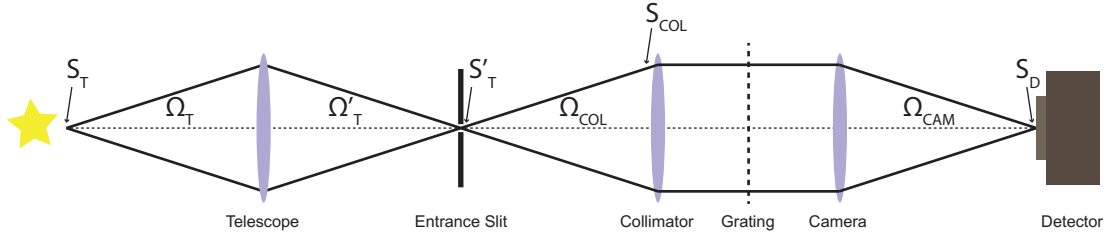


Figure 1.4: A simple schematic of an optical system that includes a telescope and spectrograph. S values indicate surface area, while Ω symbols represent the solid angle of input/acceptance. For example Ω'_T is solid angle input to the slit/focus and S'_T is the area of the telescope focus/entrance slit.

dispersion ($\frac{\delta\theta}{\delta\lambda}$) of the dispersing element, such that the angular separation of two resolved lines separated by wavelength $\Delta\lambda$ is

$$\Delta\theta = \frac{\delta\theta}{\delta\lambda}\Delta\lambda. \quad (1.9)$$

In the simplest case, a rectangular disperser with aperture width A , it is thus,

$$\mathcal{R} = A \frac{\delta\theta}{\delta\lambda}. \quad (1.10)$$

This is the most general definition of the diffraction-limited resolving power of a spectrograph, and provides a basis for determining a theoretical resolution for different apertures and illumination profiles.

A theoretical (or Rayleigh) definition of the resolving power can be defined in terms of a spectrograph's physical parameters by first noting that the spectrograph PSF will be a convolution of the instrumental PSF (i.e. the profile of grating diffraction and any blurring due to optical imaging quality¹) and the profile of the imaged entrance aperture/slit. The theoretical estimate of the resolution can thus be found by equating the size of a resolution element in the focal plane and the displacement due to $\Delta\lambda$ (this is effectively equivalent to Eqn. 1.10, but allows for a more obvious inclusion of different illumination profiles).

The angular dispersion is found by differentiating Eqn. 1.5 (assuming that the out of plane angle γ is small) and the linear dispersion (or the displacement due to $\Delta\lambda$) follows by multiplying by the camera of focal length, f_{cam} ,

$$\frac{\delta\beta}{\delta\lambda} f_{cam} = \frac{\delta x}{\delta\lambda} = 2f_{cam} \frac{1}{\lambda} \tan\beta. \quad (1.11)$$

Next, as a grating illuminated by a uniform beam with a diameter d will produce an Airy disk diffraction pattern I can use the Rayleigh criterion as a basis for the linear resolution element (assuming the grating function will dominate optical aberrations). That is, two Airy disks with an angular separation of

$$\delta\theta = 1.22 \frac{\lambda}{d} \quad (1.12)$$

¹i.e. geometric or diffractive aberration

1.4 Figures of Merit

are considered just resolved. So, for a camera with a focal length f_{cam} the linear resolution element is thus,

$$\delta x = \frac{1.22\lambda}{d} f_{\text{cam}} \quad (1.13)$$

Finally, combining Eqn. 1.11 with Eqn. 1.13 I get the following expression for the resolution limit of a uniformly illuminated typical diffraction grating with circular aperture (which may be the grating, but more typically the optics illuminating it).

$$\mathcal{R} = \frac{\lambda}{\Delta\lambda} = 1.64 \frac{d}{\lambda} \tan \theta_i \quad (1.14)$$

Slit-Limited Spectral resolution

In the seeing limited case, the slit width is now the limiting factor on resolution. The size of slit as imaged by the spectrograph is thus,

$$\delta x = w_s \frac{f_{\text{cam}}}{f_{\text{col}}} = \phi_{\text{slit}} \frac{f_{\text{tel}}}{f_{\text{col}}} f_{\text{cam}} = \lambda \phi_{\text{slit}} \frac{D_{\text{tel}}}{D_{\text{col}}} f_{\text{cam}} \quad (1.15)$$

where $\phi_{\text{slit}} = w_s f_{\text{tel}}$ is the angular size of the slit and f_{tel} is the focal length of the source telescope. This can also be expressed in terms of seeing as $\phi_{\text{slit}} = \lambda/r_0$ where r_0 is the diameter of rays that stay coherent passing through the atmosphere (i.e. the Fried length; Fried 1966). This can now be combined with Eqn. 1.11 as before to get the slit limited resolving power,

$$\mathcal{R} = \frac{D_{\text{col}}}{\phi_{\text{slit}} D_{\text{tel}}} 2 \tan \beta \quad (1.16)$$

$$= \frac{r_0 D_{\text{col}}}{\lambda D_{\text{tel}}} 2 \tan \beta \quad (1.17)$$

where D_{col} and D_{tel} are the diameters of the collimator and telescope respectively.

This result is essentially another expression of **éendue** conservation above. From it, it is clear that the only way to increase the resolving power in a seeing limited situation is to increased the size of collimator and/or to increase the angle of incidence.

Standard definition of resolution element

The resolution element used to derive Eqn. 1.14 was an obvious choice, the Rayleigh radius. However, if the illumination profile is changed the **PSF** is likewise changed, and the normal definition of Rayleigh criterion (two sources are just resolved when the maximum of one is coincident with zero of the other) is not always helpful. The most relevant example is a Gaussian illumination profile, which will produce a Gaussian (or near-Gaussian) **PSF**. In this case there is no zero or clearly defined edge. The **full width half maximum (FWHM)** is often used as alternative, but it is arguably insufficient. This is illustrated in Fig. 1.5, where the second column shows two identical Airy disk and Gaussian profiles separated by their respective **FWHM** (top and bottom respectively). The Airy disk profile is clearly not resolved per the Rayleigh criterion, and it would seem hard to justify anything different for two Gaussians. An alternative, proposed by Robertson (2013b) is to use a more generalised definition, derived from the Rayleigh

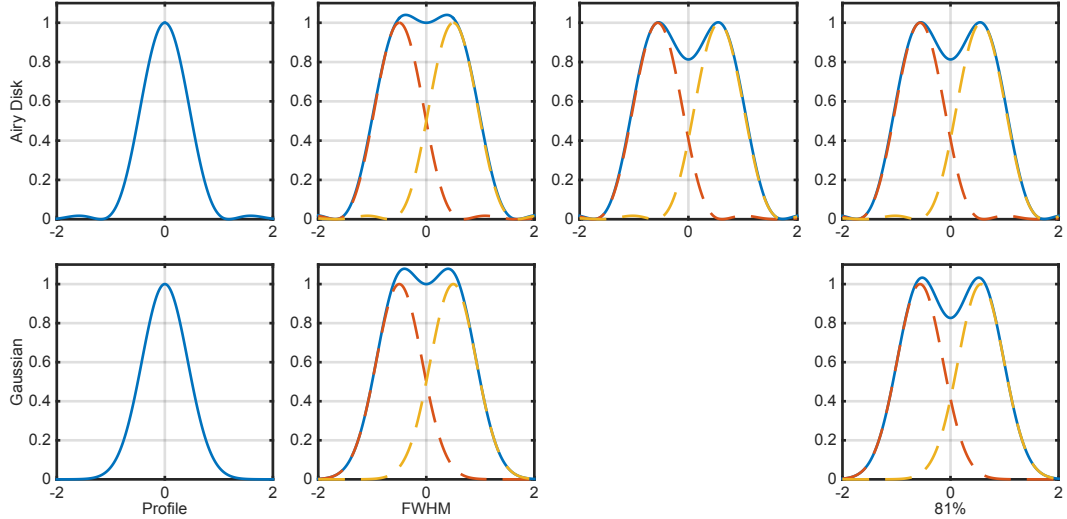


Figure 1.5: Each row shows, PSF profile (cross-cut in wavelength axis), two identical profiles separated by their FWHM, two identical profiles separated according to the Rayleigh criterion and two identical profiles separated according to the generalised Robertson-Rayleigh criterion.

criterion. This is to simply say that two profiles are resolved if they achieve the same contrast as provided by Rayleigh criterion, that is $\sim 81\%$ relative minimum between the peaks (i.e. peak to valley). This is seen in the final column of Fig. 1.5. In the case of Gaussian, it corresponds to $1.119 \times \text{FWHM}$.

1.4.3 Precision and Stability

Any changes (physical movement/flexure, pressure, humidity, etc.) in the spectrograph and its environment during an exposure can result in degradation in the quality of the spectrum (i.e. blurring of PSF or degraded SNR). Changes occurring between calibration and target exposures can also result in an inaccurate spectrum extraction and/or uncertainty in the wavelength scale. The magnitude of these changes characterises the stability and how well they can be calibrated (that is the precision is effectively a measure of stability over time and thus the ability to compare subsequent measurements). Both are normally expressed as a root mean square (RMS) Doppler velocity, but can also be expressed as a wavelength or pixel shift. Velocity is often more informative because the fields which are most influenced by stability are directly measuring physical radial velocities. The conversion from wavelength to a velocity is given by the Doppler redshift equation,

$$z = \frac{\Delta\lambda}{\lambda_0} = \sqrt{\frac{1 + \frac{\Delta\nu}{c}}{1 - \frac{\Delta\nu}{c}}} - 1 \quad (1.18)$$

1.4 Figures of Merit

where $\Delta\nu$ is the relative line of sight velocity, $\Delta\lambda$ is wavelength shift relative to λ_0 and c is the speed of light.

Depending on the observation goal, there are varying degrees of acceptable stability and precision. The stability of a spectrograph is particularly important in high-resolution astronomical spectroscopy where longer exposure times are common (ideally there would be zero changes during an exposure). The precision becomes particularly important for goals that require successive observations over a period of time much longer than the exposure time. Some of the most demanding requirements come from astro-seismology and exoplanet research. For example, Mayor and Queloz's (1995) original 'hot Jupiter', 51 Pegasi b, has a radial velocity signature with a 56 m/s amplitude and a period of 4.2 days. This corresponds to a shift of just 1/60 of pixel in a visible spectrum (assuming a resolving power of 50,000 and 2 pixel per resolution element). Thus, in order to detect 51 Pegasi b, the calibrated wavelength stability should be much less than 56 m/s for at least several multiples of the orbital period. The detection of an earth analogue would require ~10cm/s (~1/1000 pixel) precision over several years for the same resolution spectrograph.

2

Astrophotonics

Optical fibres, one of the pillars of photonics (manipulation of light), are not a stranger to astronomy, **multi-mode fibres (MMFs)** in particular. Traditionally in the photonics/telecommunications industry **MMF** has been used for short-haul telecommunication links. The large core size (and many supported propagation modes) allows light to be coupled efficiently and easily, which is also the reason it is used in astronomy. However, intermodal dispersion (group velocity dependence on both wavelength and propagation mode) causes ultrashort light pulses encoded with data propagating in **MMF** to spread, distorting the transmitted signal and limiting the effective transmission range, as a result most long distance links are almost exclusively the domain of **single-mode fibre (SMF)**. This is one of the reasons many of the technologies developed by the photonics and telecommunication industry for filtering and wavelength division multiplexing (WDM) are also **single-mode (SM)** only. The fundamental optical reason these applications are more advanced in the **SM** regime, is that the techniques rely on resonant processes that depend on how the light is confined and guided in waveguide or fibre. **SM** devices are ‘easier’ to implement, compared to highly **multi-mode (MM)** ones were the resonant process are much more difficult to control/manipulate. The field of Astrophotonics (reviewed in more detail by Bland-Hawthorn and Kern 2009, 2012) looks to harness these photonics technologies to improve and develop the instrumentation used in astronomy.

However, save for a few exceptions, **MMF** is the dominant type of fibre used in astronomical instrumentation. This is because, from an astronomers perspective, optical fibres are essentially just light pipes. Indeed, many conventional astronomical spectrographs use **MMFs** to feed light from a telescope to the spectrograph slit. **MMFs** are required to do this efficiently on most

telescopes due to atmospheric **seeing**, otherwise the system **étendue** would not be conserved (i.e. precious photons would be lost). This has been an extremely successful technique, enabling flexible observations of 100s to 1000s of objects simultaneously, allowing substantial surveys composed tens of thousands of objects. Two notable examples are the Sloan Digital Sky Survey (SDSS) which has accumulated spectra of over 3 million objects (Ahn et al. 2014) and the 2dF Galaxy Redshift Survey (2dFGRS) with spectra of nearly a 1/4 million objects (Colless et al. 2001). High resolution astronomical spectrographs ($\mathcal{R} > 20,000$) are often fed by only a few **MMFs** (a by-product of the inherent counterbalance between spectral information and spatial information being mapped to a 2D surface). Those of very high resolution ($\mathcal{R} > 60,000$) are either slit-based spectrometers or fed by ~ 2 fibres (generally one object fibre and another for simultaneous wavelength calibration or sky spectrum).

All these spectrographs have inherent limitations dictated by the source telescope and atmospheric seeing, namely the collimated beam size must increase in proportion with the telescope diameter to maintain a given resolving power (per Eqn. 1.16). One of the biggest limitations in some of the highest resolution spectrographs is the inherent modal noise of **MMF** (Schwab et al. 2012). The changes in power coupled to specific modes and interaction of these modes propagating within a **MMF** produces a wavelength and time dependent modulation, which from the perspective of the spectrograph can appear like a very small spectral shift. In contrast, a diffraction-limited spectrograph's resolving power is independent of the size of the telescope. The result is that a diffraction-limited spectrograph could be dramatically more compact than a conventional design. Of course, there is a significant caveat, as a diffraction-limited slit would have extremely poor throughput when simply combined with a conventional **MMF** (i.e. using a slit-mask) or when trying to couple the telescope image directly to a **SMF**. Even when coupling in ideal circumstances (i.e. a uniformly illuminated circular pupil, with no optical or atmospheric aberrations), the efficiency peaks at 80% and decreases proportionally to the Strehl ratio (ratio of the peak of an aberrated image with a peak of an image produced by an ideal optical system). A typical example is coupling light from a telescope where, in the presence of atmospheric turbulence, the focus can be extremely perturbed. The Strehl ratios are typically $< 1\%$ and thus couple poorly to a sole **SMF** (Horton and Bland-Hawthorn 2007; Shaklan and Roddier 1988). There is some promising work by Jovanovic et al. (2014), that uses the advanced **adaptive optics (AO)** system on the Subaru telescope to couple directly to a **SMF** with much higher efficiencies ($\sim 50\text{-}80\%$ in early experiments).

The ideal solution would be to compact one side of a **MMF** such that it was diffraction-limited in one axis, as is illustrated in Fig. 2.1. This is of course much easier said than done, or is it? In principle, this is exactly what an **integral field unit (IFU)** at a telescope does when reducing a 2D image to a linear slit. However, the 1D slit produced by the **IFU** must still be matched to the telescope properties (i.e. beam size, **focal ratio** and **seeing**). Further, the techniques of conventional **IFUs** can already be extremely complex, and requiring that they remap to even smaller sizes will invariably lead to losses of efficiency and/or increased costs. A new approach is required to efficiently reduce the slit to a diffraction-limited width.

The solution to this conundrum (that is how to operate at the diffraction limit, yet retain as

much light as possible) is a technology known as the **photonic lantern (PL)**. The **PL** allows the efficient conversion of a **MMF** to a series of **SMF**, enabling a new approach to instrument design, opening the door to a large array of **SM**- only photonics technology (e.g. fibre Bragg grating, optical circulators, array waveguide grating, ring resonators, fibre couplers/splitter etc.). into existing designs or built into compact diffraction-limited micro-spectrographs. The **PL** is in one sense the ideal image slicer, remapping the input light to a diffraction-limited format whilst effectively conserving the **étendue** (or in fibre optics terminology, conserving the number of modes in the **MMF**). However, as it does not preserve the spatial information of the input, it is in that sense a very poor image slicer and perhaps best described as an intensity slicer.

The **PL**, perhaps more than any other technology, has enabled the field of Astrophotonics to blossom over the past decade. The conversion from **MM** to **SM** decouples the spectrograph design from the light source at the **MM** input. So, instead of the telescope diameter driving the size of spectrograph, it drives the number of spectrographs required to conserve **étendue**. Nonetheless, the spectrograph design will no longer need to be matched to the focal ratio of the telescope beam, rather it is designed to match the output of an array of **SMFs** (which remain unchanged regardless of what the source at the **MM** input is). Some of the key examples of their use include:

- Broadband targeted spectral suppression: 103 of brightest night sky hydroxyl (OH) emission lines between scattered between wavelengths of 1.47 and 1.70 μm were suppressed using a double **PL** and fibre Bragg grating feed to the IRIS2 instrument on the AAT (Bland-Hawthorn et al. 2011; Ellis et al. 2010; Trinh et al. 2013)
- **integrated photonic spectrograph (IPS)**: An **arrayed waveguide grating (AWG)**-based spectrograph was demonstrated at the AAT operating in the astronomical H-band atmospheric window (1.485 - 1.825 μm). Using phased waveguides to mimic a diffraction grating, this ‘spectrograph on a chip’, achieved a resolving power of $R = 7000$ (Cvetojevic et al. 2012a, 2009).
- and *in this thesis*, I present the first implementation of a high resolution **PIMMS#0** (cf. Sec. 2.2) type spectrograph dubbed PIMMS IR and its successor PIMMS visible, a cross-

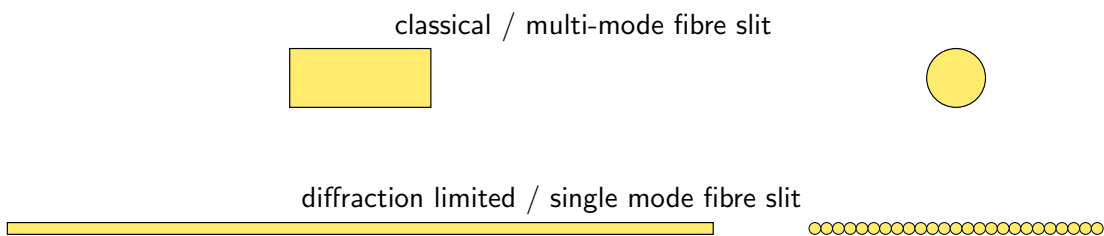


Figure 2.1: Comparison of **MM** and **SM** slit. Assuming a constant **numerical aperture (NA)** (for simplicity of the illustration) area must be conserved for the **étendue** to be conserved.

2.1 The Photonic Lantern

dispersed echelle spectrograph. As a photonic **PL** allows for a spectrograph to be fed by an array of **SMFs**, the design achieves true diffraction-limited performance in a compact package. It can also incorporate targeted spectral suppression or compact laser frequency combs for precision spectroscopy.

2.1 The Photonic Lantern

The fundamental requirement of the **PL** is that it must efficiently transform **MM** light into multiple **SM** waveguide outputs. The transition occurs in between a set of **SM** waveguides to a **MM** waveguide. Currently the most common method of fabricating a **PL** starts with a bundle of **SMFs** inserted in a low-index glass capillary. These are then fused and drawn down to form a tapered waveguide that ends in a **MM** port. At the **MM** end, the **SMFs** cladding material becomes the core and the low index glass capillary becomes the cladding. An alternative is to start with a **multi-core fibre (MCF)**; i.e. a 2D array of **SM** cores in a single fibre, which are likewise drawn down to form a tapered within a glass capillary. In both cases, the **SM** cores gradually become too small to guide light (Leon-Saval et al. 2010, 2005; Leon-Saval et al. 2013) and the light is confined by the lower index capillary jacket.

Another promising method of creating the **PL** is by directly writing waveguides in a block of glass using **ultrafast laser inscription (ULI)** (Spalenik et al. 2013; Thomson et al. 2011). The paths of the **SM** waveguides are brought closer together, such that they begin to cross-couple, thereby forming the **PL** transition and eventually producing the **MM** output waveguide. A **ULI** based **PL** of course does not have the core separation concern of the fibre based **PLs**, as the **SM** cores can be arbitrarily close, but does have its own drawbacks. A big concern is scattered light that is either not coupled to the **MM** port or that is lost due to scattering in the waveguides (Jovanovic et al. 2012). All three fabrication techniques are illustrated in Fig. 2.2.

In either method, if the taper transition from **MM** to **SM** is optically adiabatic¹, the modes of the **MMF** input will evolve into the modes of the **SM** outputs. In order for the conversion to be efficient, the number of modes supported in the **MM** (m) port should match the number of **SM** cores (n). The number of modes in a step-index **MMF** is determined by the core size and the acceptance angle (specified as a numerical aperture, **NA**) and in terms of the fibre **V** parameter (Snyder and Love 1983),

$$m \approx \frac{V^2}{4} \approx \left(\frac{\pi d}{2\lambda} \text{NA} \right)^2, \quad (2.1)$$

where d is the fibre core diameter and λ is the free space wavelength of the guided light. It should be noted that each mode is capable of carrying two polarisations. Consequently when polarisation is considered there are effectively twice as many modes. Even so, the number of **SMFs** remains the same as each **SMF** can also carry two polarisations. For low loss operation, the number of modes has to be conserved (i.e. $m = n$) at the **PL**'s design wavelength. A typical throughput of the current generation of **PLs** is 93% (0.3dB loss; Noordgraaf et al. 2012).

¹i.e. a gradual/slow taper

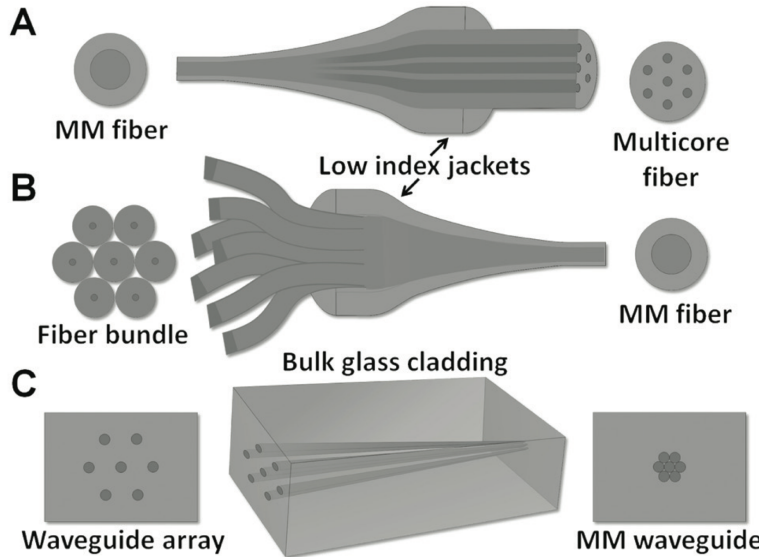


Figure 2.2: Schematic of the three **PL** fabrication techniques. Shown are: A) a **PL** formed with using a **MCF** tapered down with low-index jacket. B) a **PL** formed with bundle of **SMFs** that fused and tapered with a low-index jacket. C) a **PL** written with **ULI** techniques that creates waveguides in glass block.

Note that as λ decreases the number of modes in the **MM** port increases. This will result in an effective reduction in throughput blueward of the design wavelength when the number of modes in the **MM** port exceeds the number of modes available in **SM** outputs. In contrast, redward of the design wavelength, the number of **SM** outputs will exceed the number of modes supported in the **MM** port, thus the transition will not have a negative impact on throughput. So, an absolute limit on **PL** transmission throughput can be simply expressed by the ratio of the number of **SM** outputs to the number of modes in the **MM** input, that is

$$\text{transmission fraction} = \frac{n}{m} = \frac{n(A\Omega)_{\text{SMF}}}{(A\Omega)_{\text{MMF}}} \leq 1. \quad (2.2)$$

The number of modes can be thought of as equivalent to the **étendue** of fibre, indeed, simply multiplying by λ^2 returns the **étendue** (for low numerical apertures). Thus the **PL** is effectively chopping up the **MMF** **étendue** into n diffraction-limited components.

2.2 Photonic Integrated Multi-Mode Spectrograph

The primary focus of the later parts of this thesis is the design and implementation of the **photonic integrated multi-mode spectrograph (PIMMS)**, first introduced by Bland-Hawthorn et al. (2010) as an alternative approach to classical spectrographs. The **PL** is the key to the **PIMMS** approach as it allows for the spectrograph input (not to be confused with the entrance

slit) to be a m mode MMF and thus having a diffraction-limited entrance slit composed of m SMFs. This satisfies some of the key challenges of using a diffraction-limited spectrograph in astronomy, namely (i) the PL's MMF input is just that, a MMF, equivalent to what is already in use as the input and entrance slit of many spectrographs, astronomical or otherwise. Thus it can be efficiently coupled to light from a variety of sources; and (ii) the beam emerging from a SMF is by definition diffraction-limited, with the light propagating in the fundamental LP₀₁ fibre mode (i.e. Gaussian like; Bland-Hawthorn et al. 2010). The $f/\#$ of the SMF beam is dependent only on the refractive index contrast between the SMF core and cladding, and is thus independent of the source at the MMF input of the PL.

One of the goals of the PIMMS concept proposed by Bland-Hawthorn et al. (2010) is that it would integrate many spectrograph modules in place of a single large instrument (the ‘divide and conquer’ approach). There were two proposed configurations, the PIMMS#0, a compact bulk optics micro-spectrograph and PIMMS#1, the IPS that used an AWG. In both cases the PL was the key enabling technology to allow efficient coupling.

2.2.1 PIMMS#0

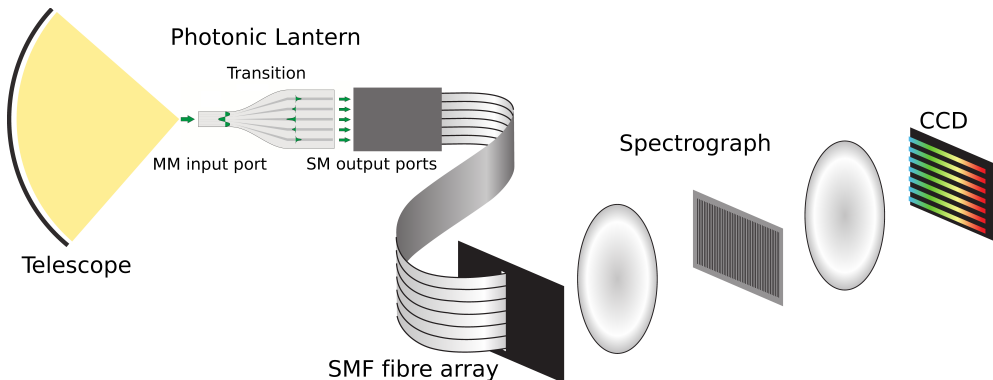


Figure 2.3: The PIMMS#0 concept combines the PL MM to SM converter with a bulk optics spectrograph. The power of the concept lies in the fact that the optical design of the spectrograph is decoupled from the original input source and the SMF pseudo slit allows it to have a diffraction-limited spectroscopic resolution.

In the PIMMS#0 (illustrated in Fig. 2.3) design the output of the PL is formed into a SMF pseudo-slit. These SMF may include fibre Bragg grating filters. The actual spectrograph is conventional in the sense that it is comprised of bulk optics (i.e. lenses, prisms, diffraction grating) components, however as the design is now diffraction-limited it can be extremely compact. For example, consider a quick comparison of an observation with a 1 m f/5 telescope with 1 arc-second seeing ($r_0 = 10$ cm) with a resolving power of 50,000. The plate scale of the telescope is $206265/(1000 * 5) = 41$ arc-seconds/mm, and so the seeing disk is thus $20 \mu\text{m}$ at the telescope focus. From Eqn. 1.17, the required beam size for a conventional spectrograph is

at least ~ 6 cm and from Eqn. 1.14 is ~ 1.5 cm (assuming an R2 echelle grating for both). The caveat of course is that the PIMMS approach requires more inputs at the entrance slit (~ 20 fibres or **SM** cores per object according to the number of modes given by Eqn. 2.1).

While the difference may not seem extreme, any degradation in seeing will increase the size of the conventional design very quickly, as will an increase in the telescope size. Perhaps more important though, is that at this size the choices for **commercial off-the-shelf (COTS)** optics and mounts are virtually non-existent, while for the diffraction-limited design they are cheap and plentiful (up to around 5 cm diameter optics).

2.2.2 PIMMS#1

In the **PIMMS#1** (illustrated in Fig. 2.4) design the **SMF** pseudo-slit is coupled to an **AWG** which acts as the primary disperser of the spectrograph. Depending on the design of the **AWG**, the output will consist of many overlapping spectra, one from each **SMF** input and each with multiple overlapping diffraction orders. This is similar to the échelle diffraction grating, as the **AWG** is operating at high diffraction orders. In order to distinguish these overlapping spectra an order sorter must be included. Again, in the same manner used with an échelle grating, the output can be cross-dispersed to distinguish the overlapping diffraction orders. An alternative is to include an interference filter to block light from undesired diffraction orders.

Many **AWG** devices will be required to replace a modern spectrograph, but they are suitable for mass production so this should not be a problem. Fewer devices will be required if the number of input fibres is maximised per **AWG**. More details on **PIMMS#1** are given by (Cvetojevic et al. 2012a,b; Cvetojevic 2013).

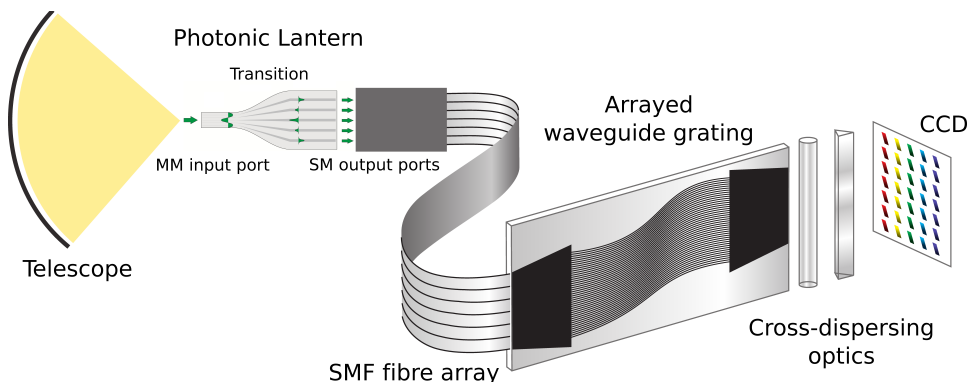


Figure 2.4: The PIMMS#1 concept. Similar to Fig. 2.3, but the bulk optics are replaced by an **AWG**. Such a device would represent perhaps the most compact spectrograph possible.

3

PIMMS Design Principles

In this thesis I focus on the development of the optimal dispersive spectrograph, the **PIMMS#0** approach. This spectrograph features the following characteristics:

- Minimal footprint — this can be achieved by minimising the slit width, thus allowing the full dispersive power of the grating or prism to be realised.
- High Efficiency — achieved by reducing losses at the slit and the number of optical surfaces. This is conventionally in conflict with minimising the slit width and very fast (low $f/\#$) optics.
- Maximise/match **étendue** — a non-diffraction-limited input to the spectrograph requires either a very fast camera and or a non-minimal slit to conserve input **étendue**.
- Minimise stray light and related noise — This is a strong function of the slit intensity profile. For example Gaussian illumination would be preferable to the uniform illumination as it produces a Gaussian **point spread function (PSF)** rather than an Airy **PSF** when diffracted.

Every spectrograph design process aims to reach an optimal balance of these factors in order to meet certain performance and science goals. This thesis offers a new approach to spectrograph design that aims to fulfil the above requirements with minimal compromise.

In Chap. 2 I raised a key challenge in high-resolution spectroscopy, namely how to get more light through a high-resolution spectrograph whilst breaking the dependence of spectrograph size on the telescope diameter or other input. The proposed solution, the **photonic lantern (PL)**, allows me to convert **multi-mode (MM)** light to a **single-mode (SM)** diffraction-limited format. **PLs** allow me to attain the goal of remapping the extent of a spectrograph's entrance slit,

3.1 Photonic Lantern as input to a spectrograph

minimising the width while conserving the effective *étendue* (visualised in Fig. 2.1). This format changes some of the approaches and considerations of more a conventional spectrograph design process. The first difference is a by-product of the nature of **PL** itself. The absolutely ideal (read simplest) diffraction-limited spectrograph consists of a uniform long thin slit replacing the comparatively short wide classical slit. However, with the **PL** there is necessarily an array of **single-mode fibre (SMF, or SM cores)** replacing a single **multi-mode fibre (MMF)**. How to format the **SM** outputs of the **PL** becomes a significant design consideration, especially for larger **PLs**. The second change is that the grating (and optics) are now illuminated with a Gaussian illumination profile. While this may seem a simple change, it has some less obvious ramifications. Finally, by stretching the slit in the cross-dispersion (or spatial) direction one might expect a need for increased detector area. However, later I will show that the resulting area increase is by and large balanced by the advantage gained from reducing the slit width in the spectral direction. However, this requires smaller pixels (and thus more pixels) in order to sample the now diffraction-limited slit.

3.1 Photonic Lantern as input to a spectrograph

As was noted in Sec. 2.1, early generations of **PLs** were formed using bundles of **SMF**, leaving the **SMF** outputs to somehow be formed into an input slit for a spectrograph. In some instances this was done using a V-groove array, for example Cvetojevic et al. (2012a). Unfortunately, this approach leaves significant space between the fibre cores resulting in wasted detector space. A proposed solution to this was to use an additional waveguide to remap the **SMF** cores closer together (Thomson et al. 2012). However, this inevitably leads to additional losses (e.g. coupling from **SMF** to the waveguide and material absorption) and complications (e.g. alignment of **SMFs** to the waveguides and transmission of uncoupled light in the remapping waveguide as seen by Jovanovic et al. 2012). So in a design/instrument intended to be as simple as possible they are not the most attractive solution. Another alternative is to reform the original **MMF** input using a second **PL** transition. This is particularly useful if your desire is to retrofit an existing spectrograph with advanced **SM** optical filters (as was done by Trinh et al. 2013), but it eliminates the diffraction-limited advantage (and is thus not considered further in this thesis).

3.1.1 Conventional V-groove

In the simplest case, the **SMF** outputs of the **PL** are formed into a linear array, as is also the common approach when multiple **MMFs** are used to form the entrance slit. The critical factor to consider when forming the entrance slit in this way is the final separation in the cross-dispersion direction between the **SM** cores when imaged by the spectrograph. If the fibres are placed in a simple linear array to form the entrance slit, there will be a significant gap between spectra at the detector. This gap between cores (typically $125\ \mu\text{m}$ for standard **SMF**) leads to wasted detector space unless some additional component is used to bring the cores closer together (e.g. micro-lens for each **SMF**, or a remapping waveguide).

3.1 Photonic Lantern as input to a spectrograph

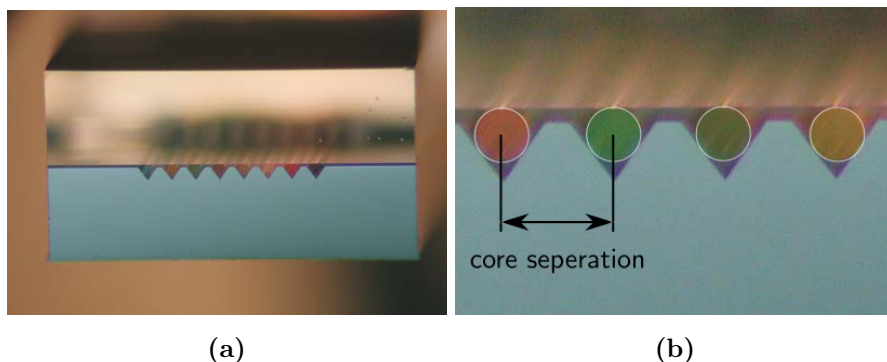


Figure 3.1: *a)* Image of an 8 fibre V-groove array. The V-groove allows for precise positioning of the fibre cores. *b)* Close up view of 4 fibres in the V-groove showing the core separation. In this case the fibres have a separation of $250\mu\text{m}$. Image originally from OzOptics (2013) V-groove data sheet.

3.1.2 Multi-core array input — the TIGER mode

The primary approach I use takes inspiration from the TIGER (Bacon et al. 1995) and SAURON (Bacon et al. 2001) integral field spectrographs. These spectrographs use a micro-lens array to sample the image plane of a telescope. Each micro-lens forms a sub-image that is treated as an individual slit in their spectrograph. The micro-lens array is rotated with respect to the dispersion axis, allowing the area between the sub-images to be used for spectral data. Optical filters are necessary in order to limit spectrum overlap on the detector. The concept is illustrated in Fig. 3.2, which shows resulting series of interlaced spectra.

A similar effect, but with some key advantages, can be achieved when the cores of a **SMF** bundle or a **multi-core fibre (MCF)** are distributed in a regular grid (a hexagonal grid is particular advantageous, which is conveniently the natural packing geometry for fibre-based **PLs**). The array of **SM** cores take the place of the micro-lens array. By keeping this geometry the number of fibres in the entrance slit can be increased while keeping the overall off-axis distance of all the fibres to a minimum.

The desired layout is illustrated in Fig. 3.3, where 19 fibres are arranged along a linear slit (as they would be arranged using a V-groove) or as a hexagonal grid. Overlaid are spectra as they would appear on the detector. The grid is rotated with respect to the dispersion axis, allowing for each spectrum to be imaged without any overlap, yet minimising their separation in the spatial (or cross-dispersion) direction. The same technique can also be used with a linear array of fibres, which is shown in the middle section of Fig. 3.3. In both cases the spectra are now offset in the dispersion direction. This results in some reduction in the effective bandwidth as the **PL** spectra must eventually be recombined. The clipping in the case of the rotated linear array will always be larger than that of the TIGER hexagonal array, particularly when compared to the **MCF** version. I refer to this hexagonal pseudo-slit as the ‘Photonic TIGER’ configuration (Leon-Saval et al. 2012).

3.1 Photonic Lantern as input to a spectrograph

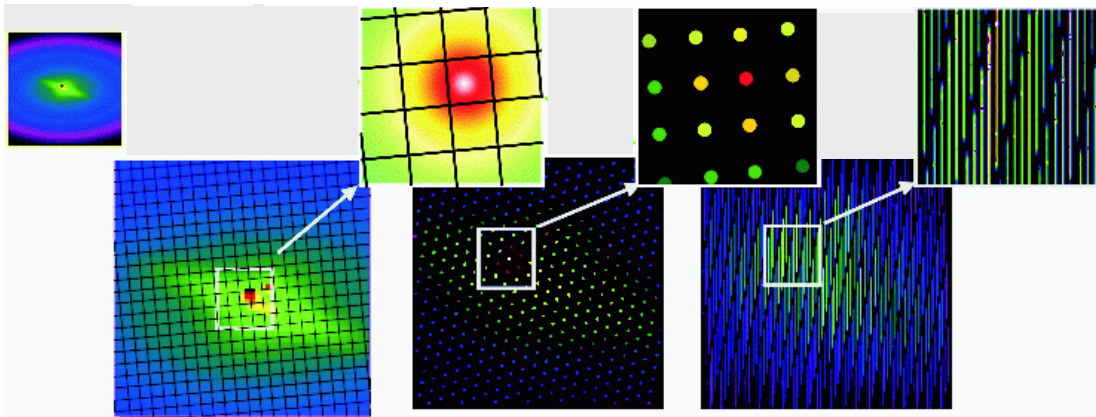


Figure 3.2: Sample image from the TIGER integral field unit (IFU) spectrograph. A micro-lens array (square in image) samples the telescope image to produce an array of sub-images. These become the slits of the spectrograph and are dispersed and re-imaged on the detector. The final result is a series of interlaced spectra. Diagram modified from Bacon et al. (2001)

In the case of MCF the cores could have slightly different geometry (i.e. a modified hexagonal grid) and their separation optimised to minimise unused detector space. As the core positions are not constrained by a need to sample an image (like the micro-lens array must), they can in theory be arbitrarily positioned or spaced. However, the positions do need to be conducive to the PL transition. So, for example, while the cores of a MCF could physically be arranged as a tightly packed linear slit, doing so would result in a poor MM to SM conversion efficiency, thus defeating the purpose (Leon-Saval et al. 2013). This also allows the cores to be arranged such that the MM end of the PL couples particularly well to a given PSF (Fontaine et al. 2012). But most importantly, from the perspective of this thesis, if the grid is sufficiently well spaced, the rotation of the grid allows the spectra to be completely independent, effectively emulating a linear slit (Leon-Saval et al. 2012). This configuration also eliminates the need for the order sorting optical filters required by the micro-lens array fed spectrographs.

Optimal Core Spacing

In order to produce N_c non-overlapping spectra, each corresponding to an individual core in the single MCF (or fibre array), the cores must have sufficient separation perpendicular to the dispersion axis. For simplicity, I will assume here that the spectrograph produces a 1:1 image at the detector, and thus the fibre separation can be discussed in terms of multiples of the mode-field diameter (MFD) of the MCF cores. Firstly, I need to determine the optimal rotation angle, θ , of the MCF (or fibre array). A schematic diagram of the hexagonal grid of cores in a 7 core MCF that has been rotated by an angle θ is given in Fig. 3.4. This is determined by equating the vertical separation (v_{sep}) of adjacent cores (i.e. A and O) and cores at opposite edges of the

3.1 Photonic Lantern as input to a spectrograph

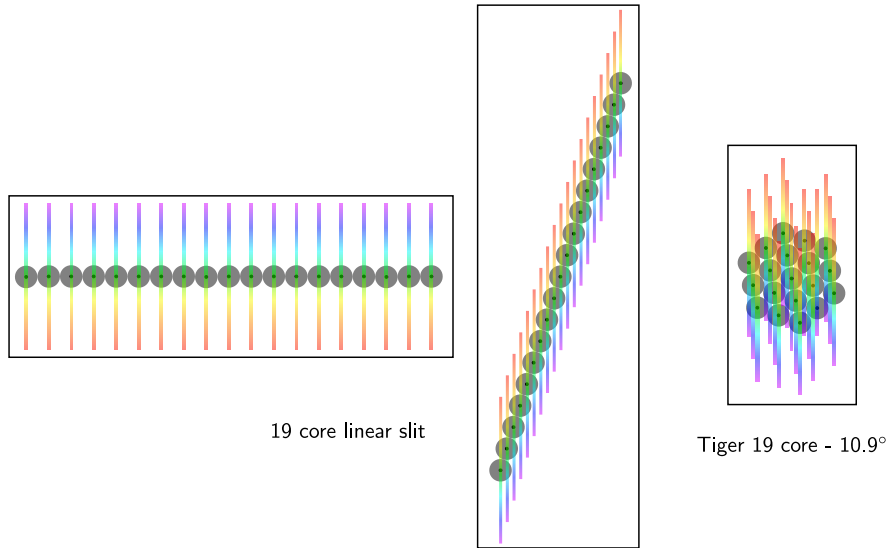


Figure 3.3: Schematic of spectra resulting linear array input vs. the hexagonal grid input. The vertical lines represent the spectra. The simplest way to form the spectrograph slit is to place the **SMF** or cores along a linear slit. However due to the size of the cladding in typical **SMF**, this results in significant waste of detector space. This can be mitigated by rotating the linear array with respect to the dispersion axis, however this reduces the effective bandwidth. A similar effect can be achieved by arranging the fibres in a hexagonal grid. This not only reduces the extent of the slit that needs to be imaged, but also reduces the bandwidth sacrifice. Further, this geometry can be encoded in a **MCF** allowing the spacing to be arbitrarily optimised.

middle row and middle ± 1 row (i.e. B and F). In doing so the rotation required to maximise the separation of each core in the fibre is found.

The vertical separation of adjacent cores A and O is simply,

$$v_{sep} = a = u \sin \theta. \quad (3.1)$$

To find the separation of B and F, labelled ‘a’ in Fig. 3.4, note that the angle $\angle CBD$ must also be θ . I can then see from Fig. 3.4 that

$$a = (d + l) \cos \theta - b \quad (3.2)$$

where d , l and b are,

$$d = u\sqrt{3}/2 \quad (3.3a)$$

$$l = \frac{u}{2} \tan \theta \quad (3.3b)$$

$$b = N_{\text{mid}} u \sin \theta. \quad (3.3c)$$

The three properties in Eqns. 3.3 are due to the regular spacing, u , of a hexagonal grid. In the case as shown in Fig. 3.4, N_{mid} is 3, but the result is general for any size grid.

3.1 Photonic Lantern as input to a spectrograph

N_c	total number of SM cores in hexagonal grid
N_{mid}	number of SM cores in middle row of hexagonal grid
u	SM core separation
θ	rotation of the MCF (or fibre array)
v_{sep}, a	vertical separation of adjacent cores

Table 3.1: Definition of key parameters in Fig. 3.4.

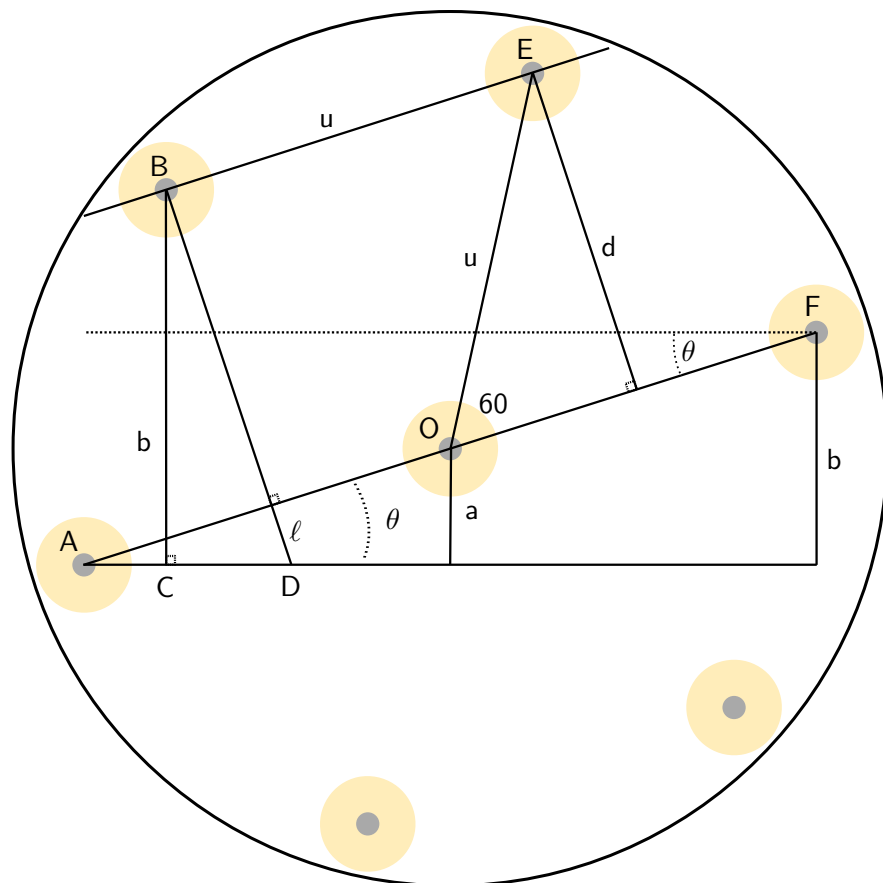


Figure 3.4: Schematic diagram of a hexagonal grid core spacing and geometry in a 7 core MCF. Grey circles indicate the position of the 7 cores. The cores are spaced by a distance u and the fibre is rotated such that each row of cores is at an angle θ to the horizontal axis. It is assumed that the direction of dispersion is vertical here.

3.1 Photonic Lantern as input to a spectrograph

Combining Eqns. 3.1, 3.2 and 3.3 leads to the expression for the optimal rotation angle of a MCF with N_{mid} cores on its middle row or N_c cores in total,

$$\tan \theta = \frac{\sqrt{3}}{2N_{\text{mid}} - 1} = \frac{3\sqrt{3}}{2\sqrt{12N_c - 3} - 3}. \quad (3.4)$$

Equation 3.4 shows the rotation required to optimised the vertical separation of a given hexagonal grid size is independent of the core spacing. However this alone does not guarantee well-separated spectra. Eliminating θ in Eqn. 3.4 using Eqn. 3.1 results in an expression describing the necessary core spacing to achieve a given v_{sep} ,

$$u = \frac{2\sqrt{(1 - N_{\text{mid}} + N_{\text{mid}}^2)}}{\sqrt{3}} v_{\text{sep}} \quad (3.5)$$

Figure 3.5 shows a set of simulated spectra that demonstrate the TIGER principle defined using Eqns. 3.5 and 3.4. It shows arrays with 7 to 127 cores, each at their optimal rotation. What this shows is that for large arrays, the required fibres are quite large. For example, the width of the array with 19 cores is ~ 20 times the MFD, or 200 μm for fibre that is SM in the near-infrared (NIR).

3.1 Photonic Lantern as input to a spectrograph

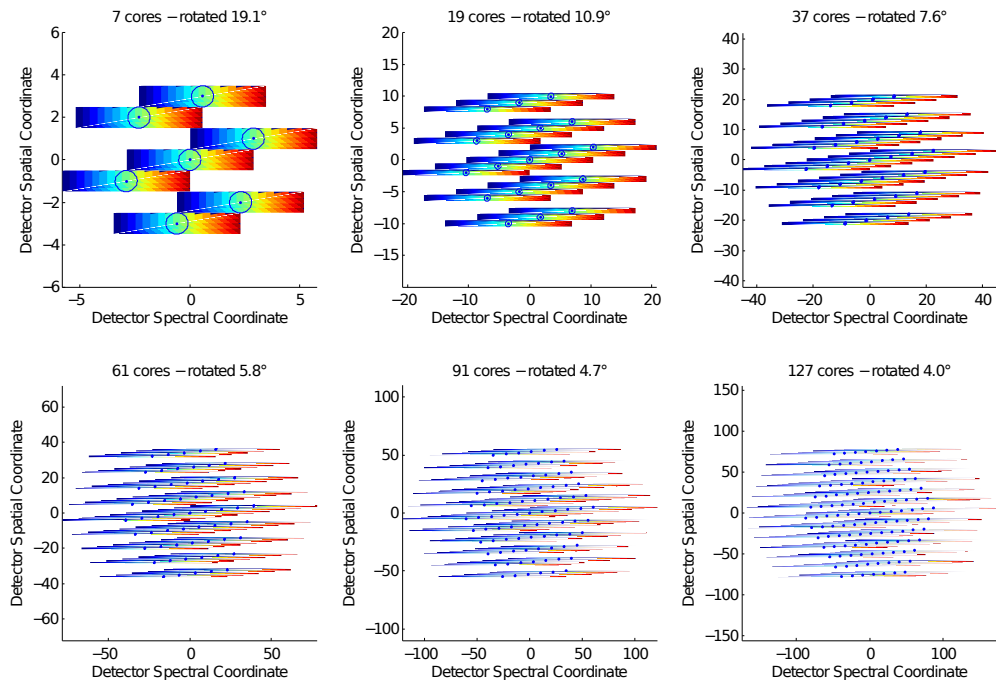


Figure 3.5: Simulated spectra with a vertical separation equal to the $1/e^2$ width of single spectrum. In all six cases this width is set to 1, and marked by a blue circle around each core. In each panel the wavelength range (length of spectrum) shown is set to be twice the distance between the central core and the edge core of the middle row.

3.2 Spectral Resolution/Resolving Power

When using a **PL** the width of the slit is brought to an absolute minimum leaving the instrumental **PSF** as the dominant factor in determining resolution. With diffraction-limited optics (without significant beam truncation) the instrumental **PSF** should reproduce the near-field output of the **PL SMFs**. As a result the instrument resolution would simply be the resolution of the diffraction grating.

In Sec. 1.4.2, I discussed the diffraction-limited and slit-limited resolving power for a uniformly illuminated diffraction grating. With the **PL SM** outputs, the illumination profile is now Gaussian. Thus the diffraction pattern is simply another Gaussian. For consistency I again apply the Rayleigh criterion and use the standard resolution element defined in Chap. 1. For a Gaussian this is 1.119 times the **full width half maximum (FWHM)**. The collimated Gaussian beam is brought to focus with a beam waist in the focal plane given by,

$$\omega_0 = \frac{\lambda f_{cam}}{\pi\omega}, \quad (3.6)$$

where ω and ω_0 are the $1/e^2$ radii of the collimated and focused Gaussian beam respectively. Therefore the linear resolution element is,

$$\delta x_{gauss} = 1.119 \times f_{cam} \left(\frac{\lambda}{\omega} \frac{\sqrt{\ln 4}}{\pi} \right), \quad (3.7)$$

noting that the Gaussian **FWHM** is equal to $\omega_0\sqrt{\ln 4}$. Finally by combining Eqn. 3.7 with the grating dispersion, Eqn. 1.11, returns the diffraction-limited resolving power for the case of Gaussian illumination,

$$\mathcal{R} = \frac{\lambda}{\Delta\lambda} = 2.38 \frac{d_{1/e^2}}{\lambda} \tan\beta. \quad (3.8)$$

For comparison, recall that the resolving power for uniform illumination is,

$$\mathcal{R} = \frac{\lambda}{\Delta\lambda} = 1.64 \frac{d}{\lambda} \tan\beta. \quad (1.14)$$

It may seem that the Gaussian illumination results in higher resolving power, however, this is only because the $1/e^2$ level is used to define a width for the Gaussian. In fact, the resolving power expressions for uniform and Gaussian illumination can be used to determine the equivalent Gaussian beam for a given uniform illumination. Equating \mathcal{R} from Eqn. 3.8 and Eqn. 1.14 shows the uniform beam diameter value is 1.43 times the Gaussian $1/e^2$ diameter value. This can be substituted into the equation of a Gaussian to find the intensity level for measuring the width of a Gaussian that is equivalent to the uniform beam, or

$$N = \exp\left(\frac{-2r^2}{\omega^2}\right) = \exp\left(-2 \frac{\left(\frac{1.43 \times d_{1/e^2}}{2}\right)^2}{\left(\frac{d_{1/e^2}}{2}\right)^2}\right) = 1.5\% \quad (3.9)$$

where $2\omega = d_{1/e^2}$ is the $1/e^2$ diameter of the Gaussian. This shows that if the Gaussian width is measured at the 1.5% level (rather than the $1/e^2$), it is directly comparable to the uniform illumination width.

3.2 Spectral Resolution/Resolving Power

One key difference to note between Gaussian and uniform illumination is where the optical power is concentrated. In a Gaussian beam 85% of the power is in a region half the size of the equivalent uniform illumination. This effectively means the Gaussian beam is more resistant to off-axis aberration effects than the equivalent uniform beam, helping to reduce the complexity required in a given design.

3.2.1 Truncation of a Gaussian beam

The resolving power given by Eqn. 3.8 assumes that the Gaussian beam is not truncated, but this is clearly not the case in any realistic optical system. When the beam passes through any aperture some of the edges will be truncated, which can lead to broadening of the beam when it is brought to focus. This can be understood as clipping the high spatial frequencies of the input slit because the process of collimated a diverging beam is analogous to a Fourier transform of the imaged object (i.e. the slit is converted to a Fourier space representation). Here, I use the examination of truncated Gaussian beams developed by Belland and Creen (1982) to obtain a corrected diffraction-limited resolving power estimate.

When a collimated Gaussian beam is truncated its beam waist is reduced and the divergence of the beam is increased. This is incorporated into Eqn. 3.8 as follows: First, let the ratio of a beam with waist, w , by an aperture with radius, a , be,

$$T = a/w. \quad (3.10)$$

According to Belland and Creen (1982), for small values of T ($\sim 1\text{-}4$), the beam waist is reduced by,

$$K = \frac{\omega'}{\omega} \simeq 1 - \sqrt{\Delta P/P} = 1 - \exp(-T^2), \quad (3.11)$$

where ω and ω' are the beam waist before and after truncation respectively. Simultaneously the divergence increases by

$$\frac{\theta'}{\theta} \simeq [1 - \sqrt{\Delta P/P}]^{-1} = [1 - \exp(-T^2)]^{-1}, \quad (3.12)$$

where θ and θ' are the beam divergence before and after truncation respectively. In both Eqn. 3.11 and Eqn. 3.12 ΔP is power lost due to the truncation and P is the initial power. Note that while the collimated beam waist is reduced, when it is brought to a focus Eqn. 3.6 dictates that the focused beam must be broadened, and accordingly the spectral resolution is reduced. Incorporating this K factor into the derivation of Eqn. 3.8 returns the truncation-corrected resolving power:

$$\mathcal{R} = \frac{\lambda}{\Delta\lambda} = 2.38 \frac{K d_{1/e^2}}{\lambda} \tan \theta_i. \quad (3.13)$$

It is notable that for even a small amount of power loss, the resolution is decreased substantially. This can be seen in Fig. 3.6 where the total transmitted power and K factor are given as a function of truncation ratio. Figure 3.6 shows that at a 1% loss in power, the resolution is decreased to 90% of its maximum. It is not until T is greater than ~ 2.5 that clipping effects become negligible.

3.3 Detector Area Implications

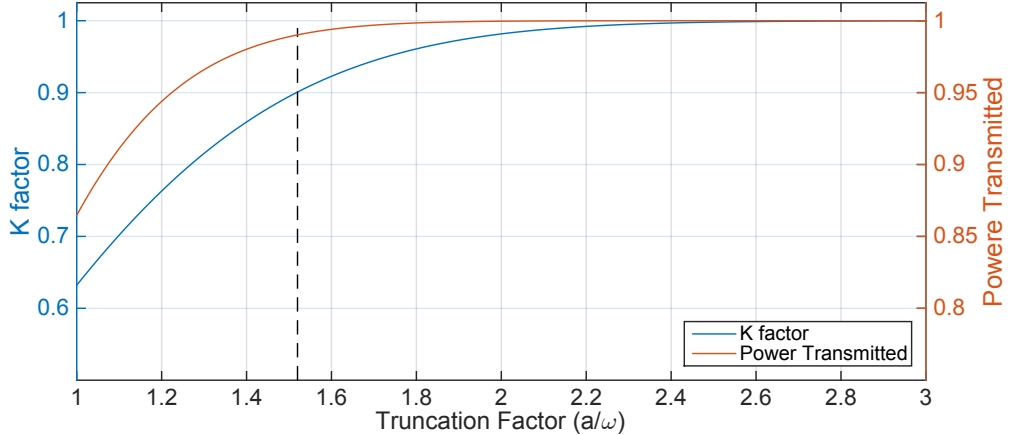


Figure 3.6: Shown are the K factor (blue) and Power transmitted for truncation ratio 1 (aperture equals the $1/e^2$ diameter) to 3 (aperture is 3 times the $1/e^2$ diameter). The dashed line is for a truncation ratio of 1.52, where just a 1% loss of power corresponds to a 10% reduction in the diffraction-limited resolving power.

3.2.2 Required beam size

The output of most commercially available SMF has a numerical aperture (NA) of around 0.1¹. This corresponds to a $f/\#$ of ~ 5 . Using this information along with Eqn. 3.8 an estimate of the required focal length (and thus the beam size) required to achieve a given resolving power can be found. Because the input $f/\#$ of the spectrograph is essentially fixed, the focal length of collimator becomes a more relevant starting point. Thus the collimator focal length design equation is,

$$f_{\text{col}} \approx 2.1 \times \mathcal{R} \frac{\lambda}{K \tan \theta_i} \quad (3.14)$$

The final K factor then becomes a parameter when choosing/designing optics of a suitable diameter. For example, one could use a 25.4 mm (1 in) lens with longer focal length (and thus larger beam, and more significant truncation) or 50.8 mm (2 in) lens with shorter focal length (and thus smaller beam, with less significant truncation) and have both achieve similar resolving powers. This is essentially treating $K f_{\text{col}}$ as a constant, such that a smaller K factor is balanced by the larger $K f_{\text{col}}$.

3.3 Detector Area Implications

The detector area required for a photonic integrated multi-mode spectrograph (PIMMS) type spectrograph is effectively the same as that required by equivalent MM spectrograph. This

¹Some confusion can be caused by supplier data-sheets. More often than not they fail to specify a width definition, and seem to rarely use the $1/e^2$ diameter.

3.3 Detector Area Implications

unexpected¹ result requires some discussion and is the focus of this section. This was originally discussed by Robertson (2013a) during the preparation of Paper 1 (Betters et al. 2013), and has been reproduced here for completeness.

First assume that the PIMMS and MM spectrographs share equal bandwidth and resolving power with a similar étendue. The detector area requirements between the MM case and PIMMS case can then be compared using their respective dispersed images. For simplicity I will assume both the MMF and SMFs have a similar NA. The input slit is illustrated in Fig. 3.7.

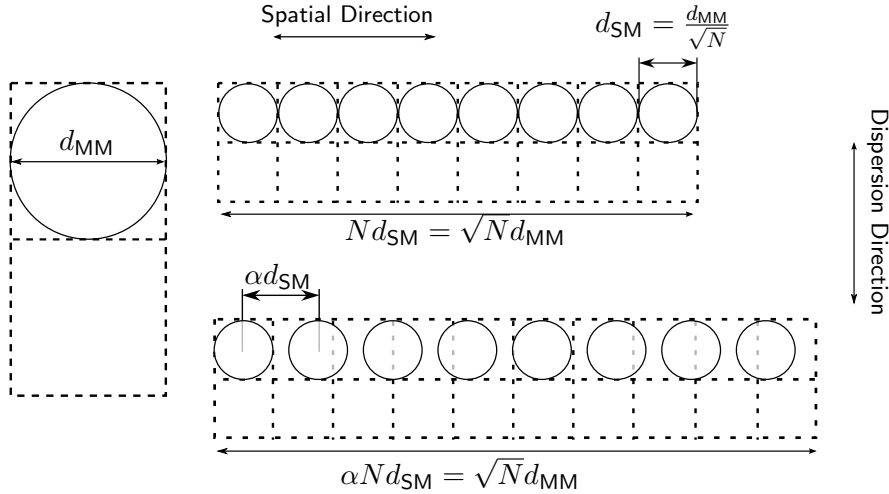


Figure 3.7: Dimensions of the MMF slit where d_{MM} is the full width at zero intensity and two SMF slits with $1/e^2$ diameter, d_{SM} . One SMF slit shows a minimum separation configuration (where the MFD of the SMF overlap in the spatial direction) and the other with a spatial separation of αd_{SM} .

3.3.1 Spatial axis

The MMF diameter at the slit is d_{MM} and it radiates at NA_{MM} , and is thus collimated by a collimator with same NA (i.e. $\text{NA}_{\text{MM}} = \text{NA}_{\text{COL}}$). This is imaged onto the detector by a camera with $\text{NA}_{\text{MM-CAM}}$. Thus the spatial width of the MMF image at the detector is

$$x_{\text{MM}} = d_{\text{MM}} \frac{\text{NA}_{\text{MM}}}{\text{NA}_{\text{MM-CAM}}}. \quad (3.15)$$

The SMF feed consist of N fibres produced by the PL conversion, where N is given by Eqn. 2.1. Each SMF has a $1/e^2$ beam diameter

$$d_{\text{SM}} = \frac{4\lambda f_{\text{COL}}}{\pi d} \quad (3.16)$$

¹Hindsight this is perhaps unsurprising as the mode count must corresponds to the slicing factor of the MMF input (i.e. the étendue is conserved), however most prior discussions had assumed PIMMS would require a larger detector in at least one axis.

3.3 Detector Area Implications

where d is beam diameter at the collimator and f_{COL} is the focal length of the collimator. The beam diameter at the detector is found using the same formula but in reverse, and substituting the camera focal length f_{SM-CAM} for collimator. Thus

$$\delta x_{SM} = \frac{4\lambda f_{SM-CAM}}{\pi d} \quad (3.17)$$

where δx_{SM} is the $1/e^2$ diameter of the detector image of one **SMF**. The camera focal length can also be replaced by its **NA**,

$$f_{cam,sms} = \frac{d}{2NA_{SM-CAM}}, \quad (3.18)$$

to get

$$\delta x_{SM} = \frac{2\lambda}{\pi NA_{SM-CAM}}. \quad (3.19)$$

The full extent of the **SMF** slit is clearly dependent on the separation of the individual **SMF** images. Here the separation of adjacent **SMF** images is defined as $\alpha\delta x_{SM}$, so the total spatial extent (ignoring off-by-one edge effects) of the slit is

$$x_{SM} = N\alpha\delta x_{SM} = \frac{2N\alpha\lambda}{\pi NA_{SM-CAM}} \quad (3.20)$$

Combining Eqns. 2.1, 3.15 and 3.20 results in

$$\frac{x_{SM}}{x_{MM}} = \alpha\sqrt{N} \frac{NA_{MM-CAM}}{NA_{SM-CAM}} \quad (3.21)$$

showing that the spatial extent of the single mode pseudo-slit image will scale as \sqrt{N} , with an additional factor α to account for the necessary separation of the **SMFs**. The separation is minimised by using an integrated optics component to bring the waveguides closer together, a micro-lens array or using an approach like the TIGER mode (cf. Sec. 3.1.2).

3.3.2 Wavelength axis

Assuming a Littrow configuration (i.e. no anamorphic magnification) it is clear that the **MMF** width in the wavelength axis is just x_{MM} from Eqn. 3.15, but with an additional factor to obtain a single resolution element. So in the **MM** case,

$$y_{MM} = \frac{\sqrt{3}}{2} \gamma_{PC} d_{MM} \frac{NA_{MM}}{NA_{MM-CAM}} \quad (3.22)$$

where the factor $\sqrt{3}/2$ converts the fibre diameter to the **FWHM** of a projected circle (PC). The γ_{PC} is a scaling factor to convert the PC width into a single resolution element consistent with the Rayleigh criterion (i.e. Chap. 1 and Robertson 2013b). The value of γ_{PC} would be about 0.85 for perfect image quality or about 0.9 - 0.95 with some aberrations.

The **SM** case is essentially the same again. Equation 3.19 is used to find the resolution element in **SM** case, that is,

$$y_{SM} = \frac{\sqrt{2 \ln 2}}{2} \gamma_G d_{SM} = \frac{\lambda \gamma_G \sqrt{2 \ln 2}}{\pi NA_{SM-CAM}} \quad (3.23)$$

3.3 Detector Area Implications

where the numerical factor and γ_G convert the $1/e^2$ diameter to a FWHM and scale the Gaussian width to a single resolution element respectively. Combining Eqns. 2.1, 3.22 and 3.23 results in

$$\frac{y_{SM}}{y_{MM}} = \sqrt{\frac{2 \ln 2}{3}} \frac{1}{\sqrt{N}} \frac{\gamma_G}{\gamma_{PC}} \frac{NA_{MM-CAM}}{NA_{SM-CAM}} \quad (3.24)$$

which shows that the diffraction-limited case has a \sqrt{N} advantage over an equivalent MMF in the wavelength direction.

3.3.3 The ratio of detector areas

Combining Eqns. 3.21 and 3.24 gives the ratio of the detector area required for the MM case and PL diffraction-limited case. This results in

$$\frac{Area_{SM}}{Area_{MM}} = \frac{x_{SM} y_{SM}}{x_{MM} y_{MM}} = \alpha \sqrt{\frac{2 \ln 2}{3}} \frac{\gamma_G}{\gamma_{PC}} \left(\frac{NA_{MM-CAM}}{NA_{SM-CAM}} \right)^2 \quad (3.25)$$

The first thing to note is that there is no apparent dependence on N. This is a direct result of the advantage the diffraction-limited slit gains in the wavelength direction being balanced by the need to increase the length of the slit. Assuming both cameras have the same *f/#* (i.e. NA) and substituting the γ values, Eqn. 3.25 simplifies to

$$\frac{Area_{SM}}{Area_{MM}} = 0.853\alpha = \frac{\alpha}{1.172}. \quad (3.26)$$

So if the separation of the SMF is less than or equal to 1.172 times their $1/e^2$ diameter, the PL spectrograph will require the same or less detector area as the equivalent MM spectrograph. Otherwise the extra area required for a SM spectrograph versus the MM spectrograph is proportional to the separation of the SMFs.

3.3.4 Area vs. Pixels

The above derivation relates to the ratio of detector areas, and not the number of pixels required. The diffraction-limited PIMMS case will require more pixels in the spatial direction unless the spectra can be effectively compressed optically or sampled with rectangular/binned pixels. The larger number of pixels for the PIMMS case has clear implications for readout noise. Related is the fact that the diffraction-limited image is much smaller than the MM image, and will thus require smaller pixels or a slower (than the MM equivalent) camera to adequately sample the PSF. As expected, Eqn. 3.25 shows that a slower camera increases the required detector area very quickly. Assuming equal sampling for a given pixel pitch (i.e. the detector images are the same size) the ratio of NA_{MM-CAM} with NA_{SM-CAM} is

$$\frac{NA_{MM-CAM}}{NA_{SM-CAM}} = \sqrt{N} \quad (3.27)$$

and Eqn. 3.25 becomes

$$\frac{Area_{SM}}{Area_{MM}} = \frac{x_{SM} y_{SM}}{x_{MM} y_{MM}} = \alpha N \sqrt{\frac{2 \ln 2}{3}} \frac{\gamma_G}{\gamma_{PC}} \quad (3.28)$$

3.3 Detector Area Implications

So for any given detector the diffraction-limited case will then only be able to image $1/N$ times the spatial information of the **MM** spectrograph using the same detector area. Conversely, in cases where the detector pixels are small, the **MM** camera would need to be \sqrt{N} faster.

4

The Spectrographs

I have designed and built three spectrographs based on the [photonic integrated multi-mode spectrograph \(PIMMS\)](#) concept. Each of these had slightly different goals intended to highlight and explore the properties of the [PIMMS](#). The first PIMMS operates in the [short-wave infrared \(SWIR\)](#) (1550 nm) and demonstrates the Gaussian like [point spread function \(PSF\)](#) and thus low scattering properties of a [single-mode fibre \(SMF\)](#) input. The second is a high resolution échelle spectrograph operating in the visible. It has been used to study how stable such a spectrograph can be made, and is intended to be a precursor for a full scientific instrument. Finally, I describe an ultra-compact visible spectrograph intended for use on a nano-satellite.

4.1 PIMMS IR

The contents of this section are based upon work published in Paper 1.

PIMMS IR is a modular spectrograph, originally designed to allow for the detailed laboratory testing of other astrophotonics technologies. I envisioned a design where I could easily substitute different diffraction gratings to quickly tune for a desired bandwidth and/or spectral resolution to suit a specific test. Further the input slit can easily be changed to interface with other instruments. The nominal grating uses a single [volume-phase holographic \(VPH\)](#) grating with a line density of 1120 lines/mm to achieve [resolving power \(\$\mathcal{R}\$ \)](#) of \sim 30,000 at λ 1550nm. The nominal slit makes use of the TIGER configuration, using a lightly fused bundle of 7 [SMFs](#)

(SMF-28e) that are spliced to a 1×7 photonic lantern (PL).

A typical SMF output in the SWIR produces a $f/5$ ($\text{NA} \approx 0.1$ or $\omega_0 = 5.25\mu\text{m}$) Gaussian beam. But the primary consideration in the overall design of this spectrograph was the size of commercially available diffraction gratings (as that sets an absolute limit on maximum beam size). The size of the diffraction grating along with the considerations discussed in Sec. 3.2.1 allows for a simple determination of the minimum $f/\#$ required of the collimator (assuming the collimated beam $1/e^2$ diameter is about 1/2 the width of the grating). The required camera $f/\#$ is of course determined by the size of the detector pixels. Here I use a Xenics¹ Xeva with $30\mu\text{m}$ pixels and a 320×240 array, and, when available, a Xenics Xeva with $20\mu\text{m}$ pixels and a 640×480 array².

The version discussed in this thesis and in Paper 1 is actually the second iteration of the design. I have specified two distinct configurations. First a mid-range option using a 600 lines/mm ‘off the shelf’ VPH from Wasatch Photonics³ with a resolving power of 15,000 (hereafter referred to as the ‘600 version’). The second is a high resolution version using a custom 1120 lines/mm grating again from Wasatch Photonics. It is hereafter referred to as the ‘1120 version’. This version has a measured resolving power of $\sim 30,000$. The 600 and 1120 version use unique collimators, while the same camera setup is used in both with slight adjustments to suit each collimator. A variant of the 1120 version includes a second grating, effectively doubling the dispersion (referred to as the ‘dual 1120 version’). A summary of differences is shown in Table 4.1. Scale diagrams of the 1120 version and the dual 1120 version are shown in Fig. 4.1. In all cases the optimal setup samples with PSF with at least 2 pixels per full width half maximum (FWHM) sampling when using a detector with $30\mu\text{m}$ pixels.

4.1.1 Optical Design

Grating

My initial goal was to use purely ‘off the shelf’ components for the entire instrument, however in order to maximise the resolving power of the spectrograph, I opted for a custom Wastach Photonics VPH grating as the primary dispersing element. This grating is 50.8 mm (2 in) in diameter with a 42.8 mm clear aperture and an equivalent ruling of 1120 lines/mm. At the design wavelength of 1550 nm it has an overall efficiency of 80% dropping to $\sim 75\%$ at 1540 nm. The Littrow grating angle at 1550 nm is 60 degrees. The high angle of incidence means that the collimated beam size must be substantially smaller than the grating. The projected size on the grating is a factor of $1/\cos\theta_i$ (or a factor of 2 in this case) times the beam width. This calls for a shorter focal length collimator than a similarly sized grating with a lower line density would need to be efficiently illuminated (per Eqn. 3.13). It also follows that a shorter focal length camera is required to attain adequate sampling of the spectrograph PSF with the

¹<http://www.xenics.com/>

²Courtesy of the Australia Astronomical Observatory — <http://www.aoa.gov.au>

³<http://wasatchphotonics.com>

4.1 PIMMS IR

Table 4.1: Summary of the key properties PIMMS IR configurations.

	600 Version	1120 version	dual 1120 version
lines/mm	600	1120	dual 1120
Efficiency @ 1550nm	80	77.5	$77.5^2 = 60$
Estimated throughput ^a (%)	80	73	56
Optical Performance	Gaussian with slight wings at edges	Near perfect Gaussian everywhere	Near perfect Gaussian everywhere
Resolving Power	15,000	32,000	60,000
resolution (pm)	103.3	48.4	25
Bandwidth (nm)	14	7.5	3.5
No. of Resolution Elements	135	155	140
Total Track (mm)	675	454.441	593
Footprint ^b (mm)	720x230	450x190	470 x 220

^a Defined as the ratio of photons detected to photons collected.

^b minimum region to contain design.

30 μm pixel detector. This also lends itself to a relatively compact setup (decreased footprint, smaller optics etc).

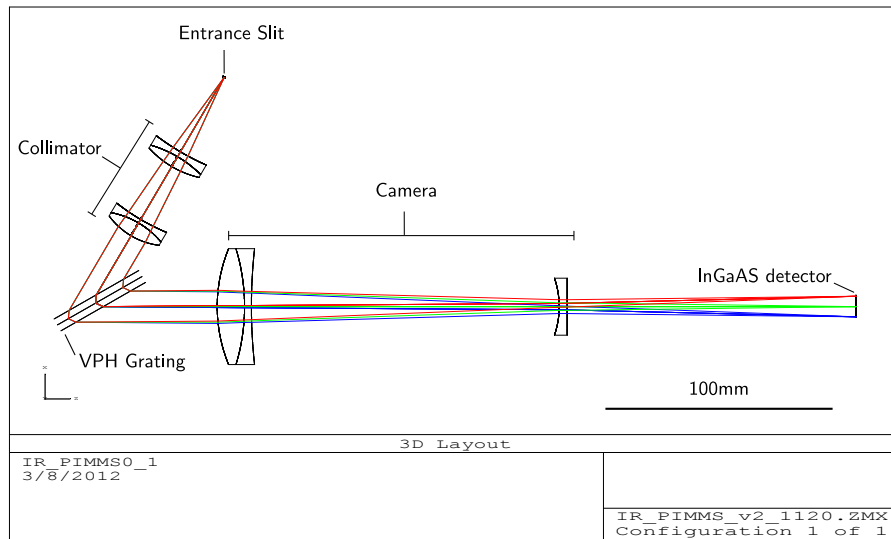
The alternative 600 lines/mm **VPH** grating has an efficiency of 85% at 1550nm. The grating angle in this case is just 27 degrees. This allows/requires an increase in the collimated beam size, and thus requires a longer focal length collimator.

Collimator

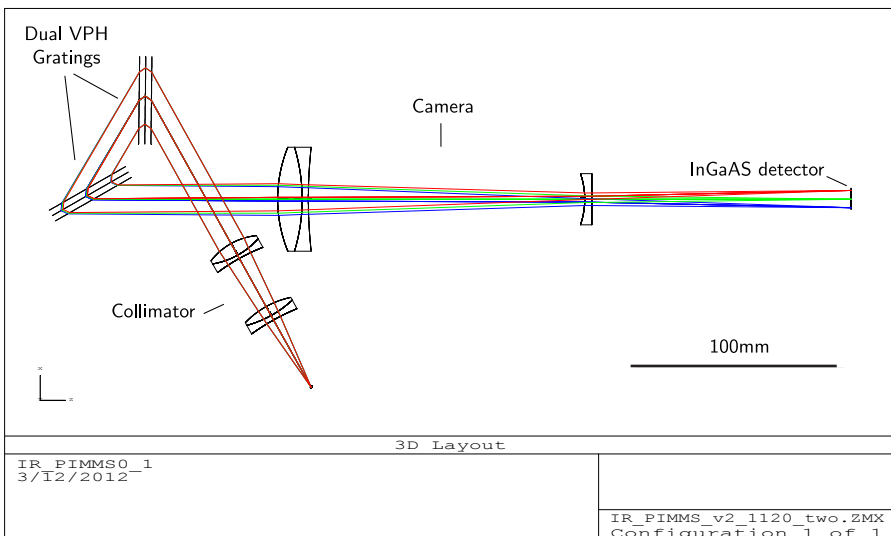
In Sec. 3.2.1 the analysis of Gaussian beam truncation indicated that the optimal $1/e^2$ beam width should not exceed half the width of the limiting aperture in the system. Using this as a starting point, the ϕ 42.8mm clear aperture of the **VPH** grating results in a maximum beam diameter, d_{max} , of $\sim 21.4\text{mm}$. Note that this is the projected beam width on the grating, thus the collimated beam width is limited to $d_{max} \cos \theta_i = 2\omega_r$. Consequently the beam from the collimator should have a width $\sim 11\text{mm}$ at 1550nm for the grating selected above. This beam width corresponds to a collimator with a focal length close to 55mm for the output of a **SMF**.

In order to achieve a diffraction-limited system, a pair of carefully selected achromatic doublets are used to collimate the beam. Several pairs were tested both via geometric ray tracing, and if performance appeared acceptable, using the ZEMAX **physical optics propagation (POP)**. The final pair selected are both 25.4 mm (1 in) achromatic doublets from the Thorlabs catalogue. The first has a focal length of 150mm and the second 100mm and the two are separated by 26.9 mm of air. The back focal length is 37.77mm. The separation was determined via a combination of ray tracing optimisation, **POP** simulations of the beam quality and finally the lengths of lens tubes required to mount the optics. The **EFL** of the collimator is nominally

4.1 PIMMS IR



(a)



(b)

Figure 4.1: 3D layouts of the PIMMS IR configurations with 1120 lines/mm VPH gratings. In both cases the same camera is used, but the spacing between the doublet and the final element (a plano-concave lens) is adjusted to change the **effective focal length (EFL)** (i.e. it behaves as a simple telephoto lens). (a) $R \sim 31000$ — 1120 version. Collimator uses 1in optics. (b) $R \sim 60,000$ — dual 1120 version. The same optics as previous version are used, but with an additional grating. The distance from the lens to gratings is increased to avoid obscurations. An additional version that uses a the 600 lines/mm grating exists that is essentially identical to 1120 version, but with a shallower angle of incidence on the grating and a slightly different in the collimator).

4.1 PIMMS IR

68.6mm, resulting in a beam diameter of ~13mm, or a truncation ratio of ~1.6 at the grating. This beam width results in some truncation related broadening in the **PSF** of ~10% due to the collimator. This was estimated by comparing the camera focal lengths required to form an equal width **PSF** with the collimator and an equivalent perfect lens using **POP**. The truncation introduced was deemed a necessary compromise as the shorter focal length configurations investigated produced poorer optical performance, which would have led to even more significant broadening.

The collimator for the 600 version uses two 50.8 mm (2 in) achromatic doublets from Thorlabs (the only manufacturer with this size **SWIR** achromats). The increased beam size of the 600 version meant larger lenses needed to be used in order to avoid significant beam truncation. A 300mm and 200mm focal length lens, with a nominal separation of 4.76mm, combine to form the 123mm collimator. The back focal length is 101.3mm. The resulting beam size is 25mm, or 28mm projected on the gratings, producing about the same fill factor as the 1120 version.

Camera and Detector

The ideal detector for PIMMS IR would have rectangular pixels that are $3 \text{ } \mu\text{m}$ wide and several microns tall. This would allow for the most compact design (shorter focal length camera) and reduce the read noise penalty of spreading the spectrum over more pixels in the spatial/cross-dispersion direction. Of course, PIMMS IR has a more conventional detector, the Xenics Xeva 1.7 320 InGaAs detector. It has a 320×240 array of square $30 \text{ } \mu\text{m}$ pixels that are sensitive to **SWIR** light ($1 \text{ } \mu\text{m}$ to $1.7 \text{ } \mu\text{m}$). In order to correctly sample spectra at the detector (i.e. > 2 pixels per FWHM) the magnification of the slit by the collimator and camera is the ratio of the **FWHM** mode field diameter of a **single-mode (SM)** input fibre ($6.2 \text{ } \mu\text{m}$ for SMF-28e) and the width of two pixels (i.e. $M = 60\mu\text{m}/6.2\mu\text{m} = 9.7$). So the magnification of the optics needs to be of order 10 or a camera focal length close to ~680mm. However, due to broadening effects, the required focal length to achieve 2 pixels per FWHM sampling was only 540mm.

The focal length difference indicates that the broadening caused by the optics and diffraction grating is of order 20%. This is consistent with the beam broadening due to truncation at the grating combined with the ~10% broadening from the collimator. The final camera is a simple telephoto lens constructed with a 200 mm achromatic doublet and a -75 mm plano-concave lens. For the 1120 version the separation is 132 mm resulting in a focal length of 540mm and a total length of 280 mm, so it has a telephoto ratio of ~0.5. With a separation of 119.5 mm the focal length is 983mm, and the total length of the lens (first surface to focus) is 437 mm, or telephoto ratio of (0.44). This is the configuration used for the 600 version. Note that the negative element is reversed in the 600 configuration with respect to the 1120 versions. This helped to balance spherical aberration and keep the system diffraction-limited. It is important to reiterate that the camera could be much smaller/shorter if the detector pixels were smaller, but that PIMMS IR is very close to the minimal configuration possible with the available components.

Hereafter, I will only be discussing the 1120 version as it was the only version actually constructed and is the subject of Paper 1.

4.1.2 ZEMAX Analysis

Ray Tracing

Perhaps one of the most fundamental analyses available within the ZEMAX optical design software is the ray tracing spot diagram. In order to generate the spot diagram, a bundle of rays is propagated through the optical system following the rules of geometric optics and their final positions recorded. Each bundle originates from a field position (the optical system objects, here positions on the input slit of the spectrograph) with a predefined distribution. In this system the properties of a **SMF** are used to define the ray bundle distribution, namely the **numerical aperture (NA)**. The ray angles have a Gaussian distribution where the $1/e^2$ diameter is the fibre **NA** (0.1 for SMF-28e). It should be noted that while ray tracing provides a good starting point in for evaluating a design, it must be done in concert with a full **POP** simulation. This is because the ‘rays’ emitted from the **SMF** are coherent, and could thus interfere destructively at the focus, while ray tracing assumes ray density is proportional to intensity (with no phase information).

ZEMAX spot diagrams for evenly spaced field positions along the length of the spectrograph slit are shown in Fig. 4.2. The spot diagrams show relatively uniform performance on and off axis and with wavelength. Position 1 corresponds to an on-axis fibre and position 2 corresponds to furthest position off-axis a fibre can be placed on the slit while still forming an image on the Xenics detector ($\sim 0.4\text{mm}$). The 3rd position corresponds to a rough limit on the size of the slit before the collimator design need to be revisited ($\sim 0.8\text{mm}$). The wavelength range shown has a bandwidth of 20nm centred on 1550nm. The central 8nm correspond to the bandwidth seen by the Xenics 320 detector, while the extended range is the bandwidth that could be seen by a $2\text{k} \times 15\ \mu\text{m}$ pixel array. A ray tracing estimate of throughput, including anti-reflective coatings on optics and diffraction grating efficiency, is approximately 70%.

The Airy disk shown in Fig. 4.2 is calculated by ZEMAX as ‘1.22 times the wavelength times the **f/#** of the beam’. While it does not directly consider diffraction, it provides a reasonable estimate as to how well the system is performing. All the spot diagrams indicate that the system should be diffraction-limited as rays are confined within the Airy disk. The wavefront error of the system further supports this. The maximum **peak to valley (PTV)** error is 0.22 waves with an **root mean square (RMS)** of 0.036 (found at the edges of the detector), fulfilling both the Rayleigh 1/4 wave **PTV** criterion and 1/14 wave **RMS** wavefront error criterion for diffraction-limited optics.

Physical Optics

To confirm a Gaussian **PSF**, and thus the diffraction-limited nature of the system, I used ZEMAX **POP** simulations, which perform full diffraction propagations of monochromatic wave-

4.1 PIMMS IR

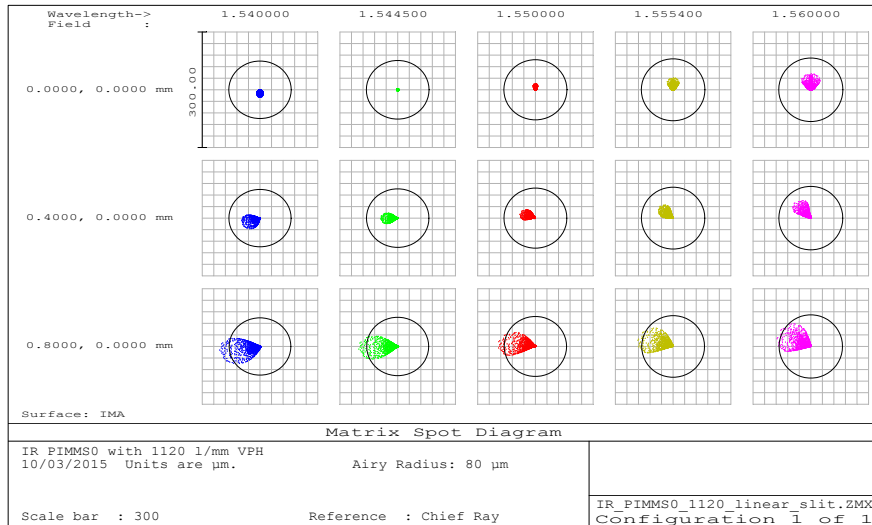


Figure 4.2: Spot diagrams for field position: Row 1 - on-axis, Row 2 - edge of Xenics camera FOV and Row 3 - Edge of diffraction-limited optical performance. Wavelength coverage is: $1550 \pm 4\text{nm}$ for the PIMMS IR detector and $1550 \pm 10\text{nm}$ corresponding to a 2K detector with $0.15\mu\text{m}$ pixels. Each diagram is confined by a $300 \mu\text{m}$ box. The black circle in each shows the estimated Airy disk.

fronts thorough the optical system. Here the pilot beam (the input) is defined as Gaussian beam with a $1/e^2$ diameter of $10.5 \mu\text{m}$ (i.e. the **mode-field diameter (MFD)** of a SMF-28e fibre). The M^2 beam quality factor is a measure of how close to diffraction-limited or Gaussian-like the beam is. It is defined as the ratio of the beam parameter products of the beam with a Gaussian beam of the same wavelength. The beam parameter product is the product of the beam $1/e^2$ radius (ω_0) and the far-field beam divergence (ISO Standard 11146 2005; Siegman 1986). For a Gaussian beam it is simply λ/π . The M^2 factor is also sometimes referred to as a ‘times diffraction-limit’ factor.

Diffraction-limited optics imply that the image of the pilot beam formed by the spectrograph should have an M^2 factor close to unity. Typical **POP** profiles for the same input field positions from Fig. 4.2 are shown in Fig. 4.3. The diagrams are show with log 10 intensity scale, thus the gaussian **PSF** should appear parabolic. Each has an M^2 value close to 1.2, increasing slightly for the extreme field position. This departure from a perfect Gaussian appears as the wings seen at the 10^{-3} level. These are predominantly due to truncation of the Gaussian at the collimator, but is also a function of the diffraction grating. There is a slight asymmetry in the profile at 1554 nm, where the wings begin to appear at the 10^{-2} level. The **POP** simulations were also used to confirm that the nominal beam $1/e^2$ diameter incident on the grating is 13 mm. According to Eqn. 3.8, the maximum resolving power this spectrograph could attain is thus ~ 34500 at 1550nm.

The resolution can also be estimated using ZEMAX to find the width of the **POP** profile and

Table 4.2: Resolving power ($\lambda/\Delta\lambda$) and effective K-factor over the specified wavelength range at the edges and centre of the detector as measured from POP simulations.

Wavelength (nm)	Resolving Power (Effective K factor)		
	On-axis	Off-axis 420 μm	Theoretical
1544.5	31000 (0.89)	30200 (0.87)	34663
1550.0	31000 (0.89)	30200 (0.87)	34574
1555.4	30700 (0.89)	30000 (0.87)	34485

assigning a wavelength scale using the linear dispersion determined via ray tracing. The same resolution element used by Eqn. 3.8 is used in calculating the resolving power ($1.119 \times \text{FWHM}$). A summary of the resolving powers measured in this way at the various wavelengths and field positions can be seen in Table 4.2. Remarkably, these values are about 90% the theoretical maximum values, indicating a reasonable balance between grating illumination and truncation. Further, the POP simulations show that approximately 1% of the initial beam power is lost through the optical system, which is consistent with Eqn. 3.11, the K-factor definition.

4.1.3 Experimental Analysis

PIMMS IR is not just a concept instrument, a prototype (the 1120 version as described above) has been constructed and in testing performs to specification. I have used this spectrograph to investigate two key characteristics of the SMF outputs of a PL. The first is scattering properties of the spectrograph, namely the quality of the PSF (amount of light in the wings vs in the core of a focus spot). It was anticipated that the diffraction-limited Gaussian beam input would result in a very low amount of scattering. This stage also allows for verification of the ZEMAX simulations. The second characteristic was spectral variability between the SM outputs of the PL. Some previous studies saw small periodic variations of the spectra in wavelength between each SM output.

PSF and scattering

To characterise the instrumental PSF, I fed the PIMMS IR spectrograph with one SMF. The input was coupled directly to a tunable laser source (Tunics 3642 HE L) set to 1550.25 nm. A typical line profile (collapsed in the spatial direction with a Gaussian weighted summation¹) is shown in Fig. 4.4, along with the best-fit Gaussian, ZEMAX POP simulations and the same laser line measured using an optical spectrum analyser (OSA; ADVANTEST Q8384). I also show the typical spectral line profiles attributed to the IRIS2 spectrograph (Tinney et al. 2004) and the AAOmega spectrograph (Saunders et al. 2004). These show that the wings in a PIMMS design are much lower than in a conventional design, bettering IRIS2 by two orders of magnitude

¹This is to be consistent with a normal 1D spectral extraction. When the spatial axis is summed it is weighted to reduce the contribution of detector read noise in final the integrated intensity.

4.1 PIMMS IR

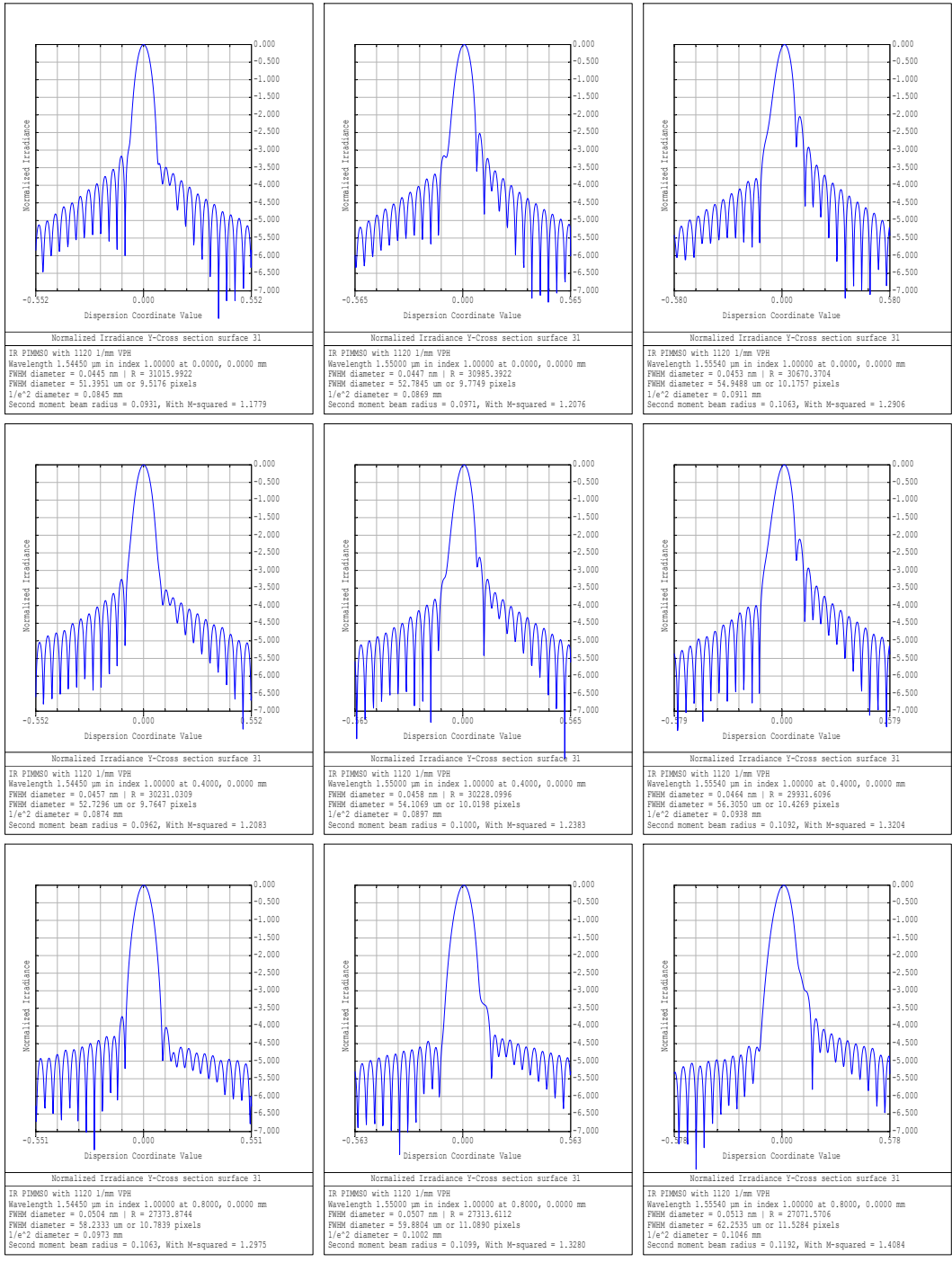


Figure 4.3: Physical optics profiles (\log_{10} intensity scale) in the spectral direction for a fibre on-axis (top row), 0.4mm off-axis (middle row) and 0.8mm off-axis (bottom row). Included is the spectral resolution element in nm, the FWHM, and the ISO standard 11146 second moment width and beam quality factor (ISO Standard 11146 2005; Siegman 1986).

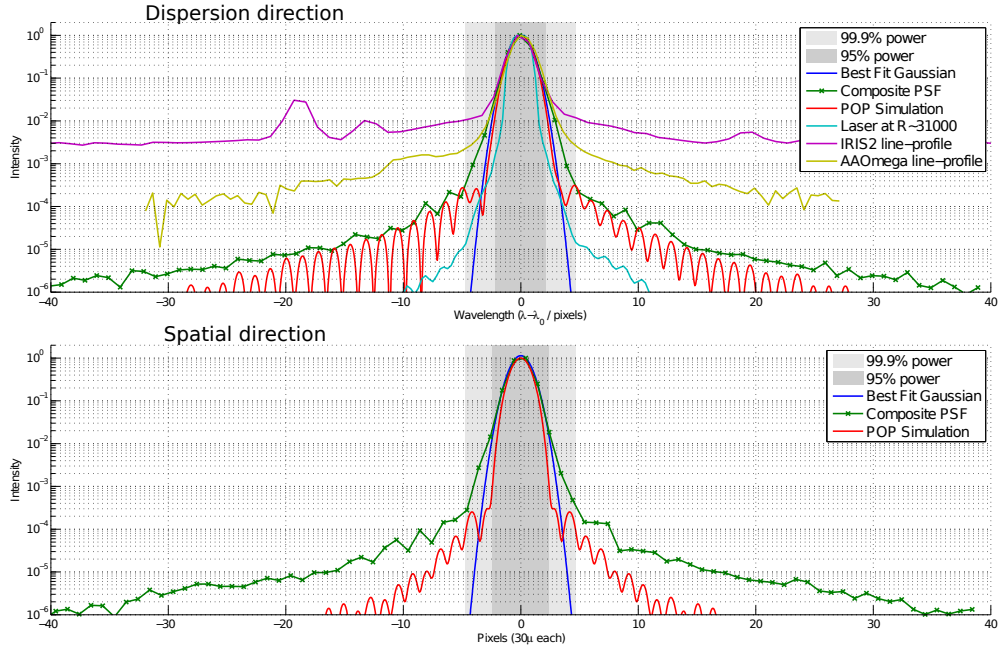


Figure 4.4: PSF line profiles (summed along the perpendicular axis with a Gaussian weighting, as would be done with real spectra) from PIMMS IR with comparisons in the spectral (top) and spatial (bottom) direction. Shown are: Green (stars) composite of underexposed and overexposed profiles as explained in text; Red ZEMAX POP simulation; Blue Best fit Gaussian; Cyan OSA spectrum of laser source; Purple and Yellow Typical line profiles attributed to the IRIS2 150 μ m slit and AAOmega fibre inputs respectively (the spectra from these spectrographs have been scaled to have the same FWHM determined from the best fit Gaussian, due to the difference in actual spectral resolution and pixel sampling). Note that the comparison spectra are shown to display the intensity level that the wings of the respective PSFs present.

and AAOmega by one. Both IRIS2 and AAOmega have lower resolutions than PIMMS IR, and operate over different wavelength ranges. To provide a fair comparison they have been scaled to have the same FWHM (in pixels), measured by their respective best-fit Gaussian, as PIMMS IR.

The measured FWHM of the PIMMS IR PSF of the spectral and spatial profiles is 57.5 μ m (1.9 pixels). This is just 3.6% larger than that predicted by the POP simulation. In the spectral profile (top part of Fig. 4.4) the wings are remarkably consistent with those predicted by ZEMAX POP simulations. At low intensity levels, they do begin to depart from the simulation. The wings of the spatial profile (bottom part of Fig. 4.4) are slightly better than the spectral profile, but not as low as expected from the POP simulation. Note that in my simulations, if the truncation factor is increased (i.e. the diameter of lens is reduced) in the collimator the wings in the spatial profile will increase until they are approximately symmetrical with the spectral

4.1 PIMMS IR

profile, at which point both the spectral and spatial wings increase in strength together. Thus, the symmetry of the measured PSF seems to indicate a broadening effect not fully accounted for in POP is the dominant cause of the discrepancies. I attribute this to the fact that (i) surface irregularities ($\lambda/4$ at 633 nm or $\lambda/10$ at 1550 nm) are on the edge of diffraction-limited, but are not accounted for in POP; and (ii) slight differences in the alignment between ZEMAX and reality (e.g. a small change in the camera element separation results in an order of magnitude larger change in focal length). These factors are all inherent drawbacks of **commercial off-the-shelf (COTS)** components, which nonetheless perform extremely well.

The FWHM of 1.9 pixels corresponds to ~ 49 pm spectrally. So the resolving power using the generalised Rayleigh criterion is $\mathcal{R} \sim 28,300$. More than 99% of the total power is concentrated in the core of the PSF where it remains Gaussian-like. Less than 1% of the power is contained in the extended wings and is in part attributable to veiling glare from the bulk COTS components. This allows the design to resolve at higher resolutions in high-contrast situations (assuming an appropriate detector of course). This has been illustrated in Fig. 4.5, where the two spectral lines of differing intensities are shown just resolved. Table 4.3 summarises the maximum dynamic range (i.e. intensity contrast between peaks) possible at spectral resolutions of 1, 2, 4 and 8 times the best resolution of PIMMS IR. For example two spectral lines that are separated by 0.11 nm are resolved if the ratio between their peak intensities is not larger than 18.9 dB (77.4:1).

A sample spectrum of several laser lines (from a tunable laser source) is shown in Fig. 4.6. From this, a 1D spectrum was extracted, shown in the middle of Fig. 4.6, using a simple triline summation (column summation is weighted evenly). A Gaussian was fit to each line to determine an accurate position (for wavelength calibration) and the width. The bottom plot in Fig. 4.6 shows the resolving power of each line, where $\Delta\lambda = 1.119 \times \text{FWHM}$. The error shown is the 95% confidence interval for the width given by the Gaussian fit. Above 1550 nm the resolving power is consistent with the predicted values. Below 1550 nm it is lower than predicted, but not drastically so.

The 1×7 Photonic Lantern

For further testing PIMMS IR was fed with a 7-mode PL¹. This was used in order to measure the performance of a PL feed. Currently, no other PL demonstrations have obtained spectra simultaneously of the complete PL feed at high resolution². A previous study of the spectral variability by Olaya et al. (2012) took spectra separately using an OSA. Demonstrations using an arrayed waveguide grating (AWG)-based PIMMS used 12 of 19 of the SM ports of that PL, primarily due to physical space restrictions imposed by 125 μm core spacing of conventional SMFs and the need to maintain sufficient separation between cross-dispersed spectra (Cvetovjevic et al. 2012b). I overcame this by (i) using a smaller PL, 1×7 vs. 1×19 ; (ii) forming the spectrograph entrance slit using the photonic TIGER configuration from Sec. 3.1.2. This

¹Lantern was manufactured in-house by Sergio Leon-Saval and Joel Rafael Salazar Gil.

²True at the publication of Paper 1, which is still the only published demonstration.

4.1 PIMMS IR

Table 4.3: Summary of the maximum contrast required to resolve neighbouring spectral lines shown in Fig. 4.5

No. Resolution elements [nm]	Dynamic Range [dB]
1 [0.0539 nm]	1:1 [0.0]
2 [0.1078 nm]	77.4:1 [18.9]
4 [0.2156 nm]	15900:1 [42.0]
8 [0.4312 nm]	148000:1 [51.7]

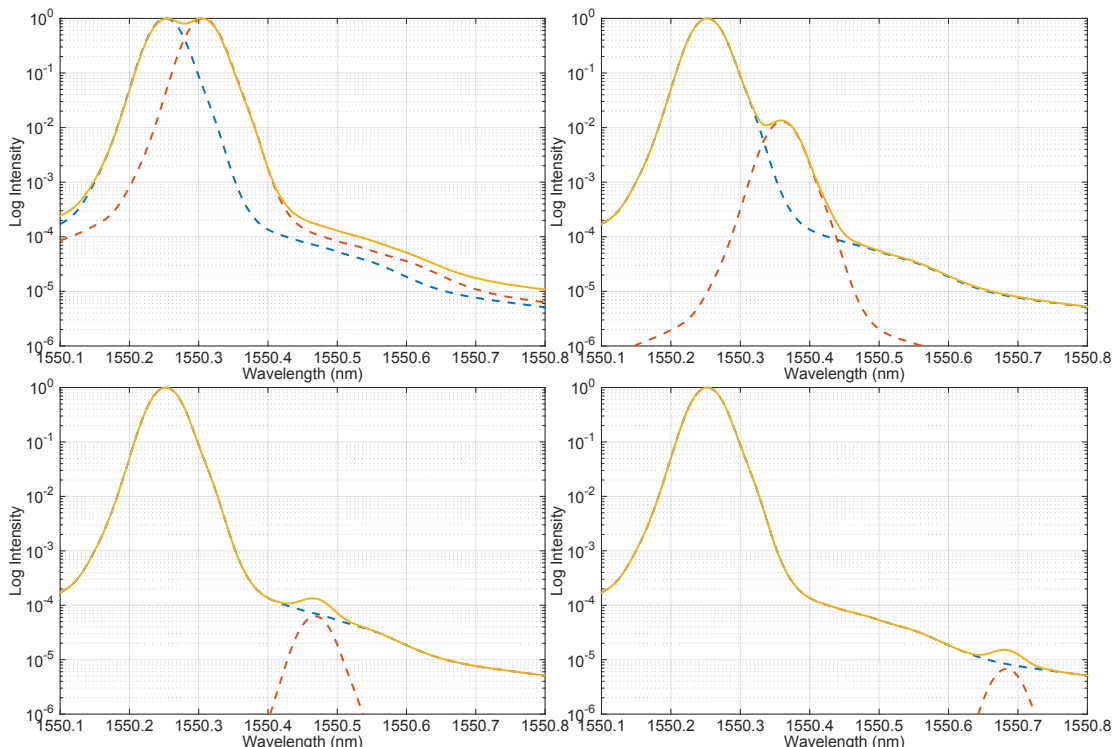


Figure 4.5: Blue and red dashed lines are two simulated spectral lines. Yellow is their combination. To be considered resolved the minimum between the two lines must be at most $\sim 81\%$ of both peaks. Top Left: Two equal strength lines are resolved with 1 resolution element (by definition). Top Right: Two lines separated by 2 resolution elements are resolved if the contrast is not more than 18.9dB. Bottom Left: Two lines separated by 4 resolution elements are resolved if the contrast is not more than 42dB. Bottom Right: Two lines separated by 8 resolution elements are resolved if the contrast is not more than 51.7dB.

4.1 PIMMS IR

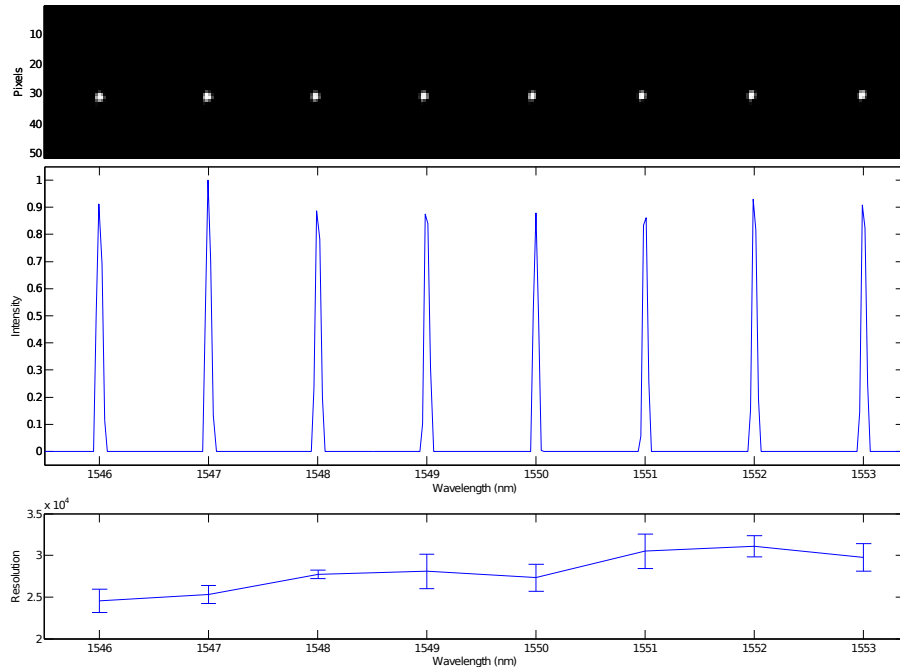


Figure 4.6: Top: Cropped raw spectrum from PIMMS IR initial testing. Image is 50x320 pixels. Adjacent spots are separated by 1nm. Middle: 1D extracted spectrum, wavelength calibrated using the laser lines. Bottom: Resolving power of each laser line calculated as $\lambda/(1.119 \times \text{FWHM})$ with 95% confidence interval of Gaussian width fit as the error.

allowed for the use of conventional 125 μm fibre and formation of a compact slit for a small sacrifice in the effective spectral bandwidth.

The format of the input slit can be clearly seen in Fig. 4.7. Here I used a 1×4 **SMF** splitter in reverse to couple two light sources into the spectrograph simultaneously. One is a PHOTONETICS TUNICS-PRI tunable laser source (1520-1600 nm) with a 2 pm linewidth and the other is a broadband (90 nm **FWHM**) Thorlabs super-luminescent diode (SLD) source centred on 1550 nm respectively. This allowed for a simultaneous image of a monochromatic spot and a broadband spectrum, essentially emulating an emission line in a flat continuum. This enabled simple evaluation and tuning of the pseudo-slits rotation with respect to the dispersion axis, as can be seen in Fig. 4.7. Thanks to the SMA connectorised input of the spectrograph and a standard Thorlabs rotation and XY adjustment stage it was trivial to rotate and fix the orientation of the core array. From my calculations shown in Sec. 3.1.2 a seven core hexagonal array pseudo-slit will need a minimum core separation of 33 μm and a rotation angle of 19.1°. Figure 4.7 shows the raw (without background or dark frame subtraction) detector image of the spectrograph at 4 different rotation configurations: 0°, 8.8°, 12.5° and 25.5°. As the prototype TIGER spacing was not optimised, having a much larger 12 μm core separation, the span of possible rotations for avoiding spectral overlap was very large. The spectra showed

4.1 PIMMS IR

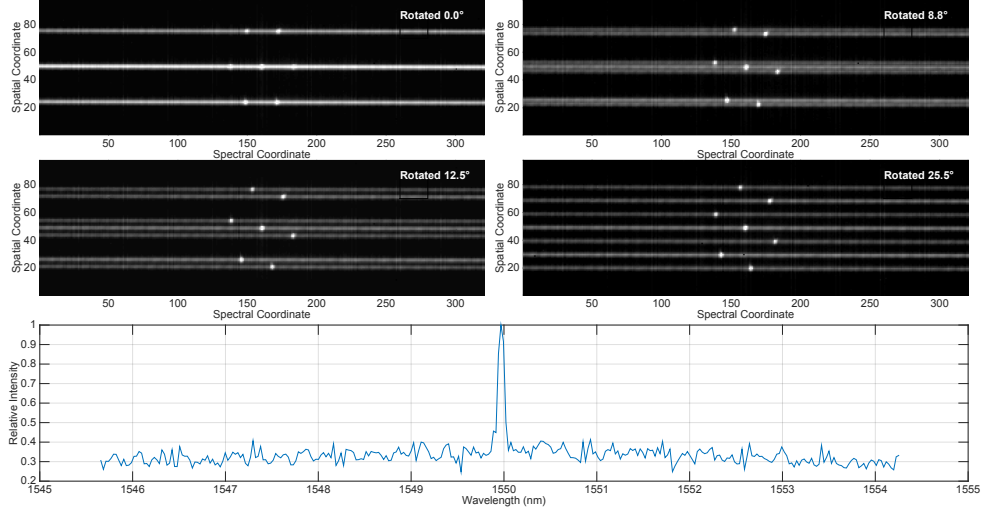


Figure 4.7: Four top panels: Spatial versus spectral coordinates detector images of the dual laser source fed Photonic TIGER spectrograph for 4 different pseudo-slit angle rotations 0° , 8.8° , 12.5° and 25.5° . The images are 100×320 pixels, raw data without background or dark frame subtraction. Bottom panel: 1D processed spectrum from the central core in the 25.5° rotated case showing the broadband source spectrum and the overlapped narrow laser source tuned at 1549.95 nm.

no overlapping for rotations between 9.5° and 35.5° .

The next test was to obtain a solar spectrum. To do this three sets of data (composed of light and dark frames) were acquired. The first was used for wavelength calibration, where the MM port of the PL is illuminated using the far-field of a SMF that is coupled to the tunable laser source. In the second, the MM port was directly illuminated with a tungsten halogen light source (Thorlabs OSL1-EC) to obtain a flat-field response. Finally, raw spectra were obtained by aiming the MM port directly at the Sun. The individual spectra are shown in the middle part of Fig. 4.8, where each spectrum is normalised and offset. Also shown here is the flat response of PIMMS IR from a halogen source and the final combined spectrum formed from the average of the individual spectra.

The noise visibly changes (the **single-to-noise ratio (SNR)** varies from about 30 to 100) in the seven individual spectra; this is consistent with the relative intensity difference between each of them (the Xenics detector has very large read-noise of ~ 400 electrons). In contrast to previous results (Olaya et al. 2012), no spectral variation is seen at narrow bandwidth and high resolution between the individual spectra of the SMF outputs of the 1×7 PL. Averaging the 7 individual spectra forms the complete PL spectrum. This is shown in the top of Fig. 4.8 along with a reference solar spectrum (Livingston and Wallace 1991) and a model telluric spectrum (Rothman et al. 2009). Both the comparison spectra were convolved with a Gaussian to have a similar resolution to the PIMMS IR spectrum ($\text{R} \sim 30,000$). In the PIMMS IR wavelength

4.1 PIMMS IR

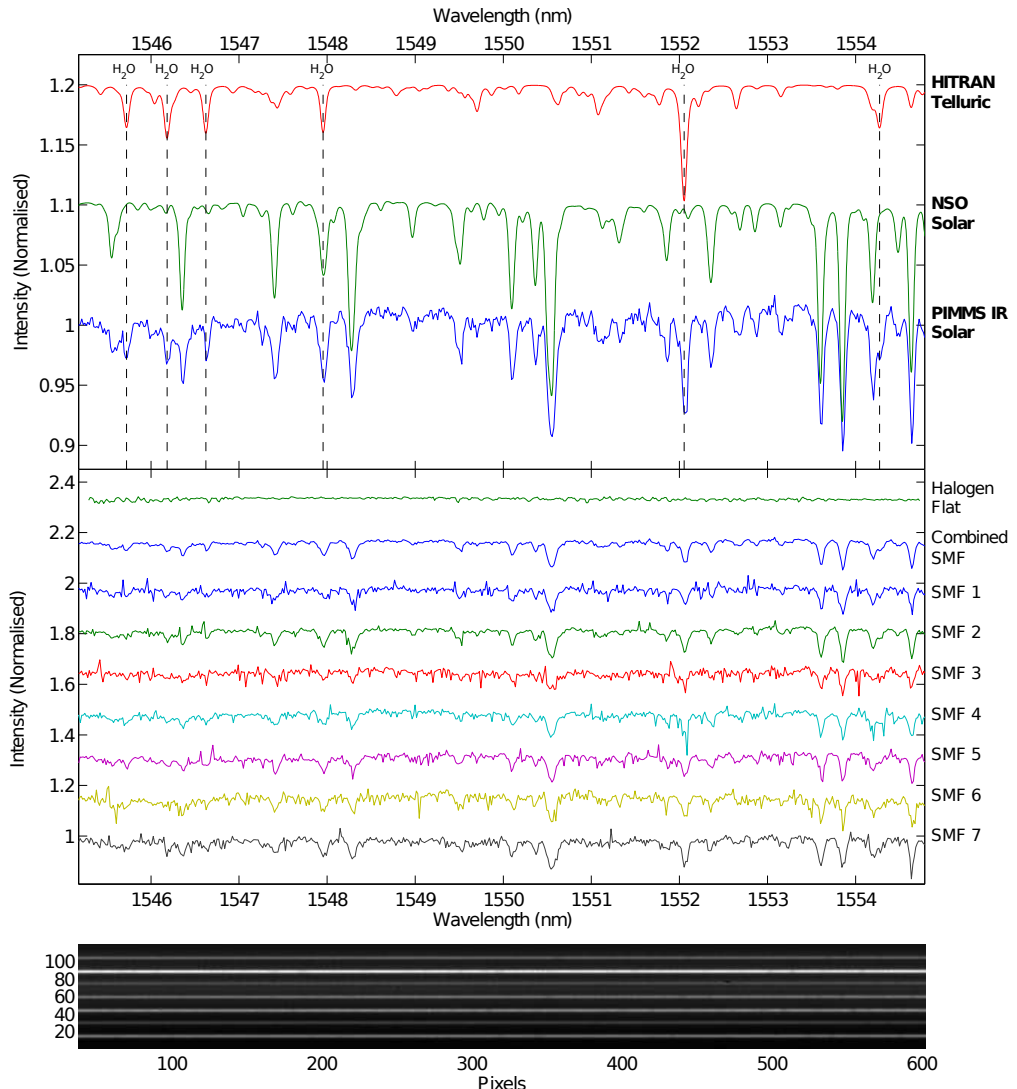


Figure 4.8: **Top:** Shown are (i) A simulated atmospheric absorption spectrum using HITRAN (Rothman et al. 2009) (ii) Reference solar spectrum from US National Solar Observatory/Kitt Peak Observatory (Livingston and Wallace 1991) convolved down to $\mathcal{R} \sim 30000$ for comparison. (iii) The PIMMS IR Solar spectrum obtained in Sydney, Australia. Spectra are offset vertically for convenience. The PIMMS IR spectrum shows the expected telluric absorption features (mostly water vapour) superimposed on the solar spectrum. **Middle:** From top to bottom the first spectrum is the response to a tungsten halogen lamp, the second is the solar spectrum obtained when combining the PL SMF outputs. The remaining seven are the individual spectra of the seven SMF outputs. Each spectrum is normalised by its respective median value, and offset for clarity. The noise level varies between spectra due to the differences in mean signal. **Bottom:** Detector image of the dispersed single-mode output fibres of the PL.

4.1 PIMMS IR

range water vapour is the dominant absorber, the six strongest lines are marked in Fig. 4.8. The throughput from slit to detector was measured using a power meter at both ends and illuminating the MM port with the tunable laser source. The measured throughput of the optics and diffraction grating is ~74%. Including a nominal detector QE of ~80% the spectrograph throughput is ~60%. The typical throughput of the current generation of 1×7 PLs is ~85%. Thus the effective throughput, of PIMMS IR, including the lantern transition is ~50%. Performance could be improved with better-matched anti-reflective (AR) coatings on all optical surfaces, the fibre end faces in particular.

4.2 PIMMS Visible

PIMMS visible is the logical continuation in developing a compact diffraction-limited spectrograph. *PIMMS IR* is a relatively simple single-order spectrograph, operating in the **SWIR** (1550 nm). PIMMS IR's high resolving power ($R \sim 30,000$) and limited detector size (640×512 pixel array) restricted the bandwidth of a single exposure to ~ 8 nm. PIMMS visible has several advantages over its sibling:

- it operates in visible wavelengths, allowing use of more cost-effective large format CCDs, with drastically better noise characteristics compared to the InGaAs array used in PIMMS IR.
- has a potential resolving power in excess of 60,000.
- uses a larger lantern, based on a 19 **multi-core fibre (MCF)** (Birks et al. 2012; Birks et al. 2011).
- the primary disperser is an échelle diffraction grating. Combined with a **VPH** grating cross-disperser it maintains high resolution and throughput, but with significantly increased bandwidth.

The optical layout and a picture of the actual setup are shown in Fig. 4.9. The whole setup fits (nearly) on a 300 mm by 600 mm breadboard (A fold mirror can be introduced to allow it to fit within the breadboard area completely). The mounts for both the échelle and cross-disperser are a combination of custom 3D-printed parts and **COTS** components (to achieve the correct angles and centre the gratings about their rotation axis).

What follows is an overview of the proposed design for the visible **PIMMS#0** échelle design using off the shelf optics. My design is a quasi-Littrow échelle configuration where the grating incidence is at an angle γ to the normal plane, thus directing the diffracted light off-axis to cross-disperser and camera (see Fig. 4.9). A summary of design specifications is shown in Table 4.4.

Table 4.4: Summary of PIMMS#0 échelle design specification

Specification	Target
grating 1/mm	31.6
Blaze	63°
Spatial modes	19
Estimated throughput (%)	50-80%
Image Quality (PSF)	Gaussian down to 10^{-6} peak power
Collimated Beam width ($1/e^2$)	10 mm
Resolving Power (\mathcal{R})	70000-80000
Spectral Resolution (FWHM $\times 1.119$)	8-11 pm
Bandwidth	$0.5832 \mu\text{m}$ to $0.6740 \mu\text{m}$ (90.7947 nm)
Total Track	516 mm
Footprint	250×700 mm

4.2 PIMMS Visible

As in the **SWIR** case, there were three guiding parameters in the design. First, it had to use an existing detector (namely an Atik 383+ with $5.4 \mu\text{m}$ pixels and a 3362×2504 array). The second was the diffraction grating size and line density. The most suitable ‘off the shelf’ échelle currently available is from Thorlabs. It measures $25 \text{ mm} \times 50 \text{ mm} \times 9.5 \text{ mm}$ with 31.6 lines/mm and a 63° blaze (i.e. an R2 échelle). Finally, the input slit is formed by a 19 core **MCF** using the TIGER configuration. I measured the TIGER **MCF** to have an **NA** of 0.077 @ 650 nm.

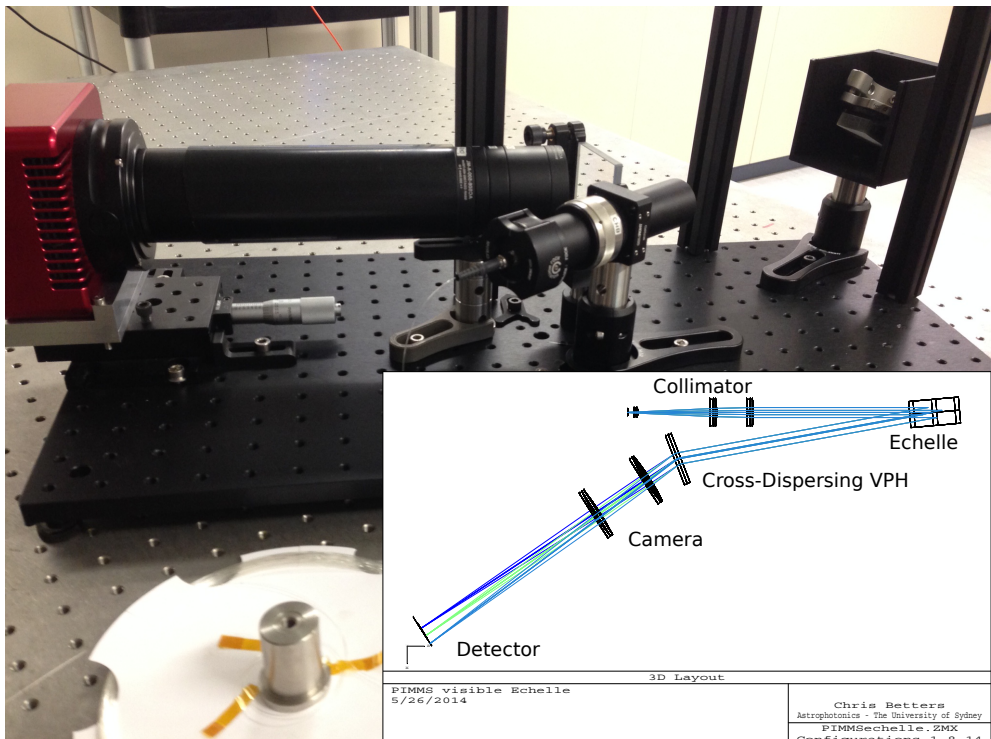


Figure 4.9: Image of the actual PIMMS visible bench setup. Inset is the layout of the optical design. The échelle dispersion is perpendicular to the plane of the page. The échelle is rotated by 4° about the y axis (perpendicular to page) in a quasi-Littrow configuration. The central wavelengths of diffraction orders 73, 79 and 86 are shown.

4.2.1 Pseudo-Slit and Photonic Lantern

Here I use a single length of a 19 **MCF** to form both the **PL** and pseudo-slit of the spectrograph¹ (this style of lantern is illustrated in Fig. 2.2). One end is tapered with a low index capillary jacket to form the **PL** transition, producing the **multi-mode (MM)** input which can be connec-

¹The 19 **MCF** was designed and fabricated by Sergio Leon-Saval, Itandehui Gris-Sánchez and Timothy Birks at The University of Bath.

torised¹. The opposing end is also connectorised and then used directly as the spectrograph input slit using the TIGER configuration discussed in Sec. 3.1.2.

The core spacing is $60\ \mu\text{m}$, which allows each core to have an effective separation in the spatial/cross-dispersion direction of $16\ \mu\text{m}$. If conventional **SMF** had been used to form a bundle this spacing would be $125\ \mu\text{m}$ or an effective spacing in the cross-dispersion direction of $33\ \mu\text{m}$ (limited by the cladding diameter). Thus with the 1×19 **MCF PL** I effectively have a $300\ \mu\text{m}$ slit with fibres every $16\ \mu\text{m}$ as opposed to a $2\ \text{mm}$ slit with fibres every $125\ \mu\text{m}$. Because the spectra are slightly offset in wavelength, when they are extracted (the process where the 2D echellogram² is processed into a set 1D spectra, detailed in Chap. 5) and combined there is a small reduction in the wavelength coverage compared with that which would be possible with a true linear slit. This was deemed a more than reasonable tradeoff as it avoids the need for remapping waveguides and/or loose **SMFs**.

An important note, that does affect the final performance of the current setup, is that the **MCF** and **PL** described above and currently used in PIMMS visible was originally intended for use at $1550\ \text{nm}$. As a result I am currently operating in a ‘few-mode’ regime, which for each **SMF** results in a broadened **PSF** (and corresponding reduction in resolution). This is not a fundamental issue, simply a by-product of the TIGER slit configuration and the particular pre-form used to manufacture the **MCF**. A visible version of the 19 **MCF** was also fabricated, however the parameters of this fibre, and in particular the core separation, were not ideal for the spectrograph configuration. The cores of the visible version were too close together to disperse without overlapping.

4.2.2 Optical Design

Grating(s)

The échelle grating is used in a quasi-Littrow configuration with a $\gamma = 4^\circ$, so the dispersed beam is diverted 8° off-axis from the collimator (when the setup is folded this can be reduced to $\gamma \approx 2^\circ$). The 63° angle of incidence and grating size set the first limit on the collimated beam size. This beam must be less than $25\ \text{mm}$ or it will overfill the grating. Gaussian beam truncation considerations indicate the beams $1/e^2$ diameter should be roughly half the aperture, thus the beam incident on the échelle should be less than $12.5\ \text{mm}$.

Similar considerations are normally required for the cross-disperser. However, the most suitable grating (based on dispersion requirements) was a VPH with an line density of $600\ \text{lines/mm}$ that is blazed for $600\ \text{nm}$ from Wasatch Photonics. This grating is a $50.8\ \text{mm}$ (2 in) square and is thus not a significant truncation concern (if the beam is appropriate size for the échelle).

¹The **PL** was fabricated by Sergio Leon-Saval in-house

²Raw detector image of an échelle spectra

4.2 PIMMS Visible

Collimator

The collimator takes some inspiration from the Amici lens proposed by Robertson and Bland-Hawthorn (2012). I instead used a small short focal length achromat to effectively slow the beam, and complete the collimation with two larger achromats. The final design is composed of a 8 mm achromatic doublet with an **EFL** of 20 mm combined with two identical 25.4 mm (1 in) achromatic doublets with **EFLs** of 200mm. Combined they have an **EFL** of 64.7 mm ($f/2.5$ overall). Here it is operating at $\sim f/6$ to give a collimated beam of 10 mm ($1/e^2$ diameter).

Camera

The camera is a simple pair of 50.8 mm (2 in) achromatic doublets with **EFLs** of 400 mm and 500 mm respectively. Combined their **EFL** is 237 mm ($f/4.6$ overall). Here it is operating at closer to $f/20$. The overall optical layout of the design is shown in Fig. 4.9. This results in a magnification of ~ 3.6 . This magnification was chosen in order to adequately sample the diffraction-limited **PSF**. That is at least two pixels per **FWHM** where the **FWHM** of the **MFD** if visible **SMF** is $\sim 3 \mu\text{m}$, so $10.8 \mu\text{m}/3 \mu\text{m} = 3.6$. Overall the optics are diffraction-limited from 500nm through to 800nm (in $\sim 100\text{nm}$ blocks). Blueward and redward of the those limits has not been explored as yet.

Detector

The detector package is an Atik 383L+¹, nominally marketed for small telescope astrophotography. The sensor is the 8-megapixel Kodak KAF-8300 CCD (3362×2504 , with a pitch of $5.4 \mu\text{m}$). It has a low read noise ($\leq 10e^-$) and dark current ($\sim 0.05 e^-/\text{s} @ -10^\circ\text{C}$). The large format coupled with the small pixels makes it ideal for the échelle design. An additional benefit is the low cost ($\sim \$2000$) and wide availability.

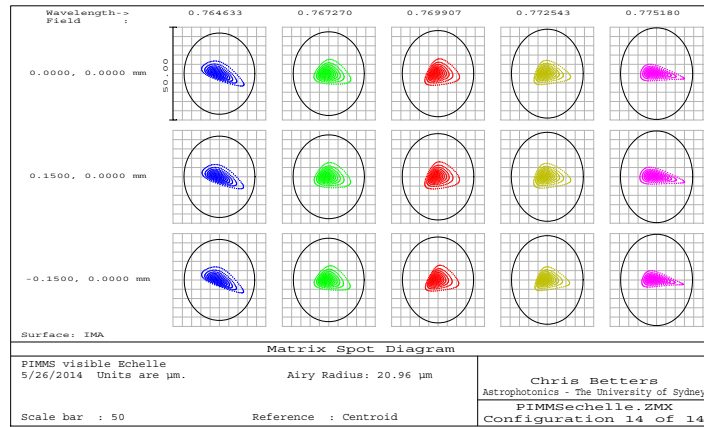
4.2.3 ZEMAX Analysis

Ray Tracing

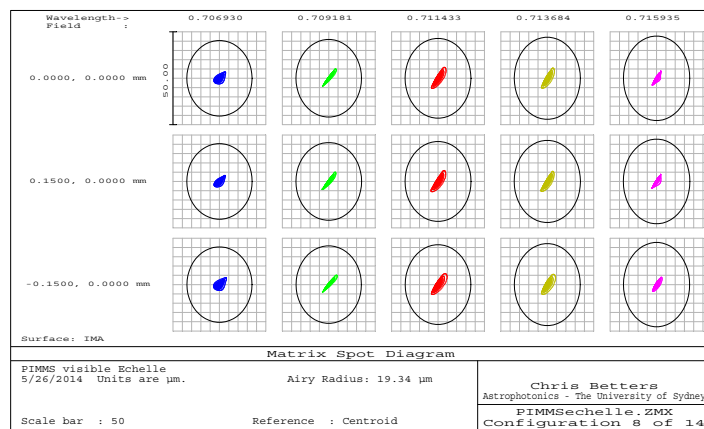
As with PIMMR IR, ray tracing spot diagrams were a key analysis during the design process. The final design performs very well, with rays well confined to the Airy disk for the entire wavelength range, showing that diffraction-limited performance is maintained by the optical system. As part of the ray tracing analysis I developed a script to fill ZEMAX configurations with appropriate wavelengths for given diffraction orders (code is shown in Appendix. B.1). This allowed for the analysis (and optimisation) of all orders and wavelengths simultaneously, dramatically simplifying the process. Shown in Fig. 4.10 are ray tracing spot diagrams for field positions on axis and at the ends of a $300 \mu\text{m}$ slit (i.e. the extent of the 1×19 TIGER slit). The three sub-diagrams each have 5 evenly spaced wavelengths that cover the **free spectral range (FSR)** of diffraction orders 73, 79 and 86. There does appear to be a small degradation in

¹<http://www.atik-cameras.com>

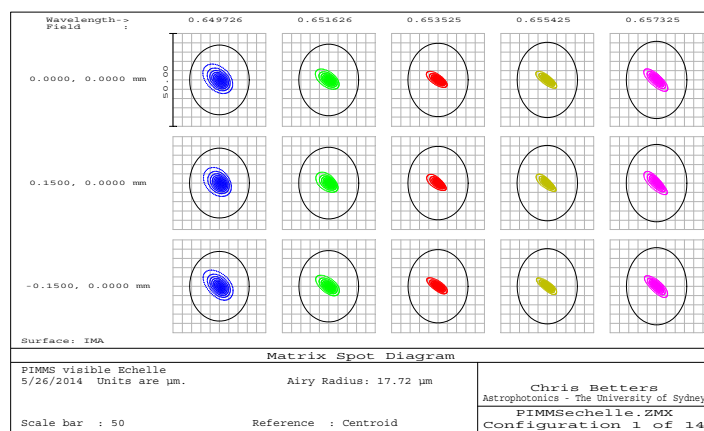
4.2 PIMMS Visible



(a) Spot Diagram - Order 73



(b) Spot Diagram - Order 79



(c) Spot Diagram - Order 86

Figure 4.10: a-c) Spot Diagrams across pseudo-slit for orders 73, 79 and 86 (top, center and bottom of detector). Wavelengths in each diagram cover the FSR ($\lambda_{\text{central}}/m$) of each order. The black oval is the indicative airy-disk. All bounding boxes are 50 μm square.

4.2 PIMMS Visible

image quality at the edge orders (73 and 86), but the ray tracing still remains well within the ZEMAX Airy radius.

Wavelength coverage

The total wavelength coverage is limited by the size of the detector (but is still notably much larger than was possible with the Xenics array used for PIMMS IR at 100 nm vs 8 nm). The current setup images orders 73 to 86, covering 125nm without gaps. The order separation after cross-dispersion allows enough room for a ~300 micron slit, or the 1×19 TIGER MCF (tightly packed). Table 4.5 lists the enumerated diffraction order limits. Simulated positions on the detectors are shown in Fig. 4.11, a ‘Full Field’ spot diagram (which shows the positions of ray traces for all fields and wavelengths in a single diagram). PIMMS visible’s nominal setup includes 14 diffraction orders (73 to 86), covering a bandwidth of 649nm to 775nm (125nm).

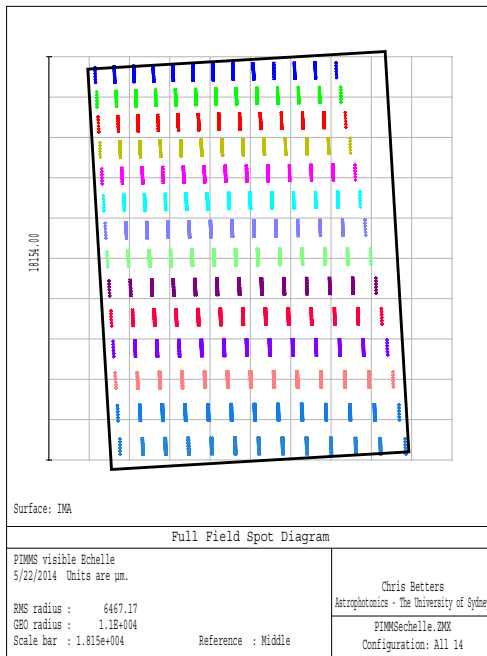


Figure 4.11: Full-field ray-trace of a 0.3 mm long slit for orders 73-86. Wavelengths span the FSR of each order. The x axis is échelle dispersion, y-axis is cross dispersion. The black box shows the Atik detector’s coverage. The sensor is 3362×2504 pixels with a $5.4 \mu\text{m}$ pitch ($18.1 \text{ mm} \times 13.5\text{mm}$).

4.2 PIMMS Visible

Physical Optics and Resolving Power

Given the ray tracing I expected the **POP** profiles to be quite good. Indeed they show excellent diffraction limited image quality. Shown in Fig. 4.12 are **POP** profiles in the cross-dispersion direction and in the echelle dispersion direction. These are representative of the central part of the detector. Both are essentially Gaussian down to $10^{-6} - 10^{-7}$ with a few artefacts seen in the centre. The residual shows some small with difference of order $\sim 10^{-3}$ in the core. This is attributable to a slight asymmetry in the profile with respect to the Gaussian fit. Nonetheless, in both axis the **POP** simulation is essentially Gaussian until about $10^{-6} - 10^{-7}$ of the peak. If the real setup has close to similar performance the **PSF** wings will be well below the dynamic range of the detector. The profile shown is actually the 2D **PSF** collapsed in each dimension. Simulated is a Gaussian beam with an NA of 0.08 (to the $1/e^2$ points), which equals the measured **NA** of the **MCF**. The grating out-of-plane tilt γ (from Eqn. 1.4) causes an anamorphic magnification of the **PSF**, so that it is slightly longer in the cross-dispersion direction.

In order to perform a more detailed analysis on more than a few wavelengths, I scripted ZEMAX to perform a similar **POP** simulation at every point in the Full Field Spot diagram Fig. 4.11 and save the dispersion for that point (from ray tracing). These were then fitted with 2D Gaussians and the dispersion estimate was used to set a wavelength scale, giving an estimate of the resolving power. Each Gaussian's **FWHM** and the corresponding resolving power are shown in Fig. 4.13a (using the $\text{FWHM} \times 1.119$ as the resolution element). The solid line in the top part of Fig. 4.13a and 4.13b shows the diffraction-limited resolution according to Eqn. 3.8. The simulations are consistent with diffraction-limited performance.

Table 4.5: Wavelengths covered in each diffraction order (same as those shown in the full field spot diagram and **POP** simulations).

ZEMAX Config	Order	Blue end (μm)	Central (μm)	Red end (μm)	FSR (nm)
1	86	0.6497	0.6535	0.6573	7.5991
2	85	0.6573	0.6612	0.6651	7.7790
3	84	0.6651	0.6691	0.6731	7.9653
4	83	0.6731	0.6771	0.6812	8.1584
5	82	0.6812	0.6854	0.6896	8.3586
6	81	0.6896	0.6939	0.6981	8.5663
7	80	0.6981	0.7025	0.7069	8.7817
8	79	0.7069	0.7114	0.7159	9.0055
9	78	0.7159	0.7206	0.7252	9.2379
10	77	0.7252	0.7299	0.7347	9.4794
11	76	0.7347	0.7395	0.7444	9.7305
12	75	0.7444	0.7494	0.7544	9.9917
13	74	0.7544	0.7595	0.7646	10.2635
14	73	0.7646	0.7699	0.7752	10.5467

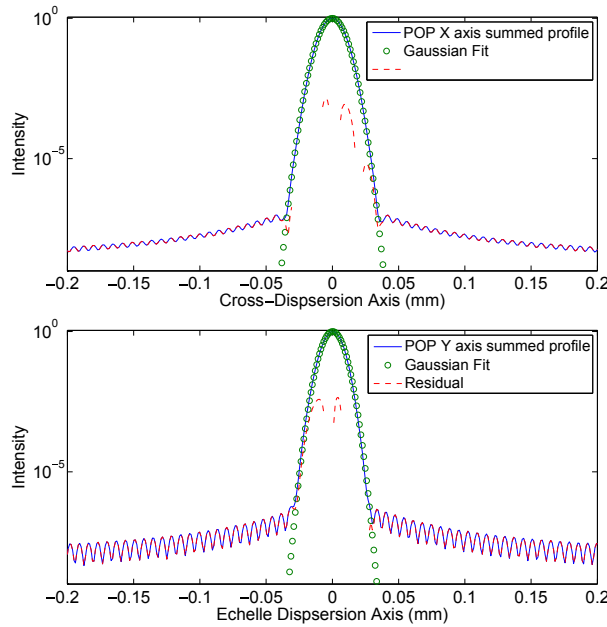


Figure 4.12: Typical profiles (in échelle dispersion and cross-dispersion direction) of the **POP** simulation (the profiles are actually the 2D image collapsed in one dimension and normalised). The red dashed line shows the residual between the Gaussian fit and **POP** simulation.

4.2.4 Experimental Analysis

PSF and Resolution

To wavelength calibrate PIMMS échelle I used a **Thorium-Argon (ThAr)** hollow cathode lamp. This provides numerous lines in each diffraction order, allowing a well-defined wavelength scale. A raw image is shown in Fig. 4.14.

To measure the operating resolution of PIMMS visible I again used a **ThAr** lamp calibration frame. The first step of the wavelength calibration (described in Chap. 5) required pairing spectral lines with a database of known **ThAr** lines. The centroids of each line determined via 1D Gaussian fits were then used to fit a wavelength scale to the spectrum. This relationship was then used to convert line-widths from pixel units to wavelength units. The results of the fitting routine are shown in the bottom graph of Fig. 4.13b, and the top is the corresponding resolving power.

The first thing to note is the larger average FWHM as compared with Fig. 4.13a (average is ~4.5 pixels vs. 2.5 pixel). This is essentially what was expected given that I have used a **MCF PL** designed for **SWIR** (1550 nm) use. Also of note is that the **POP** simulations do not include issues such as grating quality or variations between the prescriptions and the real system (although the effect of the latter should be minimal). During setup of the optical system (and

4.2 PIMMS Visible

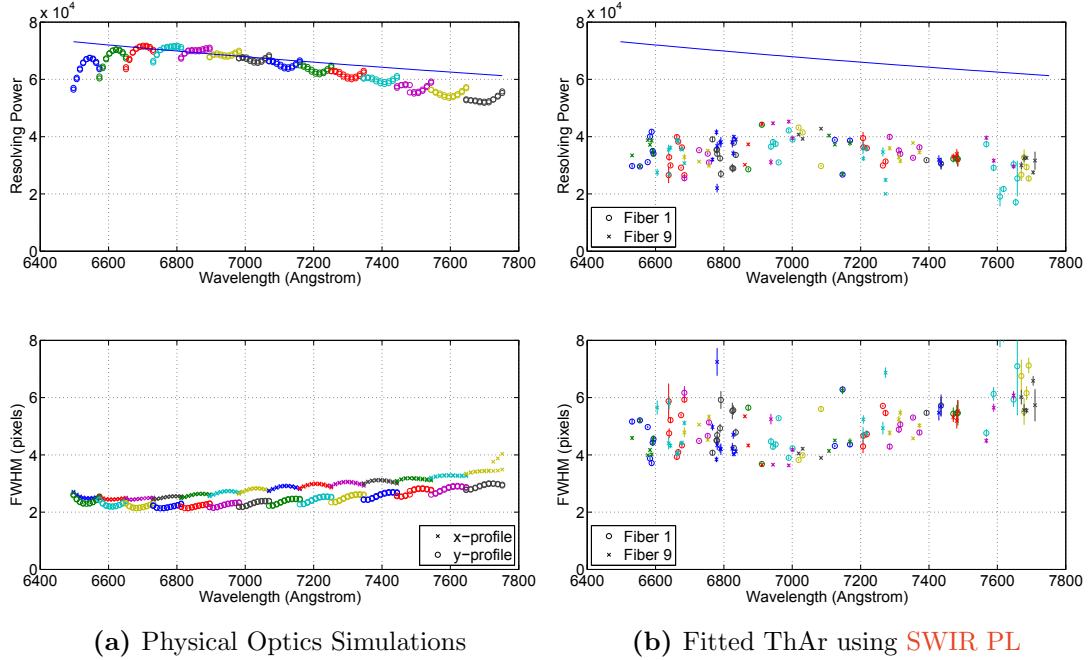


Figure 4.13: *a)* POP simulations for 9 wavelengths covering the FSR of each order and for field positions at the centre and end of a $300\text{ }\mu\text{m}$ pseudo-slit. These plots show the fitted FWHM (bottom) of each Gaussian and the corresponding resolving power (top). Colours changes indicate order changes, and the (very small) scatter in a given colour is due to different field positions. *b)* Fitted FWHM (in pixels) of ThAr lines from two fibres in Fig. 4.14 (bottom) and their corresponding resolving power (top). Changes in colour indicate each diffraction order. *In Both:* The solid blue line is Eqn. 3.8 (the diffraction limit) for the R2 échelle grating and 10mm beam.

as a sanity check) the camera and collimator were used to image (i.e. the system without the dispersing elements) the visible version of the MCF and returned PSFs with widths of order 2.5 pixels, a slight broadening vs the simulations. This is attributed to the unavoidable fact that the available COTS optics are specified to have surface quality of $\lambda/4$ at ~ 600 nm, and are thus not truly diffraction-limited. Nonetheless, even in this ‘few-mode’ configuration, PIMMS échelle has achieved a resolving power $> \sim 30,000$ over the entire echellogram.

Stability

The first step in stabilising a spectrograph is to address the pure mechanical stability; this involves controlling the temperature, and adopting a rigid design. A mechanically stable design will then become pressure limited, where changes in atmospheric pressure, and thus the refractive index of air, result in changes in the angles of diffraction. This can be addressed by placing the spectrograph in a pressure stabilised or vacuum vessel. To achieve very high stability (of

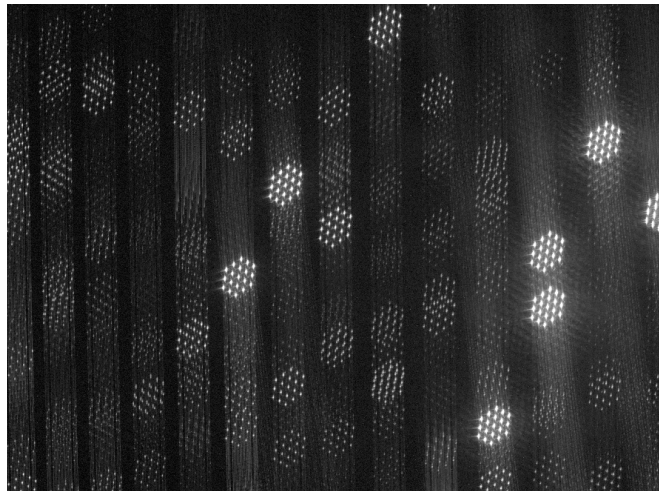


Figure 4.14: Raw ThAr echellogram, showing 14 unclipped orders. The hexagonal pattern is a result of the MCF TIGER entrance slit. Wavelength increases left to right (cross-dispersion) and top to bottom (echelle dispersion).

order m/s) generally requires some form of simultaneous calibration data taken with the target spectrum. Typically this is done by simultaneously capturing an arc lamp (such as ThAr) or a laser frequency comb or etalon (Halverson et al. 2014; Probst et al. 2015) spectrum via a secondary fibre, using a gas reference cell (such as Iodine), or combination of these.

In PIMMS visible there are few moving parts and those that are used have limited degrees of freedom, so it is already quite rigid. To stabilise the overall temperature I placed the setup in a thermally insulated box¹ and retrofitted the Atik detector with a custom water-cooling system. My goal was to see to what level the bench spectrograph could be stabilised without additional calibration. To that end I took a multiple series of ThAr arc lamp spectra over the course of several night (an example is shown in Fig. 4.14). As these have known standard wavelengths I can track their positions on the detector, and attribute any movement to flexure (temperature changes) and changes in atmospheric pressure (refractive index at the échelle grating). Also recorded were measurements of pressure and the temperature at the CDD heat sink, of the air in the thermally insulated box and of the ambient air of the laboratory (all shown in bottom part of Fig. 4.16).

To measure the stability over the series of successive spectra I used a 2D image registration technique to measure any translation between each ThAr echellogram. The algorithm, described by Guizar-Sicairos et al. (2008), first obtains a rough estimate of the cross-correlation peak via fast Fourier transform (FFT) and then obtains a precise sub-pixel measurement of the shift by up-scaling a direct Fourier transform (DFT) in the neighbourhood of the original peak. In order to simplify the comparison, the raw ThAr echellograms were first reduced into smaller frames composed of sub-images centred on the brightest (but not over-exposed) spectral lines.

¹Esky

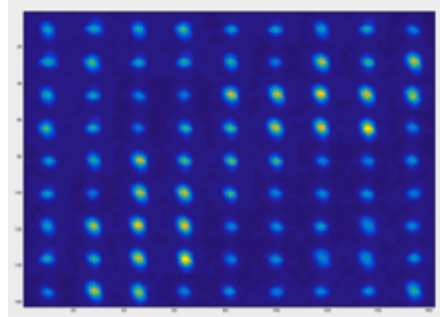


Figure 4.15: A sample of mosaic of ThAr lines used in 2D image registration. Each spot corresponds to a spectral line in the PIMMS visible ThAr spectrum with a 16 pixel-bounding box.

The subframes are then tiled in to a single image. An example of the resulting mosaic frame is shown in Fig. 4.15. This reduces both the effects of any artifacts in the image (e.g. hot pixels, bad columns etc.) and the computational overhead. This also makes it easier to only compare regions of similar wavelength. This is important because the change in refractive index with wavelength is not linear and the 2D image registration algorithm assumes a rigid transformation (i.e. all dots must move uniformly).

The results of cross-correlation can be seen in top of Fig. 4.16. The translation of the spectrum in the cross-dispersion (spatial) axis shows a slight trend over the day that correlates with the CCD heat-sink temperature. While the periodic behaviour of the cross-dispersion translation correlates with temperature fluctuations in the laboratory from the air-condition system cycling. The larger change seen in the primary échelle dispersion translation correlates very well with atmospheric pressure over the observation period. The middle plot of Fig. 4.16 contains the same data, but calibrated with a simple linear scaling and offset using the temperature and pressure data. This reduces the RMS variation to 10-20m/s over the entire 9 hours period. The next step will be to use a simultaneous reference, where it seems reasonable to assume that this already good performance can be improved upon substantially.

4.2 PIMMS Visible

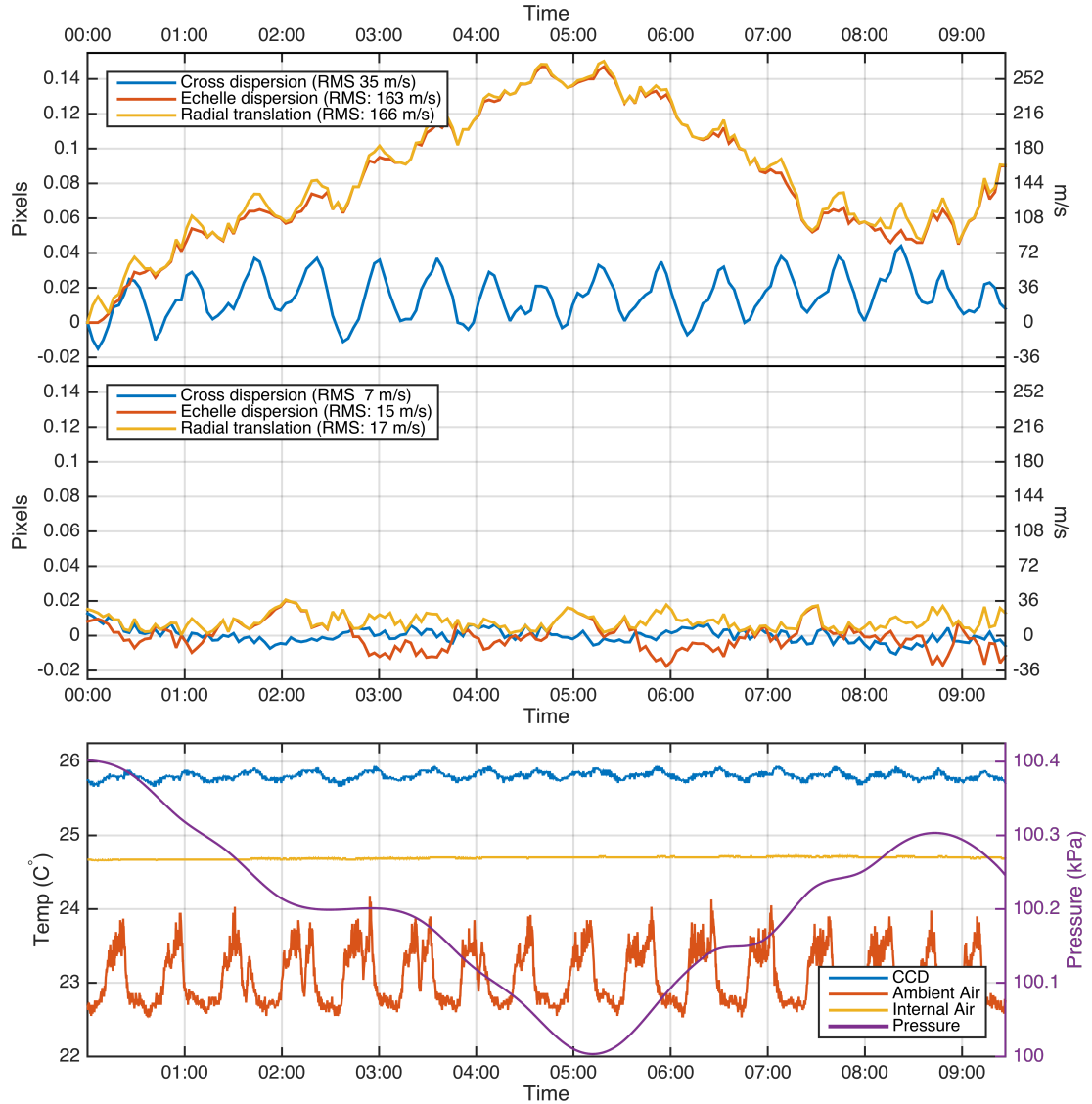


Figure 4.16: Overnight stability measurements of PIMMS visible. The three curves shown are: Blue) translation in the cross-dispersion direction; Red) translation in the primary échelle dispersion direction; Yellow) Radial translation from initial frame. Top Panel: The radial translation of the ThAr spectrum has an RMS error of 166 m s^{-1} (1/10 pixel) and maximum deviation of 250 m s^{-1} (1/8th pixel). Middle: Stability when calibrated with pressure and temperature data. The radial RMS error is reduced to 17 m s^{-1} (1/100 pixel) with a maximum deviation of 40 m s^{-1} (1/50 pixel). Bottom Panel: Shown are measurements of temperatures in the Esky, of the CCD housing and external air. Also show are measurements of atmospheric pressure.

4.3 NanoSpec

A Micro-Spectrograph for the i-INSPIRE Satellite

The goal of NanoSpec is to demonstrate the potential of photonics-driven technology in space-based applications. To that end I designed and built a ‘photonic’ spectrograph, specifically a **single-mode fibre (SMF)** diffraction-limited device, which will survive a launch into space while still providing a reasonable spectral resolution.

The natural advantage of the **photonic lantern (PL)** fed spectrograph is that by forming the entrance slit with **SMF** I can achieve an extremely compact design. While both PIMMS IR and PIMMS visible were targeted at an high spectral resolution, NanoSpec is an exercise in compactness, but with useful spectral resolution. The micro-spectrograph is one of the primary instruments in the i-INSPIRE nano-satellite. So the design needed to be compact (a nano-satellite weighs less than 1kg, and has very limited volume), but also keep the design simple to reduce complexities in alignment and construction (specifically maintaining optical alignment during and after a launch into orbit).

NanoSpec is designed to be compatible with a **PL** input, however it has not yet been determined if the final flight instrument will utilise one (the current generation of **PLs** are too large). The alternative is to form the pseudo-slit in NanoSpec with 8 independent **SMFs**. They are to be arranged in pairs and point in four different directions out the sides of the TubeSat, as illustrated by the red and blue lines in Fig. 4.17b. This arrangement is intended to maximise the chances that the orientation of the spacecraft will allow spectra to be observed of the Earth, Sun, Moon or other astronomical sources (or a combination of these). The fibres have an **numerical aperture (NA)** of 0.1 (acceptance half angle of 5.75°) corresponding to a circular area with a radius of 30 km when the fibre is aimed at the earth surface from an orbit of 310 km. Additionally, the fibre pairs consist of two different types of fibre (discussed in the optical design section) in order to test their performance in the **low earth orbit (LEO)** environment.

The i-INSPIRE satellite project is a collaboration between the School of Physics and the School of Aerospace, Mechanical and Mechatronic Engineering at the University of Sydney. It is intended for i-INSPIRE to be the first sole Australian university satellite to be launched and operated in space (cf. Fogarty et al. (2012) and Fogarty et al. (2011), for a more detailed overview of the aims of the mission). The two key instruments are NanoSpec and a radiation counter. To complement these the satellite will also carry an imager. The satellite subsystems are based upon a TubeSat design sold as part of a launch package by start-up Interorbital Systems¹ (IOS; cf. Xiao et al. (2011)). i-INSPIRE is one of 32 TubeSats and 10 CubeSats currently on the manifest for the maiden launch of IOSs N45 rocket. The launch is planned to target a high inclination polar orbit with an altitude of ~310 km and a predicted lifetime of 24 days (more than 380 orbits). Approximately every 16 orbits the satellite will move through the South Atlantic Anomaly (SAA), a region of high radiation. This region is of particular interest, as it will allow us to study the short-term effect of radiation on NanoSpec’s components and

¹www.interorbital.com, who may launch someday...

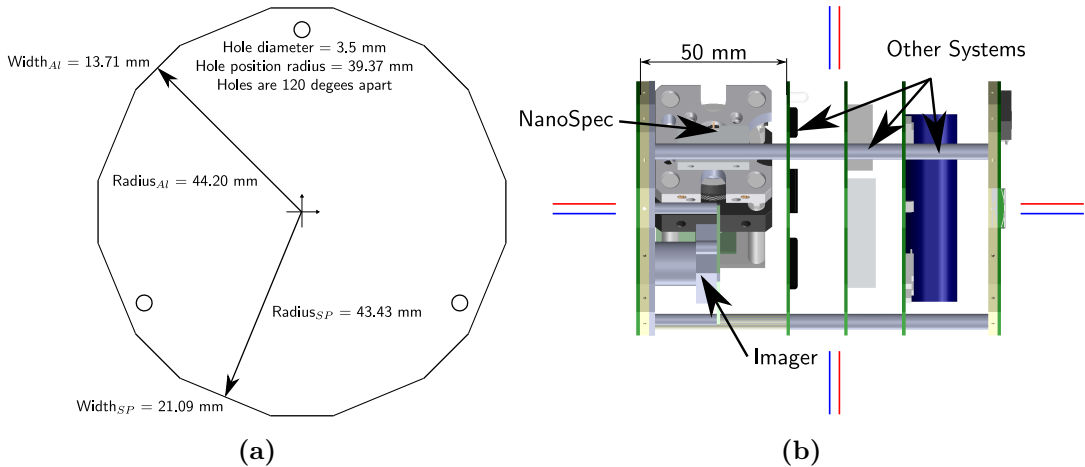


Figure 4.17: a) Diagram showing the dimensions of top view of the i-INSPIRE satellite. The NanoSpec housing must fit within this area to be compatible with the satellite design. b) Side view schematic of the satellite. The payloads, including NanoSpec, are located in the leftmost compartment, with the other satellite systems occupying the remaining space.

to possibly detect associated Čerenkov light. Here I will briefly discuss the expected radiation environment in orbit and its implications for the spectrograph design. I will then introduce the design and characterisation of NanoSpec.

4.3.1 Design Constraints

The primary constraints, and thus design drivers for NanoSpec, can be split into 3 main categories. The first is the restricted area and volume of the TubeSat, and is perhaps the most stringent constraint. Fig. 4.17a is a diagram of the [printed circuit boards \(PCBs\)](#) that form the floor and core structure of i-INSPIRE. The science payloads (including all optics, detectors/sensors and any additional control electronics) must remain within this footprint. Additionally the payload compartment, seen in the left of Fig. 4.17b limits the cumulative height of the payloads to 50 mm. The overall cost of the spectrograph is the second major factor. The i-INSPIRE mission is a one-way trip, so anything that is launched into orbit will not be recovered. In fact, given that i-INSPIRE is on the manifest for the first mission of IOSs N45 launch vehicle, there is a significant risk that the satellite will not achieve orbit. This led to the decision to keep the payload costs as low as possible, making use of commercially available parts and components where possible. Further, due to the low altitude and the fairly short mission time (< 4 weeks), the radiation hardness requirements in many of the components has been neglected. Where possible industrial or automotive versions¹ have been used. The third requirement arises from the limited power available to the payload in orbit. As an isolated system in-orbit the power budget is strict, so the power requirements of the detector used in the spectrograph are an

¹These classifications generally specify larger operating temperature ranges.

important part of its design.

In order to satisfy both the cost and the size constraints the spectrograph will operate in the visible (~ 400 nm to 700 nm). The performance of off-the-shelf achromatic lenses reduces this to a wavelength range of 450 nm to 700 nm. A visible light design is further supported by the wide availability of silicon CCD and CMOS detectors thanks to mass commercialisation of the technology.

4.3.2 LEO Radiation Environment

The radiation environment in **LEO** is a combination of Galactic cosmic rays, particles trapped in the Earth's magnetic field (also known as trapped radiation or the Van Allen belts) and particles generated by energetic solar events, such as flares or coronal mass ejections. Trapped radiation is the dominant source of high energy particles in the high inclination polar orbit planned for i-INSPIRE (Badhwar 1997; Betters et al. 2011; Heynderickx et al. 2004).

There are two hot spots of radiation: at the poles, where electron precipitation is highest, having been funnelled to this region by the Earth's magnetic field; and at the South Atlantic anomaly, where the inner radiation belt is closest to the earths surface. It is in these regions that any effects of radiation are expected to present themselves in NanoSpec and the satellite control systems.

Possible Implications

i-INSPIRE's compact size and limited weight eliminate the possibility of any substantial radiation shielding. As a result all the components will be exposed to a relatively strong radiation environment (flux $> 10^3$ particles/cm 2 /s with an energy larger than 0.2 MeV). Besides single-event upset occurrences, which can cause the computer or detector to malfunction, a particularly interesting possibility is the generation of Čerenkov light by high energy particles in the optical fibre feed of NanoSpec. Čerenkov radiation is commonly pictured as the blue glow seen around submerged nuclear reactors, but is also central to many particle, astrophysical and space experiments (Abraham et al. 2004; Fukuda et al. 1998).

Čerenkov photons are generated when a charged particle passes through a material (with refractive index n) faster than the speed of light in that material (i.e. velocity of a particle $v_p \geq c/n$). As the refractive index of silica optical fibre is ~ 1.5 , the threshold speed required to generate Čerenkov radiation is ~ 0.7 times the speed of light. This corresponds to electrons and protons with energies of ~ 0.2 MeV and ~ 0.38 GeV respectively. In LEO the average flux (particles/cm 2 /s) with energies greater than this is of order 10^4 for electrons and unity for protons.

If one (or several) of these particles intersect an optical fibre and pass near the core, the generated light can couple to a guiding mode in the fibre. In the case of NanoSpec, a dense region of radiation could lead to an additional background signal in the spectrum, thereby decreasing the signal to noise ratio. This effect has been documented in medical physics studies

where optical fibres used in dosimetry are exposed to therapeutic particle beams (Lambert et al. 2009; Law et al. 2007).

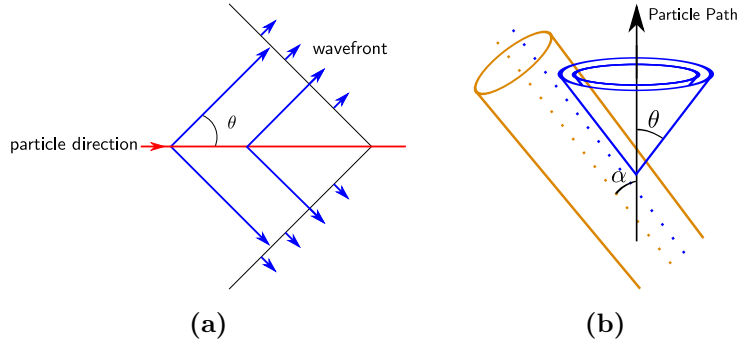


Figure 4.18: a) A plane wavefront of Čerenkov radiation is formed at an angle θ to the velocity of the particle. b) Only the portion of the Čerenkov cone that intersects with the fibre core and is within the critical angle of the fibre is trapped. Illustrated is the case where the cone is parallel to the fibre, which maximises the fraction of the cone trapped (Law et al. 2006).

Coupling of Čerenkov in optical fibres

Čerenkov photons are emitted at an angle θ with respect to the particle's direction of travel, forming the characteristic cone depicted in Fig. 4.18. This angle is given as,

$$\cos \theta = 1/(\beta n). \quad (4.1)$$

where n is the refractive index of the material, and β is the fraction of speed of light the particle is travelling at. In Fig. 4.18b a high energy particle intersects an optical fibre feed with an angle α . If the intersection occurs at such that $\alpha \approx \theta$ the generated light can be guided by the fibre, thus contaminating the spectrum.

In order to quantify the effect of Čerenkov radiation on a signal in optical fibre Law et al. (2006) calculated the fraction of a Čerenkov cone that would be trapped using a ray tracing model of fibre. The actual intensity of Čerenkov generated by a charged particle passing through an optical fibre is given by the product of the path of the particle through the fibre and the intensity of Čerenkov radiation generated per unit distance. Using the Law *et al.*, model a rough estimate of coupling that will occur in fibre used by NanoSpec suggests that of order 10-100 photons are coupled. So a single event will have likely have very little impact on NanoSpec's performance, however in regions such as the magnetic poles and the SAA the cumulative effect of many events in single exposure could result in a detectable signal.

4.3.3 Optical Design

Input Slit

The original design used 8 SMFs set in a V-groove array, forming the linear input slit for the spectrograph. The V-groove allows the fibre inputs of the spectrograph to be precisely aligned and held, but leaves a lot of wasted detector space because the fibre cores are separated by 127 μm . There are two different types of optical fibre used in NanoSpec. One is a typical step index fibre where light guiding is achieved via a higher refractive index in the core of the fibre than the cladding. The second is a photonic crystal fibre (PCF) where light is guided by a pattern of air (or vacuum once in space¹) filled holes in the core of a silica fibre (seen in Fig. 4.19b). This will be the first time the use of PCF has been demonstrated in a space environment. If NanoSpec does suffer from single-to-noise ratio (SNR) degradation due to Čerenkov light, it is expected that the PCF fibre will exhibit better performance because it has less high-index material for the charged particle to pass through.

Four of the fibres are Nufern S460-HP SMF. These have a nominal mode-field diameter (MFD) of 3.5 μm and a NA of 0.1. The remaining 4 fibres are NKT Photonics ESM-12-02 endlessly single-mode (SM) PCF. The PCF has a very similar mode field profile to conventional fibres (i.e. a Gaussian, see Fig. 4.19a) however the $1/e^2$ diameter is nearly 3 times larger, being 10 μm . The NA of this fibre is ~ 0.04 . It is expected that this fibre, with its smaller NA and reduced amount of silica (due to the holes), will result in a reduction in the amount of Čerenkov radiation that is generated and subsequently guided by the fibre. The demonstration of the PCF in space is also important as they are typically more resistant to radiation damage, which will become important for longer term missions.

The alternative is a 7 fibre bundle that is lightly fused, forming a TIGER input slit identical to that used in PIMMS IR, but with visible fibre.

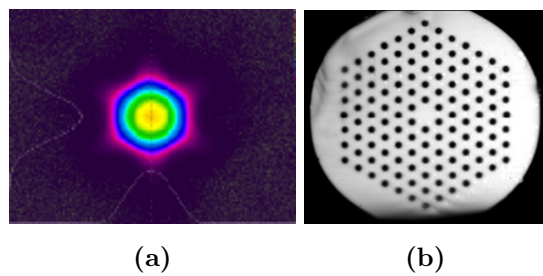


Figure 4.19: a) Mode profile of the PCF, showing x and y cross sections. b) Close up image of the end of PCF. Dark spots are the air filled holes in the fibre (Image from NKT Photonics ESM-12-02 Datasheet).

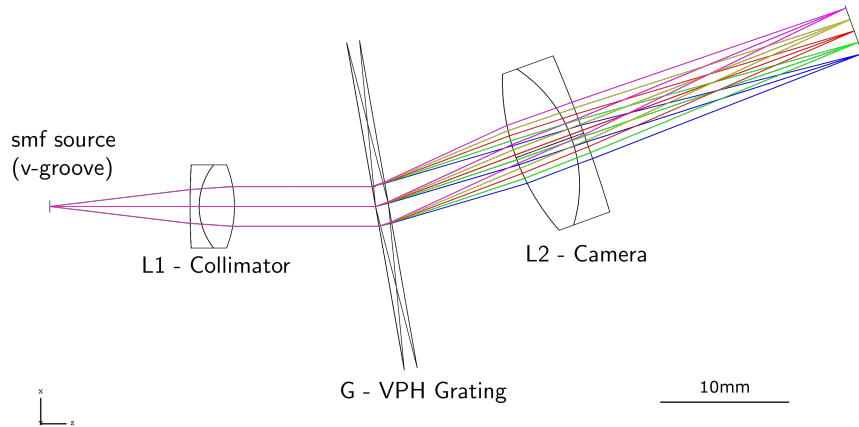


Figure 4.20: Diagram of the current design for the NanoSpec micro-spectrograph. The array of 8 input fibres at the input are aligned perpendicular to the page. The wavelengths shown are evenly spaced from 450 nm to 700 nm.

Collimator and Camera Optics

During the design of NanoSpec the goal was to create the largest collimated beam (thus reach the highest resolution), spectrograph yet remain diffraction-limited and fit within the size constraints discussed previously. The dominant parameter actually turns out to be the pixel size of detectors. A typical detector (that is low cost, monochrome and compact) had pixel sizes ranging from $\sim 2.2 \mu\text{m}$ up to $6 \mu\text{m}$. In order to sample the **point spread function (PSF)** sufficiently, the image formed by the camera-collimator pair needed to be at least 2 pixel per **full width half maximum (FWHM)**, or a magnification between ~ 1.5 to 4 . Finally, the total length must be less than ~ 70 mm to fit in the TubeSat footprint.

There are currently two versions of the collimator to suit two different detector pixel sizes ($2.2 \mu\text{m}$ and $6 \mu\text{m}$). The first is a doublet with an **effective focal length (EFL)** of 12.7 mm. It results in a collimated Gaussian beam approximately 2.5 mm in diameter ($1/e^2$ diameter). The second version introduces a second doublet with a 7 mm **EFL** positioned 1 mm in front of the first lens. This reduces the **EFL** of the collimator to 5.7 mm and the beam width to 1.2 mm. The camera lens in either case is a doublet with an **EFL** of 25.4 mm. In all instances the optics are essentially very close to diffraction-limited in the visible and have anti-reflective coating for visible light (400-700nm). A typical ray tracing spot diagram of the single optics collimator is shown in Fig. 4.21.

Grating and Resolving Power

The dispersing element in the spectrograph is a **volume-phase holographic (VPH)** grating manufactured by Wasatch Photonics. It has a line density of 600 lines/mm and has an efficiency of

¹Assuming air escapes the fibre on its journey to space.

4.3 NanoSpec

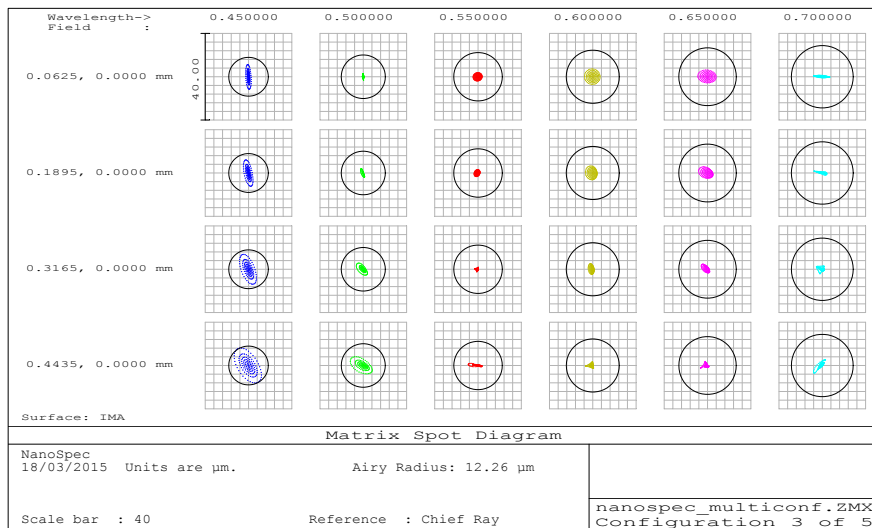


Figure 4.21: Spot diagrams for unique field positions of a centred 8 fibre V-groove. The wavelength coverage is 450 nm to 700 nm. The black circle is the ZEMAX estimated airy disk.

83.5% at 600 nm. It is also the largest optical element in the system at 25.4 mm in diameter (smaller VPH gratings were not readily available).

In Littrow configuration the angle of diffraction is $\sim 10^\circ$ for the 1st order. As the spectrograph is expected to be very close to diffraction-limited the resolving power can be estimated using Eqn. 3.8. For the 2.5 mm and 1.2 mm beams the measured resolving powers are 1900 and 900 respectively (at 500 nm; consistent with ZEMAX physical optics simulations). The optical elements are all at least 3 times the $1/e^2$ diameter of the collimated beam so truncation is not expected to be an issue.

Detector

There are two detectors used in NanoSpec, one is used for ground testing and observation and the other will primarily be used aboard the spacecraft. The first is a 5MP (2552 x 1964) detector with 2.2 μm pixels while the second is of the smaller VGA (640x480) format with 6 μm pixels. The advantages of the VGA detector vs. the 5MP detector are a simpler TTL level serial interface and higher sensitivity. However, due to the increased pixel size it must be paired with the shorter focal length collimator discussed previously (and thus has a lower resolving power). As a result the spectral resolution and range are unsurprisingly reduced. The 5MP detector has a USB interface, and allows greater control over pixel binning and exposure times. This allows for a more detailed study of NanoSpec's optical performance in the laboratory.

4.3.4 3D printed enclosure

The original NanoSpec housing uses **commercial off-the-shelf (COTS)** optical mounting components. Every effort was made to compact the design and reduce its weight (large pieces of cage plates were removed). The final design can be seen in Fig. 4.22a. The collimator and camera are both held in their own 40 mm Thorlabs cage plate. The diffraction grating is mounted in a 10° filter mount. The filter mount is intended to reduce back reflection in lens tube systems, but works quite well to set the angle of diffraction. The cage plates are joined with hinged beams, which allow adjustment of the angle of incidence. Actually configuration of this setup is less than trivial, but it remained very stable once all the screws were clamped down. Indeed, it survived the maiden voyage of i-INSPIRE on a high altitude balloon unscathed (results in Chap. 6).

The 3D-printed housing was designed to overcome some key issues with the cage based housing. Firstly, the housing was not light tight and had to have a layer of opaque tape to operate. Secondly, while it did fit within the footprint of i-INSPIRE, the fibres were subjected to significant bending to do so. Finally, it was desirable to reduce the weight as much as possible.

The housing went through several iterations, primarily to account for differences in a printed model and the CAD design. The final design is more compact and significantly lighter than the cage system which has a mass of ~200 grams. The total weight is 47 grams, with 15 grams consumed by bolts that clamp the two halves together. The design of the 3D-printed version allows the optics to be dropped in place, with no additional alignment needed. Fine tuning of the focus is achieved with spring-loaded washers on the detector mount. The 3D-printed housing could actually be reduced to about 1/2 of its current height, but is currently limited by the 1 inch diffraction grating.

There have been significant delays from the original anticipated launch with IOS (Mid 2012). At this point, while i-INSPIRE is essentially ready to go, I do not anticipate reaching space with IOS (and I believe the rest of team are in agreement). The next step will be converting to a more universal satellite platform.

4.3 NanoSpec

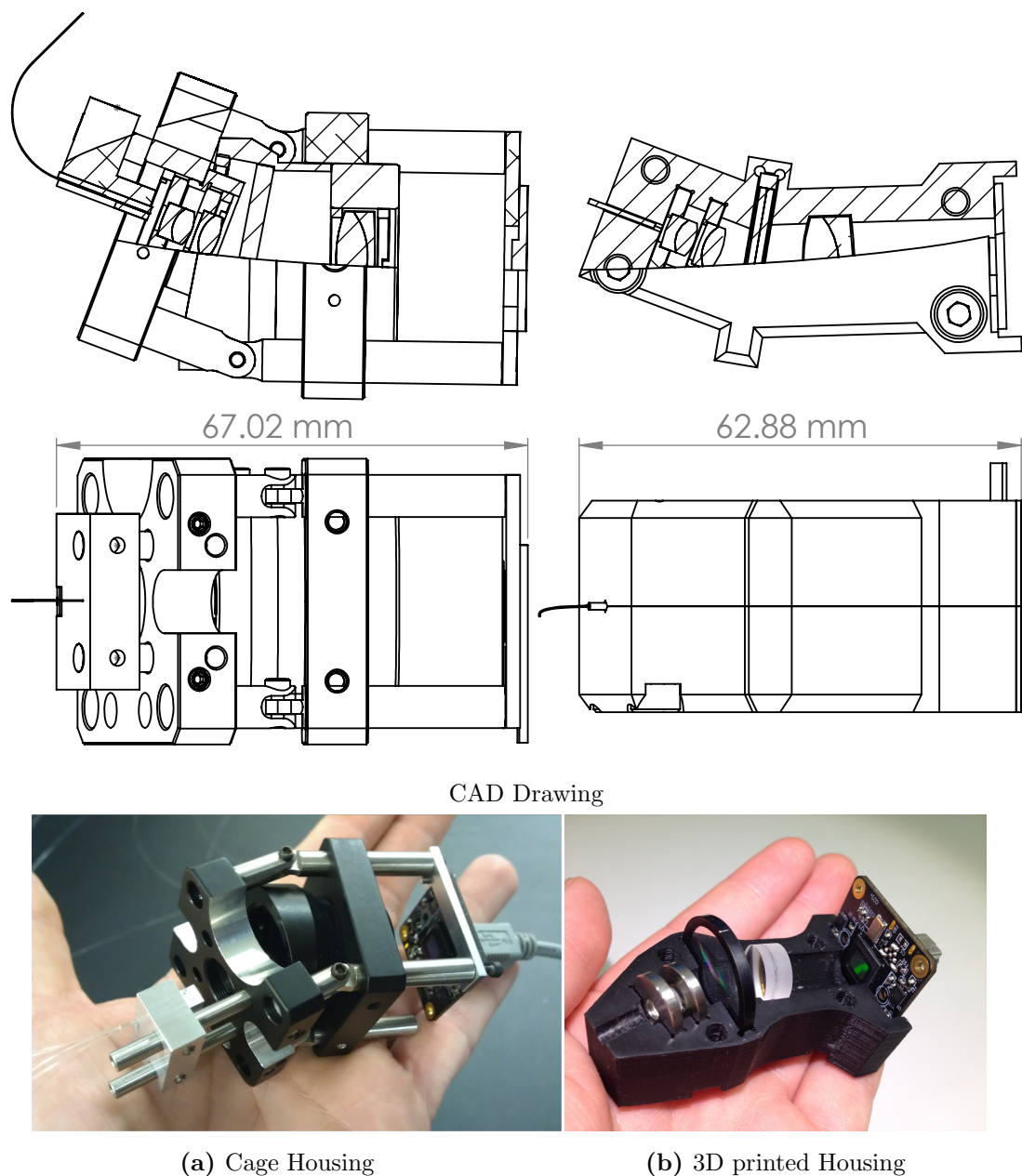


Figure 4.22: Actual Size top and side views of the cage and 3D printed housing and photos. *a)* Original cage mounting system for NanoSpec. Primarily uses off the shelf components. Total mass was ~200 grams (1/4 of total weight budget for i-INSPIRE). *b)* 3D printed housing. This allows optic spacing to be reduced and angles to be set more precisely. Housing is composed of just two pieces, with insets that hold each optic. The total Weight is less than 50 grams (15 grams of that are just the bolts used to connect the halves). The 3D housing size is limited by the diffraction grating. With a smaller grating it could be further cut down in size.

5

Reduction package and calibration

5.1 MISPRINT

MultI-order SPectroscopic ReductIoN Tool

Reduction of data from all of my PIMMS spectrographs presented some challenges, particularly with the multi-order data generated by PIMMS echelle. In order to have a better understanding of the reduction process I have avoided using ‘black box’ reduction tools like IRAF¹. Some of my earliest reduction programs were only suitable for the single order spectra that were well aligned with detector rows and columns, and required significant user input. They have evolved to be become a flexible and automated package. Currently, the only step that requires significant user input is the initial stage of wavelength calibration, where spectral lines must be manually identified and paired with a reference spectrum.

I have packaged the various routines into a unified package, dubbed MISPRINT (MultI-order SPectroscopic ReductIoN Tool). The entire package is written as a MATLAB class and can be used to process and extract spectra from PIMMS visible, PIMMS IR and NanoSpec (or any spectrograph for that matter). The following will provide an overview of the reduction process, including basic data preparation, spectra tracing (i.e. position identification), the spectral extraction algorithm and wavelength calibration. Also discussed is an image correction technique that uses a grid of spectral lines generated with a **Fabry-Pérot (FP)** laser comb to improve subsequent spectra. The outline of the complete reduction process is shown in Fig. 5.1.

¹Image Reduction and Analysis Facility — <http://iraf.noao.edu>

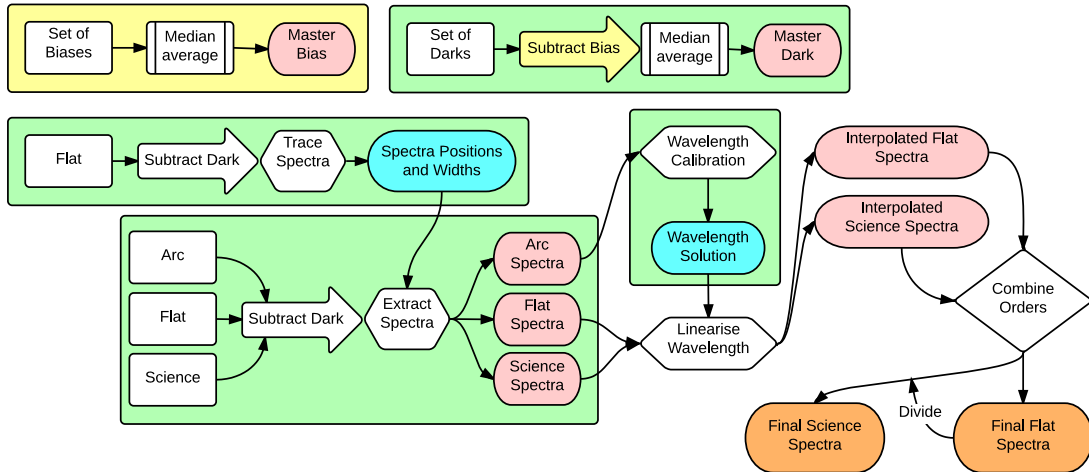


Figure 5.1: Flow Chart of the general reduction pipeline. The yellow highlighted steps are optional. The green steps are self contained methods within misprint. Red blocks indicate where intermediate files are saved. The orange blocks are the final spectra.

5.1.1 Data Preparation

Dark Subtraction

Each set of observations requires 4 key frames: (i) a flat-field, (ii) an arc lamp (or other wavelength reference), (iii) a bias (median of many zero-exposure darks), and (iv) an equal-exposure time dark. For science/light with short exposures times the bias and dark can be replaced by a median of many equal-exposure time dark frames. Every frame is first bias subtracted (unless a bias is not used, i.e. short exposure time situation described above) and the median dark is subtracted from all *Light* frames, i.e.

$$\text{Obs} = (\text{Obs} - \widehat{\text{Bias}}) - (\text{Dark} - \widehat{\text{Bias}}) = \text{Obs}_{\text{raw}} - \widehat{\text{Dark}}, \quad (5.1)$$

where $\widehat{\cdot}$ notation indicates an averaged frame. This step is encapsulated in the method `misprint.prepareFrames`. It automatically categorises FITS images within the current folder as bias, dark, flats or light using the FITS header keyword `IMAGETYP`. All bias frames (if detected) are median averaged and the result saved as ‘master-bias.fit’. This is repeated for each set of dark frames with an equal exposure time and CCD set temperature¹ (if a master bias is present, each dark is first bias subtracted). The final dark frame is saved with `IMAGETYP` keyword set to `MASTBIAS` and a filename suffix ‘-masterdark’. Finally, all light frames are dark subtracted using their corresponding dark master frames (according to integration time; and if present, the master bias). At the end of each step the raw data frames are moved into a folder names ‘processed’.

¹Target temperature of CCD PID controller. I have assumed the CCD has stabilised at this temperature before data was taken. It is not yet checked in the headers.

Table 5.1: Definitions of variables used in reduction process

Parameters	Definition
N_f	Number of fibres
N_{order}	Number of orders
N_i	Number of data pixels
η_f	integrated intensity of fibre f
var_f	variance of fibre f
ϕ_i	normalised model PSF profile of a single fibre for i th pixel
ϕ_{fi}	normalised model PSF profile of fibre f for i th pixel
M_i	combined model for all fibres
D_i	data value for i th pixel
$\text{var}(D_i)$	variance for i th pixel
RN	rms read noise in ADU
Gain	detector gain in e^-/ADU

5.1.2 Order Tracing

The next step is to *trace* the spectra in the flat-field frame. This step returns accurate positions in the spatial axis for each spectrum, which is a required input for the 1D spectrum extraction algorithm. Firstly if there are incomplete orders, these need to be masked (using a logical array with same size as the raw echellogram). This step is performed by the `misprint.getMaskForIncompleteOrders` method. The method is controlled by the ‘needsMask’ property. If no mask is required the mask is set as all ones, otherwise the top third of the echellogram is displayed and the user chooses two points just below orders that are incomplete or to be ignored. These are stored in the FITS header as `CLIPTL` and `CLIPTR` (top left and top right points respectively). This process is mirrored in the bottom third of the echellogram, and stored as `CLIPBL` and `CLIPBR` (bottom left and bottom right points respectively). The area not bounded by these points is set to zero in the mask.

The trace is encapsulated in `misprint.traceSpectra`. This method first checks for a pre-existing trace. If the initialisation included a reference filename this is used, otherwise the current target file name is used. If the property ‘forceTrace’ is set, the previous trace will be overwritten (if a reference is set an error is thrown). The actual trace is done by fitting $N_f \times N_{\text{order}}$ Gaussians through 100¹ evenly spaced columns. The clipping step ensures there are no partial diffraction orders, making it a simple task to assign sets of N_f fibres to a separate diffraction orders. For speed, each diffraction order is fit separately. Rough locations for all spectra are found using the builtin MATLAB function `findpeaks`. A sample of this detection is shown in Fig. 5.2. These are split into groups of N_f fibres. The positions are also used as a starting point in the Gaussian fits used to find an accurate spatial position. The spatial position and width across the sensor for each spectrum is then interpolated with a cubic polynomial fit

¹Default; set using the ‘numTraceCol’ property

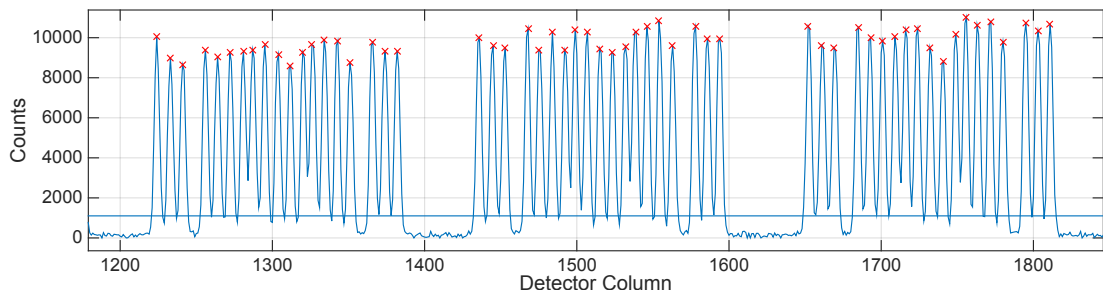


Figure 5.2: Cross-dispersion profile through 3 orders of a PIMMS visible flat-field. The red cross mark peaks detected by tracing process. The straight line shows the minimum value required for a peak to be detected.

to both the centroids and widths obtained from the Gaussian fitting. The result is shown over plotted on the raw echellogram in the left panel of Fig. 5.3. These position are later used as inputs for the 1D spectral extraction procedure.

5.1.3 Spectra Extraction

The goal of the spectral extraction is to reduce the 2D echellogram into $N_f \times N_{\text{order}}$ 1D spectra. To do so the profile of each spectrum must be integrated in the cross-dispersion direction (along detector columns) for every wavelength (along detector rows). The simplest method to do this is of course a simple trpline extraction, where a window is defined either side of the profile, and its contents are summed. This has a few disadvantages: First, the edges of the profile will have a lower signal to noise ratio, yet are given equal weight in the summation. This results in a larger uncertainty in final integrated value. The trpline window may also clip the edges of the profile, and thus underestimate the actual integrated intensity. Both these issues can be mitigated by performing a weighted summation of the fibre profile, typically by fitting the profile with a Gaussian (i.e. a Gaussian weighted summation). However, both these summation methods however are not ideal when multiple fibres are involved, particularly when they are tightly packed.

If there is some overlap in the profiles any blind summation techniques can result in significant cross-talk between spectra. In the PIMMS case, this is not a significant issue if the fibres are aligned in wavelength (recall that the **single-mode fibre (SMF)** outputs of the **photonic lantern (PL)** are all inherently intermixed). However, when using the TIGER hexagonal grid slit, this would pose a serious issue. All the fibre are offset significantly in wavelength so any cross-talk in spectra could result in spurious signals in the extracted spectrum.

A more thorough method must be used to account for the fact that there are multiple spectra that are partially blended in the spatial direction, but critically not aligned in wavelength. To do this I use the multi-profile de-convolution optimal extraction process for tightly packed fibres described in Sharp and Birchall 2010. The process requires the following inputs:

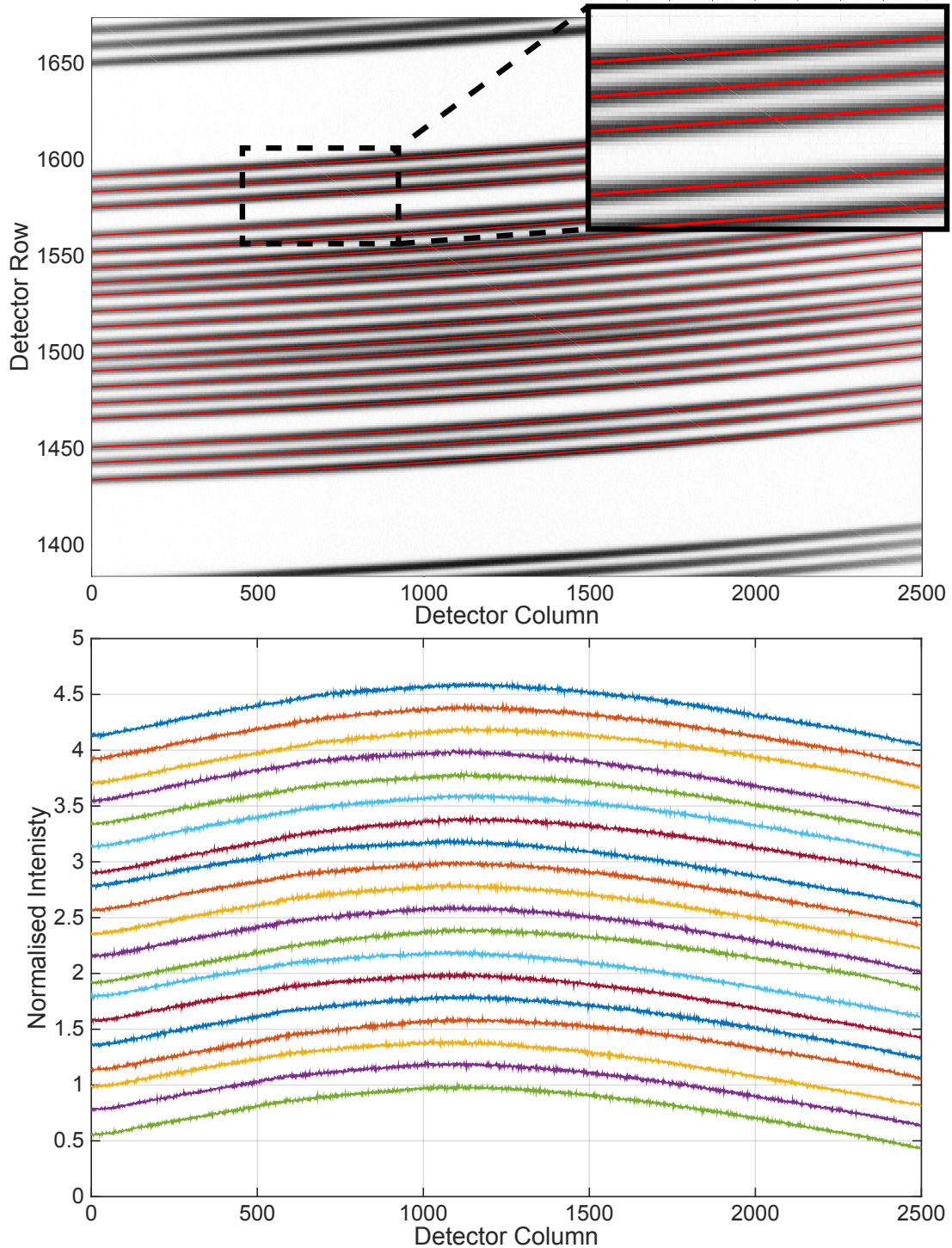


Figure 5.3: Left: Interpolated position trace of a single order (in red) plotted on the raw echellogram. Right: The corresponding extracted spectra.

5.1 MISPRINT

- the echellogram image and its corresponding variance estimate. This is assumed to be

$$\sigma_i^2 = \text{RN}^2 + D_i/\text{Gain} \quad (5.2)$$

where RN is the CCD root mean square (RMS) read noise in analogue-to-digital units (ADU) and Gain is in units of electrons per ADU.

- spectra positions and order edge definitions determined in the trace method.
- interpolated cross-dispersion (spatial) width, $w_{x\text{-disp}}$ of the spectra as a function of detector position along the dispersion axis (not this could also be included as a fit parameter when solving for integrated intensity, but would cost significantly more computation time).

Fitting for an integrated intensity: Multi-Profile Deconvolution

For simplicity (and speed), the spectra in each order are extracted independently. The extraction algorithm assumes that each column of the echellogram is independent and that the integrated intensity of fibre f , η_f , can be modelled as,

$$M_i = \sum_f \eta_f \phi_{fi}, \quad (5.3)$$

where ϕ_i is the model fibre profile and M_i is the modelled value of the i th pixel in the given detector column. The model profile for each fibre is defined to be normalised such that,

$$\sum_i \phi_{fi} = 1. \quad (5.4)$$

The model is then fitted to the real data, D_i with a variance $\text{var}(D_i)$. Thus the value of integrated intensity η for each fibre can thus be found via the minimisation of

$$R = \frac{1}{2} \sum_i \frac{(D_i - M_i)^2}{\text{var}(D_i)} \quad (5.5)$$

This produces a set of N_f coupled linear equations,

$$\sum_f \eta_f \sum_i \frac{\phi_{ji} \phi_{fi}}{\text{var}(D_i)} = \sum_i \frac{\phi_{ji} D_i}{\text{var}(D_i)}. \quad (5.6)$$

A background component (e.g. due to scattered light) can be included using additional fibre profiles (i.e. $f > N_f$), which don't necessarily need have to have the same functional form as ϕ . In my implementation I have included the option to use a straight line to fit the background signal. This works well assuming any change in shape of the background across the detector is slowly varying across the whole detector (because each order is extracted separately).

Error Propagation

The variance of each pixel was already estimated using Eqn. 5.2. To determine the variance of each fibre's integrated intensity, var_f , effectively the same process is used. The model is now

$$M_i = \left(\sum_f \phi_{if} \text{var}_k \right) + RN^2. \quad (5.7)$$

where ϕ is same fibre profile used to solve Eqn. 5.6. So the minimisation problem is now

$$R = \frac{1}{2} \sum_i \frac{(\text{var}(M_i) - M_i)^2}{\text{var}(D_i)}, \quad (5.8)$$

producing a second related set of coupled equations,

$$\sum_f \text{var}_f \sum_i (\phi_{ji} \phi_{fi}) = \sum_i (\text{var}(D_i) - RN^2) \phi_{ji} \quad (5.9)$$

Implementation

The first step in the implementation is to setup ϕ as an N_f by N_i matrix such that each row is the model profile (assumed to be Gaussian) of one fibre. The width of the spectra that were determined during tracing is used as a fixed parameter. Code 5.1 is used to generate this matrix, an example of which is shown in Fig. 5.4.

Code 5.1: This is a vectorised form of the code that generates N_f Gaussian fibres profiles each in its own row. The widths and centroids were predetermined by the tracing process.

```

1 phi=bsxfun(@times,
2     exp(
3         -(%
4             bsxfun(@rdivide, ...
5                 bsxfun(@minus, ...
6                     repmat(dataRows{col}, [self.numOfFibers, 1]), ...
7                         specCenters(col,:)) ...
8                 ), ...
9                 specWidth(col,:)) ...
10            ) ...
11            ).^2 ...
12            ), ...
13            1./ (specWidth(col,:)*sqrt(pi)) ...
14        );

```

The next step is to calculate the matrices that form the left hand side and right hand side of Eqn. 5.6, that is creating the following,

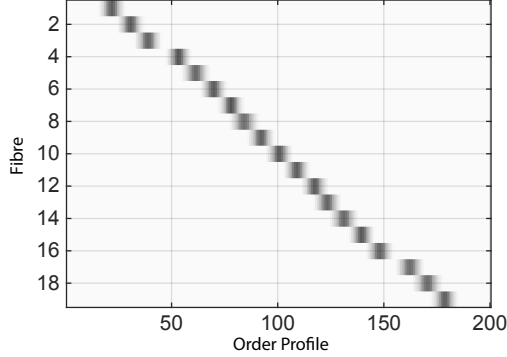


Figure 5.4: Example of the matrix ϕ model profiles used in spectral extraction. Each row is the model for single fibre. A summation over the matrix equals 19 as there are 19 fibre profiles.

$$c_{fj} = \sum_i \frac{\phi_{ji}\phi_{fi}}{\text{var}(D_i)} \quad (5.10) \qquad b_j = \sum_i \frac{\phi_{ji}D_i}{\text{var}(D_i)} \quad (5.11)$$

and for the variance equations from Eqn. 5.9 the matrices needed are

$$ce_{fj} = \sum_i \phi_{ji}\phi_{fi} \quad (5.12) \qquad be_j = \sum_i (\text{var}(D_i) - RN^2) \phi_{ji} \quad (5.13)$$

The matrix $\sum_i \phi_{ji}\phi_{fi}$ is simply given by the matrix multiplication of the ϕ matrix from Code 5.1 with its transpose. In order to evaluate Eqn. 5.10 the columns of the transpose are first divided by the vector $\text{var}(D)$. Equation 5.11 is evaluated by first multiplying the variance-weighted transpose of ϕ with the vector of real data, D . The transpose of this gives the matrix b_j . To solve for the values of η I have used MATLAB built-in function, \backslash (`mldivide`). This is an efficient linear equation solver which selects an appropriate algorithm depending on matrix inputs. A similar process is repeated to solve for the variance of each fibre, which can be seen in Code 5.2.

The Code snippets 5.1 and 5.2 are run $N_{\text{cols}} \times N_{\text{orders}}$ times, looping over each column of the detector while treating each order separately. Total computation time for the 1D spectral extraction of an echelleogram with 12 orders and 19 fibres is about ~ 20 seconds (i.e. extraction of PIMMS visible). Of this setting up ϕ consumes $\sim 45\%$. Creating the variance-weighted ϕ consumes 18% , and the final calculation of c takes 12% . Solving for $c \backslash b$ and $ce \backslash be$ consume 10% combined.

5.1.4 Arc Lamp Wavelength Calibration

The next step in the reduction is determining a wavelength scale for the spectra. The most common way of doing this is using a hollow cathode arc lamp, but it can also be done with a tunable laser, laser frequency comb or FP (essentially any source that offers repeatable and uniquely identifiable features in wavelength). In PIMMS visible, I use a Thorium-Argon (ThAr)

Code 5.2: Forming both Eqn. 5.10 and 5.11

```

1 varweightedPhi=bsxfun (@rdivide ,phi ,varProfile{ col }) ';
2 c=phi*varweightedPhi ;
3 b=(( orderProfile{ col })*varweightedPhi ) ';
4
5 ce=phi*phi ;
6 e=(( varProfile{ col }-RN^2)*phi ) ';
7
8 spectraValues (: , col )=(c\b );
9 spectraErrors (: , col )=(ce\be );

```

arc lamp (a sample is shown in Fig. 4.14), which has a large number of lines in the visible. It is this large number of lines that make it one of the most common calibration lamps found in visible high resolution astronomical spectrographs.

Line Identification GUI

The first step in the calibration is pairing known ThAr lines with their counterparts in a PIMMS visible spectrum. This step is the only interactive component of the reduction. To do this I created a MATLAB GUI which allows the user to select a PIMMS visible order and show a reference ThAr order. The interface is shown in Fig. 5.5. The key features are as follows:

1. Select reference spectrum, currently only ThAr is fully functional (This spectrum was compiled by Murphy et al. (2007)).
2. Reference order is estimated using angles of primary dispersion (i.e. 63° for R2 échelle grating). Start and End wavelength can be manually adjusted to better match the calibration spectrum.
3. When the user selects a reference line, it is compared to a database of known lines (from IRAF, Tody (1986) and Willmarth (1987)). If no line is found nearby (within 1 Å) that selection is rejected. If a line is found, it is shown on the plot and the wavelength listed in the table on the right. This ensures only lines that are accurately known are used.
4. Centroids of the calibration spectrum lines are found using Gaussian fits.
5. The wavelength scale is found by fitting a cubic polynomial. The reference and calibration spectrum are plotted with the new wavelength scale in the bottom panel, making a poor fit very obvious.
6. The wavelength solution and the selected lines are saved, and can be reloaded if necessary.

Automatic Completion and Improvement

The manual line identification is only required for a single fibre in each diffraction order. The wavelength solution for the remaining fibres is then automatically obtained. For each order the

5.1 MISPRINT

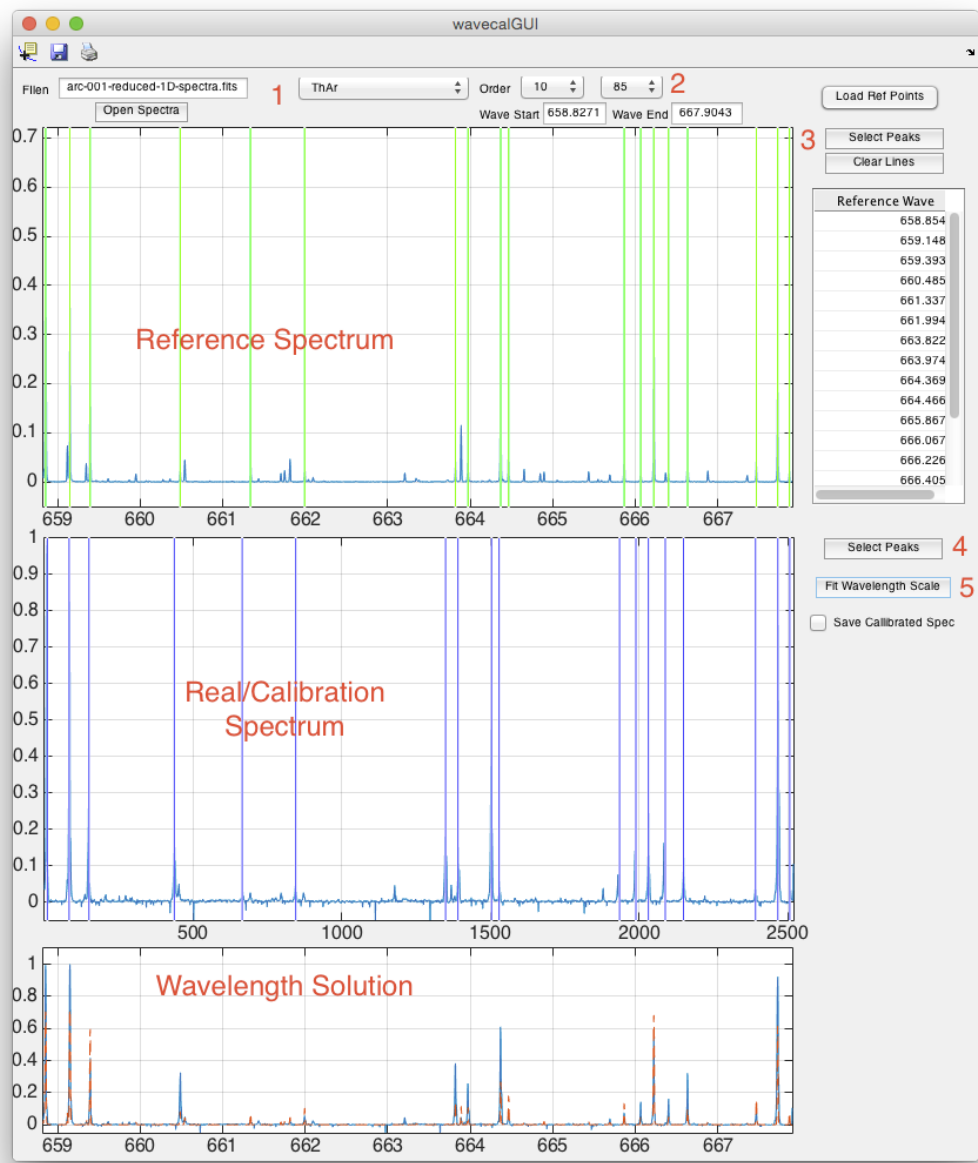


Figure 5.5: MATLAB interface for Arc lamp line pairing.

5.2 Fabry-Perot Etalon (Laser Comb) Calibration

script cross-correlates the spectra from each fibre to determine their relative offset (i.e. from the TIGER slit). This offset is applied to the line identifications previously saved and new centroids for each of the calibration spectrum lines determined with a Gaussian fit. If either the fit is poor ($R^2 < 80\%$) or the line is off the edges of the spectrum it is rejected. If too many lines are rejected an error is thrown (This normally means that too few lines were selected, or the window around each line was too small).

5.2 Fabry-Perot Etalon (Laser Comb) Calibration

An alternative/enhancement to the wavelength calibration that is under development uses a fibre based **FP** etalon. The etalon's cavity in this case is formed in the core of a **SMF**. The fibre is cleaved in two and ends are given a reflective coating, with intensity reflection coefficients R_1 and R_2 . It is then reassembled with a third short piece (length l) placed between the two reflective surfaces. The reflectivity and cavity separation are chosen to create a series of peaks, evenly distributed in frequency. The resulting spectrum is similar to that generated by laser frequency comb, but it is achieved in a passive manner¹.

The transmitted spectrum of a **FP** cavity is given by

$$A = \frac{1}{1 + \frac{4N^2}{\pi^2} \sin^2(2\pi\mu l \lambda^{-1}) \cos \theta} \quad (5.14)$$

where $N = \pi \sqrt[4]{R_1 R_2} (1 - \sqrt{R_1 R_2})^{-1}$, l and μ are the finesse, refractive index and cavity separation respectively (Bland-Hawthorn 1995). Shown in Fig. 5.6 is a PIMMS visible etalon spectrum (blue, transmitted super-continuum source) and the theoretical etalon spectrum according to Eqn. 5.14 (red). Known parameters for the cavity were used to generate the plot ($l = 408.7\mu m$ and $N \approx 40$).

The PIMMS visible **ThAr** spectrum shown was not flat-fielded in this test, the effect of which can be seen in the larger residual at the edges of the spectrum. More importantly though, the line centres are extremely well aligned. This will eventually allow the etalon to be used as the primary calibration source (it requires additional stabilisation, of the cavity, such as that demonstrated by Halverson et al. (2014)). One of the biggest advantages of the etalon is the large number of evenly spaced lines that can be used for wavelength calibration. The number of useful lines in a **ThAr** spectrum varies between ~10-20 per order and those are distributed irregularly. The etalon spectrum has ~30 lines per order and they are by definition regularly spaced. Further, the etalon lines are all of a similar brightness, while the **ThAr** lines vary dramatically in intensity, making fitting of wavelength scale by the etalon more reliable.

¹The etalon stability can be an issue. This is a subject of future work.

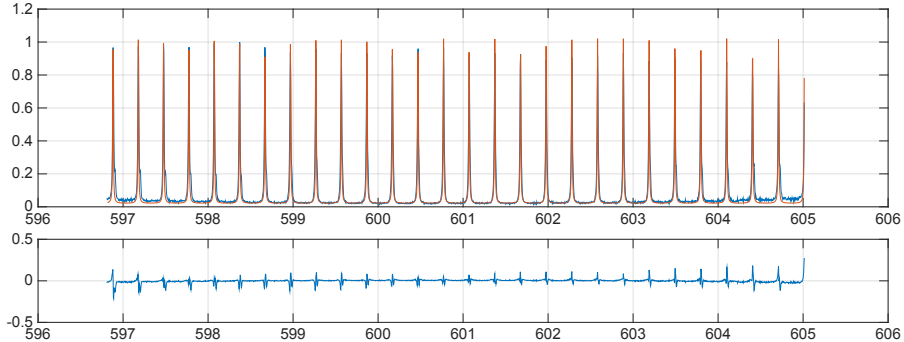


Figure 5.6: Shown is a PIMMS visible spectrum for order 94 (blue) and the theoretical spectrum for an etalon with a $408.7\text{ }\mu\text{m}$ long cavity and finesse of ~ 40 . Bottom shows the residual between the two. The PIMMS visible spectrum was not flat-fielded, which appears consistent with the larger error at the edges of the spectrum.

5.3 Image Aberration Correction

As a demonstrator of novel image correction/reconstruction techniques for spectroscopic data, I have used a modified version of the PIMMS visible spectrograph. The primary motivation here being the fact that all four HERMES (Heijmans et al. 2012) spectral windows show evidence of a strong radial aberration across the field due to imperfect camera optics. This is not a showstopper in that good elemental abundance results have already been demonstrated for large numbers of GALAH survey stars.

But I would like to investigate (a) whether these aberrations can be corrected; and (b) whether this leads to improved elemental abundances for all/more stars. This is a difficult problem that has received very little attention to date. The only related reference found is Bolton and Schlegel (2010) who discuss how this may be pursued, present an algorithm for how to extract a 1D corrected spectrum from a 2D image, but *do not supply any code for the operation*. The paper has several oddities: (i) the method is based on direct matrix inversion which is an old-fashioned concept that is almost never used in practical analysis today; (ii) the method leads to instabilities at their chosen higher resolution which they then convolve down to the sample resolution.

I have approached the problem along two different tracks experimental and analytic. On the analytic side, a search of the literature finds more robust ways to solve this problem, e.g. use regularisation/priors to recover the unknown stimulus without any instabilities. I will also treat this as a 2D problem such that you “see” the corrected spectra as a 2D image before returning the cleaned-up data back into the MISPRINT pipeline.

On the experimental side, in order to simulate a HERMES like data, but with exaggerated aberration, I use a modified version of PIMMS visible. The design normally used an échelle grating as the primary disperser with a **volume-phase holographic (VPH)** grating. Here I am

5.3 Image Aberration Correction

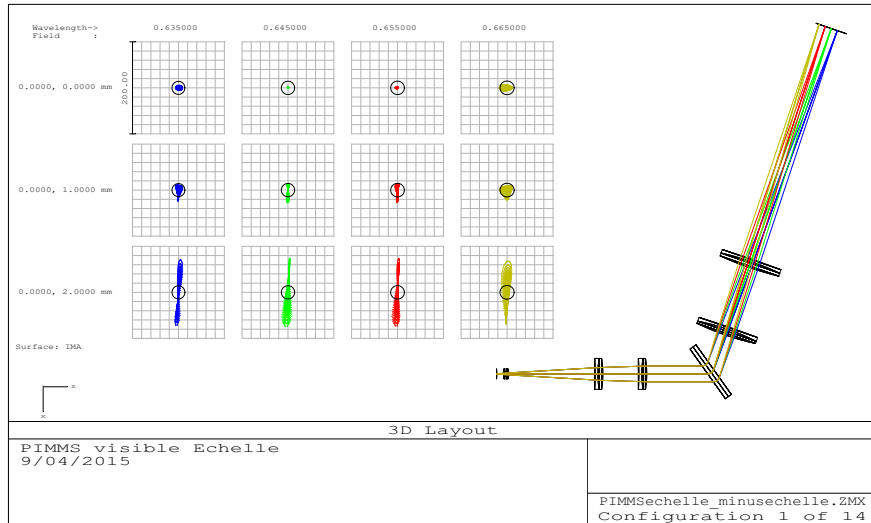


Figure 5.7: Layout and spot diagrams of the modified PIMMS visible. Shown are positions on the slit that are on-axis,

using only the collimator and camera with a 1800 lines/mm VPH grating blazed for 600 nm. This setup has diffraction-limited resolution of $R \sim 30,000$. The input is a v-groove array of several single-mode fibres with a space of $250 \mu\text{m}$, however only 4 could be fed simultaneously (via 1-4 fibre coupler). Two sets of fibres are illuminated along v-groove, a set near on-axis, and a set near the edges of the field. A ray tracing spot diagram of the setup is shown in the inset of Fig. 5.7. The on-axis (top row) input's rays are confined the Airy disk (represented by the black circles) and should thus be diffraction-limited. Further off axis (remaining rows, 1 mm and 2 mm along slit), the image quality suffers from significant astigmatism, and is thus relatively poor. This was done intentionally in order to get very good quality spectra and obviously poor quality spectra to test performance of the correction algorithm.

Three sets of data were taken with this spectrograph setup. First a flat spectra of halogen light source, followed by the etalon spectra (shown in Fig. 5.8) and finally a solar spectra. The solar spectrum was taken by simply pointing the input of the 1-4 coupler at the sun through a window. The same input was coupled to the etalon source and the halogen light source to obtain the other two spectra. The 4 outputs of the 1-4 coupler were then butt-coupled to separate fibres in the v-groove array.

A preliminary result of the correction is shown in Fig. 5.9. In the top of each panel is an example raw point spread function (PSF) obtained with the etalon input. Below that is a raw solar spectrum obtained with the same setup. Finally, the bottom of each panel shows the aberration corrected spectrum. It shows that it is possible to obtain spectra of a similar quality to the on-axis spectra (panels 2 and 3). And to even increase the working resolution by as much as 30%. Currently the operation is only functional of smaller stamps of the spectrum. Generalising this to the whole image is currently a work in progress and will be the subject of

5.3 Image Aberration Correction

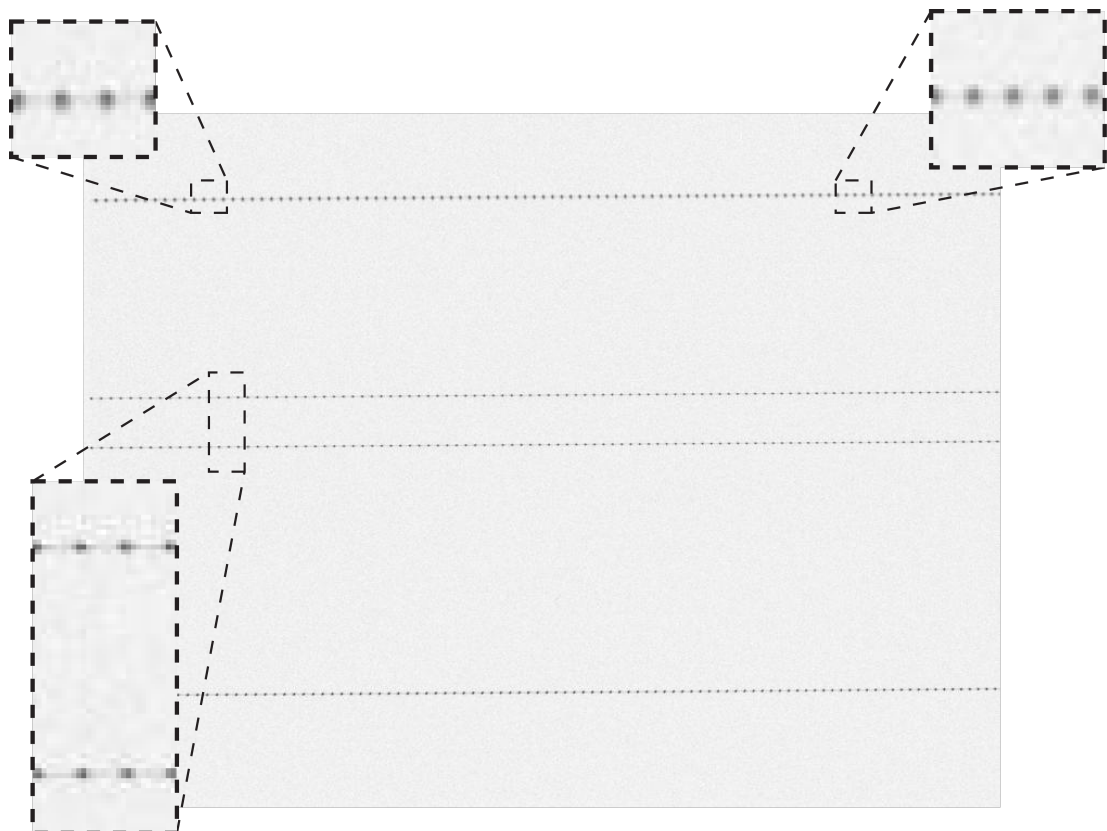


Figure 5.8: Single order etalon spectrum taken using a modified PIMMS visible. This modified version of PIMMS visible removes the échelle grating but keeps the cross-dispersing **VPH**. The now single order spectrograph is fed by 4 **SMF** fibres held in a V-groove array. The maximum fibre separation is $\sim 4\text{mm}$ (i.e. pseudo-slit length). This results in good quality imaging near the centre of the detector and poor quality at the edges (spatial/x axis).

5.3 Image Aberration Correction

a future paper.

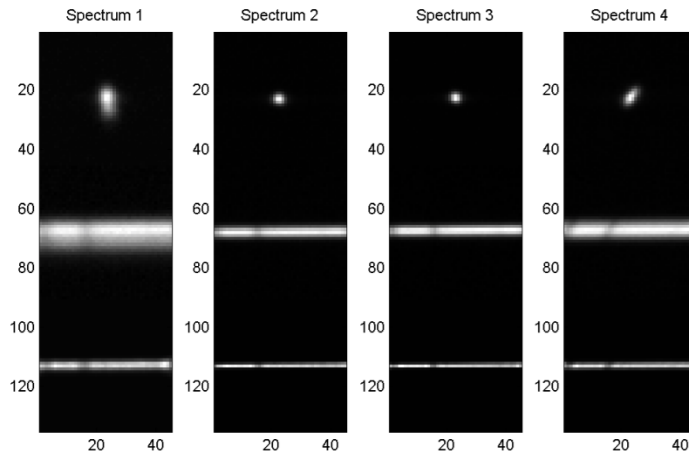


Figure 5.9: In each panel: Top) etalon PSF of modified PIMMS visible spectra in Fig. 5.8; Middle) raw solar spectrum; and Bottom) corrected solar spectrum. Note stamps #2, #3. While the plan is to correct all spectra to the on-axis resolution, it will be possible to increase the working resolution of HERMES by 30% or better for much of the data.

6

Applications of PIMMS

6.1 PIMMS Visible: Solar Oscillations

Spectroscopically the stellar p-modes present as a periodic Doppler shift of the solar absorption lines. This is the result of spherical pressure waves reverberating within the Sun. Each individual mode produces a spectral shift on order of a few cm/s with a periods centred around 5 minutes (or a frequency of 3.3 mHz). The superposition of the large number of solar modes produces an apparent shift on the order of a few m/s. Solar p-modes have been the subject of intense scrutiny over the last few decades, with networks of small telescopes (i.e. BiSON¹ and GONG²) and space-based observatories (i.e. SOHO³) providing near uninterrupted observation for extended lengths of time. With these time-series one can generate high-resolution power spectra of the Doppler shifts, and precisely determine the exact frequencies of the spherical modes of oscillation that generate them. These can be used to probe the internal characteristics of the Sun and support the development of stellar models that can be applied to distant stars. They are also an ideal test of the stability and precision achievable with PIMMS visible. Of course, such observations are not trivial and require a sufficient degree of stability and/or calibration to be successful. Observation of the p-modes pushed the current PIMMS visible design and my reduction package to their limits.

¹Birmingham Solar Oscillations Network

²Global Oscillation Network Group

³Solar and Heliospheric Observatory

6.1 PIMMS Visible: Solar Oscillations

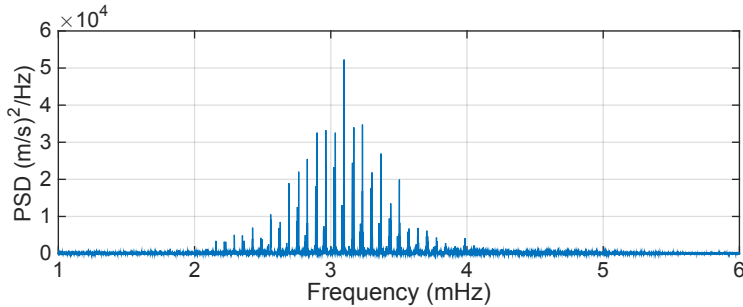


Figure 6.1: Power spectrum of BiSON 2012 time-series.

6.1.1 Simulations of Observations

There is a substantial amount of data available on the solar p-modes oscillations. The time-series of solar line shifts made available by the BiSON (Davies et al. 2014) are particularly useful. I have used their 2012 data release to simulate different sets of observations in order to determine the best setup for detecting the p-modes with PIMMS visible. The key characteristics of the simulations are the cadence of observations and strength of the noise. The BiSON data has a cadence of 40 seconds. I thus need to interpolate the BiSON data in order to generate observations with different cadences. Gaussian distributed noise (generated using the MATLAB `randn` function) is added to the data. The actual measurement of the p-modes is done by generating a power spectrum of the time-series. The signal presents as power in frequencies distributed around 3.3mHz. For very long series these form very distinct peaks which can be paired with specific oscillation modes. The power spectrum of the 2012 BiSON data is shown in Fig. 6.1.

In my simulations I randomly selected a 4 hour long window from the BiSON data. I then interpolated the data to a desired cadence and added Gaussian noise. Shown in Fig. 6.2 are 6 typical simulations, with observation cadences of 0.3, 1, 2, 7, 16 and 40 seconds (raw BiSON data). The 0.3 second cadence corresponds to a zero read-out time exposure, while the 1 and 2 second cadences are realistic read-out times of higher end detectors with similar sized arrays to that of PIMMS visible. The 7 second cadence corresponds to the fastest read-out mode of PIMMS visible sensor (but has poorer noise characteristics), while 16 seconds is the normal read-out time. In each panel there are 3 power spectra, one for data with no added noise, with 5 m/s noise root mean square (RMS) and 10 m/s RMS noise. The top panel shows the spectral shifts.

The notable, and perhaps not unsurprising, result of the simulations is that an increased cadence returns power spectra with the appropriate amount of power at the correct frequencies (compared with zero noise BiSON data). If the noise is 8 m/s RMS or larger the simulation indicates that a cadence of 2 seconds or less is needed in order to detect the p-mode oscillation. Even then, the power for each frequency will not be reliably determined. For the 7 second cadence the argument that p-modes are present can be made, but it would be tenuous at best.

6.1 PIMMS Visible: Solar Oscillations

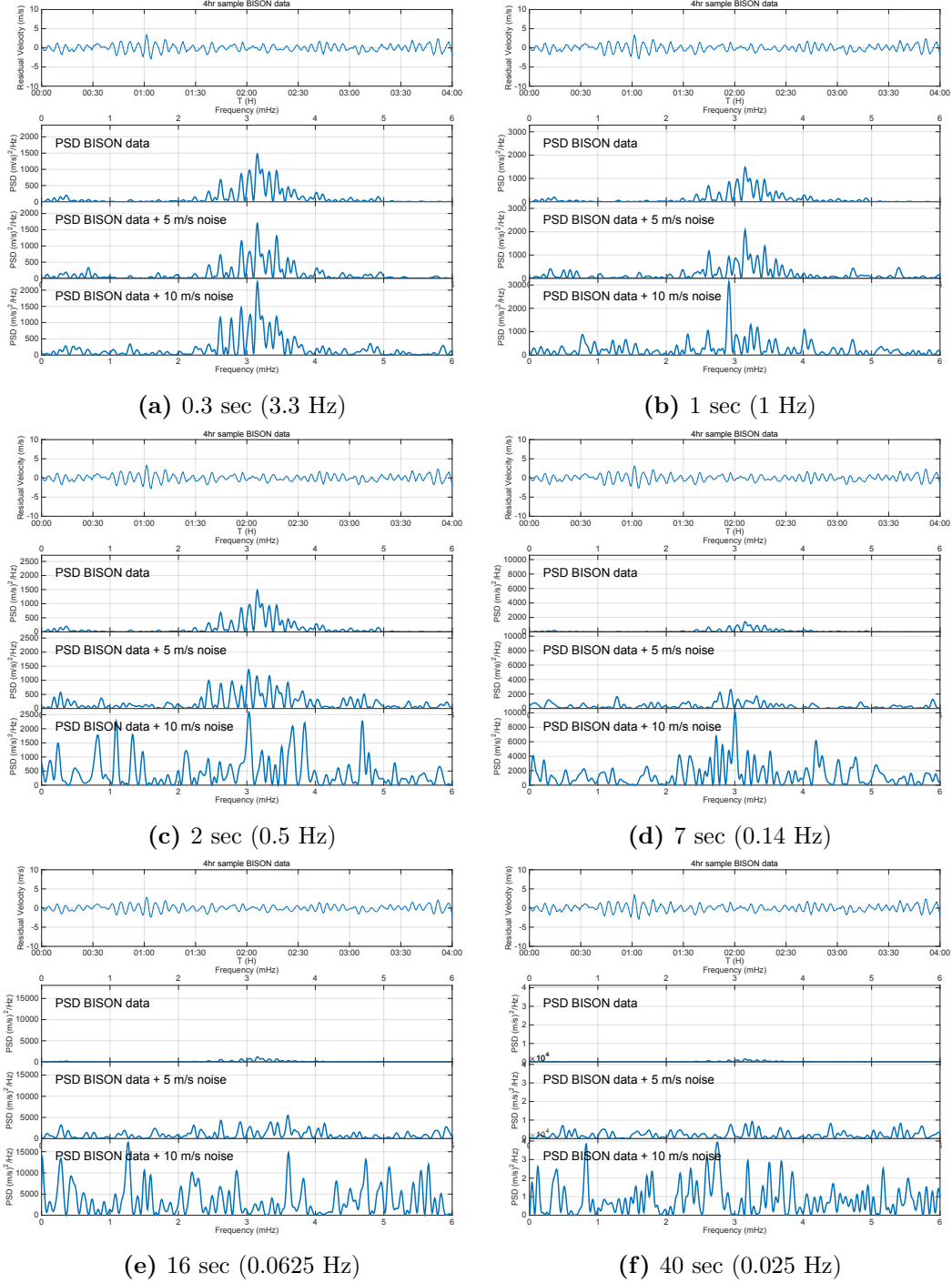


Figure 6.2: Shown in each sub-figure are BiSON time-series with cadences of 0.3, 1, 2, 7, 16, and 40 seconds along their power spectra. Top: No added noise time-series. Bottom: from top to bottom are power spectra of the time series with no added noise, 5 m/s RMS noise and 10 m/s RMS noise respectively. The scale in the power spectra changes between sub-figures.

6.1 PIMMS Visible: Solar Oscillations

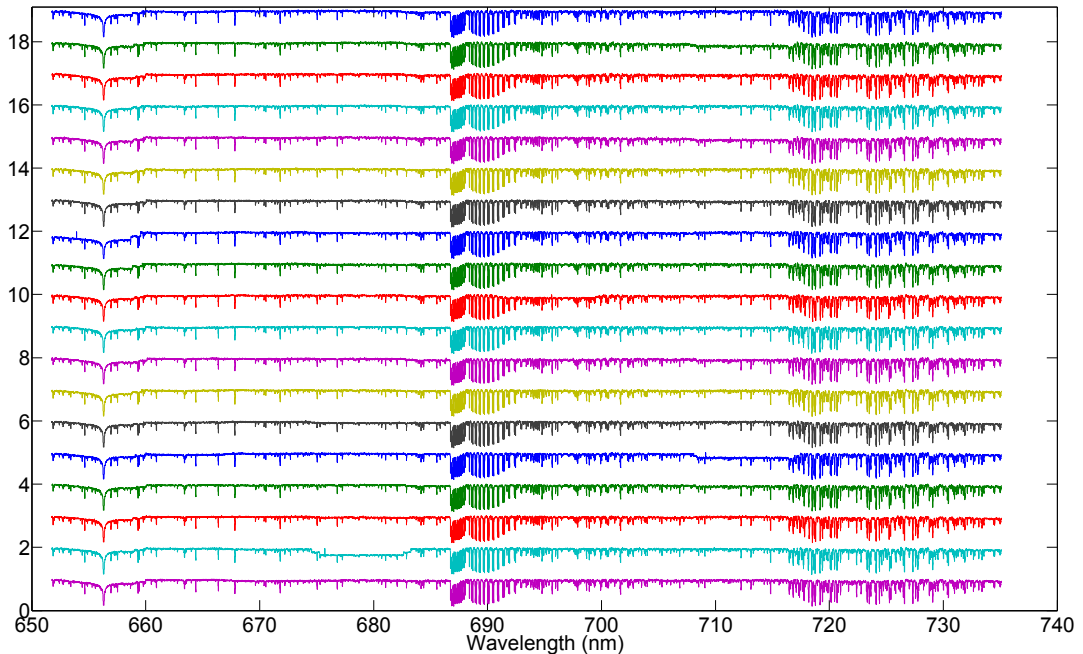


Figure 6.3: Shown is a solar spectrum taken using PIMMS visible. The spectra have been wavelength calibrated and the orders combined to produce a single spectrum for each **single-mode (SM)** core in the TIGER **multi-core fibre (MCF)**. The first prominent feature, at 656 nm, is the solar H- α line. The second, starting 688 nm is atmospheric A-band, an absorption feature of O₂. The third feature at 718 nm though ~732 nm is absorption due to water. Other weaker lines are predominantly solar features.

6.1.2 Observations

I undertook several short observation campaigns where spectra of the Sun were taken every 7 seconds (this was the shortest readout mode available on the PIMMS visible). One of these spectra is shown in Fig. 6.3, where the orders have been wavelength calibrated and combined. Because PIMMS visible is not perfectly temperature stable and not contained within a pressure vessel, spectral lines shifts by several pixels were observed. This also complicated the spectral extraction because the reduction assumes no significant shift between flats and data frames. I addressed this using a 2D image registration (Guizar-Sicairos et al. 2008) technique to determine the offset of data frame from the flat frame, using the result to correct the spectral tracing. This saved significant computation time, as otherwise each individual frame would need to be retraced.

I needed to develop a calibration routine to remove variations from purely instrumental effects. Initially, I attempted to use the temperature and pressure correction discussed in Sec. 4.2.4. However, outside the lab environment (solar observations were made from the roof of Jane Foss Russell building, University of Sydney) the temperature and pressure correction

6.1 PIMMS Visible: Solar Oscillations

proved insufficient. I was able to improve this by retrofitting the air-cooled Atik sensor with a liquid cooling system. This allowed the spectrograph enclosure temperature to reach a stable equilibrium, although the CCD heat sink was still unavoidably coupled to the outside environment. This helped reduce drifts from temperature changes, but did not eliminate them.

The ideal calibration would have been to use a simultaneous reference source. Unfortunately, the current TIGER configuration does not allow for a simultaneous calibration spectrum (and even if it did the exposure time being used for the solar observations was far too short for an effective Thorium-Argon (ThAr) spectrum). I also did not have access to an appropriate gas reference cell, such as iodine. I did however have a natural instantaneous wavelength reference already imprinted in the solar spectrum, atmospheric O₂, specifically the A-band. With this I was able correct instrumental drift from temperature changes at the CCD body and from changes in atmospheric pressure.

The precision obtainable from atmospheric lines generally depends on level of atmospheric data available (Gray and Brown 2006). However, an analysis by Figueira et al. (2012, 2010) indicates that even without correction for atmospheric phenomena (i.e. pressure, temperature, wind etc.) stabilities on the order of ~5 m/s are possible over short-time scales (one night).

Shown in Fig. 6.4 is a subset of data from an observation run on Sept. 23rd 2014. All the spectra were extracted as described in Chap. 5. I do not combine the spectra for each fibre and order, as even a small error in the wavelength solution may blur out the solar oscillations (2 m/s is equivalent to ~1 thousandth of a pixel change). The spectral shift can be done as a relative measurement, so rather than comparing to solar reference or telluric reference, I cross-correlate each spectrum with the first. In order to have a separate measurement of both solar and telluric shift, I break each spectrum into two sections. The first is composed primarily of solar features and another is dominated by the A-band.

The top panel of Fig. 6.4 contains the cross-correlation offset determined for both solar (blue) and telluric spectra features. The middle panel shows the difference between these two measurements, or the calibrated solar shifts. The final panel contains the temperature and pressure monitor's measurements from during the observation. In this subset the temperature of the spectrograph enclosure had stabilised to ±50mK, and pressure changes were fairly small (less than 1 hPa). During the observations there were 3 temperature spikes on the CCD heatsink. The exact cause remains a mystery but appears to be an error in the Atik TEC controller. However, it does provide a nice demonstration of the telluric correction.

The power spectrum of my telluric corrected shifts can be seen in Fig. 6.5. The slow variation trend is first subtracted out (shown by the fit in the first panel, and resulting in middle panel). The bottom panel shows the power spectrum of the time series shown in the middle panel. There appears to be more power around 3 mHz frequency, but it can not be considered a definitive detection of solar oscillations. The result does appear consistent with simulations, in that for RMS 8 m/s data they are not readily detectable. This result and my simulations indicate that a detector with a faster read-out time should be able to detect the solar oscillations more definitively. This will be explored in a future version of PIMMS visible, which combined with the etalon reference spectrum, discussed in Sec. 5.2, will enable far more

6.1 PIMMS Visible: Solar Oscillations

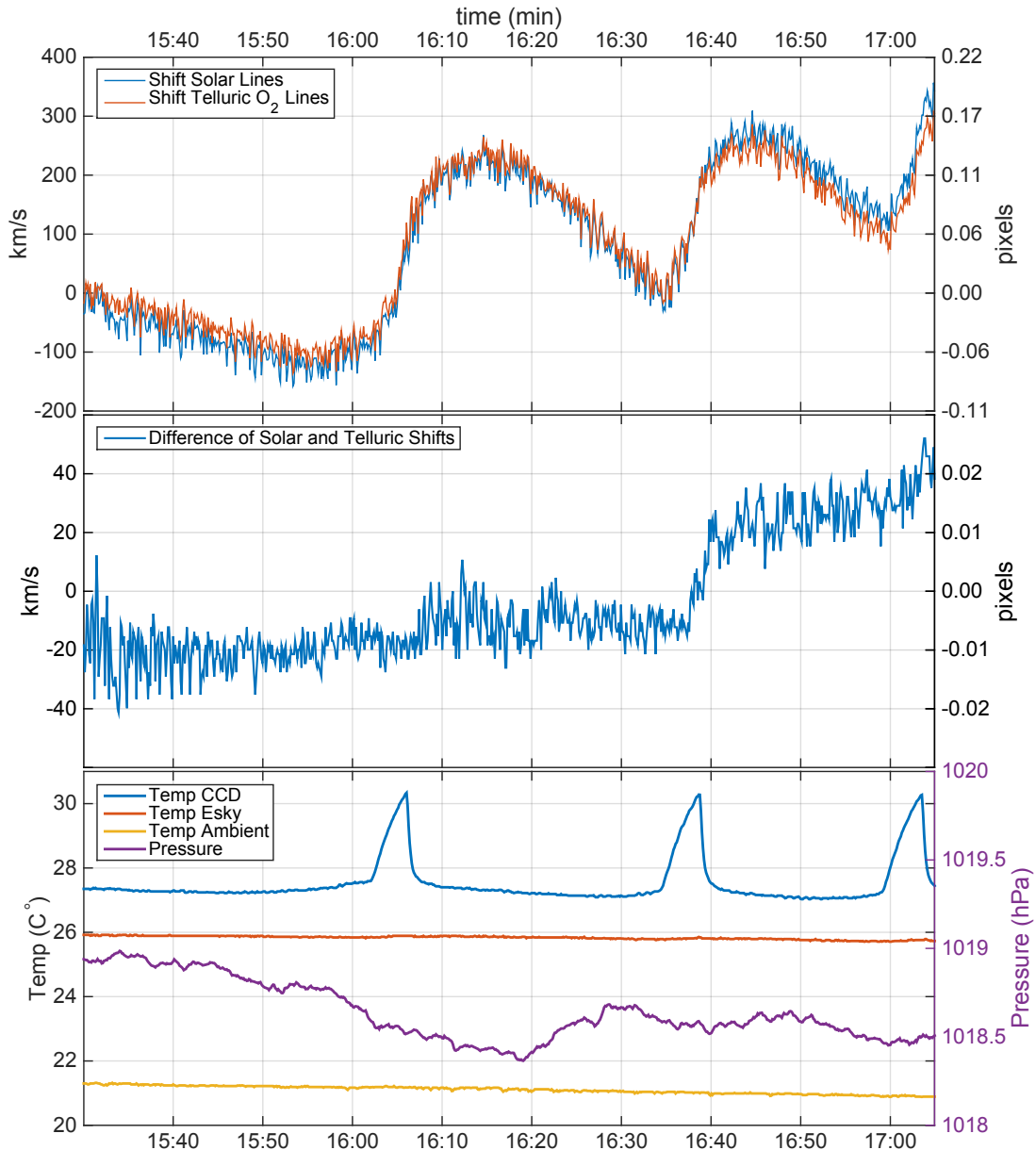


Figure 6.4: Top: 1.5hrs of relative spectral line shifts of Solar lines (blue) and O₂ A-band telluric lines (red). Middle: Solar line shifts, using the telluric shift as an instantaneous reference (i.e. solar shift minus telluric shift). Bottom: Temperature and pressure during the observation series. The temperature in the spectrograph enclosure (red) was stable to 50mK. There were three temperature spikes on the CCD heat sink (blue; caused by an error in detector TEC controller), that cause a significant shift during the observation.

6.2 PIMMS Visible: Telescope

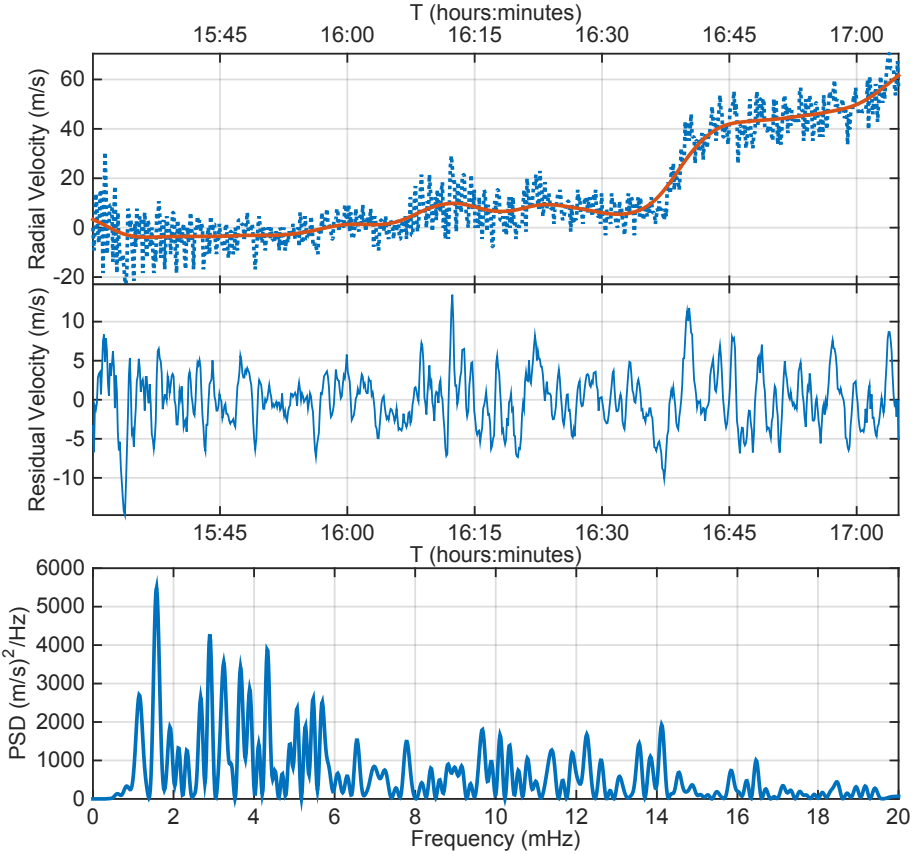


Figure 6.5: Top: Telluric corrected time-series of solar spectral line shifts. Middle panel: Slow moving variation (red fit in top panel) subtracted from corrected time series. Bottom: Power spectrum of detrended time-series. While there is more power around 3 mHz, it is not clear that this is actually due to solar oscillations. The RMS error of the detrended time series is ~ 8 m/s, which appears consistent with the telluric correction limit.

precise measurements.

6.2 PIMMS Visible: Telescope

In late April 2014 I took PIMMS échelle to the 1.2 m UK Schmidt Telescope of the Australian Astronomical Observatory (UKST) as part of preliminary testing for TAIPAN and starbugs (Kuehn et al. 2014). I had the rather straight forward goal: obtain stellar spectra with a measurable radial velocity. To that end I had two methods of coupling light from the telescope focus to the [photonic lantern \(PL\)](#). The first used a coherent fibre bundle (Goodwin et al. 2014) while the second simply placed the PL's MM input directly at the focus. In both instances of the fibres are placed in plug plate at the Schmidt telescope's prime focus and thus

6.2 PIMMS Visible: Telescope

receive an f/2.5 beam.

The coherent fibre bundles reproduces an input image at its output. Thus a guide star can be re-imaged from the focal plane of the telescope to a guider camera without additional optics in the telescope. I took an additional step of cutting a simple groove into the bundle that holds a standard multi-mode fibre (MMF) with a 50 μm core. This MMF was then coupled to the multi-mode (MM) input of the PIMMS échelle PL. This technique was particularly useful as it provided visual feedback of the location of the target star in the focal plane, allowing us to quickly position it on the ‘science fibre’. During target acquisition the collimated beam of the spectrograph was diverted to a smaller camera/CCD for use as an intensity monitor, allowing us to maximise the coupling to the PL.

Given that my previous papers/work have used the solar spectrum as a demonstration spectrum, I decided to work my way out from there, obtaining spectra of Alpha-Centauri (α -Cen). Shown in Fig. 6.6 are spectra for orders 85, 86 and 74 from a single core of the MCF slit. In each panel you can see the spectrum of α -Cen (blue), HITRAN telluric lines (red; Rothman et al. 2009), and a solar spectrum (green; Livingston and Wallace 1991), all normalised such that the continuum is at unity. In all three regions the absorption lines in the α -Cen spectra are blue shifted with respect to the solar spectrum. Note these spectra should be very similar as they are both G2V type stars. By cross-correlating the solar spectrum with the spectra of α -Cen I get an average shift of $-20.8 \pm 0.8 \text{ km/s}$ ($-0.072 \pm 0.003 \text{ nm}$; with the appropriate heliocentric correction of 10.1 km/s applied). This is consistent with the known value of -21.40 km/s¹ (Valenti and Fischer 2005). Cross-correlating with the HITRAN telluric spectrum gives an average shift of $0.006 \pm 0.8 \text{ km/s}$, confirming that the shift was not due to instrumental shifts (atmospheric lines are of course independent of the stellar spectrum). The 0.8 km/s uncertainty seems to be tied to variations in the wavelength solution between orders and fibres.

This experiment sparked the more detailed investigation of the stability of the PIMMS échelle. At the time, I had previously been operating in a domain where data, flats and Arcs were all taken in a short period of time, and thus thermal and pressure changes were not observed. In the future, I will be combining the methods of these two sections on either the UKST or a smaller telescope to observe the oscillations of α -Cen (which are similar to those of the Sun). Further, it is thought that α -Cen hosts at least one planetary body which will also be explored with the future version of PIMMS visible using the etalon reference source.

¹SIMBAD — Alpha Centauri A

6.2 PIMMS Visible: Telescope

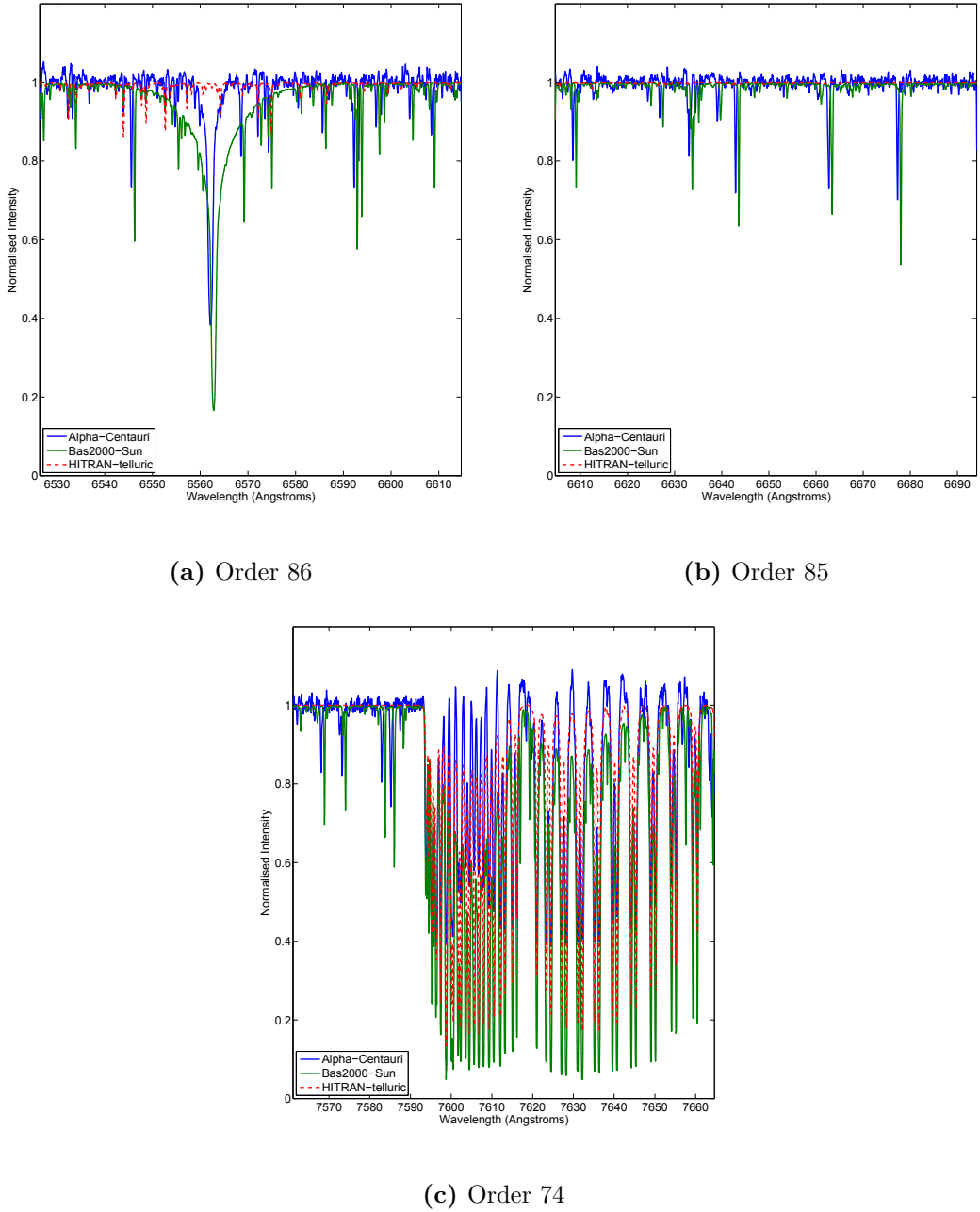


Figure 6.6: Shown in each panel: α -Cen (blue), HITRAN telluric (red; Rothman et al. 2009) and US National Solar Observatory/Kitt Peak Observatory solar spectrum (green; Livingston and Wallace 1991). *a)* Order 86 — Main feature is H-alpha. Note the continuum fit seems to have been overly aggressive, hence the narrower line in α -Cen spectrum. *b)* Order 85 — Mainly solar and stellar features. Spectra should be similar as both are G2V types stars. *c)* Primary feature is the atmospheric O₂ A-band. These lines are of course not shifted and thus provide a check for the wavelength solution.

6.3 NanoSpec: High Altitude

A key stage in the development of the i-INSPIRE satellite was a high altitude balloon test. This was the first test of the fully integrated satellite and took place in Nov. 2012. The launch of the high altitude balloon was done near Mt Barker, South Australia. Over \sim 4 hours the balloon reached 27 km, taking spectra and images every 3 minutes.

This test was done using an early version of NanoSpec (Sec. 4.3) that used the cage mount system. In order to ‘light-tight’ the spectrograph, it was given a layer of opaque black tape. NanoSpec, mounted on the payload board along with its companion imager, just before integration, can be seen in Fig. 6.7. The input used was an 8 fibre V-groove. Unfortunately only 4 fibres survived the integration process (they were broken near the V-groove). This issue was one of precipitators for the new 3D printed housing, which places less stress on the fibres.

The actual satellite was placed inside a styrofoam shell to protect at the end of the balloon journey (at peak attitude the balloon is designed to burst, and the payload then parachutes to the ground). In this casing the fibres would see very little light, so they were routed out the sides of styrofoam such that two pointed downward, and two pointed sideways.

The series of spectra taken during the flight can be seen in Fig. 6.8. Each image in the top panel shows all the spectra from each fibre (i.e. each row corresponds to a single exposure). The bottom panels show the combined spectra in green (continuum set to unity) and the reference solar spectrum in blue. The strong absorption around 750 nm is due to atmospheric O₂ (i.e. unresolved A-band). It is interesting to note that the downward facing spectra appear redder, and that the O₂ line appears stronger. These appears consistent with the fact that the light coupled through the downward facing fibre has passed through a thicker column of air than the sideward facing fibres and side facing fibres see blue sky light and clouds.

Over all the test was very successful. The satellite (and NanoSpec) were recovered undamaged, indeed the instruments were still taking data from their resting place in a wheat field. More importantly, much was learned about the instrument and several improvements in the design resulted.

6.3 NanoSpec: High Altitude

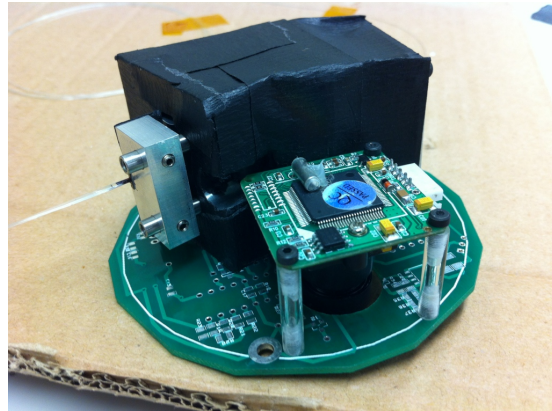


Figure 6.7: Integration Photo of NanoSpec as used for Balloon flight.

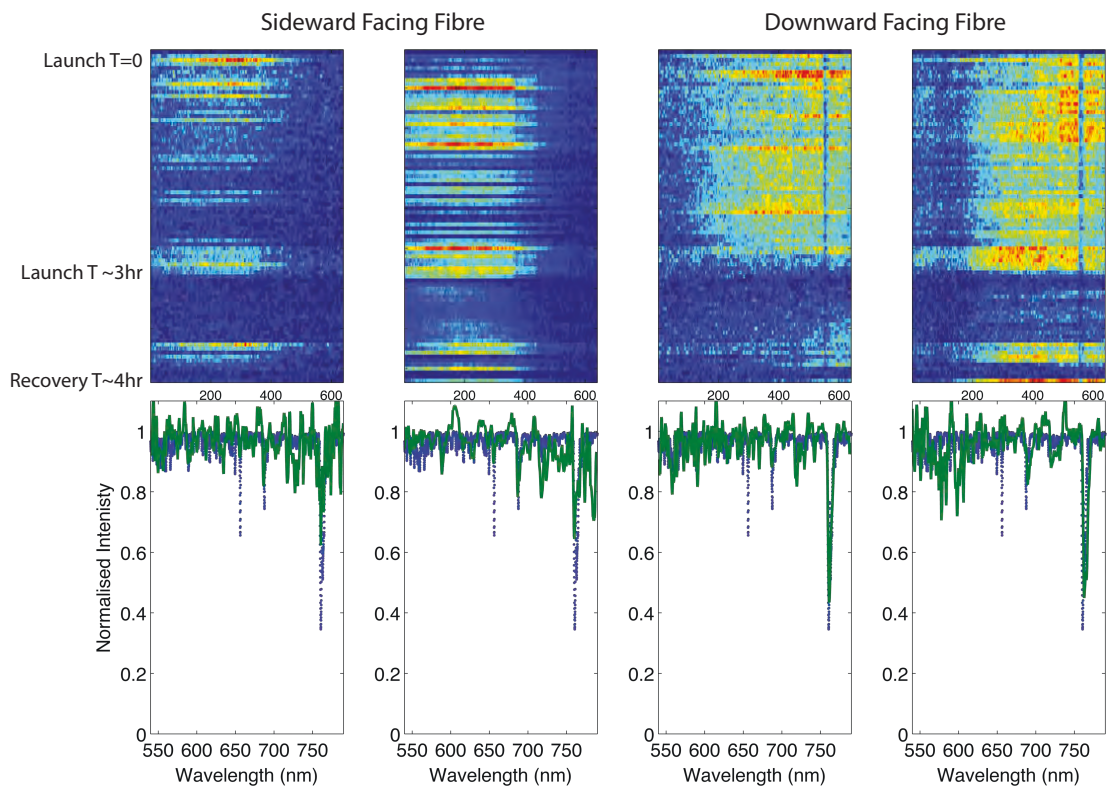


Figure 6.8: Shown are spectra from 4 fibres pointing out the of the i-INPSIRE satellite(Fogarty et al. 2012) during a high altitude balloon test (2 sideways, 2 downward). Top panel: Each row corresponds to a spectrum that was taken every ~3 minutes during flight. Bottom Panel: Shows average of each set of spectra.

7

Conclusions

Using the photonic lantern (PL) multi-mode (MM) to single-mode (SM) converter, I have demonstrated the power of the PIMMS concept. The PL allows an arbitrary input to be remapped into an array of single-mode fibres (SMFs) at the spectrograph's entrance aperture/slit, thus allowing diffraction-limited performance whilst maintaining maximal throughput (ratio of photons detected to photons collected). The spectral resolution is then truly only limited by the collimated beam size, dispersion power and, as a matter of practicality, the detector sensitivity and pixel size. This results in the most compact spectrograph possible (for a given resolving power), limited primarily by detector sampling requirements. More importantly, the spectrograph's optical design is completely decoupled from the original light source. This means that the same design could in principle be used on a 30 cm telescope, a 30 m telescope or any other source that can be coupled to a multi-mode fibre (MMF).

I have designed and built three such spectrographs:

- PIMMS IR — A single-order volume-phase holographic (VPH) dispersed spectrograph operating in the near-infrared (NIR). It demonstrated the low scattering possibilities of a SMF-fed design and pioneered the TIGER hexagonal slit input.
- PIMMS Visible — An échelle based spectrograph cross-dispersed with a VPH grating. It used the first PL formed with a 19 multi-core fibre (MCF). It was proven to be very stable (20 m/s calibrated using telluric lines).
- NanoSpec — A extremely compact moderate resolution ($\mathcal{R} \sim 2000$) spectrograph for use in a nano-satellite. It uses a unique 3D printed housing that dramatically simplifies alignment and mounting of the optics, grating and detector.

I also showed that a PIMMS style design detector requires the same area of an **MM** design, but for an **MMF** with N (dual-polarised) modes, then N **SMFs** are required. This demands at least N more pixels to appropriately sample the PIMMS spectra (in the spatial direction). For a conventional detector with square pixels, this leads to an $(N)^{1/2}$ increase in read-noise (assuming the smaller pixels have the same read-noise as the larger pixels in the **MM** case) when the final spectra are combined. This increased noise in the system could be a limitation in extremely low-level light applications. However, this is partially balanced by the decreased size of the instrument, increases in throughput over conventional designs and the trend toward lower read-noise detectors. The **point spread function (PSF)** of the **SMF** pseudo-slit also shows an additional advantage of the **PL** approach. Scattered light is significantly reduced with less than 1% of the power outside the core of the **PSF**. This could be improved further using a customised optical design rather the **commercial off-the-shelf (COTS)** components. I have shown that the photonic **PL** can faithfully reproduce the input source spectrum when combining the individual source spectra, and importantly does not appear to be affected by any wavelength dependent variation in intensity between **SMF** outputs.

7.1 Future Work

There are several projects, some underway, others planned that harness these types of spectrographs. Because my spectrographs can be so flexible these ideas are not limited to astronomical problems, indeed one of the most promising avenues of development is for the agriculture industry.

Solar Oscillations and Exoplanets With Etalon Spectrum

Currently in development is a rubidium locked version of the **Fabry-Pérot (FP)** etalon used in this thesis. This is done by scanning a tuneable laser over an etalon peak and the rubidium D₂ hyperfine absorption lines (around 780.2nm). The offset in wavelength between the two features is then used as a measure of the stability of the etalon peak (if the etalon length and/or temperature changes the peaks will move). This is used as the input to a PID¹ loop to fix the wavelength of the etalon peak using a piezo device (to adjust the length of the cavity or tension of the fibre) or a thermoelectric cooler to adjust the temperature. Using this system I will have a stable wavelength reference that can be superimposed on a source spectrum (i.e. of the sun) or fed to a secondary fibre. In either case every spectrum will now have a simultaneous absolute wavelength reference that can be used to calibrate small fluctuations in the spectrograph.

With this new reference data I plan to repeat the solar oscillation observations (which should be easily detectable now with the etalon reference). Following this, I also want to try and detect known exoplanets using a similar method. Of particular interest is the weak detection of Alpha-Centauri Bb, where I will be in a position to take a longer series of observations than most other facilities. Some other planned improvements to observations include, an improved

¹proportional-integral-derivative, a control loop feedback mechanism

7.1 Future Work

telescope interface, using the lunar reflection to help eliminate fluctuation from tracking errors (light reflected has no spatial information about Sun).

Double-pass spectrograph design

One downside of the current PIMMS visible design is that the separate collimator and camera design limited how compact it could be. In order to improve this its successor will use a double-pass design, where the primary optics of the camera and collimator are one and the same. This will allow for a much more compact design. Further, I plan to use 3D printed housing, similar to that developed with NanoSpec, to simplify assembly and alignment.

Some other improvements include using a detector purpose built with liquid cooling (FLI M830 specifically), a versatile kinematic mount for the detector that helps insulate the rest of the instruments from heat given off by the detector. The smaller instruments, and better cooling will make it easier to control temperature. It may also be possible to enclose it in a pressure vessel.

Multiplexed GMT instruments

A more long term project, is the development of an instrument (or rather a series of instruments) suitable for an extremely large telescope (ELT) like the Giant Magellan Telescope (GMT). The concept is to create **MM** to **MM** to **SM PL**, i.e. a large core **MMF** to several medium core **MMFs** that are each split into several **SMFs** or the ultimate divide and conquer **PL**. The goal here is to have a viable ‘ready to go’ instrument for first light observations, where it is conceivable that the advanced adaptive optics systems will not yet be fully optimised.

VegeBot: Raman Spectrograph

Another avenue under exploration is the development of a compact Raman spectrometer. Raman spectroscopy offers the opportunity to cheaply and rapidly detect deadly pathogenic bacteria such E. coli O157:H7, on processed lettuce and leafy vegetables, before they enter the supply chain as well as during processing, thereby protecting Australian vegetable growers from the risk of dangerous food safety outbreaks from leafy vegetables.

This is particularly important in the production of fresh produce, a major growth area of the Australian food market, that has undergone dramatic evolution in recent years. Independent farms are moving towards the vertical integration agribusiness model where companies manage the entire process “from paddock to plate.” Of increasing concern are the outbreaks of food-related illness worldwide. The independent farmer does not have the same resources as that of large producers, and the volumes processed by larger produces makes universal testing uneconomical. Nonetheless, the fresh produce industry, including domestic producers and importers, and all others engaged in the supply chain, have a responsibility to supply consumers with food that is safe. Suppliers must be able to demonstrate their adherence to food safety

7.1 Future Work

protocols. Moreover it is essential that contaminated produce can be identified and traced back to the source to prevent further outbreaks.

The project's goal is to develop a working prototype capable of detecting the presence of bacteria capable of causing food poisoning in leafy vegetables for commercial exploitation by the farming industry. This project harnesses several different aspects of the PIMMS spectrograph designs. The need for compactness is paramount, because the spectrograph will be mounted in a small autonomous farm robot under development at the Australian Centre of Field Robotics. The resolution requirements of Raman Spectrograph are between that of PIMMS visible and NanoSpec or $\mathcal{R} \sim 5000\text{-}10,000$, which corresponds to a $\sim 2\text{-}5$ mm beam with an R2 échelle grating. Further, filtering techniques enabled by the **PLs** conversion to **SM** will also allow better suppression of the Raman 'pump' laser which combined with the low scattering properties of PIMMS should allow increased sensitivity.

NanoSpec In Space

The i-INSPIRE satellite launch has been in a holding pattern for the last couple of years. The original launch partner has yet to commit to a hard timeline for launch. The next likely step will be to convert the entire satellite from the TubeSat format to a more popular CubeSat platform. The design of NanoSpec is unlikely to dramatically change, but there are few improvements that could be made. The first is to complete the implementation of a custom control board for standard CMOS sensors I started. The electrical design was completed and assembled, but the actual programming of the board has not been completed. Another goal is to source a smaller **VPH** grating (or possibly cut down the existing one). This will allow the overall size to be reduced substantially.

References

Chapter 1

- Bacon, R., M. Accardo, L. Adjali, H. Anwand, S. Bauer, I. Biswas, J. Blaizot, D. Boudon, S. Brau-Nogue, J. Brinchmann, P. Caillier, L. Capoani, C. M. Carollo, T. Contini, P. Couderc, E. Daguisé, S. Deiries, B. Delabre, S. Dreizler, J. Dubois, M. Dupieux, C. Dupuy, E. Emsellem, T. Fechner, A. Fleischmann, M. François, G. Gallou, T. Gharsa, A. Glindemann, D. Gojak, B. Guiderdoni, G. Hansali, T. Hahn, A. Jarno, A. Kelz, C. Koehler, J. Kosmalski, F. Laurent, M. Le Floch, S. J. Lilly, J.-L. Lizon, M. Loupias, A. Manescau, C. Monstein, H. Nicklas, J.-C. Olaya, L. Pares, L. Pasquini, A. Pécontal-Rousset, R. Pelló, C. Petit, E. Popow, R. Reiss, A. Remillieux, E. Renault, M. Roth, G. Rupprecht, D. Serre, J. Schaye, G. Soucail, M. Steinmetz, O. Streicher, R. Stuik, H. Valentin, J. Vernet, P. Weilbacher, L. Wisotzki, and N. Yerle (2010). “The MUSE second-generation VLT instrument”. In: *Proc. SPIE*. Vol. 7735, p. 773508. doi: [10.1117/12.856027](https://doi.org/10.1117/12.856027) (cit. on p. 2).
- Barden, S. C., J. A. Arns, W. S. Colburn, and J. B. Williams (2000). “Volume-Phase Holographic Gratings and the Efficiency of Three Simple Volume-Phase Holographic Gratings”. *PASP* 112.772, pp. 809–820. doi: [10.1086/316576](https://doi.org/10.1086/316576) (cit. on p. 7).
- Bell, R. (2012). *Introductory Fourier Transform Spectroscopy*. Elsevier Science. ISBN: 9780323152105 (cit. on p. 4).
- Berggren, Karl K., Eric A. Dauler, Andrew J. Kerman, Sae-Woo Nam, and Danna Rosenberg (2013). “Chapter 6 - Detectors Based on Superconductors”. In: *Single-Photon Generation and Detection Physics and Applications*. Ed. by Jingyun Fan Alan Migdall Sergey V. Polyakov and Joshua C. Bienfang. Vol. 45. *Experimental Methods in the Physical Sciences*. Academic Press, pp. 185–216. doi: <http://dx.doi.org/10.1016/B978-0-12-387695-9.00006-8> (cit. on p. 5).
- Bernstein, Rebecca A., Patrick J. McCarthy, Keith Raybould, Bruce C. Bigelow, Atonin H. Bouchez, José M. Filgueira, George Jacoby, Matt Johns, David Sawyer, Stephen Shectman, and Michael Sheehan (2014). “Overview and status of the Giant Magellan Telescope project”. In: *Proc. SPIE*. Vol. 9145, p. 91451C. doi: [10.1117/12.2055282](https://doi.org/10.1117/12.2055282) (cit. on p. 1).
- Bland-Hawthorn, J. (1995). “Photometry with Fabry-Perot Spectrometers”. In: *IAU Colloq. 149: Tridimensional Optical Spectroscopic Methods in Astrophysics*. Ed. by G. Comte and M. Marcellin. Vol. 71. Astronomical Society of the Pacific Conference Series, p. 72. ADS: [1995ASPC...71...72B](https://ui.adsabs.harvard.edu/abs/1995ASPC...71...72B) (cit. on pp. 4, 82).
- Bland-Hawthorn, J. and A. Horton (2006). “Instruments without optics: an integrated photonic spectrograph”. In: *Proc. SPIE*. Vol. 6269. SPIE, 62690N. doi: [10.1117/12.670931](https://doi.org/10.1117/12.670931). eprint: [astro-ph/0606290](https://arxiv.org/abs/astro-ph/0606290) (cit. on p. 1).
- Close, L. M., J. R. Males, K. B. Follette, P. Hinz, K. Morzinski, Y.-L. Wu, D. Kopon, A. Riccardi, S. Esposito, A. Puglisi, E. Pinna, M. Xompero, R. Briguglio, and F. Quiros-Pacheco (2014). “Into the blue: AO science with MagAO in the visible”. In: *Proc. SPIE*. Vol. 9148, p. 91481M. arXiv: [1407.5096 \[astro-ph.IM\]](https://arxiv.org/abs/1407.5096) (cit. on p. 2).
- Day, P. K., H. G. LeDuc, B. A. Mazin, A. Vayonakis, and J. Zmuidzinas (2003). “A broadband superconducting detector suitable for use in large arrays”. *Nature* 425, pp. 817–821. doi: [10.1038/nature02037](https://doi.org/10.1038/nature02037) (cit. on p. 5).
- Fabry, C. and A. Perot (1901). “On a New Form of Interferometer”. *ApJ* 13, p. 265. doi: [10.1086/140817](https://doi.org/10.1086/140817) (cit. on p. 3).
- Fellgett, P. B. (1951). “The multiplex advantage.” PhD thesis. University of Cambridge (cit. on p. 4).

REFERENCES

- Fried, D. L. (1966). “Optical Resolution Through a Randomly Inhomogeneous Medium for Very Long and Very Short Exposures”. *J. Opt. Soc. Am.* 56.10, pp. 1372–1379. doi: [10.1364/JOSA.56.001372](#) (cit. on p. 10).
- Hernandez, G. (1988). *Fabry-Perot Interferometers*. Cambridge Studies in Modern Optics. Cambridge University Press. ISBN: 9780521368124 (cit. on p. 4).
- Hill, Gary J (2014). “Replicated spectrographs in astronomy”. *Advanced Optical Technologies* 3.3, pp. 265–278. doi: [10.1515/aot-2014-0019](#) (cit. on p. 2).
- Hill, Gary J., Sarah E. Tuttle, Hanshin Lee, Brian L. Vattiat, Mark E. Cornell, D. L. DePoy, Niv Drory, Maximilian H. Fabricius, Andreas Kelz, J. L. Marshall, J. D. Murphy, Travis Prochaska, Richard D. Allen, Ralf Bender, Guillermo Blanc, Taylor Chonis, Gavin Dalton, Karl Gebhardt, John Good, Dionne Haynes, Thomas Jahn, Phillip J. MacQueen, M. D. Rafal, M. M. Roth, R. D. Savage, and Jan Snigula (2012). “VIRUS: production of a massively replicated 33k fiber integral field spectrograph for the upgraded Hobby-Eberly Telescope”. In: *Proc. SPIE*. Vol. 8446, 84460N. doi: [10.1117/12.925434](#) (cit. on p. 2).
- Leon-Saval, Sergio G., Alexander Argyros, and Joss Bland-Hawthorn (2013). “Photonic lanterns”. *Nanophotonics* 2.5-6. doi: [10.1515/nanoph-2013-0035](#) (cit. on pp. 2, 16, 23).
- Mayor, M. and D. Queloz (1995). “A Jupiter-mass companion to a solar-type star”. *Nature* 378, pp. 355–359. doi: [10.1038/378355a0](#) (cit. on p. 12).
- Mazin, B. A., S. R. Meeker, M. J. Strader, P. Szypryt, D. Marsden, J. C. van Eyken, G. E. Duggan, A. B. Walter, G. Ulbricht, M. Johnson, B. Bumble, K. O’Brien, and C. Stoughton (2013). “ARCONS: A 2024 Pixel Optical through Near-IR Cryogenic Imaging Spectrophotometer”. English. *PASP* 125.933, pp. 1348–1361. ISSN: 00046280 (cit. on p. 5).
- Mazin, Benjamin A., Bruce Bumble, Seth R. Meeker, Kieran O’Brien, Sean McHugh, and Eric Langman (2012). “A superconducting focal plane array for ultraviolet, optical, and near-infrared astrophysics”. *Opt. Express* 20.2, pp. 1503–1511. doi: [10.1364/OE.20.001503](#) (cit. on p. 5).
- McPherson, Alistair, Roberto Gilmozzi, Jason Spyromilio, Markus Kissler-Patig, Suzanne Ramsay, et al. (2012). “Recent progress towards the European extremely large telescope (E-ELT)”. *The Messenger* 148, pp. 1–8 (cit. on p. 1).
- Michelson, A. A. and E. W. Morley (1887). “On the relative motion of the Earth and the luminiferous ether”. *American Journal of Science* Series 3 Vol. 34.203, pp. 333–345. doi: [10.2475/ajs.s3-34.203.333](#). eprint: <http://www.ajsonline.org/content/s3-34/203/333.full.pdf+html> (cit. on p. 4).
- Rallison, Richard D., Ruth W. Rallison, and LeRoy D. Dickson (2003). “Fabrication and testing of large area VPH gratings”. In: *Proc. SPIE*. Vol. 4842. Specialized Optical Developments in Astronomy, pp. 10–21. doi: [10.1117/12.459477](#) (cit. on p. 7).
- Robertson, J. G. (2013b). “Quantifying Resolving Power in Astronomical Spectra”. *PASA* 30, e048, p. 48. doi: [10.1017/pasa.2013.26](#). arXiv: [1308.0871 \[astro-ph.IM\]](#) (cit. on pp. 10, 32).
- Steel, W.H. (1983). *Interferometry*. Cambridge Studies in Social and Emotional Development. Cambridge University Press. ISBN: 9780521253208 (cit. on p. 4).
- Stepp, Larry (2012). “Thirty Meter Telescope project update”. In: *Proc. SPIE*. Vol. 8444, 84441G. doi: [10.1117/12.928006](#) (cit. on p. 1).
- Vaughan, M. (1989). *The Fabry-Perot Interferometer: History, Theory, Practice and Applications*. Series in Optics and Optoelectronics. Taylor & Francis. ISBN: 9780852741382 (cit. on p. 4).
- Zeeuw, Tim de, Roberto Tamai, and Jochen Liske (2014). “Constructing the E-ELT”. *The Messenger* 158, pp. 3–6 (cit. on p. 1).

Chapter 2

- Ahn, C. P., R. Alexandroff, C. Allende Prieto, F. Anders, S. F. Anderson, T. Anderton, B. H. Andrews, É. Aubourg, S. Bailey, F. A. Bastien, and et al. (2014). “The Tenth Data Release of the Sloan Digital Sky Survey: First Spectroscopic Data from the SDSS-III Apache Point Observatory Galactic Evolution Experiment”. *ApJS* 211, 17, p. 17. arXiv: [1307.7735 \[astro-ph.IM\]](#) (cit. on p. 14).

REFERENCES

- Bland-Hawthorn, J., S. C. Ellis, S. G. Leon-Saval, R. Haynes, M. M. Roth, H.-G. Löhmannsröben, A. J. Horton, J.-G. Cuby, T. A. Birks, J. S. Lawrence, P. Gillingham, S. D. Ryder, and C. Trinh (2011). “A complex multi-notch astronomical filter to suppress the bright infrared sky”. *Nature Communications* 2, 581, p. 581. DOI: [10.1038/ncomms1584](https://doi.org/10.1038/ncomms1584). arXiv: [1112.1694 \[astro-ph.IM\]](https://arxiv.org/abs/1112.1694) (cit. on p. 15).
- Bland-Hawthorn, J. and P. Kern (2009). “Astrophotonics: a new era for astronomical instruments”. *Optics Express* 17.3, pp. 1880–1884. DOI: [10.1364/OE.17.001880](https://doi.org/10.1364/OE.17.001880). arXiv: [0902.0415 \[astro-ph.IM\]](https://arxiv.org/abs/0902.0415) (cit. on p. 13).
- (2012). “Molding the flow of light: photonics in astronomy”. *Physics Today* 65.5, pp. 31–37 (cit. on p. 13).
- Bland-Hawthorn, J., J. Lawrence, G. Robertson, S. Campbell, B. Pope, C. **Getters**, S. Leon-Saval, T. Birks, R. Haynes, N. Cvetojevic, and N. Jovanovic (2010). “PIMMS: photonic integrated multimode microspectrograph”. In: *Proc. SPIE*. Vol. 7735, 77350N. DOI: [10.1117/12.856347](https://doi.org/10.1117/12.856347) (cit. on pp. iv, 17, 18).
- Colless, M., G. Dalton, S. Maddox, W. Sutherland, P. Norberg, S. Cole, J. Bland-Hawthorn, T. Bridges, R. Cannon, C. Collins, W. Couch, N. Cross, K. Deeley, R. De Propris, S. P. Driver, G. Efstathiou, R. S. Ellis, C. S. Frenk, K. Glazebrook, C. Jackson, O. Lahav, I. Lewis, S. Lumsden, D. Madgwick, J. A. Peacock, B. A. Peterson, I. Price, M. Seaborne, and K. Taylor (2001). “The 2dF Galaxy Redshift Survey: spectra and redshifts”. *MNRAS* 328, pp. 1039–1063. eprint: [astro-ph/0106498](https://arxiv.org/abs/astro-ph/0106498) (cit. on p. 14).
- Cvetojevic, N., N. Jovanovic, C. **Getters**, J. S. Lawrence, S. C. Ellis, G. Robertson, and J. Bland-Hawthorn (2012a). “First starlight spectrum captured using an integrated photonic micro-spectrograph”. *A&A* 544, L1. DOI: [10.1051/0004-6361/201219116](https://doi.org/10.1051/0004-6361/201219116). arXiv: [1208.4418 \[astro-ph.IM\]](https://arxiv.org/abs/1208.4418) (cit. on pp. iii, 15, 19, 21).
- Cvetojevic, N., N. Jovanovic, J. Lawrence, M. Withford, and J. Bland-Hawthorn (2012b). “Developing arrayed waveguide grating spectrographs for multi-object astronomical spectroscopy”. *Optics Express* 20.3, p. 2062. DOI: [10.1364/OE.20.002062](https://doi.org/10.1364/OE.20.002062). arXiv: [1201.4616 \[astro-ph.IM\]](https://arxiv.org/abs/1201.4616) (cit. on pp. 19, 45).
- Cvetojevic, N., J. S. Lawrence, S. C. Ellis, J. Bland-Hawthorn, R. Haynes, and A. Horton (2009). “Characterization and on-sky demonstration of an integrated photonic spectrograph for astronomy”. *Optics Express* 17.21, pp. 18643–18650. DOI: [10.1364/OE.17.018643](https://doi.org/10.1364/OE.17.018643) (cit. on p. 15).
- Cvetojevic, Nick (2013). “Development and Implementation of the Integrated Photonic Spectrograph for Astronomy”. PhD thesis. Macquarie University (cit. on p. 19).
- Ellis, S. C., J. Bland-Hawthorn, J. S. Lawrence, J. Bryant, R. Haynes, A. Horton, S. Lee, S. Leon-Saval, Hans-Gerd Löhmannsröben, J. Mladenoff, J. O’Byrne, W. Rambold, M. Roth, and C. Trinh (2010). “GNOSIS: an OH suppression unit for near-infrared spectrographs”. In: *Ground-based and Airborne Instrumentation for Astronomy III*. Ed. by Ian S. McLean, Suzanne K. Ramsay, and Hideki Takami. Vol. 7735. Proc. SPIE. San Diego, California, USA, p. 773516. DOI: [10.1117/12.856348](https://doi.org/10.1117/12.856348) (cit. on p. 15).
- Horton, A. J. and J. Bland-Hawthorn (2007). “Coupling light into few-mode optical fibres I: The diffraction limit”. *Optics Express* 15.4, pp. 1443–1453. DOI: [10.1364/OE.15.001443](https://doi.org/10.1364/OE.15.001443) (cit. on p. 14).
- Jovanovic, Nemanja, Olivier Guyon, Frantz Martinache, Christian Schwab, and Nick Cvetojevic (2014). “How to inject light efficiently into single-mode fibers”. In: *Proc. SPIE*. Vol. 9147, 91477P. DOI: [10.1117/12.2057210](https://doi.org/10.1117/12.2057210) (cit. on p. 14).
- Jovanovic, Nemanja, Peter G. Tuthill, Barnaby Norris, Simon Gross, Paul Stewart, Ned Charles, Sylvestre Lacour, Jon Lawrence, Gordon Robertson, Alexander Fuerbach, and Michael J. Withford (2012). “Progress and challenges with the Dragonfly instrument; an integrated photonic pupil-remapping interferometer”. In: *Proc. SPIE*. Vol. 8445, p. 844505 (cit. on pp. 16, 21).
- Leon-Saval, S. G., A. Argyros, and J. Bland-Hawthorn (2010). “Photonic lanterns: a study of light propagation in multimode to single-mode converters”. *Optics Express* 18, p. 8430. DOI: [10.1364/OE.18.008430](https://doi.org/10.1364/OE.18.008430) (cit. on p. 16).
- Leon-Saval, S. G., T. A. Birks, J. Bland-Hawthorn, and M. Englund (2005). “Multimode fiber devices with single-mode performance”. *Optics Letters* 30.19, pp. 2545–2547. DOI: [10.1364/OL.30.002545](https://doi.org/10.1364/OL.30.002545) (cit. on p. 16).
- Leon-Saval, Sergio G., Alexander Argyros, and Joss Bland-Hawthorn (2013). “Photonic lanterns”. *Nanophotonics* 2.5–6. DOI: [10.1515/nanoph-2013-0035](https://doi.org/10.1515/nanoph-2013-0035) (cit. on pp. 2, 16, 23).
- Noordgraaf, D., P. M. W. Skovgaard, R. H. Sandberg, M. D. Maack, J. Bland-Hawthorn, J. S. Lawrence, and J. Lægsgaard (2012). “Nineteen-port photonic lantern with multimode delivery fiber”. *Optics Letters* 37, p. 452. DOI: [10.1364/OL.37.000452](https://doi.org/10.1364/OL.37.000452) (cit. on p. 16).

REFERENCES

- Schwab, C., S. G. Leon-Saval, C. H. **Butters**, J. Bland-Hawthorn, and S. Mahadevan (2012). “Single mode, extreme precision Doppler spectrographs”. In: *Proceedings of the 2012 IAU GA*. arXiv: [1212.4867 \[astro-ph.IM\]](#) (cit. on pp. [iv](#), [14](#)).
- Shaklan, S. and F. Roddier (1988). “Coupling starlight into single-mode fiber optics”. *Appl. Opt.* 27.11, pp. 2334–2338. doi: [10.1364/AO.27.002334](#) (cit. on p. [14](#)).
- Snyder, A.W. and J. Love (1983). *Optical Waveguide Theory*. Science paperbacks. Springer. ISBN: 9780412099502 (cit. on p. [16](#)).
- Spaleniak, I., N. Jovanovic, S. Gross, M. J. Ireland, J. S. Lawrence, and M. J. Withford (2013). “Integrated photonic building blocks for next-generation astronomical instrumentation II: the multimode to single mode transition”. *Optics Express* 21.22, p. 27197. doi: [10.1364/OE.21.027197](#). arXiv: [1311.0578 \[astro-ph.IM\]](#) (cit. on p. [16](#)).
- Thomson, R., T. Birks, S. Leon-Saval, A. Kar, and J. Bland-Hawthorn (2011). “Ultrafast laser inscription of an integrated photonic lantern”. *Optics Express* 19.6, pp. 5698–5705. doi: [10.1364/OE.19.005698](#) (cit. on p. [16](#)).
- Trinh, C. Q., S. C. Ellis, J. Bland-Hawthorn, J. S. Lawrence, A. J. Horton, S. G. Leon-Saval, K. Shortridge, J. Bryant, S. Case, M. Colless, W. Couch, K. Freeman, H.-G. Löhmannsröben, L. Gers, K. Glazebrook, R. Haynes, S. Lee, J. O’Byrne, S. Miziarski, M. M. Roth, B. Schmidt, C. G. Tinney, and J. Zheng (2013). “GNOSIS: The First Instrument to Use Fiber Bragg Gratings for OH Suppression”. *AJ* 145.2, 51, p. 51. doi: [10.1088/0004-6256/145/2/51](#). arXiv: [1212.1201 \[astro-ph.IM\]](#) (cit. on pp. [15](#), [21](#)).

Chapter 3

- Bacon, R., Y. Copin, G. Monnet, B. W. Miller, J. R. Allington-Smith, M. Bureau, C. M. Carollo, R. L. Davies, E. Emsellem, H. Kuntschner, R. F. Peletier, E. K. Verolme, and P. T. de Zeeuw (2001). “The SAURON project - I. The panoramic integral-field spectrograph”. *MNRAS* 326, pp. 23–35. eprint: [astro-ph/0103451](#) (cit. on pp. [22](#), [23](#)).
- Bacon, Roland, G. Adam, A. Baranne, G. Courtes, D. Dubet, J. P. Dubois, E. Emsellem, P. Ferruit, Y. Georgelin, G. Monnet, E Pécontal, A. Rousset, and F. Say (1995). “3D spectrography at high spatial resolution. I. Concept and realization of the integral field spectrograph TIGER.” *Astronomy and Astrophysics Supplement Series* 113, p. 347 (cit. on p. [22](#)).
- Belland, P. and J. P. Creen (1982). “Changes in the characteristics of a Gaussian beam weakly diffracted by a circular aperture”. *Appl. Opt.* 21.3, pp. 522–527. doi: [10.1364/AO.21.0000522](#) (cit. on p. [29](#)).
- Butters, C. H., S. G. Leon-Saval, J. G. Robertson, and J. Bland-Hawthorn (2013). “Beating the classical limit: A diffraction-limited spectrograph for an arbitrary input beam”. *Optics Express* 21.22, p. 26103. doi: [10.1364/OE.21.026103](#). arXiv: [1310.4833 \[astro-ph.IM\]](#) (cit. on p. [31](#)).
- Cvetojevic, N., N. Jovanovic, C. **Butters**, J. S. Lawrence, S. C. Ellis, G. Robertson, and J. Bland-Hawthorn (2012a). “First starlight spectrum captured using an integrated photonic micro-spectrograph”. *A&A* 544, L1. doi: [10.1051/0004-6361/201219116](#). arXiv: [1208.4418 \[astro-ph.IM\]](#) (cit. on pp. [iii](#), [15](#), [19](#), [21](#)).
- Fontaine, Nicolas K., Roland Ryf, Joss Bland-Hawthorn, and Sergio G. Leon-Saval (2012). “Geometric requirements for photonic lanterns in space division multiplexing”. *Opt. Express* 20.24, pp. 27123–27132 (cit. on p. [23](#)).
- Jovanovic, Nemanja, Peter G. Tuthill, Barnaby Norris, Simon Gross, Paul Stewart, Ned Charles, Sylvestre Lacour, Jon Lawrence, Gordon Robertson, Alexander Fuerbach, and Michael J. Withford (2012). “Progress and challenges with the Dragonfly instrument; an integrated photonic pupil-remapping interferometer”. In: *Proc. SPIE*. Vol. 8445, p. 844505 (cit. on pp. [16](#), [21](#)).
- Leon-Saval, S. G., C. H. **Butters**, and J. Bland-Hawthorn (2012). “The Photonic TIGER: a multicore fiber-fed spectrograph”. In: *Proc. SPIE*. Vol. 8450. The Univ. of Sydney (Australia), 84501K. doi: [10.1117/12.925254](#). arXiv: [1208.3006 \[astro-ph.IM\]](#) (cit. on pp. [iv](#), [22](#), [23](#)).
- Leon-Saval, Sergio G., Alexander Argyros, and Joss Bland-Hawthorn (2013). “Photonic lanterns”. *Nanophotonics* 2.5-6. doi: [10.1515/nanoph-2013-0035](#) (cit. on pp. [2](#), [16](#), [23](#)).

REFERENCES

- OzOptics (2013). http://www.ozoptics.com/ALLNEW_PDF/DTS0083.pdf. V-GROOVE ASSEMBLIES (cit. on p. 22).
- Robertson, Gordon (2013a). “Detector area for PIMMS IR”. Internal Memo (cit. on p. 31).
- Robertson, J. G. (2013b). “Quantifying Resolving Power in Astronomical Spectra”. PASA 30, e048, p. 48. doi: [10.1017/pasa.2013.26](https://doi.org/10.1017/pasa.2013.26). arXiv: [1308.0871 \[astro-ph.IM\]](https://arxiv.org/abs/1308.0871) (cit. on pp. 10, 32).
- Thomson, R. R., R. J. Harris, T. A. Birks, G. Brown, J. Allington-Smith, and J. Bland-Hawthorn (2012). “Ultrafast laser inscription of a 121-waveguide fan-out for astrophotonics”. *Optics Letters* 37.12, p. 2331. doi: [10.1364/OL.37.002331](https://doi.org/10.1364/OL.37.002331). arXiv: [1203.4584 \[physics.optics\]](https://arxiv.org/abs/1203.4584) (cit. on p. 21).
- Trinh, C. Q., S. C. Ellis, J. Bland-Hawthorn, J. S. Lawrence, A. J. Horton, S. G. Leon-Saval, K. Shortridge, J. Bryant, S. Case, M. Colless, W. Couch, K. Freeman, H.-G. Löhmannsröben, L. Gers, K. Glazebrook, R. Haynes, S. Lee, J. O’Byrne, S. Miziarski, M. M. Roth, B. Schmidt, C. G. Tinney, and J. Zheng (2013). “GNOSIS: The First Instrument to Use Fiber Bragg Gratings for OH Suppression”. AJ 145.2, 51, p. 51. doi: [10.1088/0004-6256/145/2/51](https://doi.org/10.1088/0004-6256/145/2/51). arXiv: [1212.1201 \[astro-ph.IM\]](https://arxiv.org/abs/1212.1201) (cit. on pp. 15, 21).

Chapter 4

- Abraham, J., M. Aglietta, I.C. Aguirre, M. Albrow, D. Allard, I. Allekotte, P. Allison, J. Alvarez Muaiz, M.G. do Amaral, M. Ambrosio, L. Anchordoqui, and R. Andrews (2004). “Properties and performance of the prototype instrument for the Pierre Auger Observatory”. *Nuclear Instruments and Methods in Physics Research Section A: Accelerators, Spectrometers, Detectors and Associated Equipment* 523, pp. 50–95. ISSN: 0168-9002. doi: [10.1016/j.nima.2003.12.012](https://doi.org/10.1016/j.nima.2003.12.012) (cit. on p. 65).
- Badhwar, Gautam D (1997). “The radiation environment in low-Earth orbit”. *Radiation research* 148, S3–S10 (cit. on p. 65).
- Betters, C, I H Cairns, J Bland-Hawthorn, X Wu, L Fogarty, J Funamoto, S G Leon-Saval, A Monger, and S Z A Xiao (2011). “Instrumentation of the i-INSPIRE satellite.” In: *Proceeding of the 11th Australian Space Science Conference*. Ed. by Wayne Short and Iver Cairns. National Space Society of Australia Ltd, Sydney, Australia, pp. 257–266. ISBN: 978-0-9775740-5-6 (cit. on p. 65).
- Birks, T. A., B. J. Mangan, A. Díez, J. L. Cruz, and D. F. Murphy (2012). ““Photonic lantern” spectral filters in multi-core Fiber”. *Optics Express* 20.13, p. 13996. doi: [10.1364/OE.20.013996](https://doi.org/10.1364/OE.20.013996) (cit. on p. 51).
- Birks, Timothy A, Brian J. Mangan, A. Diez, J. L. Cruz, S G Leon-Saval, Joss Bland-Hawthorn, and D. F. Murphy (2011). “Multicore optical fibres for astrophotonics”. doi: [10.1109/CLEOE.2011.5943675](https://doi.org/10.1109/CLEOE.2011.5943675) (cit. on p. 51).
- Cvetojevic, N., N. Jovanovic, J. Lawrence, M. Withford, and J. Bland-Hawthorn (2012b). “Developing arrayed waveguide grating spectrographs for multi-object astronomical spectroscopy”. *Optics Express* 20.3, p. 2062. doi: [10.1364/OE.20.002062](https://doi.org/10.1364/OE.20.002062). arXiv: [1201.4616 \[astro-ph.IM\]](https://arxiv.org/abs/1201.4616) (cit. on pp. 19, 45).
- Fogarty, L. M. R., S. Z. (. Xiao, J. Funamoto, I. H. Cairns, J. Bland-Hawthorn, X. Wu, C. H. **Betters**, S. G. Leon-Saval, and A. G. Monger (2012). “The i-INSPIRE satellite: a university pico-satellite project”. In: *Proc. SPIE*. Vol. 8442, 84421B. doi: [10.1117/12.925709](https://doi.org/10.1117/12.925709) (cit. on pp. iv, 63, 97).
- Fogarty, Lisa, Iver H Cairns, Joss Bland-Hawthorn, Xiaofeng Wu, Christopher H **Betters**, Jiro Funamoto, S G Leon-Saval, Tony Monger, and Size Xiao (2011). “The initial-INtegrated SPectrograph, Imager and Radiation Explorer (i-INSPIRE) - a university satellite project.” In: *Proceeding of the 11th Australian Space Science Conference*. Ed. by Wayne Short and Iver Cairns. National Space Society of Australia Ltd, Sydney, Australia, pp. 249–256. ISBN: 978-0-9775740-5-6 (cit. on pp. iii, 63).
- Fukuda, Y., T. Hayakawa, E. Ichihara, K. Inoue, K. Ishihara, H. Ishino, Y. Itow, T. Kajita, J. Kameda, S. Kasuga, K. Kobayashi, and Y. Kobayashi (1998). “Measurement of a small atmospheric ν_μ/ν_e ratio”. *Physics Letters B* 433, pp. 9–18. ISSN: 0370-2693. doi: [10.1016/S0370-2693\(98\)00476-6](https://doi.org/10.1016/S0370-2693(98)00476-6) (cit. on p. 65).
- Guizar-Sicairos, Manuel, Samuel T. Thurman, and James R. Fienup (2008). “Efficient subpixel image registration algorithms”. *Opt. Lett.* 33.2, pp. 156–158 (cit. on pp. 60, 90).
- Halverson, Samuel, Suvrath Mahadevan, Lawrence Ramsey, Fred Hearty, John Wilson, Jon Holtzman, Stephen Redman, Gillian Nave, David Nidever, Matt Nelson, Nick Venditti, Dmitry Bizyaev, and Scott Fleming (2014). “Development of Fiber Fabry-Perot Interferometers as Stable Near-infrared Calibration Sources for

REFERENCES

- High Resolution Spectrographs". *Publications of the Astronomical Society of the Pacific* 126.939, pp. 445–458. DOI: [10.1086/676649](https://doi.org/10.1086/676649) (cit. on pp. 60, 82).
- Heynderickx, D., B. Quaghebeur, J. Wera, E. J. Daly, and H. D. R. Evans (2004). "New radiation environment and effects models in the European Space Agency's Space Environment Information System (SPENVIS)". *Space Weather* 2, S10S03, p. 10. DOI: [10.1029/2004SW000073](https://doi.org/10.1029/2004SW000073) (cit. on p. 65).
- ISO Standard 11146 (2005). "Lasers and laser-related equipment – Test methods for laser beam widths, divergence angles and beam propagation ratios" (cit. on pp. 41, 43).
- Lambert, J., Y. Yin, D. R. McKenzie, S. Law, and N. Suchowerska (2009). "Cerenkov light spectrum in an optical fiber exposed to a photon or electron radiation therapy beam". *Appl. Opt.* 48.18, p. 3362. DOI: [10.1364/AO.48.003362](https://doi.org/10.1364/AO.48.003362) (cit. on p. 66).
- Law, S. H., S. C. Fleming, N. Suchowerska, and D. R. McKenzie (2006). "Optical fiber design and the trapping of Cerenkov radiation". *Appl. Opt.* 45.36, pp. 9151–9159. DOI: [10.1364/AO.45.009151](https://doi.org/10.1364/AO.45.009151) (cit. on p. 66).
- Law, S. H., N. Suchowerska, D. R. McKenzie, S. C. Fleming, and T. Lin (2007). "Transmission of Čerenkov radiation in optical fibers". *Optics Letters* 32.10, pp. 1205–1207. DOI: [10.1364/OL.32.001205](https://doi.org/10.1364/OL.32.001205) (cit. on p. 66).
- Livingston, W and L Wallace (1991). *An atlas of the solar spectrum in the infrared from 1850 to 9000 cm⁻¹ (1.1 to 5.4 micrometer)*. NSO Technical Report, Tucson: National Solar Observatory, National Optical Astronomy Observatory, 1991 (cit. on pp. 48, 49, 94, 95).
- Olaya, J.-C., S. G. Leon-Saval, D. Schirdewahn, K. Ehrlich, D. M. Haynes, and R. Haynes (2012). "1:61 photonic lanterns for astrophotometry: a performance study". *MNRAS* 427.2, pp. 1194–1208. DOI: [10.1111/j.1365-2966.2012.22043.x](https://doi.org/10.1111/j.1365-2966.2012.22043.x) (cit. on pp. 45, 48).
- Probst, R A, L Wang, H-P Doerr, T Steinmetz, T J Kentischer, G Zhao, T W Hänsch, Th Udem, R Holzwarth, and W Schmidt (2015). "Comb-calibrated solar spectroscopy through a multiplexed single-mode fiber channel". *New Journal of Physics* 17.2, p. 023048 (cit. on p. 60).
- Robertson, Gordon and Joss Bland-Hawthorn (2012). "Compact high-resolution spectrographs for large and extremely large telescopes: using the diffraction limit". In: *Ground-based and Airborne Instrumentation for Astronomy IV*. Vol. 8446. Proc. SPIE, p. 844674. DOI: [10.1117/12.924937](https://doi.org/10.1117/12.924937). arXiv: [1208.4667](https://arxiv.org/abs/1208.4667) (cit. on p. 54).
- Rothman, L. S., I. E. Gordon, A. Barbe, D. C. Benner, P. F. Bernath, M. Birk, V. Boudon, L. R. Brown, A. Campargue, J.-P. Champion, K. Chance, L. H. Coudert, V. Dana, V. M. Devi, S. Fally, J.-M. Flaud, R. R. Gamache, A. Goldman, D. Jacquemart, I. Kleiner, N. Lacome, W. J. Lafferty, J.-Y. Mandin, S. T. Massie, S. N. Mikhailenko, C. E. Miller, N. Moazzen-Ahmadi, O. V. Naumenko, A. V. Nikitin, J. Orphal, V. I. Perevalov, A. Perrin, A. Predoi-Cross, C. P. Rinsland, M. Rotger, M. Šimečková, M. A. H. Smith, K. Sung, S. A. Tashkun, J. Tennyson, R. A. Toth, A. C. Vandaele, and J. Vander Auwera (2009). "The HITRAN 2008 molecular spectroscopic database". *Journal of Quantitative Spectroscopy and Radiative Transfer* 110, pp. 533–572 (cit. on pp. 48, 49, 94, 95).
- Saunders, W., T. Bridges, P. Gillingham, R. Haynes, G. A. Smith, J. D. Whittard, V. Churilov, A. Lankshear, S. Croom, D. Jones, and C. Boshuizen (2004). "AAOmega: a scientific and optical overview". In: *Ground-based Instrumentation for Astronomy*. Ed. by A. F. M. Moorwood and M. Iye. Vol. 5492. Anglo-Australian Observatory, Australia, pp. 389–400. DOI: [10.1117/12.550871](https://doi.org/10.1117/12.550871) (cit. on p. 42).
- Siegman, A.E. (1986). *Lasers*. 663–679: University Science Books. ISBN: 9780935702118 (cit. on pp. 41, 43).
- Tinney, C. G., S. D. Ryder, S. C. Ellis, V. Churilov, J. Dawson, G. A. Smith, L. Waller, J. D. Whittard, R. Haynes, A. Lankshear, J. R. Barton, C. J. Evans, K. Shortridge, T. Farrell, and J. Bailey (2004). "IRIS2: a working infrared multi-object spectrograph and camera". In: *Ground-based Instrumentation for Astronomy*. Ed. by A. F. M. Moorwood and M. Iye. Vol. 5492. Anglo-Australian Observatory, Australia, pp. 998–1009. DOI: [10.1117/12.550980](https://doi.org/10.1117/12.550980) (cit. on p. 42).
- Xiao, Size, Xiaofeng Wu, Iver H Cairns, Joss Bland-Hawthorn, Christopher H **Butters**, Jiro Funamoto, S G Leon-Saval, Lisa Fogarty, Tony Monger, and Xueliang Bai (2011). "i-INSPIRE Tube-Satellite Bus Design". In: *Proceeding of the 11th Australian Space Science Conference*. Ed. by Wayne Short and Iver Cairns. National Space Society of Australia Ltd, Sydney, Australia, pp. 267–274. ISBN: 978-0-9775740-5-6 (cit. on pp. iv, 63).

Chapter 5

- Bland-Hawthorn, J. (1995). "Photometry with Fabry-Perot Spectrometers". In: *IAU Colloq. 149: Tridimensional Optical Spectroscopic Methods in Astrophysics*. Ed. by G. Comte and M. Marcellin. Vol. 71. Astronomical Society of the Pacific Conference Series, p. 72. ADS: [1995ASPC...71...72B](#) (cit. on pp. 4, 82).
- Bolton, A. S. and D. J. Schlegel (2010). "Spectro-Perfectionism: An Algorithmic Framework for Photon Noise-Limited Extraction of Optical Fiber Spectroscopy". *PASP* 122, pp. 248–257. doi: [10.1086/651008](#). arXiv: [0911.2689 \[astro-ph.IM\]](#) (cit. on p. 83).
- Halverson, Samuel, Suvrath Mahadevan, Lawrence Ramsey, Fred Hearty, John Wilson, Jon Holtzman, Stephen Redman, Gillian Nave, David Nidever, Matt Nelson, Nick Venditti, Dmitry Bizyaev, and Scott Fleming (2014). "Development of Fiber Fabry-Perot Interferometers as Stable Near-infrared Calibration Sources for High Resolution Spectrographs". *Publications of the Astronomical Society of the Pacific* 126.939, pp. 445–458. doi: [10.1086/676649](#) (cit. on pp. 60, 82).
- Heijmans, Jeroen, Martin Asplund, Sam Barden, Michael Birchall, Daniela Carollo, Joss Bland-Hawthorn, Jurek Brzeski, Scott Case, Vladimir Churilov, Matthew Colless, Robert Dean, Gayandhi De Silva, Tony Farrell, Kristin Fiegert, Kenneth Freeman, Luke Gers, Michael Goodwin, Doug Gray, Ron Heald, Anthony Heng, Damien Jones, Chiaki Kobayashi, Urs Klauser, Yuriy Kondrat, Jon Lawrence, Steve Lee, Darren Mathews, Don Mayfield, Stan Miziarski, Guy J. Monnet, Rolf Muller, Naveen Pai, Robert Patterson, Ed Penny, David Orr, Andrew Sheininis, Keith Shortridge, Scott Smedley, Greg Smith, Darren Stafford, Nicholas Staszak, Minh Vuong, Lewis Waller, Denis Whittard, Elisabeth Wylie de Boer, Pascal Xavier, Jessica Zheng, Ross Zhelem, and Daniel Zucker (2012). "Integrating the HERMES spectrograph for the AAT". In: *Proc. SPIE*. Vol. 8446, 84460W. doi: [10.1117/12.925806](#) (cit. on p. 83).
- Murphy, M. T., P. Tzanavaris, J. K. Webb, and C. Lovis (2007). "Selection of ThAr lines for wavelength calibration of echelle spectra and implications for variations in the fine-structure constant". *MNRAS* 378, pp. 221–230. doi: [10.1111/j.1365-2966.2007.11768.x](#). arXiv: [astro-ph/0703623 \[astro-ph.IM\]](#) (cit. on p. 80).
- Sharp, R. and M. N. Birchall (2010). "Optimal Extraction of Fibre Optic Spectroscopy". *PASA* 27.1, pp. 91–103. doi: [10.1071/AS08001](#). arXiv: [0912.0558 \[astro-ph.IM\]](#) (cit. on p. 75).
- Tody, Doug (1986). "The Iraf Data Reduction And Analysis System". In: *Proc. SPIE*. Vol. 0627, pp. 733–748. doi: [10.1117/12.968154](#) (cit. on p. 80).
- Willmarth, D. (1987). *A CCD Atlas of Comparison Spectra: Thorium-argon Hollow Cathode 3180 Å [Angstroms] - 9540 Å [Angstroms]*. Kitt Peak National Observatory (cit. on p. 80).

Chapter 6

- Davies, G. R., W. J. Chaplin, Y. Elsworth, and S. J. Hale (2014). "BiSON data preparation: a correction for differential extinction and the weighted averaging of contemporaneous data". *Monthly Notices of the Royal Astronomical Society* 441.4, pp. 3009–3017. eprint: <http://mnras.oxfordjournals.org/content/441/4/3009.full.pdf+html> (cit. on p. 88).
- Figueira, P., F. Kerber, A. Chacon, C. Lovis, N. C. Santos, G. Lo Curto, M. Sarazin, and F. Pepe (2012). "Comparing radial velocities of atmospheric lines with radiosonde measurements". *MNRAS* 420, pp. 2874–2883. arXiv: [1110.3820 \[astro-ph.IM\]](#) (cit. on p. 91).
- Figueira, P., F. Pepe, C. Lovis, and M. Mayor (2010). "Evaluating the stability of atmospheric lines with HARPS*". *A&A* 515, A106. doi: [10.1051/0004-6361/201014005](#) (cit. on p. 91).
- Fogarty, L. M. R., S. Z. (Xiao, J. Funamoto, I. H. Cairns, J. Bland-Hawthorn, X. Wu, C. H. **Butters**, S. G. Leon-Saval, and A. G. Monger (2012). "The i-INSPIRE satellite: a university pico-satellite project". In: *Proc. SPIE*. Vol. 8442, 84421B. doi: [10.1117/12.925709](#) (cit. on pp. iv, 63, 97).
- Goodwin, Michael, Samuel Richards, Jessica Zheng, Jon Lawrence, Sergio Leon-Saval, Alexander Argyros, and Belen Alcalde (2014). "Miniaturized Shack-Hartmann wavefront sensors for starbugs". In: *Proc. SPIE*. Vol. 9151, 91514T (cit. on p. 93).

REFERENCES

- Gray, D. F. and K. I. T. Brown (2006). "Precise Spectroscopic Radial Velocity Measurements Using Telluric Lines". PASP 118, pp. 399–404 (cit. on p. 91).
- Guizar-Sicairos, Manuel, Samuel T. Thurman, and James R. Fienup (2008). "Efficient subpixel image registration algorithms". *Opt. Lett.* 33.2, pp. 156–158 (cit. on pp. 60, 90).
- Kuehn, Kyler, Jon Lawrence, David M. Brown, Scott Case, Matthew Colless, Robert Content, Luke Gers, James Gilbert, Michael Goodwin, Andrew M. Hopkins, Michael Ireland, Nuria P. F. Lorente, Rolf Muller, Vijay Nichani, Azizi Rakman, Samuel N. Richards, Will Saunders, Nick F. Staszak, Julia Tims, and Lewis G. Waller (2014). "TAIPAN: optical spectroscopy with StarBugs". In: *Proc. SPIE*. Vol. 9147, p. 914710 (cit. on p. 93).
- Livingston, W and L Wallace (1991). *An atlas of the solar spectrum in the infrared from 1850 to 9000 cm⁻¹ (1.1 to 5.4 micrometer)*. NSO Technical Report, Tucson: National Solar Observatory, National Optical Astronomy Observatory, 1991 (cit. on pp. 48, 49, 94, 95).
- Rothman, L. S., I. E. Gordon, A. Barbe, D. C. Benner, P. F. Bernath, M. Birk, V. Boudon, L. R. Brown, A. Campargue, J.-P. Champion, K. Chance, L. H. Coudert, V. Dana, V. M. Devi, S. Fally, J.-M. Flaud, R. R. Gamache, A. Goldman, D. Jacquemart, I. Kleiner, N. Lacome, W. J. Lafferty, J.-Y. Mandin, S. T. Massie, S. N. Mikhailenko, C. E. Miller, N. Moazzen-Ahmadi, O. V. Naumenko, A. V. Nikitin, J. Orphal, V. I. Perevalov, A. Perrin, A. Predoi-Cross, C. P. Rinsland, M. Rotger, M. Šimečková, M. A. H. Smith, K. Sung, S. A. Tashkun, J. Tennyson, R. A. Toth, A. C. Vandaele, and J. Vander Auwera (2009). "The HITRAN 2008 molecular spectroscopic database". *Journal of Quantitative Spectroscopy and Radiative Transfer* 110, pp. 533–572 (cit. on pp. 48, 49, 94, 95).
- Valenti, J. A. and D. A. Fischer (2005). "Spectroscopic Properties of Cool Stars (SPOCS). I. 1040 F, G, and K Dwarfs from Keck, Lick, and AAT Planet Search Programs". ApJS 159, pp. 141–166 (cit. on p. 94).

Acronyms and Definitions

Symbols

étendue ($A\Omega$) geometric characterisation of an optical systems ability to accept light. Defined as product of area and solid angle of acceptance.

A

ADU analogue-to-digital units.

AO adaptive optics.

AR anti-reflective.

AWG arrayed waveguide grating; a device with a series single mode waveguides where each waveguide has increases in length by a fixed phase offset, producing a high order diffraction/dispersion.

C

COTS commercial off-the-shelf.

D

DFT direct Fourier transfrom.

E

EFL effective focal length.

F

FFT fast Fourier transfrom.

focal ratio ($f/\#$) ratio of focal length and aperture/pupil diameter, defined as $f/\# = F/D$.

FP Fabry-Pérot.

FSR free spectral range.

FT Fourier transform.

FTS Fourier transform spectrometer.

FWHM full width half maximum.

I

IFU integral field unit.

IPS integrated photonic spectrograph; spectrograph composed of integrated photonics technologies, i.e. **ultrafast laser inscription (ULI)** photonics lantern fused to **arrayed waveguide grating (AWG)**.

L

LEO low earth orbit is considered to be between 160 km to 2000 km.

M

MCF multi-core fibre.

MFD diameter of the intensity profile of light at the out put of fibre. Normally measured at the width at the $1/e^2$ intensity level.

MM multi-mode.

MMF multi-mode fibre.

MOS multi-object spectrograph.

N

NA numerical aperture.

Acronyms and Definitions

NIR light with wavelength $0.7 \mu\text{m}$ to $1 \mu\text{m}$, or edge of human vision to the silicon sensitivity cutoff.

P

PCB printed circuit board.

PCF photonic crystal fibre.

PIMMS photonic integrated multi-mode spectrograph.

PIMMS#0 Hybrid (photonic and bulk optic) version of PIMMS.

PIMMS#1 Fully photonic version of PIMMS.

PL photonic lantern; a multi-mode to single-mode converter.

POP physical optics propagation.

PSF point spread function.

PTV peak to valley.

R

resolving power (\mathcal{R}) quantitative measure of a spectrographs ability to resolve neighbouring spectral features. Defined as $\mathcal{R} = \lambda/\Delta\lambda$.

RMS root mean square.

S

seeing the blurring of a telescope image due to atmospheric turbulence and varying the optical refractive index.

SM single-mode.

SMF single-mode fibre.

SNR single-to-noise ratio.

SWIR light with wavelengths from $1 \mu\text{m}$ to $3 \mu\text{m}$.

T

ThAr Thorium-Argon.

throughput ratio of photons detected to photons collected..

U

ULI ultrafast laser inscription.

UV light with wavelength 10 nm to 400 nm .

V

VPH volume-phase holographic.

A

MISPRINT Class

,

Code A.1: MISPRINT primary class

```
1 classdef misprint < handleAllHidden
2     %MISPRINT MultiOrder SPectroscopic ReductIoN Tool
3 %
4 % Properties are set using key value pairs.
5 %
6 % Sample Usage:
7 %     s2r = misprint('sciencespectrum','reference','flatspectrum','plotAlot',true,...
8 %                     'usecurrentfolderonly',true,...
9 %                     'numOfOrders',14,'numOfFibers',29,...
10 %                    'forceTrace',false,'forceExtract',false,...
11 %                    'forceDefineMaskEdge',false,'needsMask',false,...
12 %                    'peakcut',0.07,'minPeakSeparation',3,...
13 %                    'numTraceCol',40,'firstCol',140,'lastCol',300,...
14 %                    'parallel',false);
15 %
16 %     self.getMaskForIncompleteOrders;
17 %     self.traceSpectra;
18 %     self.extractSpectra;
19 %     self.getP2PVariationsAndBlaze(false);
20 %
21 %     self.plotSpectraFor(1:14,true,false)
22 %
23 % Copyright (C) Chris Betters 2012–2014
24
25 properties
26     targetBaseFilename,      % base filename of target (file with spectra to be extracted)
27     ↪ fits file.
28     targetPath,             % path to target fits file.
29     rootDirectory,          % path to current directory, should equal [pwd '/'].
30     referenceBaseFilename, % base filename of reference fits file (i.e. a flat frame).
31     referencePath,          % path to reference fits file.
32     usecurrentfolderonly,   % flag to note use my maximumDL/PIMMS echelle file structure.
```

```

32
33     SpectraFitsSaveFileName , % filename of fits file to save extracted
34     spectra_to . % spectra to .
35     ReferenceSpectraFitsSaveFileName , % spectra previously extracted from the
36     reference fits file .
37     FlatReferenceSpectraFitsSaveFileName , % filename of fits file to for use as a flat
38     reference .
39
40     spectraTracePath , % path to previously saved trace data for reference fits file .
41
42     useReference , % flag to indicate if valid reference data has been set/ found .
43     plotA lot , % flag to show raw image and plots during tracing . It plots a lot
44     . % forceTrace , % flag to force a trace of spectra in the current image . Can not
45     be set with a reference .
46     forceExtract , % flag to force a new extraction of the current image . This will
47     overwrite the default save file if it exists .
48     forceDefineMaskEdge , % flag to force a new definition of the mask/clipping region .
49     needsMask , % flag to indicate if image requires clipping .
50     clipping , % vector of pixels from [ left top right bottom ] to clip .
51     parallel , % flag tin indicate if parallel computing toolbox should / can be
52     used .
53
54     gain , % gain ( e-/adu ) read from fits file
55     readNoise , % read noise ( rms e- ) read from fits file
56     dispAxis , % axis of primary dispersion read from fits file
57     targetHeader , % structure with target fits header .
58     referenceHeader , % structure with reference fits header .
59
60
61     imdata , % target image data .
62     imvariance , % estimated variance for target image data .
63     mask , % mask of clipped regions .
64     imdim , % size of imdata ( equals size ( imdata ) )
65     flatImdata ,
66
67
68     spectraValues , % extracted spectra values ( fibres , data , orders ) .
69     spectraVar , % var for extracted spec values .
70     backgroundValues , % background value from extraction
71
72     orderEdges , % detected edges of the orders
73     specCenters , % polynomial interpolated fitted y axis centeres of the spectra from
74     gaussain fit .
75     specWidth , % polynomial interpolated width of the spectra from gaussain fit .
76     meanSpecWidth , % mean width of spectra in each order .
77     meanOrderWidth , % mean width of each order
78
79     fittedCenters , % center of spectrum ( vertical ) from gaussian fit
80     fittedCol , % column used to get progile for fit
81     fittedWidth , % width of specturm ( vertical ) from gaussain fit
82     fittedParamters , % all fit paramaters from trace
83
84
85     finalSpectra , % linearised version of complete spectrum for individual fibre ( all
86     orders )
87     finalSpec , % linearised combined spectrum
88     finalSpectraVar , % varience for finalSpectra
89     finalSpecVar , % varience for finalSpec
90     finalWave , % linearised wavelength scale for finalSpectra and finalSpec
91
92     referenceSpectraValues , % extracted spectraValues of reference / flat
93     P2PVariationValues , % pixel to pixel variation from reference .
94     flatBlaze , % estimated blaze from reference .
95
96     wavematfile , % mat file with wavelength fit paramaters
97     wavefit , % wavelength soultion for each fibre
98     diffractionOrder , % estimated diffraction order from wavefit
99
100    numOfOrders , % number of diffraction orders in image .
101    numOfFibers , % number of spectra ( fibres ) in each order .

```

```

93     numTraceCol,           % number of columns to use when tracing .
94     firstCol,             % first column of trace
95     lastCol,              % last column of trace
96     minPeakSeparation,    % min peak separation for tracing and peakfinder
97     peakcut,               % MINPEAKHEIGHT for spectra tracing detection. (fraction of mean
  ↪ of current profile).
98
99     treatFibresAsOrders, % allows for overlapping orders, ie AWG spectra
100
101    badpixelmask,
102
103    OXmethod, % name of method to use for the optimal extraction.
104 end
105
106 methods
107     function self=misprint(targetBaseFilename ,varargin)
108         % init the MISPRINT class. Parse all inputs, load relevant files .
109
110 %% Pre Initialization %%
111     parser = inputParser;
112
113     parser.addRequired('targetBaseFilename' , @(x) ischar(x));
114     parser.addOptional('reference' , '');
115     parser.addValue('forceTrace' , false , @(x) islogical(x));
116     parser.addValue('forceExtract' , false , @(x) islogical(x));
117     parser.addValue('plotAlot' , false , @(x) islogical(x));
118     parser.addValue('forceDefineMaskEdge' , false , @(x) islogical(x));
119     parser.addValue('needsMask' , false , @(x) islogical(x));
120     parser.addValue('numOfOrders' , 15 , @(x) isnumeric(x));
121     parser.addValue('numOfFibers' , 19 , @(x) isnumeric(x));
122     parser.addValue('usecurrentfolderonly' , false , @(x) islogical(x));
123     parser.addValue('peakcut' , 0.8 , @(x) isnumeric(x));
124     parser.addValue('parallel' , false , @(x) islogical(x));
125     parser.addValue('numTraceCol' , 10 , @(x) isnumeric(x));
126     parser.addValue('dispAxis' , [] , @(x) isnumeric(x));
127     parser.addValue('wavesolution' , '' , @(x) ischar(x));
128     parser.addValue('minPeakSeparation' , 8 , @(x) isnumeric(x));
129     parser.addValue('firstCol' , 0 , @(x) isnumeric(x));
130     parser.addValue('lastCol' , 0 , @(x) isnumeric(x));
131     parser.addValue('clipping',[0 0 0 0] , @(x) isnumeric(x) && length(x)==4);
132     parser.addValue('OXmethod' , 'MPDoptimalExtBack' , @(x) ismethod(self ,x));
133     parser.addValue('orderWidth' , [] , @(x) isnumeric(x));
134     parser.addValue('treatFibresAsOrders' , false , @(x) islogical(x));
135
136
137     parser.parse(targetBaseFilename , varargin{:});
138
139     self.numOfOrders=parser.Results.numOfOrders;
140     self.numOfFibers=parser.Results.numOfFibers;
141     self.forceExtract=parser.Results.forceExtract;
142     self.forceTrace=parser.Results.forceTrace;
143     self.plotAlot=parser.Results.plotAlot;
144     self.forceDefineMaskEdge=parser.Results.forceDefineMaskEdge;
145     self.needsMask=parser.Results.needsMask;
146
147     self.usecurrentfolderonly=parser.Results.usecurrentfolderonly;
148     self.peakcut=parser.Results.peakcut;
149
150     self.parallel=parser.Results.parallel;
151     self.numTraceCol=parser.Results.numTraceCol;
152     self.firstCol=parser.Results.firstCol; %if zero set to 20 minus miage size (at
  ↪ end)
153     self.lastCol=parser.Results.lastCol; %if zero set to 20 minus miage size (at end
  ↪ of init)
154     self.dispAxis=parser.Results.dispAxis;
155
156     self.minPeakSeparation=parser.Results.minPeakSeparation;
157
158     self.clipping=parser.Results.clipping;

```

```

160         self.OXmethod=parser.Results.OXmethod;
161
162         self.meanOrderWidth=parser.Results.orderWidth;
163         self.treatFibresAsOrders=parser.Results.treatFibresAsOrders;
164
165         %% start matlabpool if parallel computing tool box available
166         if self.parallel
167             if license('test', 'distrib_computing_toolbox')
168                 if isempty(gcp('nocreate'))
169                     parpool('local')
170                 end
171             else
172                 warning('MISPRINT:init:useDistribComputingToolbox:notAvailable','The
173             → parallel computing toolbox is not available, but has been requested.')
174             end
175
176         %% root path
177         self.rootDirectory=[pwd '/'];
178
179         %% main reduction target path construction
180         self.targetBaseFilename=parser.Results.targetBaseFilename;
181
182         if ~self.usecurrentfolderonly
183             self.targetPath = [self.rootDirectory self.targetBaseFilename '/reduced/';
184             → self.targetBaseFilename '-master.fit'];
185         else
186             self.targetPath = [self.rootDirectory self.targetBaseFilename '.fit'];
187         end
188         % check the file is a valid fits.
189         self.checkForReducedFitsAt(self.targetPath);
190
191         % get fits header
192         self.targetHeader=fitsheader(self.targetPath);
193
194         %% reference target path construction
195         self.referenceBaseFilename=parser.Results.reference;
196
197         if isempty(self.referenceBaseFilename)
198             self.useReference = false;
199             self.spectraTracePath = [self.rootDirectory self.targetBaseFilename '-
200             → mat'];
201         else
202             self.useReference = true;
203             self.spectraTracePath = [self.rootDirectory self.referenceBaseFilename '-
204             → trace.mat'];
205
206             if ~self.usecurrentfolderonly
207                 self.referencePath = [self.rootDirectory self.referenceBaseFilename '/-
208             → reduced/ self.referenceBaseFilename '-master.fit'];
209             else
210                 self.referencePath = [self.rootDirectory self.referenceBaseFilename '-
211             → fit'];
212             end
213             % check the file is a valid fits.
214             self.checkForReducedFitsAt(self.targetPath);
215
216             % get fits header
217             self.referenceHeader = fitsheader(self.referencePath);
218
219             self.ReferenceSpectraFitsSaveFileName=[self.referenceBaseFilename '-1D-
220             → spectra.fits'];
221             self.referenceSpectraValues=fitsread(self.ReferenceSpectraFitsSaveFileName);
222
223             self.FlatReferenceSpectraFitsSaveFileName=[self.referenceBaseFilename '-
224             → flatten-1D-spectra.fits'];
225
226             %assertWarn(isfield(self.referenceHeader,'IMAGETYP') && strcmp(self.
227             → referenceHeader.IMAGETYP,'Flat Frame'),...
228                 '%      'MISPRINT:init:referenceNotAFlat ',...

```

```

221      %     'Reference Frame has not been tagged as a flat in fits header')
222      end
223
224      %% 1D spectra filenames
225      self.SpectraFitsSaveFileName=[self.targetBaseFilename '-1D-spectra.fits'];
226
227      %% check for required cards in fits header and read the values. add defaults
228      %> where unavailable.
229      if isfield(self.targetHeader, 'READNOIS')
230          self.readNoise=self.targetHeader.READNOIS;
231      elseif isfield(self.targetHeader, 'RO_NOISE')
232          self.readNoise=self.targetHeader.RO_NOISE;
233      else
234          self.readNoise=11.3; % atik default
235          %             if strcmp(self.targetHeader.INSTRUME, 'ArtemisHSC')
236          %                 fitsAddHeaderKeyword(self.targetPath, 'READNOIS', self.
237          %> readNoise, ' ')
238          %                     end
239
240          if isfield(self.targetHeader, 'GAIN')
241              self.gain=self.targetHeader.GAIN;
242          elseif isfield(self.targetHeader, 'RO_GAIN')
243              self.gain=self.targetHeader.RO_GAIN;
244          else
245              self.gain=0.43; % fli default
246              %                 if strcmp(self.targetHeader.INSTRUME, 'ArtemisHSC')
247              %                     fitsAddHeaderKeyword(self.targetPath, 'GAIN', self.gain,
248          %> ')
249              %                     end
250
251          if isempty(self.dispAxis)
252              if isfield(self.targetHeader, 'DISPAXIS')
253                  self.dispAxis=self.targetHeader.DISPAXIS;
254              else
255                  self.dispAxis=2; % atik default
256                  %if strcmp(self.targetHeader.INSTRUME, 'ArtemisHSC')
257                  %    fitsAddHeaderKeyword(self.targetPath, 'DISPAXIS', self.dispAxis, ' ');
258                  %end
259              end
260          %% load misprint, and orientate so echelle dispersion is horizontal
261          self.imdata=fitsread(self.targetPath);
262
263          if self.useReference
264              self.flatImdata=fitsread(self.referencePath);
265          end
266          if self.dispAxis==1
267              self.imdata=fliplr(self.imdata); %
268
269              if self.useReference
270                  self.flatImdata=fliplr(flatImdata');
271              end
272
273          end
274
275          if sum(self.clipping)
276              %[left top right bottom]
277              self.imdata=self.imdata(max([1 self.clipping(2)] : end-self.clipping(4), max([1
278              %> self.clipping(1)]) : end-self.clipping(3));
279
280              if self.useReference
281                  self.flatImdata=self.flatImdata(max([1 self.clipping(2)] : end-self.
282              %> clipping(4), max([1 self.clipping(1)]) : end-self.clipping(3));
283                  end
284
285              if ~isempty(self.wavefit)
286                  self.wavefit=self.wavefit(:, max([1 self.clipping(1)]) : end-self.clipping
287              %> (3) ,:);

```

```

285         end
286     end
287
288     %self.imdata=rot90(self.imdata,2);
289     self.imdim=size(self.imdata);
290     self.imvariance=(self.readNoise/self.gain)^2 + abs(self.imdata) / self.gain; %
291     ↪ http://cxc.cfa.harvard.edu/mta/ASPECT/aca-read-noise/
292
293     %% trace col
294     if ~self.lastCol
295         self.lastCol=self.imdim(2)-20;
296     end
297     if ~self.firstCol
298         self.firstCol=20;
299     end
300
301     if self.treatFibresAsOrders && (self.numOfOrders>1)
302         assert(~(self.treatFibresAsOrders & (self.numOfOrders>1)),...
303             'MISPRINT:init:treatFibresAsOrdersWithMutipleOrders','Can not treat
304             fibres as orders when mutiple orders are set.')
305     end
306
307     %% load wavelength solution if supplied
308     if ~isempty(parser.Results.wavesolution)
309         self.wavematfile=parser.Results.wavesolution;
310         try
311             wavepayload=load(self.wavematfile,'p','S','mu');
312             p=wavepayload.p;
313             S=wavepayload.S;
314             mu=wavepayload.mu;
315             self.wavefit=zeros(self.numOfFibers,self.imdim(2),self.numOfOrders);
316             for o=1:self.numOfOrders;
317                 for f=1:self.numOfFibers;
318                     self.wavefit(f,:,:)=polyval(p(f,:,:),1:self.imdim(2),S(f,:,:),mu);
319             ↪ f,:,:));
320                 end
321             end
322             catch err
323                 wavepayload=load(self.wavematfile,'wavefit');
324                 self.wavefit=wavepayload.wavefit;
325             end
326             self.diffractionOrder=1;%round(2*1e-3/31.6*cosd(5)*sind(63.2)./(mean(squeeze(
327             ↪ mean(self.wavefit,2)),1)*1e-9));
328         end
329     end
330
331     function runDefaultExtraction(self)
332         % run default set of extraction commands
333
334         self.getMaskForIncompleteOrders;
335         self.traceSpectra;
336         self.extractSpectra;
337         self.getP2PVariationsAndBlaze
338     end
339
340     function traceSpectra(self,varargin)
341         % trace spectra from flat.
342         %
343         % optional inputs misprint.traceSpectra(inputimage,numOfOrders,numOfFibers)
344         % inputimage is same format as misprint.imread
345
346         %% initial setup
347         % if preexisting trace exists it is loaded (unless forceTrace set)
348         if nargin==1
349             if (~exist(self.spectraTracePath,'file')) || self.forceTrace ) && ~self.
350             ↪ useReference
351
352             assertWarn(self.forceTrace & exist(self.spectraTracePath,'file'),...
353                 'MISPRINT:traceSpectra:TraceForced',...
354                 'Tracing was forced, this will overwrite previous trace.')

```

```

350
351         if ~exist( self.spectraTracePath , 'file' ); disp(['Tracefile: ' self.
352     spectraTracePath ' does not exist.']);end
353     else
354         assert(~(self.forceTrace & self.useReference) ,...
355             'MISPRINT:traceSpectra:TraceForcedWithUseReferenceSet',...
356             'Tracing can not be forced when useReference is set')
357
358         assert(~(self.useReference & ~exist( self.spectraTracePath , 'file' )),...
359             'MISPRINT:traceSpectra:ReferecnceTraceFileNotFound',...
360             [ self.spectraTracePath ' was not found and is required as a reference
361             '. Aborting.])
362
363         load( self.spectraTracePath , 'specCenters' , 'specWidth' , 'orderWidth' ,
364             'orderEdges' , 'means' , 'columns' , 'widths' , 'fitxs' )
365
366         if self.useReference
367             %disp(['Using reference trace: ' self.spectraTracePath])
368         else
369             disp(['Using previous trace: ' self.spectraTracePath])
370         end
371
372         self.meanSpecWidth=squeeze(mean(specWidth,2));
373         if isempty( self.meanOrderWidth )
374             self.meanOrderWidth=squeeze(mean(orderWidth,2));
375         end
376         self.specCenters=specCenters;
377         self.specWidth=specWidth;
378         self.orderEdges=orderEdges;
379
380         self.fittedCenters=means;
381         self.fittedCol=columns;
382         self.fittedWidth=widths;
383         self.fittedParamters=fitxs;
384
385         return % end function call after loading data
386     end
387
388 %% load data into local variables
389 x=1:self.imdim(1);
390 if nargin==4
391     inputimage = varargin{1};
392     numOrders = varargin{2};
393     numFibers = varargin{3};
394 else
395     inputimage=self.imdata;
396     numOrders = self.numOfOrders;
397     numFibers = self.numOfFibers;
398 end
399
400 imdata=inputimage.* self.mask;
401
402 %% find orders
403 if ( self.numTraceCol>=self.imdim(2))
404     columns=1:self.imdim(2);
405     warning('MISPRINT:fitAllOfTheThings','You just asked for a fit to every
406     column.')
407     reply = input('Are your sure?? Y/N [Y]: ', 's');
408     if ~strcmpi('Y',reply)
409         error('MISPRINT:traceSpectra:userInterupt','MISPRINT termintated in
410             traceSpectra.')
411     end
412     else
413         columns=round(linspace(self.firstCol , self.lastCol , self.numTraceCol));
414     end
415
416 imcol=imdata(:,columns); % sliced image

```

```

415         disp('Running order tracer. This may take some time.')
416         for i=1:length(columns)
417             [yp,index]=findpeaks(imcol(:,i), 'NPEAKS',numOfOrders*numOfFibers, '
418             ↪ 'MINPEAKHEIGHT',max(imcol(:,i))*self.peakcut,'MINPEAKDISTANCE',self.minPeakSeparation);
419             if self.plotAlot
420                 figure(i);clf
421                 plot(x,imcol(:,i),index,yp,'xr');
422                 line([1 length(imcol(:,i))],[max(imcol(:,i)) max(imcol(:,i))]*self.
423             ↪ peakcut)
424                 title([num2str(columns(i))])
425             end
426             if numOfOrders==1
427                 orderWidth=self.imdim(1);
428                 orderCenter=round(self.imdim(1)/2);
429                 orderEdges(:,i)=[1 self.imdim(1)];
430             else
431                 orderWidth=diff(index(1:numOfFibers:end));
432                 orderCenter=mean([index(numOfFibers:numOfFibers:end) index(1:numOfFibers:
433             ↪ end)],2);
434                 %error(' ')
435                 orderEdges(:,i)=[orderCenter(1)-orderWidth(1)/2;...
436                     mean([index(numOfFibers:numOfFibers:end)-numOfFibers...
437                         index(numOfFibers+1:numOfFibers:end)],2); orderCenter(end)+orderWidth
438             ↪ (end)/2];
439             end
440
441             %
442             if self.plotAlot
443                 plot(imcol(:,i))
444                 hold on
445                 %
446                 %line(repmat(orderEdges(:,i),[2,1]),[zeros(1,size(
447             ↪ orderEdges(:,i),2)); ones(1,size(orderEdges(:,i),2))*max(imcol)])
448                 %
449                 hold off
450             end
451             %error(' ')
452             %% trace orders
453             % fit gaussian to profile in columns for each order.
454             fitxs=zeros(numOfOrders,3*numOfFibers+1,length(columns));
455             for i=1:length(columns)
456                 for order=1:numOfOrders
457                     disp(['Column: ' num2str(columns(i)) '| Fitting Spectra in Order: '
458             ↪ num2str(order)])
459                     orderProfileX=round(max(orderEdges(order,i),1):min(orderEdges(order+1,i),
460             ↪ self.imdim(1)));
461                     orderProfile=imcol(orderProfileX,i);
462                     orderProfile=orderProfile/max(orderProfile);
463
464                     [~, means(order,:,:,i), widths(order,:,:,i), fitxs(order,:,:,i)] = ...
465                         self.fitNGaussainsAlt(numOfFibers,orderProfileX, orderProfile, self.
466             ↪ peakcut);
467                     %
468                     [~, means(order,:,:,i), widths(order,:,:,i), fitxs(order
469             ↪ ,:,:,i)] = ...
470                     %
471                     fitNGaussains(numOfFibers,orderProfileX,
472             ↪ orderProfile, self.peakcut, false);
473                     if self.plotAlot
474                         figure(i);clf;
475                         %subplot(5,4,columns)
476                         plot(orderProfileX,sum(self.nGausFunc(fitxs(order,:,:,i),orderProfileX,
477             ↪ numOfFibers),2),'r-',...
478                             orderProfileX,orderProfile,'-')
479                         title(['Order: ' num2str(order) ' Column: ' num2str(columns(i))])
480                         %pause(0.1)
481                         drawnow
482                     end
483                 end
484             end

```

```

474
475     specCenters=self.polyfitwork(self.imdim,means,columns,2);
476     specWidth=self.polyfitwork(self.imdim,widths,columns,3);
477     meanSpecWidth=squeeze(mean(self.specWidth,3));
478
479     self.fittedCenters=means;
480     self.fittedCol=columns;
481     self.fittedWidth=widths;
482
483     self.meanSpecWidth=meanSpecWidth;
484     self.specCenters=specCenters;
485     self.specWidth=specWidth;
486     self.orderEdges=orderEdges;
487     self.fittedParamters=fitxs;
488     if isempty(self.meanOrderWidth)
489         self.meanOrderWidth=squeeze(mean(orderWidth,2));
490     end
491
492     save(self.spectraTracePath,'specCenters','specWidth','orderWidth','orderEdges',...
493     ↪ means,'columns','widths','fitxs')
494 end
495
496 function getMaskForIncompleteOrders(self)
497
498     % get mask for incomplete orders
499
500     if ~self.needsMask
501         self.mask=ones(self.imdim);
502         return % no clip, so mask is ones.
503     end
504
505     if isfield(self.targetHeader,'CLIPTL') && isfield(self.targetHeader,'CLIPTR') &&
506     ↪ isfield(self.targetHeader,'CLIPBL') && isfield(self.targetHeader,'CLIPBR')
507         topEdges=[self.targetHeader.CLIPTL self.targetHeader.CLIPTR];
508         bottomEdges=[self.targetHeader.CLIPBL self.targetHeader.CLIPBR];
509     else
510         self.forceDefineMaskEdge=true; % override default as clipping is needed, and
511     ↪ data not defined
512     end
513
514     if self.forceDefineMaskEdge
515         echfig=figure(1);
516         imagesc(self.imdata);
517         %axis([1 self.imdim(2) 1 self.imdim(1)*0.5]) % show top half of image
518         [~,y]=getpts(echfig);
519         topEdges=[y(1) y(2)];
520         %axis([1 self.imdim(2) self.imdim(1)-self.imdim(1)*0.3 self.imdim(1)]) % show
521     ↪ bottom third of image
522         [~,y]=getpts(echfig);
523         bottomEdges=[y(1) y(2)];
524     end
525
526     % make mask of image to exclude incomplete orders
527     xi=[0; self.imdim(2); self.imdim(2); 0];
528     yi=[0; topEdges(2); topEdges(1)];
529     BW1 = roipoly(self.imdata,xi,yi);
530
531     xi=[0; self.imdim(2); self.imdim(2); 0];
532     yi=[self.imdim(1); self.imdim(1); bottomEdges(2); bottomEdges(1)];
533     BW2 = roipoly(self.imdata,xi,yi);
534     self.mask=~BW1 & ~BW2;
535
536     if self.forceDefineMaskEdge
537         imagesc(self.imdata.*self.mask)
538         reply = input('Should I add to Fits Header Y/N [N]: ', 's');
539         if isempty(reply)
540             reply = 'N';
541         end
542         if strncmpi(reply, 'Y', 1)

```

```

540         disp('saving clips to header')
541         fitsAddHeaderKeyword(self.targetPath, 'CLIPTL',topEdges(1), ' ');
542         fitsAddHeaderKeyword(self.targetPath, 'CLIPTR',topEdges(2), ' ');
543         fitsAddHeaderKeyword(self.targetPath, 'CLIPBL',bottomEdges(1), ' ');
544         fitsAddHeaderKeyword(self.targetPath, 'CLIPBR',bottomEdges(2), ' ');
545     end
546 end
547
548 if self.plotAlot
549     figure(1)
550     imagesc(self.imdata.*self.mask)
551 end
552 end
553
554 function getBadPixelMask(self)
555     try
556         matpayload=load(self.spectraTracePath, 'badpixel');
557         badpixel=matpayload.badpixel;
558     catch err
559         if self.useReference
560             imdatafilt=medfilt2(self.flatImdata,[1 5]);
561             diffimage=self.flatImdata-imdatafilt;
562             badpixel=abs(diffimage-mean2(diffimage)) > std2(diffimage)*3;
563             %save(self.spectraTracePath, 'badpixel', '-append')
564         else
565             imdatafilt=medfilt2(self.imdata,[1 5]);
566             diffimage=self.imdata-imdatafilt;
567             badpixel=abs(diffimage-mean2(diffimage)) > std2(diffimage)*3;
568         end
569     end
570     self.badpixelmask=badpixel;
571     %sum(badpixel(:))
572     self.imdata(self.badpixelmask)=NaN;
573     %self.imdata(self.imdata<0)=NaN;
574     self.imdata=inpaint_nans(self.imdata,3);
575 end
576
577
578 function getP2PVariationsAndBlaze(self, varargin)
579     % get smoothed version of flat spectrum (ie blaze) and pixel to
580     % pixel variations (flatspectrum./smooth flat spectrum)
581     %
582     % load reference
583     if length(varargin)==2
584         referenceFile=varargin{2};
585     elseif self.useReference
586         referenceFile=self.ReferenceSpectraFitsSaveFileName;
587     end
588
589     if ~isempty(varargin)
590         force=varargin{1};
591     else
592         force=false;
593     end
594
595     matpayload=load(self.spectraTracePath, 'flatBlaze', 'P2PVariationValues');
596     if ~force && isfield(matpayload, 'flatBlaze') && isfield(matpayload,
597     ↪ P2PVariationValues)
598         self.flatBlaze=matpayload.flatBlaze;
599         self.P2PVariationValues=matpayload.P2PVariationValues;
600     else
601         disp('Re-doing blaze/flat')
602         assertWarn(force, 'MISPRINT:getP2PVariationsAndBlaze:forced', 'P2P and blaze
603     ↪ forced')
604         mask=ones(self.numOffibers, self.imdim(2));
605         %
606         mask(end-50:end)=NaN;
607         %
608         mask(1:50)=NaN;
609
610         if self.useReference
611             spectraValues=self.referenceSpectraValues;

```

```

608         spectraValues=spectraValues;%(2^14);
609     end
610     %
611     %           for or=1:self.numOfOrders
612     %               spectraValues(:, :, or)=bsxfun(@rdivide,spectraValues
613     %                   (: ,:, or).*mask,max(spectraValues (: ,:, or) ') ');
614     %               end
615     flatBlaze=zeros(size(self.spectraValues));
616     P2PVariationValues=zeros(size(self.spectraValues));
617
618     for f=1:self.numOfFibers
619         for or=1:self.numOfOrders
620             %error(' ')
621             flatBlaze(f ,: , or)=csaps(1: self.imdim(2),spectraValues(f ,: , or),1e-8,1;
622             %flatBlaze(f ,: , or)=smooth(spectraValues(f ,: , or),100);
623         end
624         P2PVariationValues=spectraValues ./ flatBlaze;
625         %error(' ')
626         for order=self.numOfOrders
627             flatBlaze_norm(:, :, order)=bsxfun(@rdivide,flatBlaze(:, :, order),max(
628             flatBlaze(:, :, order) ') );
629         end
630
631         self.flatBlaze=flatBlaze_norm;
632         self.P2PVariationValues=P2PVariationValues;
633
634         self.flatBlaze(isnan(self.flatBlaze))=1;
635         self.P2PVariationValues(isnan(self.P2PVariationValues))=1;
636
637         flatBlaze=flatBlaze_norm;
638         save(self.spectraTracePath,'flatBlaze','P2PVariationValues','append')
639     end
640
641     function getBlazeAlt(self,varargin)
642         if ~isempty(varargin)
643             force=varargin{1};
644         else
645             force=false;
646         end
647
648         matpayload=load(self.spectraTracePath,'flatBlaze','P2PVariationValues');
649         if ~force && isfield(matpayload,'flatBlaze') && isfield(matpayload,
650             'P2PVariationValues')
651             self.flatBlaze=matpayload.flatBlaze;
652             self.P2PVariationValues=matpayload.P2PVariationValues;
653         else
654             assertWarn(force,'MISPRINT:getP2PVariationsAndBlaze:forced','P2P and blaze
655             forced')
656
657             %%%
658             x=[1:2498];
659
660             opts1 = fitoptions('Method', 'LinearLeastSquares' );
661             opts1.Normalize = 'on';
662             ft1=fittype('poly2');
663
664             opts2 = fitoptions('Method', 'LinearLeastSquares' );
665             opts2.Normalize = 'on';
666             ft2=fittype('poly3');
667
668             for f=1:self.numOfFibers
669                 for o=1:self.numOfOrders
670                     spec=self.spectraValues(f ,: , o);
671
672                     % ft=fittype('smoothingspline');
673                     % opts = fitoptions('Method', 'SmoothingSpline' );
674                     % opts.Normalize = 'on';

```

```

673         % opts.SmoothingParam = 1e-5;
674
675         [ fitresult , gof] = fit( x' , spec' , ft1 , opts1);
676         %plot(detrend(spec'./feval(fitresult ,x))+1); grid on
677
678         ignore=detrend(spec'./ feval(fitresult ,x))+1 < 1;
679
680         [ fitresult , gof] = fit( x(~ignore)' , medfilt1(spec(~ignore),10)' , ft2
681         ↪ , opts2);
682
683         blaze=feval(fitresult ,x);
684         flatBlaze(f,:,:)=blaze./max(blaze);
685         %plot(x,squeeze(flatBlaze(f,:,:)),x, self.spectraValues(f,:,:))/max(
686         ↪ self.spectraValues(f,:,:))
687         %pause(0.2)
688         end
689     end
690
691     P2PVariationValues=ones( size(flatBlaze));
692     self.flatBlaze=flatBlaze;
693     self.P2PVariationValues=P2PVariationValues;
694
695     %save( self.spectraTracePath , 'flatBlaze ','P2PVariationValues' , '-append')
696 end
697
698 function plotSpectraValuesFor( self , orders , shouldFlat , shouldP2PV , xlims , ylims )
699
700     % plot spectra orders specified. three arguments orders ,shouldFlat ,shouldP2PV
701
702     if shouldFlat && shouldP2PV
703         FlattenedSpectra=self.spectraValues ./ self.flatBlaze ./ self.P2PVariationValues;
704     elseif shouldFlat && ~shouldP2PV
705         FlattenedSpectra=self.spectraValues ./ self.flatBlaze ;
706     elseif ~shouldFlat && shouldP2PV
707         FlattenedSpectra=self.spectraValues ./ self.P2PVariationValues ;
708     else
709         FlattenedSpectra=self.spectraValues ;
710     end
711
712     if isempty( self.wavefit )
713         for order=orders
714             figure(order); clf ;
715
716             p=panel();
717             p.pack('h',[1/2 []]);
718             p.margin = [23 15 10 5];
719
720             p(1).select();
721             %imagesc(log10(self.imdata-min2(self.imdata)+1))
722             imagesc(self.imdata)
723             colormap gray
724             %set(gca , 'CLim',[0 1000])
725             ylim([min2(squeeze(self.specCenters(order ,:,:)))-50 max2(squeeze(self.
726             ↪ specCenters(order ,:,:))+50])
727             hold on
728             plot(1:self.imdim(2) ,squeeze(self.specCenters(order ,:,:)) , 'LineWidth' ,1)
729             %axis image
730             xlabel('Detector Column')
731             ylabel('Detector Row')
732
733             p(2).select();
734             for f=1:self.numOfFibers
735                 FlattenedSpectraNorm(f,:,:,order)=FlattenedSpectra(f,:,:,order)/(max2(
736                 ↪ FlattenedSpectra(f,120:220,order)));
737                 plot(1:self.imdim(2) ,FlattenedSpectraNorm(f,:,:,order)+(self.
738                 ↪ numOfFibers-f)*1)
739                 hold all
740             end
741             %ylim([0 max([ FlattenedSpectraNorm(:)*1.01; 2^14])]);
742             ylim(ylimits)

```

```

738         xlim(xlimits)
739         hold off
740         grid on
741         xlabel('Detector Column')
742         ylabel('Normalised Intensity')
743     end
744
745     else
746         for order=orders
747             figure(order); clf;
748
749                 subplot(1,2,1)
750                 imagesc(log10(self.imdata-min2(self.imdata)+1))
751                 %imagesc(self.imdata)
752                 %set(gca, 'CLim',[0 1000])
753                 ylim([min2(squeeze(self.specCenters(order,:,:)))-50 max2(squeeze(self.
754             specCenters(order,:,:))+50)])
755                 hold on
756                 plot(1:self.imdim(2),squeeze(self.specCenters(order,:,:)), 'k', 'LineWidth'
757             ,1.5)
758                 %title(['Order ' num2str(self.diffractionOrder(order))])
759                 xlabel('Primary-dispersion axis (pixels)')
760                 ylabel('Cross-dispersion axis (pixels)')
761
762                 subplot(1,2,2)
763                 for f=1:self.numOfFibers
764                     FlattenedSpectraNorm(f,:,: ,order)=FlattenedSpectra(f,:,: ,order)/max(
765             FlattenedSpectra(f,:,: ,order));
766                     plot(self.wavefit(f,:,: ,order), FlattenedSpectraNorm(f,:,: ,order)+(self.
767             numOfFibers-f)*0.2)
768                     hold all
769                 end
770
771             %
772             %
773             end
774         end
775
776     function p=plotSingleFibre(self,f,shouldFlat,shouldP2PV)
777         % plot spectra for single fibre across multiple orders, three arguments fibre,
778         % shouldFlat,shouldP2PV
779         if shouldFlat && shouldP2PV
780             FlattenedSpectra=self.spectraValues ./ self.flatBlaze ./ self.P2PVariationValues;
781         elseif shouldFlat && ~shouldP2PV
782             FlattenedSpectra=self.spectraValues ./ self.flatBlaze;
783         elseif ~shouldFlat && shouldP2PV
784             FlattenedSpectra=self.spectraValues ./ self.P2PVariationValues;
785         else
786             FlattenedSpectra=self.spectraValues;
787         end
788
789         if isempty(self.wavefit)
790             p=plot(bsxfun(@plus, repmat([1:self.imdim(2)], [self.numOfOrders 1])',[0:self.
791             numOfOrders-1]*self.imdim(2)),squeeze(FlattenedSpectra(f,:,:)));
792         else
793             p=plot(squeeze(self.wavefit(f,:,:)),squeeze(FlattenedSpectra(f,:,:)));
794         end
795         ylim([0 max(p.YData)*1.1])
796     end
797
798     function plotFinalSpectra(self)
799         for f=1:self.numOfFibers
800             plot(self.finalWave, self.finalSpectra(f,:)+(self.numOfFibers-f)*2)
801             hold all

```

```

801         end
802         hold off
803         xlabel('Wavelength (nm)')
804         hold on
805         orderwaveedges=squeeze(max(min(self.wavefit,[],2),[],1));
806         line([orderwaveedges orderwaveedges], [0 40], 'LineWidth',1, 'Color','k')
807
808         hold off
809     end
810
811     function plotFinalSpec(self)
812         % [sunflux, sunwave] = getsunspec(min(self.finalWave), max(self.
813         % finalWave), 0.022);
814         % [telflux, telwave] = getTelluricSpec(min(self.finalWave), max(self.
815         % finalWave), 0.022);
816         %
817         % plot(sunwave,sunflux,telwave,telflux)
818         % hold all
819         % plot(self.finalWave,self.finalSpec/max(self.finalSpec))
820         orderwaveedges=squeeze(max(min(self.wavefit,[],2),[],1));
821         hold on
822         line([orderwaveedges orderwaveedges], [0 1], 'LineWidth',2, 'Color','k')
823
824         hold off
825         xlabel('Wavelength (nm)')
826     end
827
828     function filterBadPixels(self,Nsigma,thresh,shouldPlot)
829         % filter bad pixels. three arguments Nsigma,thresh,shouldPlot
830         im=self.imdata;
831         im(im<=0)=1;
832
833         imdiff=medfilt2(im,[2 2])./im; % try and highlight odd pixels
834
835         imdiff=imdiff-mean2(imdiff); % set mean to zero
836
837         bad1=imdiff>thresh; % very larger value can bias std, so clip them.
838
839         badpixel=(imdiff>std2(imdiff(~bad1))*Nsigma | imdiff<-std2(imdiff(~bad1))*Nsigma
840         | bad1);
841
842         self.imdata(badpixel)=NaN;
843
844         self.imdata=inpaint_nans(self.imdata);
845
846         if shouldPlot
847             figure(shouldPlot); clf
848             [badx, bady]=find(badpixel);
849
850             imagesc(self.imdata)
851             hold on
852             shouldPlot(bady,badx,'wx')
853             hold off
854         end
855
856         function blurred=removeIntensityGradientInImdata(self,avgWin)
857             % smooth whole image, then divided original by that. Usefull for to
858             % improve flat tracing. one arguments avgWin (window for smoothing)
859             PSF = fspecial('average', [1 1]*avgWin);
860
861             blurred = imfilter(self.imdata, PSF, 'conv', 'symmetric');
862             blurred=blurred/mean2(blurred);
863
864             if self.plotAlot
865                 subplot(1,3,1)
866                 imagesc(self.imdata)
867                 subplot(1,3,2)
868                 imagesc(blurred)

```

```

868         subplot(1,3,3)
869         imagesc(self.imdata./blurred)
870     end
871     %self.imdata=self.imdata./blurred;
872 end
873
874 function getBackgroundBetweenOrders( self )
875     self.imdata( self.imdata<0)=0;
876     locs= self.orderEdges';
877     locs(locs>3362)=3362;
878
879     imagesc(log10( self.imdata ))
880     hold on;
881     plot(self.fittedCol,locs,'bx')
882     hold off;
883     pks=[];
884
885
886     filteredimdata=medfilt2( self.imdata );
887
888     %locs(89,:)=(locs(88,:)+locs(90,:))/2;
889
890     for i = 1:size(locs,2)
891         % pks(i,:)=self.imdata(self.fittedCol,round(self.orderEdges(:,i)));
892         p = impixel(filteredimdata, self.fittedCol, locs(:,i)');
893         pks(:,i) = p(:,1);
894     end
895
896
897     cols= self.fittedCol;
898
899
900
901 %% scattered light estimate
902
903     invertedimdata=(1./( self.imdata)).* self.mask;
904     invertedimdata(isinf(invertedimdata))=0;
905     figure(1)
906     imagesc(log10(invertedimdata))
907     x=1: self.imdim(1);
908
909
910     inverpks=1./pks;
911     cols2=repmat(cols,[ size(locs,2),1] );
912     figure(3); clf
913     h(2)=surface(cols2,locs,pks,'EdgeColor','none');
914     xlim([1 self.imdim(2)])
915     ylim([1 self.imdim(1)])
916     set(get(h(2),'Parent'),'YDir','reverse')
917
918
919     figure(2); clf
920     sfun=scateringTestFit(cols2, locs, inverpks);
921
922
923
924
925     figure(4); clf
926     [XI,YI]=meshgrid(1: self.imdim(2), 1: self.imdim(1));
927
928     subplot(1,2,2)
929     imagesc(1./feval(sfun,XI,YI).* self.mask)
930     title('Estimated Scattering (from Inter-Order Regions)')
931
932     subplot(1,2,1)
933     h(2)=surface(cols2,locs,1./pks,'EdgeColor','none');
934     xlim([1 self.imdim(2)])
935     ylim([1 self.imdim(1)])
936     set(get(h(2),'Parent'),'YDir','reverse')
937

```

```

938
939      %self.imdata=self.imdata-feval(sfun,X,Y)
940      imagesc(self.imdata-1./feval(sfun,XI,YI))
941      hold on; plot(cols2,locs,'wx'); hold off
942      title('PIMMS Echelle Detector Image')
943
944      %self.imdata=self.imdata-1./feval(sfun,XI,YI)
945
946
947      %%%
948
949      imagesc(log10(self.imdata))
950
951      return
952      self.forceTrace=true;
953      self.forceExtract=true;
954
955      self.getMaskForIncompleteOrders;
956      self.traceSpectra;
957      %self.specCenters=self.specCenters;
958      self.extractSpectra;
959      self.getP2PVariationsAndBlaze
960      set(0,'DefaultFigureWindowStyle','docked')
961
962 end
963
964 function spectraValues=extractSpectra(self)
965     % extract spectra using trace - each order done individually (faster).
966
967     if ~exist(self.SpectraFitsSaveFileName,'file') || self.forceExtract
968         spectraValues=zeros(self.numOfFibers,self.imdim(2),self.numOfOrders);
969         spectraVar=zeros(self.numOfFibers,self.imdim(2),self.numOfOrders);
970         backgroundValues=zeros(size(self.imdata)); self.imdata;
971
972         assertWarn(self.forceExtract,...,
973             'MISPRINT:extractSpectra:forceExtractFlagSet',...
974             'Force extraction flag set, starting extraction. Data will be overwritten
975             ');
976         RN=self.readNoise/self.gain;
977         for order=1:self.numOfOrders
978             spectra=zeros(self.numOfFibers,self.imdim(2));
979             specVar=zeros(self.numOfFibers,self.imdim(2));
980             %background=zeros(size(self.imdata));
981
982             %disp(['Extracting Order: ' num2str(order)])
983             orderSpecCenters=shiftdim(self.specCenters(order,:,:),1); % clips order
984             % dim (1,f,col) > (f,col)
985
986             % split into apertures
987             for col=1:self.imdim(2)
988
989                 orderCenter=mean(orderSpecCenters(:,col));
990                 profileAperature{col}=max(round(orderCenter-self.meanOrderWidth/2),1)
991                 % ...
992                 min(round(orderCenter+self.meanOrderWidth/2),self.imdim(1));
993
994                 orderProfile{col}=self.imdata(profileAperature{col},col)';
995                 varProfile{col}=self.imvariance(profileAperature{col},col)';
996
997                 end
998
999                 % do extraction
1000                 % for col=1:self.imdim(2)
1001                 % [spectra(:,col), specVar(:,col), background(:,col
1002                 % ,:)] = self.(self.OXmethod)(...
1003                 % % profileAperature{col,:},orderProfile{col,:},
1004                 % % varProfile{col,:},...
1005                 % % squeeze(self.specCenters(order,:,:)),...
1006                 % % squeeze(2*log(2)*self.specWidth(order,:,:)));
1007
1008             end

```

```

1002             % self.readNoise/self.gain);
1003             %
1004         end
1005     [spectra, specVar, background]=self.(self.OXmethod) (...  

1006         profileApeture,orderProfile,varProfile,...  

1007         (shiftdim(self.specCenters(order,:,:),1)),...  

1008         2*log(2)*(shiftdim(self.specWidth(order,:,:),1)),...  

1009         RN);
1010
1011
1012
1013     % unfold into final variables
1014     for col=1:self.imdim(2)
1015         backgroundValues(profileApeture{col},col)=background{col};
1016     end
1017     spectraValues(:,:,order)=spectra;
1018     spectraVar(:,:,order)=specVar;
1019 end
1020
1021 spectra1DHDR=createcards('NUMORDER',self.numOfOrders,'number of orders');
1022 spectra1DHDR.addcard('NUMFIBER',self.numOfFibers,'number of fibers')
1023 spectra1DHDR.addcard('TRACE',self.spectraTracePath,'')
1024
1025 fitswrite(spectraValues,self.SpectraFitsSaveFileName,spectra1DHDR.cards)
1026 fitswrite(spectraVar,self.SpectraFitsSaveFileName,'writemode','append')
1027 fitswrite(backgroundValues,self.SpectraFitsSaveFileName,'writemode','append')
1028 else
1029     disp(['Pre-existing extraction data found at: ' self.SpectraFitsSaveFileName
1030     ↪ ])
1031
1032     spectraValues=fitsread(self.SpectraFitsSaveFileName);
1033     spectraVar=fitsread(self.SpectraFitsSaveFileName,'image',1);
1034     backgroundValues=fitsread(self.SpectraFitsSaveFileName,'image',2);
1035 end
1036 if self.treatFibresAsOrders
1037     warning(' ')
1038     self.spectraValues(1,:,:)=permute(spectraValues,[2 1]);
1039     self.spectraVar(1,:,:)=permute(spectraVar,[2,1]);
1040
1041     self.specCenters=permute(self.specCenters,[2 1 3]);
1042
1043     self.numOfOrders=self.numOfFibers;
1044     self.numOfFibers=1;
1045 else
1046     self.spectraValues=spectraValues;
1047     self.spectraVar=spectraVar;
1048 end
1049
1050 function [spectraValues, spectraErrors, background, chi2]=MPDoptimalExtBack(self,
1051     ↪ dataRows,orderProfile,varProfile,specCenters,specWidth,RN)
1052     % Multi-Profile Deconvolution Optimal Extraction as described by Sharp & Birchall
1053     ↪ (2010)
1054     %
1055     % paper: Sharp R., Birchall M. N. (2010) Optimal Extraction of Fibre Optic
1056     ↪ Spectroscopy. PASA 27, pp. 91–103.
1057     % http://dx.doi.org/10.1071/AS08001
1058
1059     if iscolumn(orderProfile); orderProfile=orderProfile'; disp(1); end
1060     if iscolumn(varProfile); varProfile=varProfile'; disp(2); end
1061     if iscolumn(dataRows); dataRows=dataRows'; disp(3); end
1062     if isrow(specCenters); specCenters=specCenters'; disp(4); end
1063     if isrow(specWidth); specWidth=specWidth'; disp(5); end
1064     %
1065     % error(' ')
1066     % save('testing.mat','self','dataRows','orderProfile','varProfile',
1067     ↪ 'specCenters','specWidth','RN')

```

```

1066         phi=self.getPhi(dataRows,specCenters,2*log(2)*specWidth,[ones(length(specCenters)
1067             ,1)]);
1068         [xout,~,~,~] = fminsearch(@optimizeBackgroundFit, polyfit(dataRows,orderProfile/
1069             sum(orderProfile),1));
1070         [chi2, fittedValues, fittedErrors, M]=optimizeBackgroundFit(xout);
1071         spectraValues=fittedValues(1:end-1);
1072         spectraErrors=fittedErrors(1:end-1);
1073         background=fittedValues(end)*polyval(xout,dataRows)/sum(polyval(xout,dataRows));
1074
1075         function [chi2, fittedValues, fittedErrors, M]=optimizeBackgroundFit(x)
1076             %setup
1077             phifit=[phi; polyval(x,dataRows)/sum(polyval(x,dataRows))];%ones(1,size(phi
1078             ,2))/size(phi,2) %([1:size(phi,2)]*x(1)+x(2)) / sum([1:size(phi,2)]*x(1)+x(2))
1079             sigmaweightPhi=bsxfun(@rdivide,phifit,sqrt(varProfile));
1080             c=phifit*sigmaweightPhi;
1081             b=((orderProfile)*sigmaweightPhi);
1082
1083             %setup error
1084             ce=phifit*phifit';
1085             be=((varProfile-RN^2)*phifit)';
1086
1087             %solve
1088             fittedValues=c\b;
1089             fittedErrors=ce\be;
1090
1091             %Model
1092             M=sum(bsxfun(@times,phifit,fittedValues),1);
1093
1094             chi2=sum(((orderProfile-M).^2./varProfile)/(size(M,2)-size(fittedValues,1)-
1095                 length(x)));
1096                 % if chi2>1
1097                 % plot(1:195,M,1:195,orderProfile)
1098                 % drawnow;
1099             end
1100         end
1101
1102         function [spectraValues, spectraErrors, background]=MPDoptimalExt(self,dataRows,
1103             orderProfile,varProfile,specCenters,specWidth,RN)
1104             % Multi-Profile Deconvolution Optimal Extraction as described by Sharp & Birchall
1105             % (2010)
1106             % paper: Sharp R., Birchall M. N. (2010) Optimal Extraction of Fibre Optic
1107             % Spectroscopy. PASA 27, pp. 91–103.
1108             % http://dx.doi.org/10.1071/AS08001
1109
1110             %setup
1111             % if 0
1112             % phi=self.getPhi(dataRows,specCenters,specWidth,ones(length(
1113                 specCenters),1));
1114                 %%phi
1115                 % else
1116                 % phi1=;
1117                 % phi2=;
1118                 % phi3=;
1119                 spectraValues=zeros(size(specCenters'));
1120                 spectraErrors=spectraValues;
1121                 background=cellfun(@(x) zeros(size(x)),orderProfile,'UniformOutput',false);
1122                 for col=1:size(specCenters,1)
1123                     phi=bsxfun(@times, exp(-bsxfun(@rdivide, bsxfun(@minus, repmat(dataRows{col
1124                         },..., [self.numOfFibers,1]),specCenters{col,:}'), specWidth{col,:}').^2), 1./(
1125                         specWidth{col,:}'*sqrt(pi)));
1126                     %phi=bsxfun(@times, phi4, specPeaks);
1127                     %phi=sparse(phi);
1128                     phi(phi<1e-6)=0;
1129                     %
1130                 end

```

```

1126
1127         % if 1
1128         varweightedPhi=bsxfun(@rdivide,phi,varProfile{col})';
1129         c=phi*varweightedPhi;
1130         b=((orderProfile{col})*varweightedPhi)';
1131         %
1132         % sigmaweightedPhi=bsxfun(@rdivide,phi,sqrt(varProfile))';
1133         % c=mtimesx(phi,sigmaweightedPhi,'MATLAB');
1134         % b=mtimesx(orderProfile, sigmaweightedPhi,'MATLAB')';
1135         %
1136
1137         %setup error
1138         ce=phi*phi';
1139         be=((varProfile{col}-RN^2)*phi)';
1140
1141         %solve
1142         spec=(c\b);
1143         spectraValues(:,col)=spec;
1144         %spectraValues=linsolve(c,b);
1145         errors=ce\be;
1146         spectraErrors(:,col)=errors;
1147         %background{col}=zeros(size(orderProfile{col}))+spec(end);
1148         %spectraErrors=linsolve(ce,be);
1149         %assert(~(col==400))
1150
1151         %background=cellfun(@(x) zeros(size(x)),orderProfile,'UniformOutput',false);
1152         spectraValues(spectraValues<0)=0;
1153
1154     end
1155
1156     function [spectraValues, spectraErrors, background]=MPDoptimalExtDCBack( self ,dataRows
1157     ↪ ,orderProfile ,varProfile ,specCenters ,specWidth ,RN)
1158     % Multi-Profile Deconvolution Optimal Extraction as described by Sharp & Birchall
1159     % (2010)
1160     % paper: Sharp R., Birchall M. N. (2010) Optimal Extraction of Fibre Optic
1161     % Spectroscopy. PASA 27, pp. 91–103.
1162     % http://dx.doi.org/10.1071/AS08001
1163
1164     %setup
1165     % if 0
1166     % phi=self.getPhi(dataRows,specCenters,specWidth,ones(length(
1167     ↪ specCenters),1));
1168     %
1169     %%phi
1170     % else
1171     % phi1=;
1172     % phi2=;
1173     % phi3=
1174     spectraValues=zeros(size(specCenters));
1175     spectraErrors=spectraValues;
1176     background=cellfun(@(x) zeros(size(x)),orderProfile,'UniformOutput',false);
1177     for col=1:size(specCenters,1)
1178         phi=bsxfun(@times, exp(-(bsxfun(@rdivide, bsxfun(@minus, repmat(dataRows{col
1179     ↪ } ,..., [self.numOfFibers,1]),specCenters{col,:}), specWidth{col,:})^2), 1./(
1180     ↪ specWidth{col,:}.*sqrt(pi)));
1181         %phi=bsxfun(@times, phi4, specPeaks);
1182         %phi=sparse(phi);
1183         phi=[phi; ones(1,size(phi,2))];
1184         phi(phi<1e-6)=0;
1185         %
1186         %
1187         % if 1
1188         varweightedPhi=bsxfun(@rdivide,phi,varProfile{col})';
1189         c=phi*varweightedPhi;
1190         b=((orderProfile{col})*varweightedPhi)';
1191         %
1192         % sigmaweightedPhi=bsxfun(@rdivide,phi,sqrt(varProfile))';
1193         % c=mtimesx(phi,sigmaweightedPhi,'MATLAB');
1194         % b=mtimesx(orderProfile, sigmaweightedPhi,'MATLAB')';

```

```

1190           %           end
1191
1192         %setup error
1193         ce=phi*phi';
1194         be=((varProfile{col}-RN^2)*phi')';
1195
1196         %solve
1197         spec=(c\b);
1198         spectraValues(:,col)=spec(1:end-1);
1199         %spectraValues=linsolve(c,b);
1200         errors=ce\be;
1201         spectraErrors(:,col)=errors(1:end-1);
1202         background{col}=zeros(size(orderProfile{col}))+spec(end);
1203         %spectraErrors=linsolve(ce,be);
1204         %assert(~(col==400))
1205     end
1206     %background=cellfun(@(x) zeros(size(x)),orderProfile,'UniformOutput',false);
1207     spectraValues(spectraValues<0)=0;
1208
1209 end
1210
1211 function [spectraValues, spectraErrors, background]=MPDoptimalExtOld(self,dataRows,
1212   orderProfile, varProfile, specCenters, specWidth, RN)
1213   % Multi-Profile Deconvolution Optimal Extraction as described by Sharp & Birchall
1214   % (2010)
1215   %
1216   % paper: Sharp R., Birchall M. N. (2010) Optimal Extraction of Fibre Optic
1217   % Spectroscopy. PASA 27, pp. 91–103.
1218   % http://dx.doi.org/10.1071/AS08001
1219
1220   %setup
1221   %           if 0
1222   %           phi=self.getPhi(dataRows,specCenters,specWidth,ones(length(
1223   % specCenters),1));
1224   %           %%phi
1225   %           else
1226   %             phil=bsxfun(@minus, repmat(dataRows,[length(specCenters),1]),specCenters);
1227   %             phi2=@rdivide, phil, specWidth);
1228   %             phi3=exp(-(phi2).^2);
1229   %             phi=bsxfun(@times, phi3, 1./(specWidth*sqrt(pi)));
1230   %             %phi=bsxfun(@times, phi4, specPeaks);
1231   %             %phi=sparse(phi);
1232   %             phi(phi<1e-8)=0;
1233   %           end
1234
1235   %           if 1
1236   %             sigmaweightedPhi=bsxfun(@rdivide, phi, sqrt(varProfile));
1237   %             c=phi*sigmaweightedPhi;
1238   %             b=((orderProfile)*sigmaweightedPhi);
1239   %           else
1240   %             sigmaweightedPhi=bsxfun(@rdivide, phi, sqrt(varProfile));
1241   %             c=mtimesx(phi,sigmaweightedPhi,'MATLAB');
1242   %             b=mtimesx(orderProfile,sigmaweightedPhi,'MATLAB');
1243   %           end
1244
1245   %setup error
1246   ce=phi*phi';
1247   be=((varProfile-RN^2)*phi')';
1248
1249   %solve
1250   spectraValues=(c\b);
1251   %spectraValues=linsolve(c,b);
1252   spectraErrors=(ce\be);
1253   %spectraErrors=linsolve(ce,be);
1254   background=zeros(size(orderProfile));
1255
end
function phi=getPhi(~,dataRows,specCenters,specWidth,specPeaks)
    phil=bsxfun(@minus,repmat(dataRows,[length(specCenters),1]),specCenters);

```

```

1256     phi2=bsxfun(@rdivide, phi1, specWidth);
1257     phi3=exp(-(phi2).^2);
1258     phi4=bsxfun(@times, phi3, 1./(specWidth*sqrt(pi)));
1259     phi=bsxfun(@times, phi4, specPeaks);
1260     %phi=pause(phi);
1261     phi(phi<1e-8)=0;
1262 end
1263
1264 function [spectraValues, spectraErrors, background]=boxcarExt(self,dataRows,
1265 % Multi-Profile Deconvolution Optimal Extraction as described by Sharp & Birchall
1266 % (2010)
1267 %
1268 % paper: Sharp R., Birchall M. N. (2010) Optimal Extraction of Fibre Optic
1269 % Spectroscopy. PASA 27, pp. 91–103.
1270 % http://dx.doi.org/10.1071/AS08001
1271
1272 %setup
1273 % if 0
1274 % phi=self.getPhi(dataRows,specCenters,specWidth,ones(length(
1275 % specCenters),1));
1276 % %%phi
1277 % else
1278 % phi1=;
1279 % phi2=;
1280 % phi3=
1281 % spectraValues=zeros(size(specCenters));
1282 % spectraErrors=spectraValues;
1283 % for col=1:size(specCenters,1)
1284 %     assert(~(col==300))
1285 %     spectraValues(:,col)=sum(orderProfile{col}([round([-specWidth(col)*2:specWidth
1286 % (col)*2]+self.meanOrderWidth/2)));
1287 %     spectraErrors(:,col)=sum(varProfile{col}([round([-specWidth(col)*2:specWidth(
1288 % (col)*2]+self.meanOrderWidth/2)));
1289 % end
1290
1291 background=cellfun(@(x) zeros(size(x)),orderProfile,'UniformOutput',false);
1292
1293 end
1294
1295 function lineariseAndCombineSpectrum(self,saveFiles)
1296
1297 if nargin==1
1298 saveFiles=false;
1299 end
1300
1301 spec=(self.spectraValues);%./self.P2PVariationValues;%./self.flatBlaze;%%
1302 specVar=(self.spectraVar);%./self.P2PVariationValues;%./self.flatBlaze;%%
1303
1304 % for or=1:self.numOfOrders
1305 % specVar(:,:,or)= bsxfun(@rdivide,specVar(:,:,or),max(spec(:,:,or)));
1306 % spec(:,:,or) = bsxfun(@rdivide,spec(:,:,or),max(spec(:,:,or)));
1307 % end
1308
1309 longwavelinear=linspace(min(self.wavefit(:)),max(self.wavefit(:)),self.imdim(2)*
1310 self.numOfOrders);
1311 speclinearlong=zeros(self.numOfFibers,self.imdim(2)*self.numOfOrders,self.
1312 numOfOrders);
1313 spectraVarlinearlong=zeros(self.numOfFibers,self.imdim(2)*self.numOfOrders,self.
1314 numOfOrders);
1315
1316 for o=1:self.numOfOrders
1317     for f=1:size(spec,1);
1318         speclinearlong(f,:,:,:)=interp1(self.wavefit(f,:,:,:),spec(f,:,:,:),
1319         longwavelinear,'spline',0);
1320         spectraVarlinearlong(f,:,:,:)=interp1(self.wavefit(f,:,:,:),specVar(f,:,:,:),
1321         longwavelinear,'spline',0);

```

```

1313
1314         specflatlong(f,:,:,o)=interp1(self.wavefit(f,:,:,o),self.flatBlaze(f,:,:,o),
1315             longwavelinear,'spline',0);
1316     end
1317
1318     %specflatlong=ones(size(speclinearlong));
1319
1320     finalspeclong=nansum(speclinearlong,3)';%./nansum(specflatlong,3)';
1321     finalspecVarlong=nansum(spectraVarlinearlong,3)';%./nansum(specflatlong,3)';
1322     flatspeclong=nansum(specflatlong,3)';
1323
1324     finalspeclong=finalspeclong./bsxfun(@rdivide,flatspeclong,mean(flatspeclong));
1325     finalspecVarlong=finalspecVarlong./bsxfun(@rdivide,flatspeclong,mean(flatspeclong
1326             ));
1327
1328     toclip=isnan(sum(finalspeclong,2));
1329
1330     longwavelinear_clipped=longwavelinear(~toclip);
1331     finalspecVarlong_clipped=finalspecVarlong(~toclip,:);
1332     finalspeclong_clipped=finalspeclong(~toclip,:);
1333
1334     self.finalSpectra=squeeze(finalspeclong_clipped)';
1335     self.finalSpectraVar=squeeze(finalspecVarlong_clipped)';
1336     self.finalWave=longwavelinear_clipped;
1337
1338     self.finalSpec=squeeze(sum(finalspeclong_clipped,2)');
1339     self.finalSpecVar=squeeze(sum(finalspecVarlong_clipped,2)');
1340
1341     if 0
1342         %% for i=1:size(finalspecVarlong_clipped,2)
1343             smoother(:,i)=csaps(self.finalWave,finalspecVarlong_clipped(:,i)
1344             ,0.0000001,self.finalWave);
1345             end
1346             %% smoother=mean(smoother,2)';
1347             %[smoother] = blazeCorrection(self.finalSpec, self.finalWave,0.98)';
1348         else
1349             smoother=1;
1350             end
1351             error(' ')
1352         self.finalSpec=self.finalSpec./smoother;
1353         self.finalSpecVar=self.finalSpecVar./smoother;
1354
1355         if saveFiles
1356             header=self.targetHeader;
1357             header.IMAGETYP='SPECTRUM';
1358             header.CRPIX1=round(length(self.finalWave)/2);
1359             header.CRVAL1=self.finalWave(header.CRPIX1);
1360             header.CTYPE1='Wavelength';
1361             header.CUNIT1='nm';
1362             header.CDELT1=mean(diff(self.finalWave));
1363             header.UTC=round((header.JD-floor(header.JD))*24*60*60);
1364             header.MJD=header.JD-2400000.5;
1365             header.DLAT=-33.873651000000000000;
1366             header.DLONG=151.206889600000070000;%sydney
1367             header.GEOELV=100;
1368
1369             headercell1=fitstructure2cell(header);
1370
1371             header2.EXTNAME='FLUXERROR';
1372             headercell2=fitstructure2cell(header2);
1373
1374             fitswrite(finalspeclong_clipped,[self.targetBaseFilename '-IndivCalSpec.fit'
1375             ],'keywords',headercell1(8:end,:))
1376                 fitswrite(finalspecVarlong_clipped,[self.targetBaseFilename '-IndivCalSpec.
1377                 fit'], 'writemode','append','keywords',headercell2)
1378
1379             fitswrite(self.finalSpec,[self.targetBaseFilename '-CombCalSpec.fit'],
1380             'keywords',headercell1(8:end,:))

```

```

1376         fitsfwrite( self .finalSpecVar , [ self .targetBaseFilename '-CombCalSpec.fit'] , '
1377             ↪ writemode ', 'append' , 'keywords' , headercell2 )
1378             end
1379         end
1380     end
1381
1382     methods ( Static , Access = private )
1383         function answer=checkForReducedFitsAt(path)
1384             % check for a reduced target
1385             try
1386                 import matlab.io.*
1387                 fptr = fits.openFile( path );
1388                 fits.closeFile(fptr);
1389                 answer=1;
1390             catch err
1391                 if strcmp(err.identifier , 'MATLAB:imagesci:fits:libraryError')
1392                     error('MISPRINT:checkForReducedTarget:fitsOpenError','Reduced fits file
1393             ↪ does not exist.')
1394                 else
1395                     rethrow(err)
1396                 end
1397             end
1398         end
1399         methods ( Static )
1400             [ specCenters , p , mu]=polyfitwork(imdim,means,column,polyorder,offset,plotalot)
1401             prepareFrames
1402             [peaks,means,widths,xfitted] = fitNGaussainsAlt(N,x,y,peakcut,plotting)
1403             out=nGausFunc(x,xData,N)
1404             wavecalGUI
1405             autoimprovewavelength(varargin)
1406         end
1407     end

```

B

ZEMAX Macro to setup échelle wavelength and orders

Code B.1: ZEMAX macro to fill appropriate wavelengths for échelle orders in separate configurations.

```
1 firstOrder=83 #81
2 lastOrder=74 #97
3 orderIncrement=-1
4 numberOfWorks=12
5 numberOfWorks=(lastOrder-firstOrder)/orderIncrement + 1
6
7 PRINT
8 FORMAT 1.0
9 PRINT " Setting Up Echelle with ", numberOfWorks, " orders, from ",firstOrder, " to ",
   ↪ lastOrder, "."
10 FORMAT 4.4
11 PRINT
12
13 !define pi
14 pi=ACOS(0.5)*3
15
16 ! find grating surfaces
17 FOR currentSurf, 1, NSUR(), 1
18   dummy = SPRO(currentSurf, 0)
19   currentSurfType$ = $BUFFER()
20   dummy = SPRO(currentSurf, 1)
21   currentSurfComment$ = $BUFFER()
22   IF (currentSurfType$ $$== "DGRATING") & (currentSurfComment$ $$== "ECHELLE") THEN
      ↪ echelleSurf=currentSurf
23   IF (currentSurfType$ $$== "DGRATING") & (currentSurfComment$ $$== "X-DISP") THEN xdispSurf=
      ↪ currentSurf
24   IF (currentSurfType$ $$== "COORDBRK") & (currentSurfComment$ $$== "gamma in") THEN
      ↪ echelleGammaSurf=currentSurf
25 NEXT
```

```

26
27 theta_i=ABSO(SPRX(echelleSurf -1,10,3))/180*pi
28 d_eche=(1e-6/SPRX(echelleSurf ,10 ,1))*COSI(SPRX(echelleGammaSurf ,10 ,4)/180*pi)
29
30 theta_xdsip=ABSO(SPRX(xdispSurf -1,10,3))/180*pi
31 d_xdisp=le-6/SPRX(xdispSurf ,10 ,1)
32
33 ! delete all existing configs and MCOS
34 numOldConfigs=NCON()
35 FOR currentConfig ,1 ,numOldConfigs ,1
36   DELETECONFIG 1
37 NEXT
38 FOR i,1,100,1
39   DELETEMCO 1
40 NEXT
41
42 !create required MCO operands
43 SETSYSTEMPROPERTY 201, numberOfWaves # set number of waves
44
45 FOR currentWave ,1 , numberOfWaves ,1
46   INSERTMCO currentWave
47   SETMCOPERAND currentWave , 0, "WAVE" ,0
48   SETMCOPERAND currentWave , 0, currentWave ,1
49 NEXT
50 SETMCOPERAND currentWave ,      0, "PRAM"      , 0
51 SETMCOPERAND currentWave ,      0, echelleSurf , 1
52 SETMCOPERAND currentWave ,      0, 2           , 2
53
54 maxwave=0
55 minwave=100
56
57 currentOrder=firstOrder
58 PRINT "Config , Order , Blue , Central , Red , FSR (nm) , Littrow X-Disp"
59 For currentConfig ,1 ,numberOfOrders ,1
60   # insert configs , skip first
61   IF currentConfig > 1 THEN INSERTCONFIG currentConfig
62
63 # setup wavelength limits and increments
64 centralWave=2*d_eche*SINE(theta_i)/currentOrder/1e-6
65 FSR=centralWave/currentOrder
66 blueEnd=centralWave-FSR*0.5
67 redEnd=centralWave+FSR*0.5
68 waveInc=(redEnd-blueEnd)/(numberOfWaves-1)
69
70 #save max and min waves
71 IF redEnd > maxwave THEN maxwave=redEnd
72 IF blueEnd < minwave THEN minwave=blueEnd
73
74 # set waves and orders in MCDE
75 FOR currentWave,1 , NWAV() ,1
76   SETMCOPERAND currentWave , currentConfig , blueEnd+(currentWave-1)*waveInc ,0
77 NEXT
78 SETMCOPERAND currentWave , currentConfig , currentOrder , 0
79
80 # print summary, comma seperated
81 #PRINT currentConfig , ",", currentOrder , ",",
82 #      blueEnd , ",",
83 #      centralWave , ",",
84 #      redEnd ,
85 #      FSR*1e3 , ",",
86 #      ASIN((1e-6*centralWave)/(2 *d_xdisp))/pi*180
87 PRINT currentConfig , " & ", currentOrder , " & ", blueEnd , " & ", centralWave , " & ",
88 #      redEnd , " & ", FSR*1e3 , " \\#," & ", ASIN((1e-6*centralWave)/(2 *d_xdisp))/pi*180
89
90 #increment diffraction order counter
91 currentOrder=currentOrder+orderIncrement
92 Next
93
94 PRINT
95 PRINT " Bandwidth is " , minwave , " to " , maxwave , " ( , (maxwave-minwave)*1e3 , " nm)"
96
97 PRINT " Done"

```

C

Included Papers

Beating the classical limit: A diffraction-limited spectrograph for an arbitrary input beam

Christopher H. Betters,^{1,2,*} Sergio G. Leon-Saval,¹ J. Gordon Robertson,^{1,2}
and Joss Bland-Hawthorn^{1,2}

¹ Institute of Photonics and Optical Science, School of Physics, University of Sydney, 2006, Australia

² Sydney Institute for Astronomy, School of Physics, University of Sydney, 2006, Australia

*.c.betters@physics.usyd.edu.au

Abstract: We demonstrate a new approach to classical fiber-fed spectroscopy. Our method is to use a photonic lantern that converts an arbitrary (e.g. incoherent) input beam into N diffraction-limited outputs. For the highest throughput, the number of outputs must be matched to the total number of unpolarized spatial modes on input. This approach has many advantages: (i) after the lantern, the instrument is constructed from ‘commercial off the shelf’ components; (ii) the instrument is the minimum size and mass configuration at a fixed resolving power and spectral order; (iii) the throughput is better than 60% (slit to detector, including detector QE of ~80%); (iv) the scattered light at the detector can be less than 0.1% (total power). Our first implementation operates over 1545–1555 nm (limited by the detector) with a spectral resolution of 0.055nm ($R\sim 30,000$) using a 1×7 (1 multi-mode input to 7 single-mode outputs) photonic lantern. This approach is a first step towards a fully integrated, multimode photonic microspectrograph.

©2013 Optical Society of America

OCIS codes: (350.1260) Astronomical optics; (300.6190) Spectrometers; (060.2430) Fibers, single-mode; (060.2350) Fiber optics imaging.

References and links

1. J. Bland-Hawthorn, J. Lawrence, G. Robertson, S. Campbell, B. Pope, C. Betters, S. Leon-Saval, T. Birks, R. Haynes, N. Cvetojevic, and N. Jovanovic, “PIMMS: photonic integrated multimode microspectrograph,” Proc. SPIE **7735**, 77350N, 77350N-9 (2010).
2. S. G. Leon-Saval, A. Argyros, and J. Bland-Hawthorn, “Photonic lanterns: a study of light propagation in multimode to single-mode converters,” Opt. Express **18**(8), 8430–8439 (2010).
3. S. G. Leon-Saval, T. A. Birks, J. Bland-Hawthorn, and M. Englund, “Multimode fiber devices with single-mode performance,” Opt. Lett. **30**(19), 2545–2547 (2005).
4. D. Noordegraaf, P. M. W. Skovgaard, R. H. Sandberg, M. D. Maack, J. Bland-Hawthorn, J. S. Lawrence, and J. Lægsgaard, “Nineteen-port photonic lantern with multimode delivery fiber,” Opt. Lett. **37**(4), 452–454 (2012).
5. D. Noordegraaf, P. M. Skovgaard, M. D. Nielsen, and J. Bland-Hawthorn, “Efficient multi-mode to single-mode coupling in a photonic lantern,” Opt. Express **17**(3), 1988–1994 (2009).
6. J. Bland-Hawthorn, S. C. Ellis, S. G. Leon-Saval, R. Haynes, M. M. Roth, H. G. Löhmansröben, A. J. Horton, J. G. Cuby, T. A. Birks, J. S. Lawrence, P. Gillingham, S. D. Ryder, and C. Trinh, “A complex multi-notch astronomical filter to suppress the bright infrared sky,” Nat Commun **2**, 581 (2011).
7. C. Q. Trinh, S. C. Ellis, J. Bland-Hawthorn, J. S. Lawrence, A. J. Horton, S. G. Leon-Saval, K. Shortridge, J. Bryant, S. Case, M. Colless, W. Couch, K. Freeman, H.-G. Löhmansröben, L. Gers, K. Glazebrook, R. Haynes, S. Lee, J. O’Byrne, S. Miziarski, M. M. Roth, B. Schmidt, C. G. Tinney, and J. Zheng, “GNOSIS: The First Instrument to Use Fiber Bragg Gratings for OH Suppression,” Astron. J. **145**(2), 51 (2013).
8. S. Shaklan and F. Roddier, “Coupling starlight into single-mode fiber optics,” Appl. Opt. **27**(11), 2334–2338 (1988).
9. A. J. Horton and J. Bland-Hawthorn, “Coupling light into few-mode optical fibres I: The diffraction limit,” Opt. Express **15**(4), 1443–1453 (2007).
10. R. R. Thomson, R. J. Harris, T. A. Birks, G. Brown, J. Allington-Smith, and J. Bland-Hawthorn, “Ultrafast laser inscription of a 121-waveguide fan-out for astrophotonics,” Opt. Lett. **37**(12), 2331–2333 (2012).
11. S. G. Leon-Saval, C. H. Betters, and J. Bland-Hawthorn, “The Photonic TIGER: a multicore fiber-fed spectrograph,” Proc. SPIE **8450**, 84501K, 84501K-8 (2012).

12. R. R. Thomson, T. A. Birks, S. G. Leon-Saval, A. K. Kar, and J. Bland-Hawthorn, "Ultrafast laser inscription of an integrated photonic lantern," *Opt. Express* **19**(6), 5698–5705 (2011).
13. I. Spaleniak, N. Jovanovic, S. Gross, M. Ireland, J. Lawrence, and M. Withford, "Enabling photonic technologies for seeing-limited telescopes: fabrication of integrated photonic lanterns on a chip," *Proc. SPIE* **8450**, 845015, 845015-8 (2012).
14. A. W. Snyder and J. Love, *Optical Waveguide Theory* (Springer, 1983).
15. C. Palmer and E. Loewen, *Diffraction Grating Handbook*, 6 ed. (Newport Corporation, 2005).
16. J. G. Robertson, "Quantifying resolving power in astronomical spectra," *Publ. Astron. Soc. Aust.* **30**, e048 (2013).
17. J. G. Robertson and J. Bland-Hawthorn, "Compact high-resolution spectrographs for large and extremely large telescopes: using the diffraction limit," *Proc. SPIE* **8446**, 844623, 844623-13 (2012).
18. P. Belland and J. P. Crenn, "Changes in the characteristics of a Gaussian beam weakly diffracted by a circular aperture," *Appl. Opt.* **21**(3), 522–527 (1982).
19. C. H. Betters, S. G. Leon-Saval, J. Bland-Hawthorn, and G. Robertson, "Demonstration and design of a compact diffraction limited spectrograph," *Proc. SPIE* **8446**, 84463H, 84463H-9 (2012).
20. C. G. Tinney, S. D. Ryder, S. C. Ellis, V. Churilov, J. Dawson, G. A. Smith, L. Waller, J. D. Whittard, R. Haynes, A. Lankshear, J. R. Barton, C. J. Evans, K. Shortridge, T. Farrell, and J. Bailey, "IRIS2: a working infrared multi-object spectrograph and camera," *Proc. SPIE* **5492**, 998–1009 (2004).
21. W. Saunders, T. Bridges, P. Gillingham, R. Haynes, G. A. Smith, J. D. Whittard, V. Churilov, A. Lankshear, S. Croom, D. Jones, and C. Boshuizen, "AAOmega: a scientific and optical overview," *Proc. SPIE* **5492**, 389–400 (2004).
22. J. C. Olaya, S. G. Leon-Saval, D. Schirdewahn, K. Ehrlich, D. M. Haynes, and R. Haynes, "1:61 photonic lanterns for astrophotometry: a performance study," *Mon. Not. R. Astron. Soc.* **427**(2), 1194–1208 (2012).
23. N. Cvetojevic, N. Jovanovic, C. H. Betters, J. S. Lawrence, S. C. Ellis, G. Robertson, and J. Bland-Hawthorn, "First starlight spectrum captured using an integrated photonic micro-spectrograph," *Astron. Astrophys.* **544**, L1 (2012).
24. N. Cvetojevic, N. Jovanovic, J. Lawrence, M. Withford, and J. Bland-Hawthorn, "Developing arrayed waveguide grating spectrographs for multi-object astronomical spectroscopy," *Opt. Express* **20**(3), 2062–2072 (2012).
25. W. Livingston and L. Wallace, *An atlas of the solar spectrum in the infrared from 1850 to 9000 cm-1 (1.1 to 5.4 micrometer)* (NSO Technical Report, Tucson: National Solar Observatory, National Optical Astronomy Observatory, 1991).
26. L. S. Rothman, I. E. Gordon, A. Barbe, D. C. Benner, P. F. Bernath, M. Birk, V. Boudon, L. R. Brown, A. Campargue, J. P. Champion, K. Chance, L. H. Coudert, V. Dana, V. M. Devi, S. Fally, J. M. Flaud, R. R. Gamache, A. Goldman, D. Jacquemart, I. Kleiner, N. Lacome, W. J. Lafferty, J. Y. Mandin, S. T. Massie, S. N. Mikhailenko, C. E. Miller, N. Moazzen-Ahmadi, O. V. Naumenko, A. V. Nikitin, J. Orphal, V. I. Perevalov, A. Perrin, A. Predoi-Cross, C. P. Rinsland, M. Rotger, M. Šimečková, M. A. H. Smith, K. Sung, S. A. Tashkun, J. Tennyson, R. A. Toth, A. C. Vandaele, and J. Vander Auwera, "The HITRAN 2008 molecular spectroscopic database," *J. Quant. Spectrosc. Radiat. Transf.* **110**(9–10), 533–572 (2009).

1. Introduction

One of the fundamental design characteristics of any spectrograph is the amount of light collected, dispersed and re-imaged onto a detector. This quantity is characterized by the étendue (or $A\Omega$ factor, defined as the product of entrance/collection surface area, A , and the solid angle of acceptance of the optical system, Ω). Conventionally, in order to maximize the throughput (ratio of photons detected to photons collected) of a spectrograph, the étendue of all optical elements (e.g. from a telescope to the detector) must be well matched.

The most challenging spectrographs are those that operate at high spectral resolution ($R = \lambda/\Delta\lambda > 20,000$). When observing faint sources, there is a strong tension between the need to broaden the slit to allow for more light from the source while preserving the spectroscopic performance of the instrument. An additional challenge is that for a spectrograph operating at a resolving power R matched to natural seeing (i.e. a fixed angular resolution limit measured in arcseconds), the size of the instrument scales in proportion to the telescope diameter [1]. Modern high-resolution astronomical spectrographs are already meter-scale instruments and are required to be even larger on the next generation of extremely large telescopes (25–40 m diameter). This is the impasse reached in the design of high-resolution spectrographs; maximizing collection area requires the physical size to increase in order to maintain a given resolution. Adaptive optics (AO) is one route to mitigate this problem, reducing the extent of an image on the spectrograph slit. In the visible region, the blue end in particular, current AO

techniques are somewhat limited. However, in any wavelength range, the spectrograph designs are still paired with a given telescope/AO system.

Here we raise two key challenges: (i) to get more light through a high-resolution spectrograph; and (ii) to break the dependence of spectrograph size on the telescope diameter or other input. We solve both of these problems simultaneously through our new approach to spectrograph design. The basic principle is to remap the extent of the entrance slit, minimizing the width while conserving the effective étendue. The result is a long thin slit (ideally diffraction-limited in width) replacing the comparatively short wide classical slit. In principle, this is exactly what an integral field unit (IFU) does when reducing a 2D image to a linear slit. However, the devices used in conventional IFUs can already be extremely complex, so requiring they remap to even smaller sizes will invariably lead to losses of efficiency or increased cost (if not both). A new approach is required to efficiently reduce the slit to a diffraction-limited width.

In [1], Bland-Hawthorn et al. introduced the concept of a photonic integrated multimode microspectrograph (PIMMS) that promised a fundamental shift in spectrograph design which we now demonstrate for the first time. The proposal harnessed an emerging technology, known as the photonic lantern (PL), to allow efficient conversion of an essentially arbitrary input (e.g. a combination of arbitrarily excited modes) to the consistent and diffraction-limited format of single-mode fibers (SMFs) [2–5]. The PL remaps the entrance slit of the spectrograph, thus achieving throughput equivalent to a multimode fiber (MMF) design and the spectral resolution of a diffraction-limited slit width.

The PL's conversion from MM to SM completely decouples the spectrograph design from the light source at the MM input, resulting in a spectrograph design that no longer need match the input beam of a specific telescope (or any other source for that matter). Instead, it is designed to match the output of the array of SMFs (whose output remains fundamentally unchanged regardless of the source at the MM input). The conversion also allows single-mode photonic technologies to be incorporated into new and pre-existing spectrographs, the most successful so far being fiber Bragg gratings for sky OH suppression [6,7].

In this paper, we will briefly describe the design considerations and figures of merit for a SMF fed spectrograph, including an overview of the 1×7 (1 MM to 7 SM) PL used. This is followed by a laboratory characterization of the prototype spectrograph, dubbed PIMMS IR.

2. Diffraction-limited design considerations

2.1 Entrance slit

The beam emerging from an SMF is diffraction-limited by definition [1] (i.e. the étendue or $A\Omega = \lambda^2$), with the light propagating in the LP01 mode (Gaussian like). Coupling to a SMF efficiently is not trivial. When coupling in ideal circumstances (i.e. a uniformly illuminated circular pupil), the efficiency peaks at 80% and decreases proportionally to the Strehl ratio. A typical example is coupling light from a telescope where, in the presence of atmospheric turbulence, the focus can be extremely perturbed, and the Strehl ratios are typically less than <1% and thus couple poorly to a sole SMF [8,9]. The PL alleviates the coupling concern while simultaneously allowing the spectrograph's entrance slit to be formed by an array of SMF.

A factor to consider when forming the entrance slit in this way is the distance between the SM cores. If the fibers are placed in a simple linear array to form a “pseudo-slit,” there will be a significant gap between spectra at the detector. This gap between cores (typically 125 μm for standard SMF) leads to wasted detector space unless some additional component is used to bring the cores closer together. Ultrafast laser inscription of waveguides offers a path to do just that, with appropriate devices already demonstrated [10]. However, the addition of components can lead to further complication and become an additional source of aberration in a design intended to be as simple as possible. Another solution is to form the pseudo-slit with

a hexagonal bundle of SMFs or a multi-core fiber, constructed and positioned such that each core forms an independent spectrum when dispersed [11]. However, for simplicity (and as it does not significantly affect the actual spectrograph design), we will assume in later sections that the SMF cores are aligned to form a linear pseudo-slit with an optimal spacing unless otherwise specified.

2.2 Throughput/Étendue of a photonic lantern

The fundamental requirement of the PL is that it efficiently transforms MM light into SM waveguide outputs. Currently the most common method of fabricating a PL starts with a bundle of SMFs inserted in a low-index glass capillary. Those are fused and drawn down together to form a composite tapered waveguide that ends in a MM port. At the MM end, the SMFs cladding material becomes the core and the low index glass capillary becomes the cladding. An alternative is to start with a multi-core fiber (MCF; i.e. a 2D array of SM cores in a single fiber), which are again drawn down and tapered within a glass capillary. In both cases, the cores of the SMFs become too small to guide light [2–5]. Another promising method is directly writing waveguides using ultrafast laser inscription, forming a PL in a solid block of glass [12,13].

In either method, if the taper transition from MM to SM is optically adiabatic, the modes of the MMF input will evolve into the modes of the SM outputs. In order for the conversion to be efficient, the number of modes supported in the MM (m) port should match the number of SM fibers (n). The number of modes in a step-index MMF is determined from the core size and the acceptance angle (specified as a numerical aperture, NA) or in terms of the fiber V parameter [14],

$$m \approx \frac{V^2}{4} \approx \left(\frac{\pi d}{2\lambda} \text{NA} \right)^2, \quad (1)$$

where d is the fiber core diameter and λ is the free space wavelength of the guided light. It should be noted that each mode is capable of carrying two polarizations. Consequently when polarization is considered there are effectively twice as many modes. Even so, the number of SMFs remains the same as each fiber can also carry two polarizations.

For low loss operation, the number of modes has to be conserved (i.e. $m = n$) at the PL's design wavelength. A typical throughput of the current generation of lanterns is ~93% (0.3dB loss) [5]. Note that as λ decreases the number of modes in the MM port increases. This will result in an effective reduction in throughput blueward of the design wavelength when the number of modes in the MM port exceeds the number of modes available in SM outputs. In contrast, redward of the design wavelength, the number of SM outputs will exceed the number of modes supported in the MM port, thus the transition will not have a negative impact on throughput. So, an absolute limit on PL transmission throughput can simply be expressed by the ratio of the number of SM outputs and number of modes in the MM input, i.e.

$$\text{transmission fraction} = \frac{n}{m} = \frac{n(A\Omega)_{\text{SMF}}}{(A\Omega)_{\text{MMF}}}. \quad (2)$$

The number of modes can be thought of as equivalent to the étendue of fiber, indeed, simply multiplying by λ^2 returns the étendue for low numerical apertures.

2.3 Resolving power

Another key figure of merit for a spectrograph is its minimum resolvable wavelength difference or resolution ($\Delta\lambda$), often expressed as the resolving power ($R = \lambda/\Delta\lambda$). This is a convolution of the instrumental point spread function (PSF; i.e. the grating resolution and

imaging quality) and the width of the imaged entrance slit. In conventional spectrographs the slit width is generally the limiting factor [15]. Using the PL, the width of the slit can be brought to an absolute minimum leaving the instrumental PSF as the dominant factor in determining resolution. With diffraction-limited optics (without significant beam truncation) the instrument PSF should reproduce the near-field output of the SM fiber, and instrument resolution is then dependent only on the resolution of the diffraction grating.

For the case of a truncated Gaussian with a $1/e^2$ width, d , and angle of incidence, θ , the resolving power is thus

$$R = \frac{\lambda}{\Delta\lambda} = 2.38 \frac{Kd}{\lambda} \tan \theta. \quad (3)$$

where a generalized form of the Rayleigh criterion, where the resolution element is $1.112 \times$ FWHM, was used in Eq. (3) to provide a realistic estimate of the resolving power [16,17]. The factor K accounts for the broadening effect seen when bringing a collimated Gaussian beam that has been truncated to a focus [17–19].

2.4 Detector area implications of the photonic lantern

The detector area required for a PIMMS type spectrograph is effectively the same as that required by equivalent MM spectrograph. This unexpected result requires some discussion and is illustrated in Fig. 1. Assume that the PIMMS and MM spectrographs share equal bandwidth and resolving power. The PIMMS case has an increase in the spatial extent of the spectrum (i.e. pseudo-slit length) that proportional to \sqrt{N} . This is balanced by a \sqrt{N} reduction of space required in the wavelength direction (i.e. the PIMMS resolution element is related to the width of the MM case by a factor $1/\sqrt{N}$). So when determining the total area, the factor \sqrt{N} is eliminated, with two qualifications. Firstly, the actually area required by the PIMMS design is dependent on the spacing of the SM cores at the pseudo-slit, but the spacing can be designed such that there is no difference. Secondly, while the detector areas are equal, the PIMMS case requires smaller pixels to adequately sample the PSF of the SM pseudo-slit. Indeed, it is clear that the pixels must be at least a factor $1/\sqrt{N}$ times smaller than those required for the MM case (as we must have same number of resolution elements in the wavelength axis for both the PIMMS and MM case). This indicates that PIMMS IR needs N more pixels than the MM case. This assumes that the spatial extent needs the same degree of sampling (i.e. pixels per FWHM) as the wavelength axis, which is not necessarily the case. One could conceive a detector for PIMMS IR that has rectangular pixels, where the long axis is aligned with the spatial extent of the slit, and the short edge matched to adequately sample a resolution element. In such a case the number of extra pixels required is εN , where ε is the ratio of SM sampling and MM sampling.

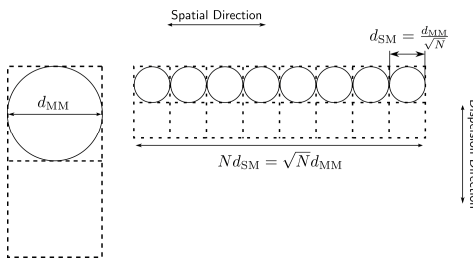


Fig. 1. Illustrated are the images of a MM spectrograph slit (left) and the pseudo-slit of a PIMMS spectrograph (right) where both PSFs are sampled by 1 pixel. The relationship between d_{SM} and d_{MM} is found by equating the étendue. We can see a \sqrt{N} decrease in the wavelength direction width is balanced by a \sqrt{N} increase in width in the spatial direction, thus conserving area. In the case of equal sampling it is clear that we require N more pixels in the PIMMS case.

3. PIMMS IR – A single-mode fiber fed spectrograph

3.1 Design

The key components of the PIMMS design are illustrated in Fig. 2. Light is coupled into the multimode port of the 1×7 PL, where it is converted to an array of SMFs. The SMFs form the pseudo-slit for a compact and diffraction-limited spectrograph, here dubbed PIMMS IR. In the PIMMS IR design we use a collimator and camera combination with effective magnification of 7.7. The collimated beam has a $1/e^2$ diameter of 13mm and is dispersed by a volume phase holographic grating manufactured by Wasatch Photonics, Inc. with 1120 lines/mm. The primary detector is a Xenics Xeva series 320×256 InGaAs array with a pixel pitch of 30 microns ($9.6\text{mm} \times 7.68\text{mm}$). We also use an alternate model with a 640×512 array with 20 microns pixels. The other optical components are drawn from the Thorlabs, Inc. catalogue.

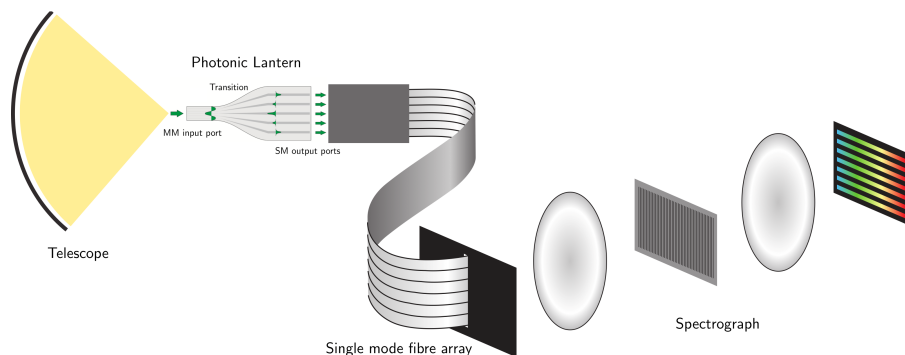


Fig. 2. Schematic of PIMMS IR setup. Light from any source, in this case a telescope, is coupled to the MM port of a PL. The PL produces multiple SMFs that form the pseudo-slit of a compact diffraction-limited bulk optic spectrograph.

3.2 Instrumental PSF

To characterize the instrumental PSF, we fed the PIMMS IR spectrograph with one SMF. The input was coupled directly from a tunable laser source (Tunics 3642 HE L) set to 1550.25 nm. A typical line profile (collapsed in the spatial direction with a Gaussian weighted summation) is shown in Fig. 3, along with the best-fit Gaussian, ZEMAX physical optics propagation (POP) simulations and the same laser line measured using an OSA (ADVANTEST Q8384). We also show the typical spectral line profiles attributed to the IRIS2 spectrograph [20] and the AAOmega spectrograph [21]. These show that the wings in a PIMMS design are much weaker than in a conventional design, besting IRIS2 by two orders of magnitude and AAOmega by one. Both IRIS2 and AAOmega have lower resolutions than PIMMS IR, and operate over different wavelength ranges. To provide a fair comparison they have been scaled to have the same FWHM, measured by their respective best-fit Gaussian, as PIMMS IR.

The measured FWHM of the PIMMS IR PSF of the spectral and spatial profiles is $\sim 57.5\mu\text{m}$ (1.9 pixels). This is just 3.6% larger than that predicted by the POP simulation. In the spectral profile (top part of Fig. 3) the wings are remarkably consistent with those predicted by ZEMAX POP simulations. At low intensity levels, they do begin to depart from the simulation. The wings of the spatial profile (bottom part of Fig. 3) are slightly better than the spectral profile, but not as low as expected from the POP simulation. We note that in our simulations, if the truncation factor is increased (i.e. the diameter of lens is reduced) in the collimator the wings in the spatial profile will increase until they are approximately symmetrical with the spectral profile, at which point both the spectral and spatial wings increase in strength together. Thus, the symmetry of the measured PSF seems to indicate a broadening effect not fully accounted for in POP is the dominant cause of the discrepancies.

We attribute this to the fact that (i) surface irregularities ($\lambda/4$ at 633 nm or $\sim\lambda/10$ at 1550 nm) are on the edge of diffraction-limited, which is not accounted for in POP; and (ii) slight differences in the alignment between ZEMAX and reality (e.g. a small change in the camera element separation results in an order of magnitude change in focal length). These factors are all inherent drawbacks of COTS components, which nonetheless perform extremely well.

The FWHM of 1.9 pixels corresponds to ~ 49 pm spectrally. So the resolving power using the generalized Rayleigh width (Eq. (3)) is $R \sim 28,300$. More than 99% of the total power is concentrated in the core of the PSF where it remains Gaussian-like. Less than 1% of the power is contained in the extended wings and is in part attributable to veiling glare from the bulk COTS components. This allows the design to resolve at higher resolutions in high contrast situations (assuming an appropriate detector of course). Table 1 summarizes the maximum dynamic range (i.e. intensity contrast between peaks) possible at spectral resolutions of 1, 2, 4 and 8 times the best resolution of PIMMS IR. For example two spectral lines that are separated by 0.11 nm are resolved if the ratio between their peak intensities is not larger than 17.5 dB (57:1).

Table 1. Maximum resolution attainable at various contrast levels with the PIMMS IR spectrograph.

No. Resolution elements	Dynamic Range (dB)
1 (0.0548 nm)	0 (1:1)
2 (0.110 nm)	17.5 (57:1)
4 (0.219 nm)	42 (16500:1)
8 (0.438 nm)	51 (130,000:1)

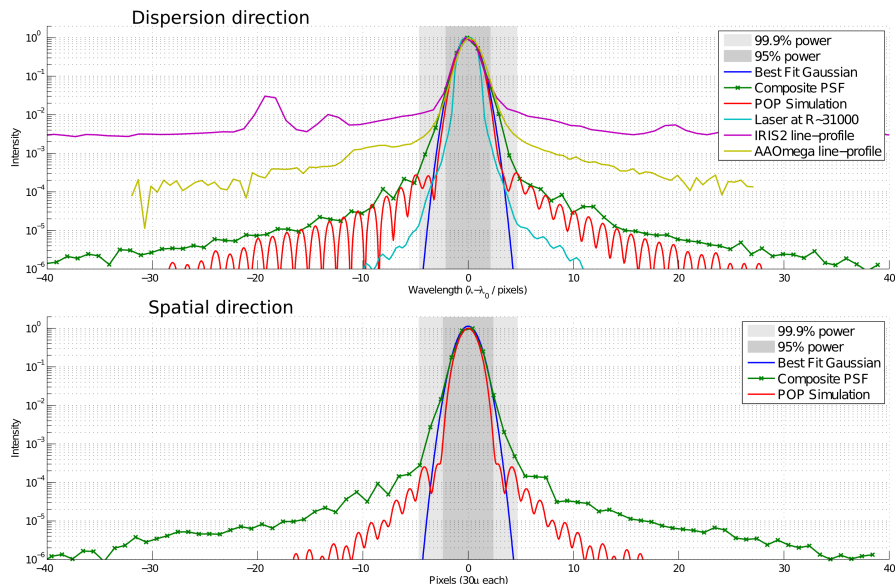


Fig. 3. PSF line profiles (summed along the perpendicular axis with a Gaussian weighting, as would be done with real spectra) from PIMMS IR with comparisons in the spectral (top) and spatial (bottom) direction. Shown are: Green (stars) – composite of underexposed and overexposed profiles as explained in text; Red – ZEMAX POP simulation; Blue – Best fit Gaussian; Cyan – OSA spectrum of laser source; Purple and Yellow – Typical line profiles attributed to the IRIS2 150um slit and AAOmega fiber inputs respectively (The spectra from these spectrographs have been scaled to have the same FWHM determined from the best fit Gaussian, due to the difference in actual spectral resolution and pixel sampling). Note that the comparison spectra are shown to display the intensity level that wings of the respective PSF present.

3.3 Photonic lantern input

We then fed the PIMMS IR spectrograph with a nominally 7-mode PL device in order to measure the performance of a photonic lantern feed. To our knowledge, no other PL demonstrations have obtained spectra simultaneously of the complete PL feed. Studies of the spectral variability took spectra separately using an OSA [22]. A previous demonstration using an AWG-based PIMMS only used 12 of 19 of the SM ports of that PL, primarily due to physical space restrictions imposed by 125 μ m core spacing of conventional SMF and the need to maintain sufficient separation between cross-dispersed spectra [23,24]. We overcame this by (i) using a smaller lantern, 1 \times 7 vs. 1 \times 19; (ii) forming the spectrograph entrance slit using the photonic TIGER configuration [11]. This allowed us to use conventional 125 μ m fiber and form a compact slit for a small sacrifice in the effective spectral bandwidth.

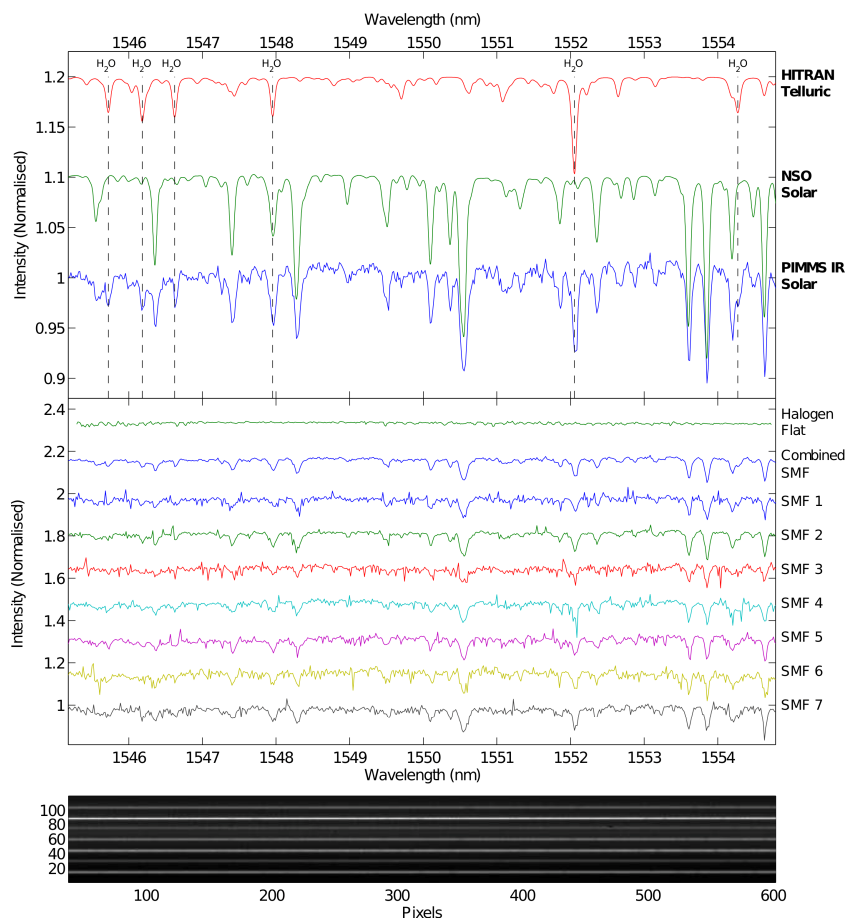


Fig. 4. *Top:* Shown are: (i) A simulated atmospheric absorption spectrum using HITRAN [26]; (ii) Reference solar spectrum from NSO/Kitt Peak Observatory [25] convolved down to R~30000 for comparison. (iii) The PIMMS IR Solar spectrum obtained in Sydney, Australia. Spectra are offset vertically for convenience. The PIMMS IR spectrum shows the expected telluric absorption features (mostly water vapor) superimposed on the solar spectrum. *Middle:* From top to bottom the first spectrum is the response to a tungsten halogen lamp, the second is the solar spectrum obtained when combining the PL SMF outputs. The remaining seven are the individual spectra of the seven SMF outputs and their combination. Each spectrum is normalized by its respective median value, and offset for clarity. The noise level varies between spectra due to the differences in mean signal. *Bottom:* Detector image of the dispersed single-mode output fibers of the PL.

To obtain a final spectrum three sets of data (composed of light and dark frames) were acquired. The first was used for wavelength calibration, where the MM port of the PL is illuminated using the far-field of a SMF that is coupled to our tunable laser source. In the second, the MM port was directly illuminated with a tungsten halogen light source (Thorlabs OSL1-EC) to obtain a flat field response. Finally, raw spectra were obtained by aiming the MM port directly at the Sun. The individual spectra are shown in the middle part of Fig. 4, where each spectrum is normalized and offset. Also shown here is the flat response of PIMMS IR from a halogen source and the final combined spectrum formed from the average of the individual spectra. The noise visibly changes in the seven individual spectra; this is consistent with the relative intensity difference between each of them. In contrast to previous results [22], no spectral variation is seen at narrow bandwidth and high resolution between the individual spectra of the SMF outs of the 1×7 PL. Averaging the 7 individual spectra forms the complete lantern spectrum. This is shown in the top of Fig. 4 along with a reference solar spectrum [25] and a model telluric spectrum [26]. Both the comparison spectra were convolved with a Gaussian to have a similar resolution to the PIMMS IR spectrum. In the PIMMS IR wavelength range water vapor is the dominant absorber, the six strongest lines are marked in Fig. 4.

The throughput from slit to detector is simply measured using a power meter at both ends and illuminating the MM port with the tunable laser source. The measured throughput of the optics and diffraction grating is $\sim 74\%$. Including a nominal detector QE of $\sim 80\%$ the spectrograph throughput is $\sim 60\%$. The typical throughput of the current generation of 1×7 lanterns is $\sim 85\%$. Thus the effective throughput, of PIMMS IR, including the lantern transition is $\sim 50\%$. Performance could be improved with better-matched AR coatings on all optical surfaces.

4. Conclusion

Using a MM to SM converter known as a photonic lantern, we have demonstrated the power of the PIMMS concept. The photonic lantern allows us to remap an arbitrary input to an array of SMFs at the spectrograph's entrance slit, thus resulting in a diffraction-limited slit. This results in the most compact spectrograph possible (for a given resolving power) limited only by detector sampling requirements. More importantly, the spectrograph's optical design is completely decoupled from original light source. This means that the same design could in principle be used on a 30 cm telescope, a 30 m telescope or any other source that can be coupled to an MMF. The PIMMS IR detector requires the same area of an MM design, but for an MMF with N (unpolarized) modes, we require N SMFs. This demands at least $\varepsilon.N$ more pixels to appropriately sample the PIMMS spectra. For a conventional detector with square pixels, this leads to an $(\varepsilon.N)^{1/2}$ increase in read noise (assuming the smaller pixels have the same read noise as the larger pixels in the MM case) when the final spectra are combined. This increased noise in the system could be a limitation in extremely low-level light applications. However, this is partially balanced by the decreased size of the instrument, increases in throughput over conventional designs and the trend toward lower read noise detectors. In a subsequent paper, we show that the read noise penalty can be mitigated with a customized detector employing rectangular pixels. An initial design of such a device is under development with e2v (UK).

The PSF of the SMF pseudo-slit also shows an additional advantage of the photonic lantern approach. Scattered light is significantly reduced with $<1\%$ of the power outside the core of the PSF. This could be improved further using a customized optical design rather the COTS components. We also showed the photonic lantern faithfully reproduces the input source spectrum when combining the individual source spectra, and importantly does not appear to be affected by any wavelength dependent variation in intensity between SMF outputs.

Acknowledgments

This research was supported by JBH through a Federation Fellowship from the Australian Research Council. Authors would also like to thank Jon Lawrence at AAO for use of equipment and Joel Rafael Salazar Gil for assistance in the fabrication of the 1×7 photonic lantern.